EXPLORATION OF THE SUB-NANOSECOND MAGNETISATION DYNAMICS OF PARTIALLY BUILT HARD DISK DRIVE WRITE-HEAD TRANSDUCERS AND OTHER TOPICAL MAGNETIC AND SPINTRONIC MATERIALS AND DEVICES

Submitted by

ROBERT ALEXANDER JAMES VALKASS

to the

UNIVERSITY OF EXETER

as a thesis for the degree of

DOCTOR OF PHILOSOPHY IN PHYSICS

in

AUGUST 2017

I certify that all material in this thesis which is not my own work has been identified and that no material has previously been submitted and approved for the award of a degree by this or any other University.

. . . .
Robert Alexander James Valkass

For Donald Seymour Baker

Abstract

In this thesis both the static and dynamic magnetic behaviour of complex three-dimensional nanoscale commercial hard disk drive write heads and thin film structures of interest to emerging spintronic devices have been investigated using a plurality of experimental techniques. The magneto-optical Kerr effect (MOKE) provides the basis for an optical microscopy technique sensitive to the magnetisation of a sample, detectable as a change in polarisation of light reflected from the sample surface. With a modelocked laser light source, synchronised electrical pulse generator and lock-in amplifier (LIA), a stroboscopic technique has been used to observe the magnetisation dynamics of hard disk drive write heads at 600 nm spatial resolution and 10 ps time resolution in response to a driving electrical pulse. The equilibrium magnetic state of these devices has been directly imaged by x-ray photo-emission electron microscopy (XPEEM), as well the stability of the equilibrium state in response to the application of an external bias field. Direct images of the equilibrium state obtained by XPEEM were found to agree with inferences made from MOKE images. Time-resolved scanning Kerr microscopy (TRSKM) images of magnetisation dynamics showed that flux does not form in 'beams' as commonly believed, but instead nucleates in separate sites across the writer.

Static and time-resolved x-ray techniques have also been used to investigate a number of thin films of interest to spintronics. Spin pumping and spin transfer torque in Co_2MnGe / Ag / $Ni_{81}Fe_{19}$ spin valves were explored using time-resolved x-ray ferromagnetic resonance (XFMR) carried out at Diamond Light Source (DLS),

as well as static x-ray magnetic circular dichroism (XMCD) for sample characterisation. This has provided element-specific measurements of the spin state in the source and sink layers of the spin valve, revealing a clear sign of spin transfer torque, while also investigating the role of sink layer thickness in spin pumping and damping.

Ferrimagnetic yttrium iron garnet ($Y_3Fe_2(FeO_4)_3$) (YIG), a material of great interest in spintronics, has been studied by static and dynamic XMCD in comparison with ferromagnetic Co. While static and dynamic spectra for Co were identical, those for YIG differed markedly. While this may hint at a phase difference between the precession of Fe moments on different lattice sites, the true source of this difference has not been identified. Comparisons between vector network analyser ferromagnetic resonance (VNA-FMR) and XFMR measurements further suggest the presence of long-range inhomogeneities in the YIG.

The spin dynamics of an antiferromagnet being driven by a ferromagnet have also been investigated using XMCD and x-ray magnetic linear dichroism (XMLD). A CoO / Fe / $Ni_{81}Fe_{19}$ trilayer wherein the thickness of the CoO layer varies across the sample has been thoroughly characterised by static XMCD and XMLD, providing information necessary to fully interpret time-resolved MOKE measurements on these samples. Measurements have shown that even small amounts of ordered CoO significantly modify the resonant field and linewidth of the adjacent ferromagnetic layers. Phase-resolved measurements of CoO spins have shown these spins to precess in phase with those of the adjacent Fe. The viability of dynamic XMLD measurements has also been confirmed.

Finally, potential directions for future work in each project are discussed.

Acknowledgements

Amongst my many mistakes to date, I chose to leave writing this section of my thesis until the very end. I realise now that this is by far the hardest part to write.

Firstly, I am indebted to my supervisor Prof. Rob Hicken not only for his calming, rational influence and for sharing his wisdom which extends far beyond the realm of physics, but also for making sure my PhD involved visits to such exotic destinations as Honolulu, Berlin, San Francisco, York, Leeds, Manchester, Glasgow and an industrial park six miles south-west of Didcot. My average speed remained in excess of 25 miles per hour for over three weeks at one point.

I am also grateful to Seagate Technology for their funding throughout my PhD, and to Tring Charities Millennium Education Foundation for their vital support in helping me to complete my undergraduate master's degree.

Thank you to my mentor, Misha Portnoi, and my second supervisor, Volodymyr Kruglyak, for making the time dedicated to our mandatory regular meetings as useful as any of us could ever have hoped for.

Beamtimes can be a very stressful time for all involved, so thank you Elke Arenholz, Alex Baker, Stuart Cavill, Sarnjeet Dhesi, Adriana Figueroa, Florian Kronast, Gerrit van der Laan, Yanwei Liu, Francesco Maccherozzi, Padraic Shafer, and all the other staff at the ALS, BESSY and Diamond for always making us feel welcome and making sure things went as smoothly as possible.

During my time in Exeter I had the good fortune to work with many fantastic people who ensured that frustration in the lab was always punctuated with laughter, or at least the reassurance that I wasn't alone in my troubles. Thank you Chris,

Erick, Haidar, Leigh, Nick, Paul, Reem, Tim and Wei. And of course, thank you Tom—who'd have thought tackle-hugging me to the ground on the first day of the first year undergraduate lab would have got us both this far?

My final and most heartfelt thanks are of course reserved for Emily. Thank you for sticking by me through all the stress every time I had a beamtime, five home moves, and many long nights writing this thesis. Despite searching for a considerable length of time, I simply cannot find the words to describe the encouragement, support and love you have shown me over the years.

Contents

List of Figures

List of Tables

Author's Declaration

The work presented in this thesis is the result of collaboration between a great many people. Specific acknowledgements of contributions from colleagues will be made throughout the text, but a summary is provided below. In all cases, collaborators are presented alphabetically by surname.

I draw particular attention to the contributions made by my Ph.D. supervisor, Prof. Rob Hicken, which are far too numerous to mention individually.

Chapter 2: Background physics

This chapter contains the background magnetic theory necessary for an understanding of the results presented within this thesis. The content has been compiled by myself after an extensive review of the literature, and all authors and their works are acknowledged throughout the chapter.

Chapter 3: Experimental techniques

The principles of magneto-optic effects and x-ray characterisation techniques are not the result of my own work. The explanations I present have been compiled by myself, and authors and their works are acknowledged throughout.

The Kerr microscopy experiments at the University of Exeter were built and developed by Dr Anjan Barman, Prof. Rob Hicken, Dr Paul Keatley, Prof. Volodymyr

Kruglyak, Dr Yanwei Liu, Dr Tom Loughran, Dr Leigh Shelford, Dr Ralph Wilks, Dr Jing Wu, and Dr Wei Yu.

The vector network analyser ferromagnetic resonance (VNA-FMR) experiment at the University of Exeter was built and developed by Prof. Rob Hicken, Dr Max Marcham and Dr Leigh Shelford.

X-ray experiments were performed at three synchrotrons: Diamond Light Source (DLS) in Didcot, UK; the Advanced Light Source (ALS) in Berkeley, California, USA; and Berliner Elektronenspeicherring-Gesellschaft für Synchrotronstrahlung (BESSY II) in Berlin, Germany. Individual experimental teams are acknowledged in full below.

Chapter 4: Imaging the remanent state and magnetisation dynamics of partially-built hard disk writers

The samples studied in this chapter were fabricated by Seagate Technology under the supervision of Dr Muhammad Asif Bashir, Dr Peter Czoschke, Dr Mark Gubbins and Dr Radek Lopusnik. Further sample processing to make the samples suitable for x-ray measurements was carried out by Mark Heath, Dr Leigh Shelford, Dr Wei Yu and myself at the University of Exeter.

X-ray photo-emission electron microscopy (XPEEM) images were obtained at DLS and BESSY II. On beamline I06 at DLS images were obtained with the assistance of Dr Stuart Cavill, Prof. Sarnjeet Dhesi, and Dr Francesco Maccherozzi. The experimental team from the University of Exeter comprised Dr Paul Keatley, Dr Leigh Shelford and myself. Images taken at BESSY II were obtained using the SPEEM end station of beamline UE49-PGMa with the assistance of Dr Florian Kronast, with the experimental team comprising Prof. Rob Hicken and myself. Time-resolved scanning Kerr microscopy (TRSKM) measurements were performed by

Dr Wei Yu and myself at the University of Exeter in the labs of Prof. Rob Hicken. Data analysis of both XPEEM and TRSKM results was conducted by myself.

Chapter 5: Time-resolved scanning Kerr microscopy of flux beam formation in hard disk write heads

The samples studied in this chapter were fabricated by Seagate Technology under the supervision of Dr Muhammad Asif Bashir, Dr Peter Czoschke, Dr Mark Gubbins and Dr Radek Lopusnik. Images were recorded using the time-resolved scanning Kerr microscope in the labs of Prof. Rob Hicken. Data were acquired by Erick Burgos, Tim Spicer and myself.

Chapter 6: Spin pumping and spin transfer torque in Co_2MnGe / Ag / $Ni_{81}Fe_{19}$ spin valve structures

Samples were grown by Dr Jeff Childress and Dr Jordan Katine at Hitachi Global Storage Technologies (HGST). VNA-FMR measurements were performed by Dr Chris Durrant and Dr Leigh Shelford at the University of Exeter in the labs of Prof. Rob Hicken. Macrospin modelling code was developed by Prof. Rob Hicken and modified by Dr Chris Durrant.

X-ray measurements were performed by Dr Leigh Shelford and myself at both DLS and ALS. From the Magnetic Spectroscopy Group at DLS, thanks go to Dr Alex Baker, Dr Adriana Figueroa-Garcia, and Prof. Gerrit van der Laan with further assistance provided by Liam Duffy of the Clarendon Laboratory at the University of Oxford. From beamlime I10 at DLS, thanks go to Dr Raymond Fan and Dr Paul Steadman. From beamlines 4.0.2 and 6.3.1 at ALS, thanks go to Prof. Elke Arenholz, Christoph Klewe, Dr Alpha N'Diaye, and Dr Padraic Shafer.

Chapter 7: Time-resolved x-ray spectroscopy of thin film yttrium iron garnet

Yttrium iron garnet ($Y_3Fe_2(FeO_4)_3$) (YIG) samples were grown at the University of Leeds by Dr Scott Marmion in the labs of Prof. Bryan Hickey.

Measurements were performed with the assistance of a great number of collaborators at two synchrotrons. From the Magnetic Spectroscopy Group at DLS, thanks go to Dr Alex Baker, Dr Adriana Figueroa-Garcia, and Prof. Gerrit van der Laan. From beamline I06 at DLS, thanks go to Prof. Sarnjeet Dhesi, Dr Yanwei Liu, and Dr Francesco Maccherozzi. From beamlime I10 at DLS, thanks go to Dr Raymond Fan and Dr Paul Steadman. From beamlines 4.0.2 and 6.3.1 at ALS, thanks go to Prof. Elke Arenholz, Dr Alpha N'Diaye, and Dr Padraic Shafer.

Along with myself, the experimental team from Exeter at various times comprised Prof. Rob Hicken, Dr Haidar Mohamad, and Dr Leigh Shelford, with further assistance from Dr Stuart Cavill at the University of York. Data analysis was performed by Dr Leigh Shelford and myself. Theoretical modelling of the behaviour of the different iron sites was performed by Prof. Gerrit van der Laan.

Chapter 8: Spin dynamics of an antiferromagnet driven by interfacial coupling to a ferromagnet

Samples were grown by Dr Jia Li and Dr Ali Tan in the labs of Prof. Zi Qiu at the University of California, Berkeley.

Measurements were performed on beamlines I06 and I10 at DLS using the portable octupole magnet system (POMS) end station provided by the Magnetic Spectroscopy Group. From DLS thanks go to Dr Alex Baker, Dr Adriana Figueroa-Garcia, Prof. Gerrit van der Laan, and Dr Yanwei Liu. The experimental team from Exeter comprised Dr Leigh Shelford and myself, with further assistance from Dr Stuart Cavill at the University of York.

List of Publications

R. A. J. Valkass, W. Yu, L. R. Shelford, P. S. Keatley, T. H. J. Loughran, R. J. Hicken, S. A. Cavill, G. van der Laan, S. S. Dhesi, M. A. Bashir, M. A. Gubbins, P. J. Czoschke, and R. Lopusnik. Imaging the equilibrium state and magnetization dynamics of partially built hard disk write heads. *Applied Physics Letters* **106**, 232404 (2015).

R. A. J. Valkass, T. M. Spicer, E. Burgos Parra, R. J. Hicken, M. A. Bashir, M. A. Gubbins, P. J. Czoschke, and R. Lopusnik. Time-resolved scanning Kerr microscopy of flux beam formation in hard disk write heads. *Journal of Applied Physics* **119**, 233903 (2016).

C. J. Durrant, L. R. Shelford, R. A. J. Valkass, R. J. Hicken, A. I. Figueroa, A. A. Baker, G. van der Laan, L. B. Duffy, P. Shafer, C. Klewe, E. Arenholz, S. A. Cavill, J. R. Childress, and J. A. Katine. Dependence of spin pumping and spin transfer torque upon $Ni_{81}Fe_{19}$ thickness in Ta / Ag / $Ni_{81}Fe_{19}$ / Ag / Co_2MnGe / Ag / Ta spin-valve structures. *Physical Review B* **96**, 144421 (2017).

H. J. Mohamad, L. Shelford, M. Aziz, U. Al-Jarah, R. Al-Saigh, R. A. J. Valkass, S. Marmion, B. J. Hickey, and R. J. Hicken. Thermally induced magnetization dynamics of optically excited YIG/Cu/$Ni_{81}Fe_{19}$ trilayers. *Physical Review B* **96**, 134431 (2017).

List of Acronyms

A

AC alternating current

ALS Advanced Light Source

B

BESSY II Berliner Elektronenspeicherring-Gesellschaft für Synchrotronstrahlung

BL bridge length

BW bridge width

C

CPW co-planar waveguide

D

DC direct current

DLS Diamond Light Source

F

FMR ferromagnetic resonance

FWHM full width at half maximum

G

GGG gadolinium gallium garnet ($Gd_3Ga_5O_{12}$)

GMR giant magnetoresistance

H

HAMR heat-assisted magnetic recording

HGST Hitachi Global Storage Technologies

I

IPA propan-2-ol, also known as isopropyl alcohol

L

LIA lock-in amplifier

LLG Landau-Lifshitz-Gilbert

M

MBE molecular beam epitaxy

MOKE magneto-optical Kerr effect

MRAM magnetic random-access memory

N

NA numerical aperture

P

PCB printed circuit board

PEEM photoemission electron microscopy

PMMA poly(methyl 2-methylpropenoate), also known as poly(methyl methacrylate)

POMS portable octupole magnet system

PW paddle width

R

RF radio frequency

S

SPEEM spin-resolved photo-emission electron microscope

STO spin transfer oscillator

STT spin transfer torque

SUL soft magnetic underlayer

T

TRSKM time-resolved scanning Kerr microscopy

V

VMM vector magnet magnetometer

VNA vector network analyser

VNA-FMR vector network analyser ferromagnetic resonance

VSM vibrating sample magnetometer

X

XAS x-ray absorption spectroscopy

XEOL x-ray excited optical luminescence

XFMR x-ray ferromagnetic resonance

XMCD x-ray magnetic circular dichroism

XMLD x-ray magnetic linear dichroism

XPEEM x-ray photo-emission electron microscopy

XPS x-ray photoelectron spectroscopy

Y

YIG yttrium iron garnet ($Y_3Fe_2(FeO_4)_3$)

YR yoke recess

CHAPTER 1

Introduction

Humankind has been recording information since at least the beginning of written history in around 3500 BCE, with the recording of numbers dating back even further, to over 20 000 years ago.[1] Initially, recording and storing information of any significant quantity required considerable physical effort, skill and dexterity. A number of significant recent inventions, including the printing press and computer, caused a rapid increase in our ability to both generate and store information. By 2007, humankind had the ability to store around 3×10^{20} B of information, doubling every three years.[2] To keep pace with this ever-growing supply of information, the field of magnetic data storage has necessarily remained an area of very active research. For the last decade or so, perpendicular ferromagnetic recording has been the technology of choice for commercial hard disk drives. In that time, improvements in the media, read head and write head, along with technologies such as heat-assisted magnetic recording (HAMR), have driven storage densities past the $1\,\mathrm{Tbit\,in^{-2}}$ barrier.[3] There will, however, come a time when the physical limits of perpendicular ferromagnetic recording can be pushed no further. Recording technologies based on spintronics are a promising candidate for next-generation magnetic storage devices, promising greater storage densities, faster access times and lower power usage.

This thesis is positioned at the junction between these two fields, covering both conventional perpendicular ferromagnetic hard disk drives, and materials of topical interest to emerging spintronic devices. The first half of this thesis presents detailed studies of both the equilibrium state and magnetodynamics of hard disk drive write heads commonly used in commercially produced hard disk drives. The latter half focuses on x-ray measurements of materials of particular interest for spintronic storage devices.

Chapter 2 begins by outlining the theory relevant to thin film magnetic structures and devices. The classical description of magnetism is presented, providing the groundwork for a brief introduction to the relevant quantum mechanics necessary for a more complete understanding of ferromagnetism. The concepts relevant to magnetism on a micro- and nanoscopic scale are introduced, as well as a discussion of magnetisation precession. Finally, the specifics of perpendicular hard disk recording head design are presented, including the magnetic processes which occur in the write head.

This theoretical basis is put to use in Chapter 3, which details the experimental techniques relevant to the results presented in this thesis. The chapter begins by explaining the origins of the magneto-optical Kerr effect (MOKE) before describing how it has been measured during the studies presented in later chapters. The interaction between x-rays and magnetic materials is also introduced. A discussion of magnetic dichroism and the orbital and spin sum rules is presented, which is particularly relevant to the dynamic x-ray ferromagnetic resonance (XFMR) measurements presented in later chapters. The principles of x-ray photo-emission electron microscopy (XPEEM) are also introduced, which are relevant to Chapter 4.

Chapters 4 and 5 are concerned with studies of perpendicular magnetic recording heads fabricated by Seagate Technology for use in commercial hard disk drives. In Chapter 4 static XPEEM measurements of a range of different geometric designs of write head are presented, allowing a comparison between the equilibrium states of different writer designs, and between nominally identical writers. The effect of an applied field on the equilibrium state is also presented, allowing the stability of the equilibrium state to be investigated. Finally, the equilibrium state measured by XPEEM is compared to observations of dynamic time-resolved scanning Kerr microscopy (TRSKM) measurements, as well as the equilibrium states inferred from those measurements. XPEEM and TRSKM measurements were found to be in agreement, with XPEEM further revealing that crystalline anisotropy dominates the equilibrium state of these write heads, but the competition between shape and crystalline anisotropy determines how stable and repeatable that equilibrium state is.

In Chapter 5 TRSKM measurements of flux beam formation in hard disk write heads are presented, with a focus on the spatial distribution of flux during the rise of the driving current given different driving coil distributions. The increased time resolution presented here compared to previous measurements provides evidence that the belief that flux forms in uniform "beams" which then propagate through the writer is somewhat misplaced. The considerable variations in observed dynamics on the picosecond timescale instead suggest that the equilibrium magnetic state of an individual writer has just as much influence over the generated flux as the spatial distribution of the driving coils.

Chapters 6 to 8 move away from perpendicular recording and towards materials of relevance to emerging spintronic storage technologies such as magnetic random-access memory (MRAM) and racetrack memory. In Chapter 6 x-ray measurements of spin pumping and spin transfer torque (STT) in Co_2MnGe / Ag / $Ni_{81}Fe_{19}$ spin valve structures are presented. Phase-resolved XFMR measurements provide element-specific measurements of the spin state in the different layers of the spin valve, and reveal clear signs of spin pumping due to STT.

In Chapter 7 both static and time-resolved x-ray spectroscopy of thin-film yttrium iron garnet ($Y_3Fe_2(FeO_4)_3$) (YIG) are presented. Static and dynamic x-ray magnetic circular dichroism (XMCD) spectra of Fe in ferrimagnetic YIG show significant differences which are not typically observed in ferromagnetic materials. These differences may hint at a possible phase difference between spin precession on different Fe sites within the YIG lattice. However, despite the consideration of a number of corrective measures, the true origin of this discrepancy could not be identified. Further research is therefore needed before firm conclusions can be drawn.

The penultimate chapter, Chapter 8, is the final experimental chapter and is concerned with spin dynamics of antiferromagnetic CoO driven by interfacial coupling to a ferromagnet. Time-resolved MOKE, static XMCD and x-ray magnetic linear dichroism (XMLD), and dynamic XMCD XFMR measurements have been combined to characterise the magnetic state of the CoO / Fe / $Ni_{81}Fe_{19}$ structure, and to make phase-resolved measurements of precessing Fe moments adjacent to different CoO layer thicknesses. It has been shown that a small amount of ordered antiferromagnetic CoO significantly modifies the resonant field and linewidth of the adjacent ferromagnetic layer, and the first evidence of antiferromagnetic CoO spins precessing in phase with ferromagnetic Fe has been presented.

Finally, Chapter 9 details the conclusions of the work presented in this thesis. The potential direction of future work in each study is also outlined.

CHAPTER 2

Background physics

2.1 Introduction

The work presented in this thesis revolves around the study of magnetic thin films and nanoscale three-dimensional structures. This chapter will therefore outline the theoretical concepts of magnetism necessary to understand the results presented herein.

This chapter begins with the classical description of paramagnetism and magnetic moments before approaching the concept of ferromagnetism. At this point it is necessary to introduce a quantum mechanical treatment, although a derivation from first principles is far beyond the scope of this chapter. The role of ferromagnetism in the operation of a hard disk drive write head forms the final section of this chapter.

2.2 Classical Descriptions of Magnetism

The classical treatment of magnetic effects as the result of orbiting electric charges, while failing to describe permanent magnetisation and long range ordering of moments, provides a good starting point.

For an electron moving with angular velocity $\boldsymbol{\omega}$ in a circular orbit of radius $\boldsymbol{r}$ around an atomic nucleus, the electron's angular momentum $\boldsymbol{L}$ is given by[4]

$$\boldsymbol{L} = \boldsymbol{r} \times \boldsymbol{p} = m_e \left(\boldsymbol{r} \times \boldsymbol{v}\right) = m_e \left(\boldsymbol{r} \times \left(\boldsymbol{\omega} \times \boldsymbol{r}\right)\right) = m_e \omega r^2 \hat{\boldsymbol{\omega}} \tag{2.1}$$

where m_e is the mass of the electron and $\boldsymbol{p}$ is its linear momentum. Being a charge in motion, the electron has an associated current I:

$$I = \frac{-|e|\omega}{2\pi} \tag{2.2}$$

where e is the elementary positive charge (an electron therefore having a charge equal to $-e$). Knowing this allows for calculation of the magnetic moment $\boldsymbol{\mu}$ as the product of the current and the area of the orbit, $\boldsymbol{A} = \pi r^2 \hat{\boldsymbol{\omega}}$:

$$\boldsymbol{\mu} = I\boldsymbol{A} = \frac{-|e|\omega}{2\pi} \pi r^2 \hat{\boldsymbol{\omega}} \,. \tag{2.3}$$

This means $\boldsymbol{\mu}$ and $\boldsymbol{L}$ are parallel, and we have a simple ratio between the two:

$$\boldsymbol{\mu} = \frac{-|e|}{2m_e} \boldsymbol{L} \,. \tag{2.4}$$

The Bohr model of the hydrogen atom allows us to attach a value to $\boldsymbol{\mu}$. Knowing that $\boldsymbol{L}$ must be an integer multiple of $\hbar$, the smallest possible value of μ is therefore given by

$$\mu_H = \frac{-|e|\hbar}{2m_e} \equiv \mu_B \tag{2.5}$$

with μ_B being known as the Bohr magneton.

While Equation (2.4) provides a satisfying and intuitive result, it is also the first place at which classical electromagnetism falls down. Equation (2.4) holds true for the oribtal motion of an electron, however quantum mechanics tells us that the electron's angular momentum has a further contribution in the form of the electron's spin. This contribution to the magnetic moment, $\boldsymbol{\mu}_s$, is twice as large as predicted by classical electromagnetism:[4]

$$\boldsymbol{\mu}_s = \frac{-|e|}{m_e} \boldsymbol{s} \tag{2.6}$$

where $\boldsymbol{s}$ is the electron's spin angular momentum. The total magnetic moment $\boldsymbol{\mu}$ of an atom is therefore due to some combination of the orbital angular momentum and the spin angular momentum:

$$\boldsymbol{\mu} = -g\frac{|e|}{2m_e}\boldsymbol{j} \tag{2.7}$$

where $\boldsymbol{j}$ is the combined orbital and spin contributions to the angular momentum. The scaling factor g is a dimensionless constant called the Landé g-factor and depends on the atomic state of the atom in question. For a purely orbital atomic moment $g = 1$, whereas a purely spin moment gives $g = 2$. For any realistic system such as an atom g lies somewhere between these extremes, however predicting the value of g for any given atomic state is far beyond the limits of classical calculations.

2.2.1 Precession of Magnetic Moments

Equation (2.7) leads to an interesting consequence: having the magnetic moment aligned with the electron's angular momentum will cause the magnetic moment to precess when placed in an external magnetic field. When placed in an external magnetic field $\boldsymbol{B}$, the magnetic moment will experience a torque $\boldsymbol{\tau}$ given by:

$$\boldsymbol{\tau} = \boldsymbol{\mu} \times \boldsymbol{B} \tag{2.8}$$

which will try to align the magnetic moment with the external field direction. However, the angular momentum $\boldsymbol{j}$ causes the magnetic moment to act like a gyroscope and precess about the applied external field, as shown in Figure 2.1.

Assume that in a time $\mathit{\Delta} t$ the angular momentum of a magnetic moment changes from $\boldsymbol{j}$ to $\boldsymbol{j}'$ at an angular frequency $\boldsymbol{\omega}$ and at a fixed angle ϑ relative to the axis of the applied field $\boldsymbol{B}$. The change in angular momentum $\mathit{\Delta} j$ is given by

$$\mathit{\Delta} j = \omega \mathit{\Delta} t |\boldsymbol{j}| \sin\vartheta \tag{2.9}$$

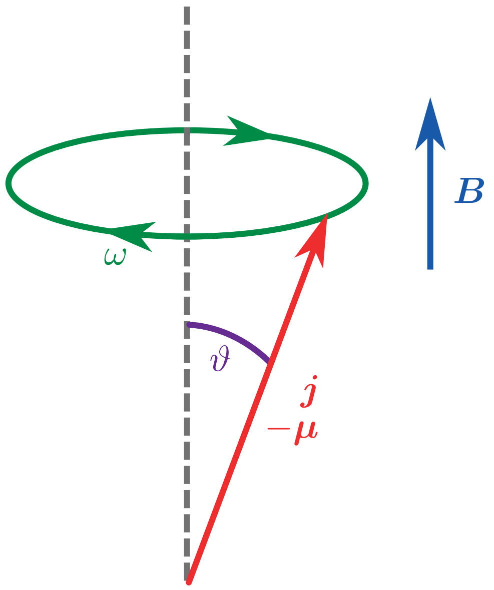

Figure 2.1: A magnetic moment $\boldsymbol{\mu}$ subjected to an external magnetic field $\boldsymbol{B}$ will precess with angular velocity $\boldsymbol{\omega}$ due to its associated angular momentum $\boldsymbol{j}$.

which can be rearranged for the rate of change of angular momentum. Combined with Equation (2.8) we can calculate angular frequency in terms of the applied field:

$$\tau = \frac{\mathrm{d}j}{\mathrm{d}t} = \omega j \sin\vartheta = \mu B \sin\vartheta \tag{2.10}$$

$$\Rightarrow \omega = \frac{\mu B}{j} \tag{2.11}$$

and combine this with Equation (2.7) to find the angular frequency in terms of the fundamental electron properties:

$$\omega = \frac{geB}{2m_e} \approx 5.6 \times 10^{11}\,\mathrm{rad\,s^{-1}\,T^{-1}}\,gB \tag{2.12}$$

2.2.2 Classical Paramagnetism

Langevin first proposed a theory of paramagnetism in 1905. Langevin proposed that every electron had an associated magnetic moment μ caused by the electron, and its accompanying charge, orbiting about its axis in a manner analogous to a macroscopic current loop through a wire. In most cases, the total angular momentum of all of an atom's electrons sums to zero, i.e. there is no net magnetic moment. However, in some cases an atom may have a net magnetic moment $\mu \approx \mu_B$. In the presence of an externally applied field $\boldsymbol{B}_{\text{ext.}} \neq 0$ each moment experiences a torque $\boldsymbol{\tau} = \boldsymbol{\mu} \times \boldsymbol{B}_{\text{ext.}}$ which acts to align each magnetic moment with the applied field direction, thus tending towards the state of lowest potential energy.

As an orbiting electric charge in a magnetic field, each electron also produces its own magnetic field. The total of this additional field is proportional to the density of magnetic moments in the material, i.e. the total magnetic moment $\boldsymbol{\mu}_{\text{total}}$ per unit volume V:

$$\boldsymbol{M} = \frac{\boldsymbol{\mu}_{\text{total}}}{V} \tag{2.13}$$

where the quantity $\boldsymbol{M}$ is known as the magnetisation of the material, giving an additional magnetic field $\boldsymbol{B}_{\text{add.}} = \mu_0 \boldsymbol{M}$.

The total magnetic field within such a material is therefore slightly greater than that of the free space surrounding it:

$$\boldsymbol{B}_{\text{total}} = \boldsymbol{B}_{\text{ext.}} + \boldsymbol{B}_{\text{add.}} = \boldsymbol{B}_{\text{ext.}} + \mu_0 \boldsymbol{M} \,. \tag{2.14}$$

Materials exhibiting such behaviour are paramagnetic, and the relative increase in magnetic field within the material relative to the equivalent free space is termed the material's relative permeability, K_m, such that a material's permeability μ can be defined:

$$\mu = K_m \mu_0 = (\chi_m + 1)\, \mu_0 \tag{2.15}$$

where the quantity χ_m is known as a material's magnetic susceptibility.

However, thermal fluctuations prevent complete alignment and lead to slight randomisation in the orientation of individual atomic magnetic moments. As the temperature increases, so too do the thermal fluctuations, and the net magnetisation tends to decrease.

The energy cost E of any misalignment ϑ with the applied field $\boldsymbol{B}_{\text{ext.}}$ is $-\boldsymbol{\mu} \cdot \boldsymbol{B}_{\text{ext.}}$. The net magnetisation of any individual atom can be calculated using a Boltzmann distribution, assuming the applied field is parallel to the z direction:

$$\langle \mu_z \rangle = \frac{\int_0^\pi \mu \cos\vartheta e^{(\mu B_{\text{ext.}} \cos\vartheta)/(k_B T)} \sin\vartheta \, \mathrm{d}\vartheta}{\int_0^\pi e^{(\mu B_{\text{ext.}} \cos\vartheta)/(k_B T)} \sin\vartheta \, \mathrm{d}\vartheta} . \tag{2.16}$$

The fraction of the moment which is aligned with $\boldsymbol{B}_{\text{ext.}}$ can then be expressed as the Langevin function:

$$\frac{\langle \mu_z \rangle}{\mu} = \coth\left(\frac{\mu B_{\text{ext.}}}{k_B T}\right) - \frac{k_B T}{\mu B_{\text{ext.}}} \equiv \mathcal{L}\left(\frac{\mu B_{\text{ext.}}}{k_B T}\right) . \tag{2.17}$$

When $\mu B_{\text{ext.}} \ll k_B T$, the small angle approximation

$$\coth(x) \approx \frac{1}{x} + \frac{x}{3} + \cdots \tag{2.18}$$

can be applied, giving

$$\frac{\langle \mu_z \rangle}{\mu} \approx \frac{\mu B_{\text{ext.}}}{3 k_B T} . \tag{2.19}$$

The total magnetisation M of a bulk material is simply the product of $\langle \mu_z \rangle$ and the number density of magnetic moments:

$$M = \frac{n \mu^2 B_{\text{ext.}}}{3 k_B T} = \frac{n \mu^2 \mu_0 H}{3 k_B T} . \tag{2.20}$$

The quantity M/H is equal to the magnetic susceptibility χ_m:

$$\chi_m = \frac{n \mu^2 \mu_0}{3 k_B T} . \tag{2.21}$$

This is Curie's law, and the material-specific constant $(n\mu^2\mu_0) / (3k_B)$ is known as a material's Curie constant.

While not paramagnetic, in those materials where the total angular momentum of all of an atom's electrons sums to zero, i.e. there is no net magnetic moment, there is still a magnetic effect. In these materials, an applied magnetic field acts to cause the electrons to align so as to generate a magnetic field to oppose that applied field. Such materials are termed diamagnetic, and have $\chi_m < 0$ (or $K_m < 1$).

For most materials, $|\chi_m|$ is typically very small. For example, copper has a susceptibility[5] $\chi_{\text{Cu}} = -9.63 \times 10^{-6}$ making it weakly diamagnetic. Aluminium has[6]

$\chi_{\mathrm{Al}} = 2.2 \times 10^{-5}$. For materials such as these, this classical analysis is sufficient as the internal magnetic field generated by the moments is negligible. However, a material like iron has[5] $\chi_{\mathrm{Fe}} = 200\,000$, or roughly ten billion times greater than aluminium's response to the same applied field. For these materials, another effect is clearly involved.

2.2.3 Weiss Domains

Pierre-Ernest Weiss was the first to attempt to explain, in 1906, the phenomenon of ferromagnetism in terms of an internal "molecular field". This molecular field works to align the dipoles of atoms within a ferromagnetic material despite thermal fluctuations attempting to disorder them.[7] Above the Curie temperature the thermal excitation of the atomic moments is sufficient to overcome the molecular field, resulting in random orientation of the moments and therefore a net zero magnetisation.

Weiss posited a further mechanism[8] to explain the phenomenon of hysteresis. Regions of a ferromagnetic material, called "domains", were each magnetised to the same saturation magnetisation M_{s} but in arbitrary directions. The measured magnetisation along any axis could therefore vary between 0 and M_{s} depending on the degree of alignment of domains along that axis. The application of an external magnetic field would cause the magnetisation within individual domains to align with the field, until all domains are aligned and the measured magnetisation across all domains reaches M_{s}.

Despite offering absolutely no justification or explanation for his two fundamental ideas, Weiss was surprisingly close to currently accepted theory and experimental results. Ferromagnetic domains were first directly imaged in 1931 by Francis Bitter[9] and the molecular field, as Weiss called it, is now better understood as the exchange field. However, Weiss' theory still had a few flaws. Firstly, below the Curie temperature the magnetisation $\boldsymbol{M}$ would have a fixed value, which was known not to be the case.[10] Secondly, his model did not quantitatively agree with experimental results: where Weiss predicted the magnitude of the molecular field to be $1 \times 10^8\,\mathrm{A\,m^{-1}}$, a field of $100\,\mathrm{A\,m^{-1}}$ is sufficient to reorient the domains in iron.

2.2.4 Classical Ferromagnetism

The high susceptibility of ferromagnetic materials such as iron and nickel implies the presence of a strong interaction which acts to align neighbouring magnetic moments parallel to one another. The interaction can be considered as an internal magnetic field B_{int}, the strength of which must be equivalent to the thermal excitation energy at the Curie temperature:[11]

$$\mu_B B_{\mathrm{int}} \approx k_B T_C \,. \tag{2.22}$$

Given that the Curie temperature of iron is $1043\,\mathrm{K}$, the internal field $B_{\mathrm{int}} \approx 1500\,\mathrm{T}$, which was far greater than any observed field.

Despite its flaws, Weiss' classical theory of ferromagnetism allowed for two useful developments. Firstly, Curie's law could be updated to describe a ferromagnet's behaviour above the Curie temperature, i.e. when behaving paramagnetically:

$$\chi = \frac{C}{T - T_C} \,. \tag{2.23}$$

Secondly, the total field affecting a material could be described as stemming from two contributions: the externally applied field, and the internal molecular field, which Weiss discovered phenomenologically to be proportional to the magnetisation of the material:

$$B_{\mathrm{total}} = B_{\mathrm{ext}} + B_{\mathrm{int}} = B_{\mathrm{ext}} + \gamma M \tag{2.24}$$

where γ is a proportionality constant known as the Weiss molecular field constant.

However, fully describing the behaviour of ferromagnets, particularly below their Curie temperature, is beyond the realms of classical mechanics; it is now necessary to introduce quantum mechanics.

2.3 Quantum Mechanics of Ferromagnetism

Ferromagnetism stems from two fundamental quantum mechanical effects: electron spin and the Pauli exclusion principle.[4] The spin of an electron, along with its orbital angular momentum, causes it to behave as a magnetic dipole. From Equations (2.5) and (2.7):

$$\boldsymbol{\mu} = \frac{-g\mu_{\mathrm{B}}}{\hbar}\boldsymbol{j} \tag{2.25}$$

where j can represent the orbital angular momentum, spin angular momentum or total angular momentum (all follow the same form of Equation (2.25)).[12] Each electron magnetic dipole moment is responsible for a small magnetic field. If these magnetic moments were to align, the net result would be a larger, measurable magnetic field.

However, it is known from the Pauli exclusion principle that two electrons cannot occupy exactly the same state, i.e. they cannot be in exactly the same location with the same spin orientation. This means that two electrons in the same space must have opposite spin orientations: one spin-up, the other spin-down. In areas of high electron density, such as chemical bonds, it is therefore energetically favourable to have pairs of electrons with opposing spins rather than parallel spins. The apparent “force” causing this spin arrangement is known as the exchange force, and is the cause of most materials lacking ferromagnetism: the magnetic spin dipole moments of the individual electrons arrange themselves into the lowest energy state, with a net zero magnetic moment..[4] However, to decipher the origins of ferromagnetism it is necessary to delve deeper into quantum mechanics.

2.3.1 The Heitler-London Model

Consider a quantum mechanical system comprising hydrogen atoms, and therefore two electrons with wavefunctions Φ_{a} and Φ_{b} at positions r_1 and r_2 respectively. As electrons are fermionic (spin-$\frac{1}{2}$) particles, the wavefunction of the system overall must be antisymmetric under exchange of the two electrons:

$$\Psi(r_1, r_2) = -\Psi(r_2, r_1) \tag{2.26}$$

Neglecting the spin component and working only with the positions of the two electrons, it is possible to construct the form of this antisymmetric wavefunction:

$$\Psi_{\mathrm{A}}(r_1, r_2) = \frac{1}{\sqrt{2}} \left(\Phi_{\mathrm{a}}\left(r_1\right) \Phi_{\mathrm{b}}\left(r_2\right) - \Phi_{\mathrm{a}}\left(r_2\right) \Phi_{\mathrm{b}}\left(r_1\right)\right) \tag{2.27}$$

The symmetric wavefunction can also be constructed:

$$\Psi_{\mathrm{S}}(r_1, r_2) = \frac{1}{\sqrt{2}} \left(\Phi_{\mathrm{a}}\left(r_1\right) \Phi_{\mathrm{b}}\left(r_2\right) + \Phi_{\mathrm{b}}\left(r_1\right) \Phi_{\mathrm{a}}\left(r_2\right)\right) \tag{2.28}$$

The above equations have so far neglected the spin of the electrons. It is possible to construct symmetric and antisymmetric combinations of spin in a similar manner to Equations (2.27) and (2.28). The antisymmetric case is simple:

$$\chi_{\mathrm{A}}(a, b) = \frac{1}{\sqrt{2}} \left(s_{\mathrm{a}}\left(\uparrow\right) s_{\mathrm{b}}\left(\downarrow\right) - s_{\mathrm{a}}\left(\downarrow\right) s_{\mathrm{b}}\left(\uparrow\right)\right) \tag{2.29}$$

The symmetric spin case, however, has a number of possibilities:

$$\chi_{\mathrm{S}}(a, b) = \begin{cases} s_{\mathrm{a}}\left(\uparrow\right) s_{\mathrm{b}}\left(\uparrow\right) & m_s = +1 \\ \frac{1}{\sqrt{2}} \left(s_{\mathrm{a}}\left(\uparrow\right) s_{\mathrm{b}}\left(\downarrow\right) + s_{\mathrm{a}}\left(\downarrow\right) s_{\mathrm{b}}\left(\uparrow\right)\right) & m_s = 0 \quad S = 1 \\ s_{\mathrm{a}}\left(\downarrow\right) s_{\mathrm{b}}\left(\downarrow\right) & m_s = -1 \end{cases} \tag{2.30}$$

The total wavefunction for the two electron system is the product of the spin and spatial wavefunctions. Therefore, in order for the two electron wavefunction overall to remain antisymmetric it is necessary to combine the symmetric spin wavefunction with the antisymmetric spatial wave function, or *vice versa*. This restriction on the wavefunction for the system as a whole, as a function of the electrons' spin, results in two distinct possibilities for the overall wavefunction of the system. Those two overall wavefunctions have two different energy solutions, which leads to an interesting observation: the energy of the system depends on the spin of the electrons.

The resulting ground state energy for the system can be written in the form:[13]

$$E = 2E_0 + \varDelta E \tag{2.31}$$

where $2E_0$ represents the ground state energy of the two hydrogen atoms, and $\varDelta E$ is the change to this energy due to the interaction between these two atoms. The value of $\varDelta E$ has two possibilities, depending on the spin of the electrons, which are typically written in the form:

$$\varDelta E_{\uparrow\uparrow} = \frac{C(R) - X(R)}{1 - S(R)} \tag{2.32}$$

$$\varDelta E_{\uparrow\downarrow} = \frac{C(R) + X(R)}{1 + S(R)} \tag{2.33}$$

where R is the interatomic spacing, and S, C and X are known as the overlap, Coulomb and exchange integrals, respectively. These take the values:

$$S = \int \varPhi_a^* (r_1) \varPhi_b^* (r_2) \varPhi_a (r_2) \varPhi_b (r_1) \, \mathrm{d}r_1 \, \mathrm{d}r_2 \tag{2.34}$$

$$C = \int \varPhi_a^* (r_1) \varPhi_b^* (r_2) U \varPhi_a (r_1) \varPhi_b (r_2) \, \mathrm{d}r_1 \, \mathrm{d}r_2 \tag{2.35}$$

$$X = \int \varPhi_a^* (r_1) \varPhi_b^* (r_2) U \varPhi_a (r_2) \varPhi_b (r_1) \, \mathrm{d}r_1 \, \mathrm{d}r_2 \tag{2.36}$$

where U is the energy which stems from the interaction between the two atoms (the interaction of each electron with the ‘other’ nucleus, electron-electron interactions and repulsion between the two nuclei) given as:[13]

$$U = \frac{e^2}{4\pi\epsilon_0} \left(\frac{1}{R} + \frac{1}{|r_1 - r_2|} - \frac{1}{|R_a - r_2|} - \frac{1}{|R_b - r_1|} \right) \tag{2.37}$$

where R_a and R_b are the locations of the two nuclei.

These contributions to the energy have relatively intuitive origins. The overlap integral S is the simple overlap of the two wavefunctions. The Coulomb integral C represents the electrostatic interaction between the two atoms with each electron being coupled to its parent nucleus. The exchange integral X represents the Coulomb interaction from electron exchange between the two atoms.

The overlap integral S diminishes rapidly with increasing atomic spacing, allowing an approximation to be made that $S \approx 0$. The ground state energy given in Equation (2.31) can therefore be simplified:

$$E \approx (2E_0 + C) \pm X \,. \tag{2.38}$$

In minimising the overall ground state energy of the system, the sign of X therefore becomes the determining factor. Where the exchange integral is positive, the overall energy is reduced for the case where the spins are aligned parallel. This net spin alignment leads to an overall net magnetic moment, resulting in ferromagnetism. Where X is negative, however, overall energy is reduced when the spins are antiparallel, leading to antiferromagnetism.

This exchange energy is, however, not the only energy that must be considered when investigating the magnetic properties of a material as will be seen in Section 2.5.3 on page 72.

2.3.2 Stoner Model and Spin-Polarised Band Structure

The Stoner model, formalised by Stoner in (1936) provides a simple band-like model of ferromagnetic materials.[14] The major assumption of the Stoner model is that interactions between $3d$ electrons result in their energies forming a continuous band. This is shown in Figure 2.2 on the next page. For a paramagnetic or diamagnetic material in the presence of an externally applied field, $\boldsymbol{B}_{\mathrm{ext.}}$, states of opposite spin exhibit a shift $\varDelta$ in their relative energies as a result of the Zeeman effect. However, for ferromagnetism to be observed in a material such splitting must occur spontaneously.

At absolute zero (temperature $T = 0$) all states below the Fermi energy E_{F} are occupied. These states are known as “electron states”. The unfilled states above E_{F} are “hole states”.

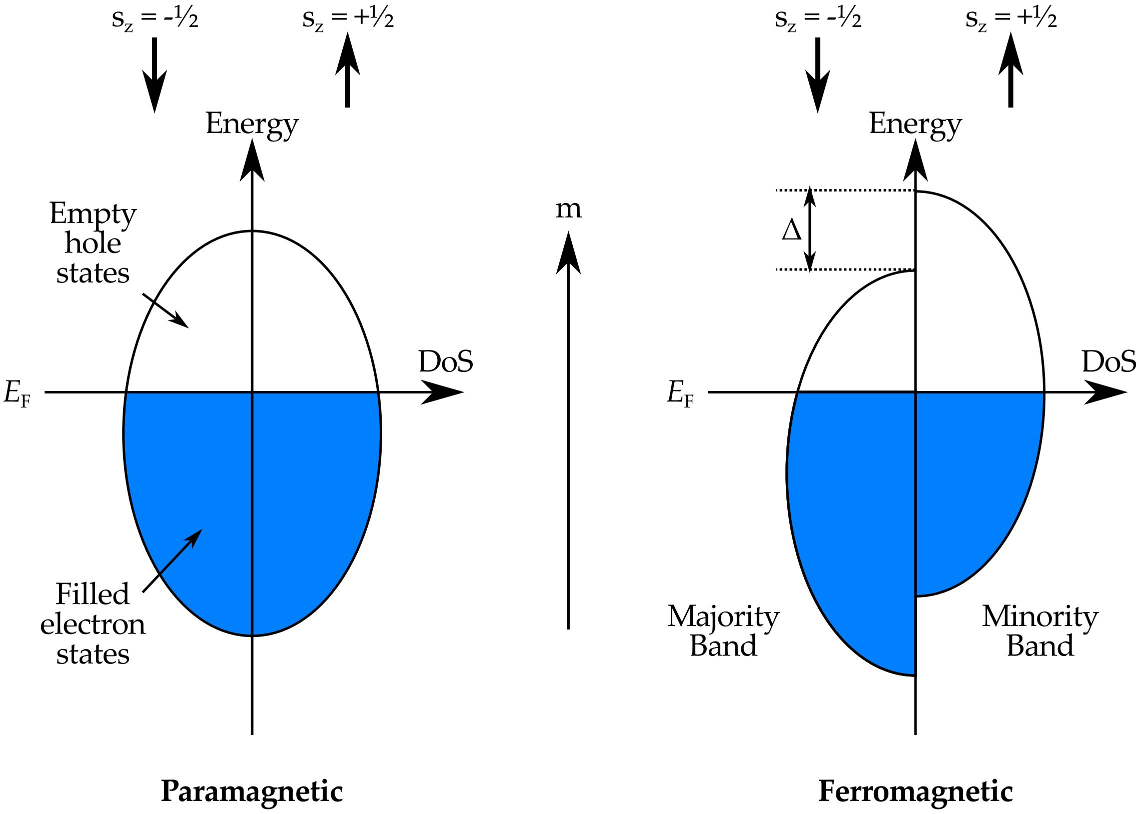

Figure 2.2: The Stoner model of spin-split energy bands in ferromagnets. The density of spin-up and spin-down states is split in energy by an amount $\varDelta$.

The two bands (spin-up and spin-down) are named according to their relative electron populations. The band with the larger electron population is known as the “majority band”, and the smaller electron population is the “minority band”.

This model makes a calculation of the internal magnetic moment $\boldsymbol{m}$ possible. Each electron has a magnetic moment equal to $\pm\mu_B$, meaning each electron gains an additional energy $\pm\mu_B B_{\mathrm{ext.}}$ depending on whether the electron’s spin is parallel or anti-parallel to $\boldsymbol{B}_{\mathrm{ext.}}$. The energy difference between the two populations is therefore $\varDelta = 2\mu_B B_{\mathrm{ext.}}$.

The electrons repopulate the available states so as to minimise their total energy, resulting in a reduction of their Zeeman energy, but a increase in kinetic energy. An induced magnetisation M results from the product of the number of excess spins (spin-down as shown in Figure 2.2) and the magnetic moment carried by each spin:

$$M = (2\mu_B B_{\text{ext.}}) \left(\frac{D\left(E_{\text{F}}\right)}{2} \right) \mu_B \, . \tag{2.39}$$

We can further calculate the specific susceptibility as:

$$\chi_p = \frac{M}{H} = \frac{\mu_0 M}{B_{\text{ext.}}} = \mu_0 \mu_B^2 D\left(E_{\text{F}}\right) \, . \tag{2.40}$$

The induced magnetisation M can be treated as providing an additional contribution to Weiss' molecular field experienced by a magnetic dipole. Using Equations (2.39) and (2.40):

$$\boldsymbol{B_m} = \boldsymbol{B}_{\text{ext.}} + \lambda \mu_0 \boldsymbol{M} \tag{2.41}$$

$$M = \chi_p \left(H + \lambda M\right) = \chi H \, . \tag{2.42}$$

Then working with Equation (2.42):

$$\chi_p \left(1 + \lambda \chi\right) = \chi \tag{2.43}$$

$$\chi \left(1 - \lambda \chi_p\right) = \chi_p \tag{2.44}$$

$$\chi = \frac{\chi_p}{1 - \lambda \chi_p} \, . \tag{2.45}$$

The ferromagnetic state occurs as the temperature is reduced such that the susceptibility χ diverges. Equation (2.45) tells us that this occurs as $\lambda \chi_p \to 1$. From Equation (2.40) we can therefore derive the required conditions for ferromagnetism:

$$\lambda \chi_p = \lambda \mu_0 \mu_B^2 D\left(E_{\text{F}}\right) = X D\left(E_{\text{F}}\right) \tag{2.46}$$

$$\therefore X D\left(E_{\text{F}}\right) > 1 \, . \tag{2.47}$$

For ferromagnetism to be observed, the product of the exchange integral X (defined in Equation (2.36)) and the density of states at the Fermi energy must be greater than 1. This is known as the Stoner criterion for ferromagnetism, and helps to explain why the $3d$ transition metals are ferromagnetic: these metals have their Fermi energy in the middle of the $3d$ band, where the density of states $D\left(E_{\text{F}}\right)$ is large.

2.4 Hysteresis and Magnetisation Reversal

Hard disk drives rely on the principle of hysteresis to store data without the continuous application of an external magnetic field or energy input to the recording medium. Hysteresis is a non-linear relationship between $\boldsymbol{M}$ and $\boldsymbol{H}$, the magnetisation and external magnetic field strength respectively.

Hysteresis curves, in general, follow the shape shown in Figure 2.3 on the following page. Starting from the origin, where $\boldsymbol{M} = \boldsymbol{H} = 0$ and gradually increasing the applied field, the magnetisation of the material will follow the initial magnetisation curve (origin → a). For increasing external field, the magnetisation eventually reaches a point known as magnetisation saturation, M_{S}, after which magnetisation increases at a far reduced rate.[15]

If $\boldsymbol{H}$ is now reduced, $\boldsymbol{M}$ will not follow the same path back to the origin. When $\boldsymbol{H} = 0$, $\boldsymbol{M}$ will retain a positive value known as the saturation remanence M_{rs}. Reducing $\boldsymbol{H}$ further still, to negative values, will eventually force the magnetisation back to zero. The magnitude of the necessary applied field to accomplish this is known as the coercive field of the material, H_{c}.[15] A complete typical hysteresis loop can be seen in Figure 2.3 on the next page.

2.4.1 The Stoner-Wohlfarth Model

The Stoner-Wohlfarth[16] and Néel[17] models provide a theory of magnetisation reversal by uniform rotation. This is most often observed in magnetic samples that are too small to reliably form domain walls, and therefore behave as a "macrospin". The maximum size of these samples can be calculated as follows:[18]

$$d = \sqrt{\frac{A}{K_{\mathrm{u}}}} \tag{2.48}$$

where A is the exchange stiffness constant and K_{u} is the magnetocrystalline anisotropy, defined in the anisotropy energy term (see Section 2.5.3 on page 72). The length d is often referred to as the exchange length. It is also important to note

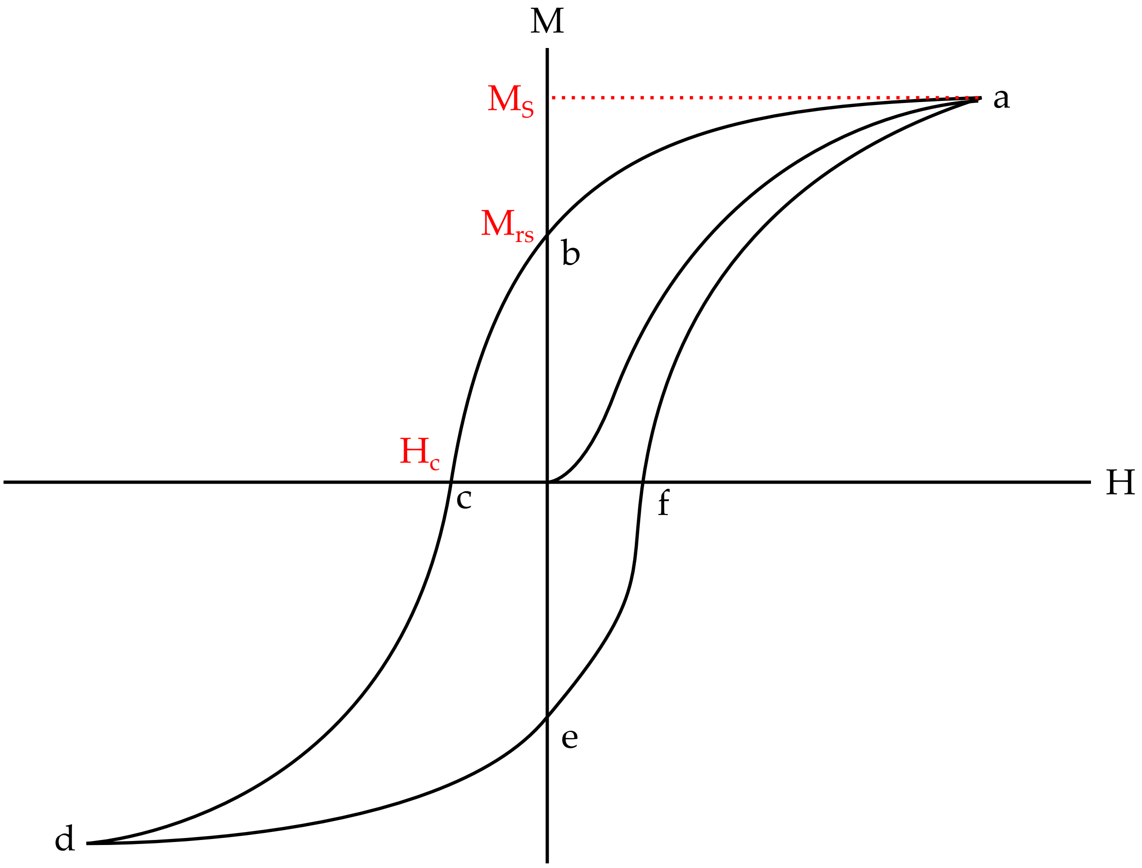

Figure 2.3: A typical hysteresis curve. Point (a) represents the saturation magnetisation M_{S}. When $\boldsymbol{H}$ is restored to 0 some remanent field M_{rs} remains, (b). A coercive field H_{c} must be applied to bring the internal magnetisation back to zero, (c).

that sometimes K_{u} may in fact be the demagnetisation energy. A full derivation can be seen in Hubert and Schäfer [19]. Setting the wall thickness d to the typical size of a nanoparticle reveals that this effect only occurs for nanoparticles containing approximately 10^4 to 10^6 Bohr magnetons.[18] In these particles, changes in magnetisation are expected to occur by uniform rotation of the magnetisation vector $\boldsymbol{M}$.

The energy of a single domain particle with uniaxial anisotropy constant K, volume V and placed in a uniform magnetic field H is given by:[18]

$$E = KV \sin^2 \gamma - MVH \cos(\phi - \gamma) \tag{2.49}$$

where γ and ϕ are the angles between the easy axis of magnetisation and the vectors $\boldsymbol{M}$ and $\boldsymbol{H}$ respectively. The first term is the magnetic anisotropy energy,

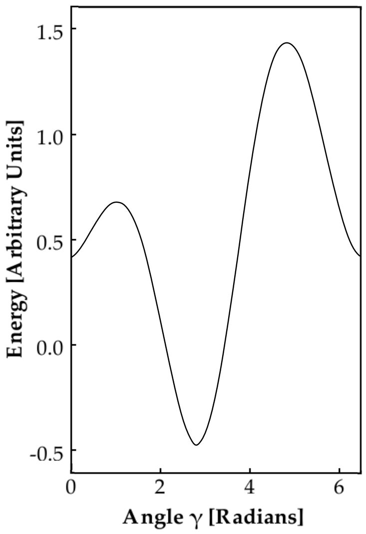

Figure 2.4: The energy of a single domain particle in the Stoner-Wohlfarth model as a function of the magnetisation angle relative to the easy axis of the crystal.

while the second is the Zeeman energy. Equation (2.49) on page 66 has two minima (Figure 2.4), separated by a potential barrier, providing a source for the shape of a typical hysteresis loop.

The obtained hysteresis loop depends on ϕ, the orientation of the applied field $\boldsymbol{H}$ relative to the sample's easy axis. Typical hysteresis loops for varying values of ϕ are shown in Figure 2.5 on the next page.

2.5 Micromagnetism

2.5.1 Domain Walls

If the direction of magnetisation for a ferromagnetic material was determined solely by the spin-orbit interaction (causing magnetocrystalline anisotropy), the sample would be homogeneously magnetised along its easy axis. In the real world, this is very unlikely to occur due to the macroscopic shape of the sample. This leads to the formation of stray field around the sample, at a not-insignificant energy cost E_d:[18]

$$E_\mathrm{d} = \frac{\mu_0}{2} \underset{\text{all space}}{\iiint} \boldsymbol{H}^2 \,\mathrm{d}V = -\frac{1}{2} \underset{\text{sample}}{\iiint} \boldsymbol{H}_\mathrm{d} \boldsymbol{M} \,\mathrm{d}V \tag{2.50}$$

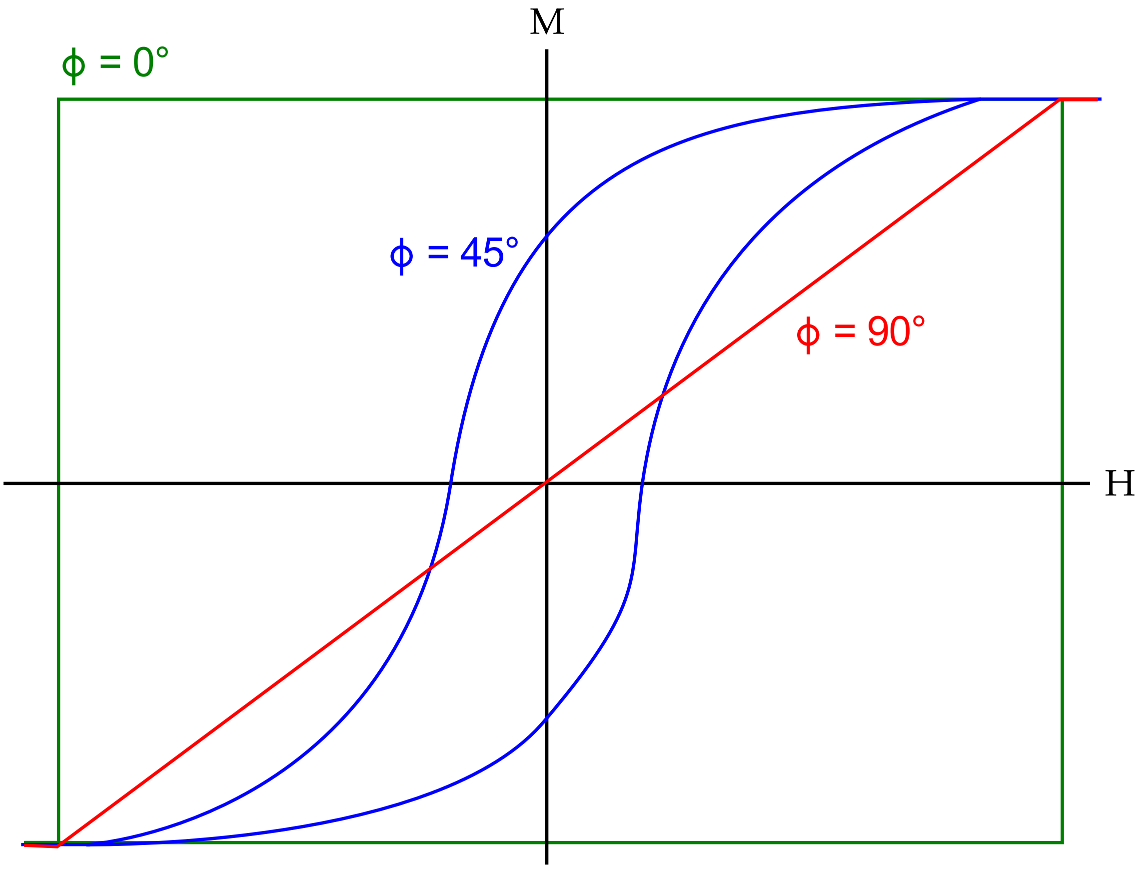

Figure 2.5: Field dependence of the component of internal magnetisation parallel to the applied field according to the Stoner-Wohlfarth model for various values of the angle between the applied field and the easy axis.

In an attempt to minimise the stray field, and therefore the energy required to maintain it, the magnetisation across the sample will split into domains oriented in multiple different directions. In terms of energy, the most favourable formation is that of a “magnetic ring” as shown in Figure 2.6 on the facing page.

While neatly explaining microscopic magnetisation in terms of energy, domains by their very existence throw up another problem: how does the magnetisation direction transition between these domains? These transition regions, called domain “walls”, also have an energy cost associated with their formation.

Figure 2.7 on the next page shows two possibilities for the transition of the magnetisation direction inside a domain wall. Figure 2.7(a) on the facing page shows a Bloch wall, and Figure 2.7(b) on the next page depicts a Néel wall. These configurations differ in terms of the plane in which the magnetisation rotates. In a

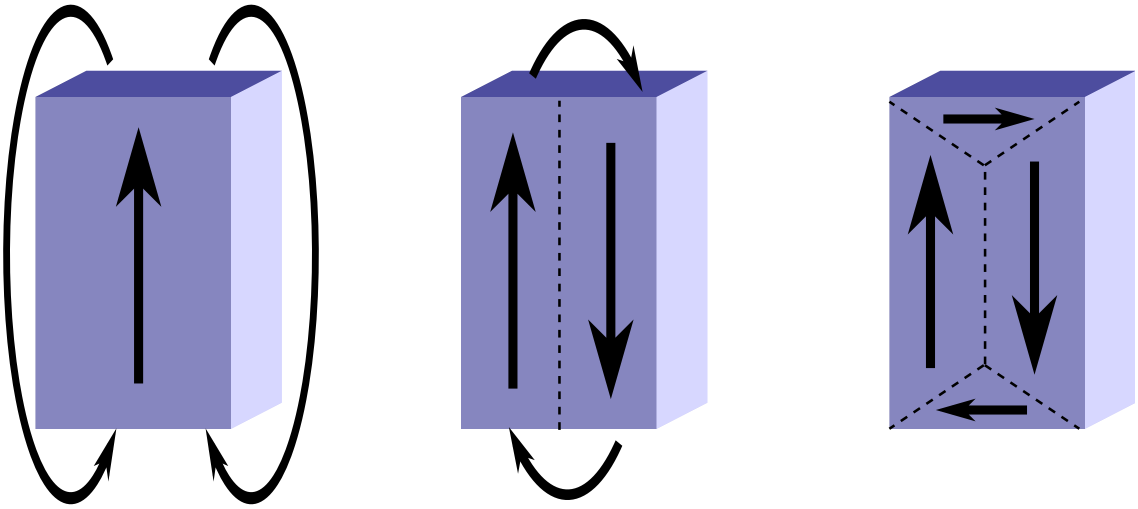

Figure 2.6: The minimisation of stray field and energy through the mechanism of magnetic domains. In the single domain case (left) a large stray field is formed around the sample, requiring significant energy to maintain. In the two domain case (centre) the stray field is reduced, but is still non-zero. The magnetic ring structure (right) makes use of closure domains to avoid any external stray field, and is therefore a minimum energy case.[20]

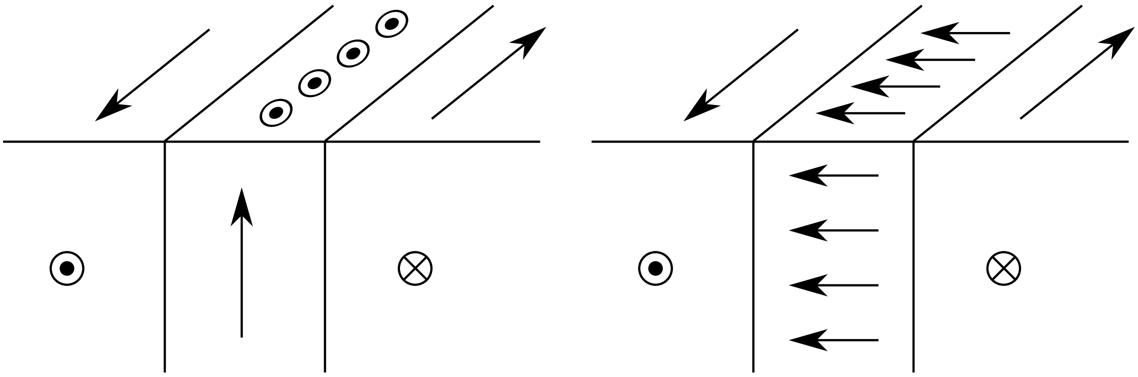

(a) Bloch wall

(b) Néel wall

Figure 2.7: Typical domain wall structures observed in thin films. The Bloch wall has the magnetisation rotating out of the plane of the film, leading to stray field from the film surfaces. The Néel wall rotates the magnetisation in-plane. While this leads to an elimination of stray field, the wall itself is wider and poorly defined. Adapted from Bertotti [21].

Bloch wall the magnetisation rotates in the plane of the wall. For a Néel wall, the magnetisation instead rotates perpendicular to the plane of the wall. In general, Néel walls are more common in thin films, as the magnetisation in the wall remains parallel to the surface of the film, therefore minimising any surface stray field.

2.5.2 Domain Wall Energy

As shown in Figure 2.7 on page 69, the magnetisation direction rotates throughout a domain wall. This results in two energy costs: firstly, an exchange energy cost stems from adjacent moments not being aligned with one another; secondly, an anisotropy energy cost is associated with the fact that moments within the domain wall do not lie along the crystal's easy axis.[11]

The first of these contributions, the exchange energy cost F_e, is reduced by having the magnetisation direction rotate gradually through a wall of finite width. The exchange energy between any two adjacent atoms can be calculated as

$$F_e = J_e S^2 \phi^2 \tag{2.51}$$

where J_e is the exchange integral and ϕ is the angle between the spins of adjacent atoms. For the case of an immediate $180°$ change, this becomes

$$F_{e,\mathrm{immediate}} = J_e S^2 \pi^2 \,. \tag{2.52}$$

However, splitting the angular change equally over N atoms results in an angular change of $\frac{\pi}{N}$ between adjacent atoms, giving a total exchange energy of

$$F_{e,\mathrm{gradual}} = N J_e S^2 \left(\frac{\pi}{N}\right)^2 = \frac{1}{N} J_e S^2 \pi^2 \,. \tag{2.53}$$

From Equation (2.53) it would seem that getting N as high as possible would be the lowest energy state, i.e. any crystal should be entirely occupied by a single, gradual domain wall. Such "circular" domains have not been observed,[11] however, meaning a second energy cost must be limiting the maximum wall size.

This second energy cost is the crystalline anisotropy energy F_K, which can be calculated for per unit area of a wall in a simple cubic lattice as

$$F_K = K_1 N a \tag{2.54}$$

where K_1 is the anisotropy constant and a the lattice constant. The exchange energy per unit area of a domain wall can also be calculated, knowing that the number of rows of atoms per unit area of the wall is $\frac{1}{a^2}$:

$$F_e = \frac{1}{a^2}\frac{1}{N} J_e S^2 \pi^2 \,. \tag{2.55}$$

The total energy of a domain wall, F_{wall} is therefore given by

$$F_{\text{wall}} = F_e + F_K = \frac{1}{Na^2} J_e S^2 \pi^2 + K_1 N a \tag{2.56}$$

in which the physical width of the wall, δ, is simply the number of atoms in the wall multiplied by the lattice constant:

$$F_{\text{wall}} = F_e + F_K = \frac{1}{\delta a} J_e S^2 \pi^2 + K_1 \delta \,. \tag{2.57}$$

Differentiating with respect to the width of the wall allows the conditions for minimum energy cost to be found:

$$\frac{\partial F_{\text{wall}}}{\partial \delta} = -\frac{1}{\delta^2 a} J_e S^2 \pi^2 + K_1 = 0 \tag{2.58}$$

and rearranged in terms of the wall thickness δ:

$$\delta = \left(\frac{J_e S^2 \pi^2}{K_1 a} \right)^{\frac{1}{2}} \tag{2.59}$$

which can then be used to find the minimum total energy cost per unit area of a domain wall using Equation (2.57):

$$F_{\text{wall}} = 2S\pi \sqrt{\frac{J_e K_1}{a}} \,. \tag{2.60}$$

Substituting typical values for iron[18] gives a domain wall width $\delta \approx 500$ Å $\approx 200a$ and a wall energy $F_{\text{wall}} \approx 5\,\mathrm{mJ\,m^{-2}}$. Hubert et al. [19] provide more detailed calculations for a range of different materials.

The properties of domain walls are therefore determined by the competition between the exchange energy F_e and the crystalline anisotropy energy F_K, which together account for the total domain wall energy F_{wall}. The total domain wall energy cost therefore increases with either an increase in exchange energy or an increase in crystalline anisotropy. The minimum energy cost determines a finite domain wall width, which increases with exchange energy but decreases as crystalline anisotropy increases.

2.5.3 Magnetic Free Energy

Ultimately the micromagnetic domain structure and behaviour of any material is governed by the process of minimising the free energy of the sample:[22]

$$E = E_{\text{exch.}} + E_{\text{D}} + E_k + E_\sigma + E_H \tag{2.61}$$

where the energy terms represent contributions from (in order, left to right) exchange interaction, magnetostatic energy, magnetocrystalline anisotropy, magnetoelastic anisotropy and Zeeman energy.

The exchange term, $E_{\text{exch.}}$, is a result of the quantum mechanical exchange interaction causing independent magnetic moments to align parallel to one another. This is most often defined as:

$$E_{\text{exch.}} = \frac{1}{2}\sum_i \sum_j -\jmath \boldsymbol{S_i} \cdot \boldsymbol{S_j} \tag{2.62}$$

where the sums represent summation over every particle in a sample (i) and each particle's nearest neighbours (j), $\boldsymbol{S_i}$ and $\boldsymbol{S_j}$ are the spin vectors for the particle and its nearest neighbour, respectively, and $\jmath$ is the exchange integral:

$$\jmath = \frac{Aa}{\eta S^2}\,. \tag{2.63}$$

Here a is the lattice parameter, A is a material dependent exchange stiffness term and η varies depending on the specific crystal structure ($\eta = 1$ for simple cubic, $\eta = 2$ for body-centred cubic and $\eta = 4$ for face-centred cubic).

The magnetostatic term, E_{D}, results from the interaction of magnetic moments with each other, and is often known as the "demagnetising energy" or "dipolar energy". Two magnetic moments at positions $\boldsymbol{r_i}$ and $\boldsymbol{r_j}$ have dipolar energy

$$E_{\text{D}}^{i,j} = \mu_0 \left(\frac{\boldsymbol{\mu_i} \cdot \boldsymbol{\mu_j}}{|\boldsymbol{r_{ij}}|^3} - \frac{3\left(\boldsymbol{\mu_i} \cdot \boldsymbol{r_{ij}}\right)\left(\boldsymbol{\mu_j} \cdot \boldsymbol{r_{ij}}\right)}{|\boldsymbol{r_{ij}}|^5} \right) \tag{2.64}$$

where $\boldsymbol{r_{ij}}$ is the vector between the two magnetic moments. Individual $E_{\text{D}}^{i,j}$ can then be summed over N magnetic moments within a sample, giving the total dipolar energy

$$E_{\mathrm{D}} = \frac{1}{2} \sum_{i=1}^{N} \sum_{j \neq i} E_D^{i,j} \,. \tag{2.65}$$

The magnetocrystalline term, E_k, is the result of the magnetisation having preferred orientation along certain crystal axes within a material. The spin-orbit interaction couples the total angular momentum of each electron to these preferential lattice directions, making the energy dependent upon the relative orientation of the magnetisation and preferred “easy” axis. In the case of a uniaxial crystal structure,

$$E_k = K_1 V \sin^2 \gamma + K_2 V \sin^4 \gamma + K_3 V \sin^6 \gamma + \cdots \tag{2.66}$$

where V is the volume of the sample, K_i are material dependent anisotropy constants (units of energy per unit volume) and γ is the angle between the magnetisation and easy axis.

The magnetoelastic term, E_σ, stems from magnetostriction - the link between sample shape and magnetisation. This can be expressed as:[20]

$$E_\sigma = \frac{3}{2} \lambda_s \sigma \sin^2 \theta \tag{2.67}$$

where λ_s is a material dependent expansion at saturation, σ is the applied stress and θ is the angle between the applied stress and the saturation magnetisation direction.

The Zeeman term, E_H, results from the application of an external magnetic field to the sample. It is defined as

$$E_H = -\mu_0 \int_V \boldsymbol{M} \cdot \boldsymbol{H} \,\mathrm{d}V \tag{2.68}$$

where V is the volume of the sample, $\boldsymbol{H}$ is the applied external field and $\boldsymbol{M}$ is the local magnetisation. It is clear to see that E_H is minimised when the dot product is at a maximum, i.e. $\boldsymbol{M} \parallel \boldsymbol{H}$.

The interplay between these energy terms determine the micromagnetic behaviour of ferromagnetic materials. The formation, growth, destruction and orientation of domains all result from a minimisation of the total free energy of a given sample under its current conditions. This in turn affects the stray, or demagnetising, field $\boldsymbol{H}_{\text{eff}}$:[23]

$$\boldsymbol{H}_{\text{eff}} = -\frac{1}{M}\boldsymbol{\nabla} E \tag{2.69}$$

2.6 Magnetisation Precession

The strong exchange interaction between the moments of a ferromagnetic material tends to cause coherence between the motion of atomic moments. Under the application of a steady magnetic field strong enough to destroy the domain structure of the material, atomic moments coherently precess about their equilibrium position and can therefore be treated as a macroscopic precession of the magnetisation vector $\boldsymbol{M}$.

2.6.1 Magnetisation Precession and the Landau-Lifshitz-Gilbert Equation

The macroscopic precession of the magnetisation vector $\boldsymbol{M}$ is usually described in terms of the equation of motion derived by Landau and Lifshitz:[7]

$$\frac{\mathrm{d}\boldsymbol{M}}{\mathrm{d}t} = -\gamma \boldsymbol{M} \times \boldsymbol{H}_{\text{eff}} + \text{damping} \tag{2.70}$$

where γ is the electron gyromagnetic ratio, given by $\gamma = \frac{g\mu_B}{\hbar}$, and $\boldsymbol{H}_{\text{eff}}$ is an effective resultant magnetic field applied to the material resulting from crystalline anisotropy and demagnetising fields, any applied external field, and any other fields which may happen to be present. The damping term is usually a phenomenological term, with Landau and Lifshitz suggesting the following form:

$$\frac{\mathrm{d}\boldsymbol{M}}{\mathrm{d}t} = \gamma \boldsymbol{M} \times \boldsymbol{H}_{\text{eff}} - \frac{\alpha\gamma}{M}\boldsymbol{M} \times (\boldsymbol{M} \times \boldsymbol{H}_{\text{eff}}) \tag{2.71}$$

where α is an experimentally determined dimensionless “damping factor”.

This damping term is often rewritten in a form proposed by Gilbert:[24]

$$\frac{\mathrm{d}\boldsymbol{M}}{\mathrm{d}t} = -\gamma \boldsymbol{M} \times \boldsymbol{H}_{\text{eff}} + \frac{\alpha}{M}\left(\boldsymbol{M} \times \frac{\mathrm{d}\boldsymbol{M}}{\mathrm{d}t}\right) . \tag{2.72}$$

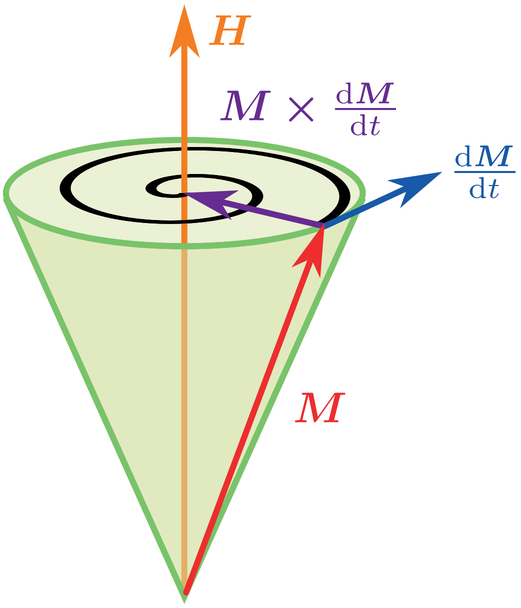

Figure 2.8: The damped precessional motion of the magnetisation vector described by the Landau-Lifshitz-Gilbert equation. In the free induction decay case, the moment follows the black spiral path to its new equilibrium orientation.

The first term of Equations (2.71) and (2.72) on page 74 describes a torque that results in uniform precession of the magnetisation about $\boldsymbol{H}_{\mathrm{eff}}$, while the damping term describes a force drawing the magnetisation to align with $\boldsymbol{H}_{\mathrm{eff}}$ and therefore causes the precession to decay into the helical path shown in Figure 2.8.

2.7 Hard Disk Recording Head Design

2.7.1 Reader and Shields

The read head of a modern recording head consists of a spintronic device based on the giant magnetoresistance (GMR) effect, sandwiched between two “shields” as shown in Figure 2.9 on the next page.

The shields play a vital role during the write and read processes. They work to absorb flux with a low spatial frequency, reducing the width of the pulse received by the GMR sensor. This reduces the dynamic range requirement of the sensor, allowing it to have maximum sensitivity on low flux levels seen in high density

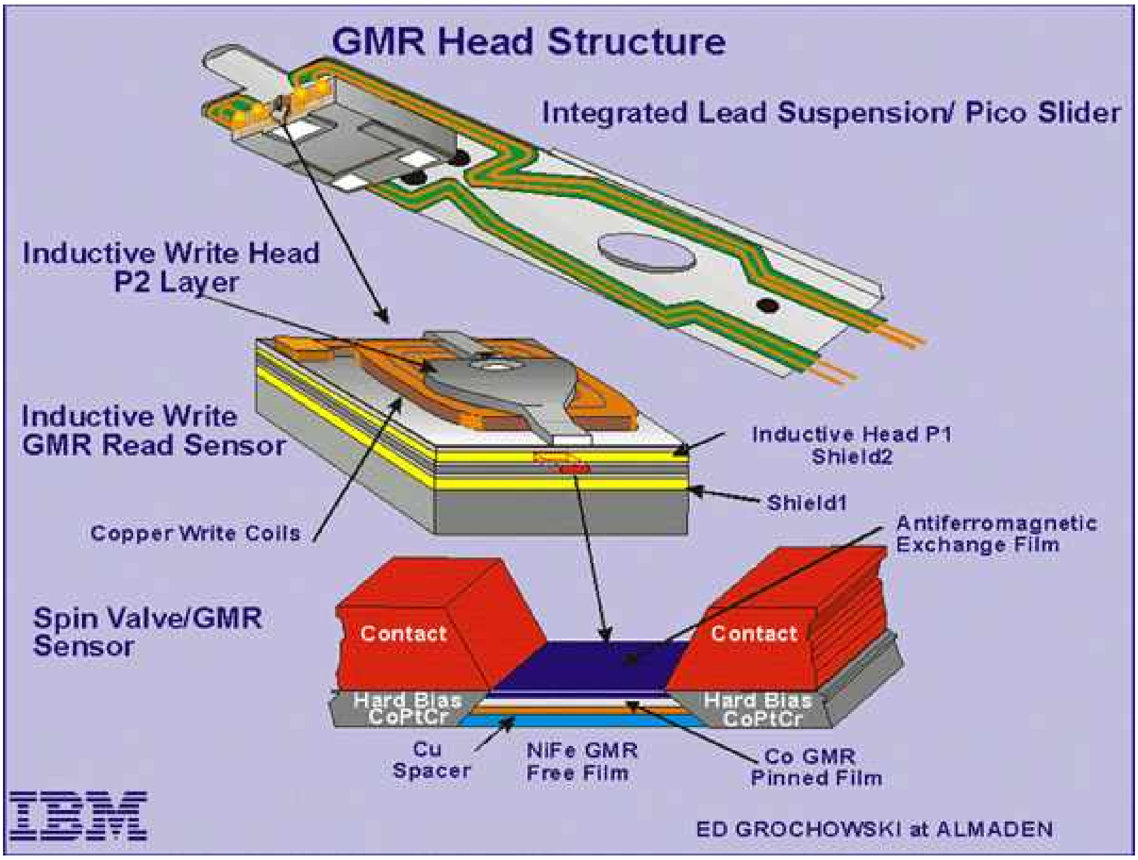

Figure 2.9: The structure of a typical GMR read head in the context of the complete recording head. The write head, centre, is typically on the order of 10 µm long and 6.5 µm wide, narrowing to tens of nm at the tip. Reproduced from Grochowski [25].

media. Without the shields the GMR sensor would be pushed into saturation, making its response non-linear in flux.

The top shield is often used as part of the write structure (in this instance called a “shared shield”). However, with recent developments in perpendicular recording it has become increasingly common to see a separate shield dedicated to the writer. This avoids the read shield being subjected to high fields during write processes, which can cause “domain instabilities” that distort read-back waveforms.[26]

2.7.2 Writer

A perpendicular write head consists of a narrow main write pole and a far wider return pole, separated by a space known as the “recording gap”. These are at the

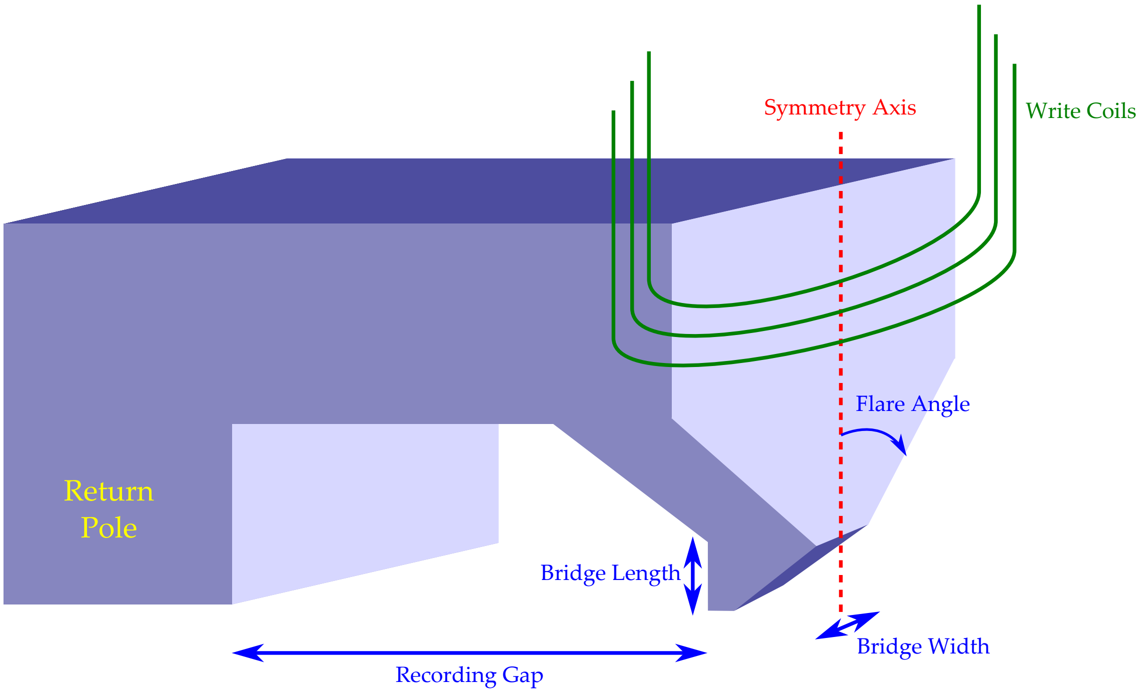

Figure 2.10: A typical perpendicular write head. The write pole is a complex three-dimensional structure, ending in a narrow chamfered tip with a bridge width of approximately 200 nm. Adapted from Taratorin [27].

front of the recording head, allowing for data to be read immediately after write, ensuring data integrity. These structures are shown schematically in Figure 2.10.

The latest perpendicular write heads also feature a “trailing shield” placed in the recording gap, closely following the write pole. This serves to ensure the write field dies away as rapidly as possible as the disk moves from under the write pole to under the shield. The sharp gradient and steep field angle introduced into the write field allow for much more sharply defined transitions between bits written to the recording medium. This reduces the error rate when reading data back, and increases areal density as bits can be made physically smaller.[28]

The writer is accompanied by a number of electrically conductive coils used to induce a magnetic flux in the region around the yoke. Passing a current through these coils triggers changing magnetisation dynamics within the write pole, allowing data to be written to the recording medium. This process is discussed in more detail in Section 2.7.5 on page 80. The coils themselves typically fall into one of

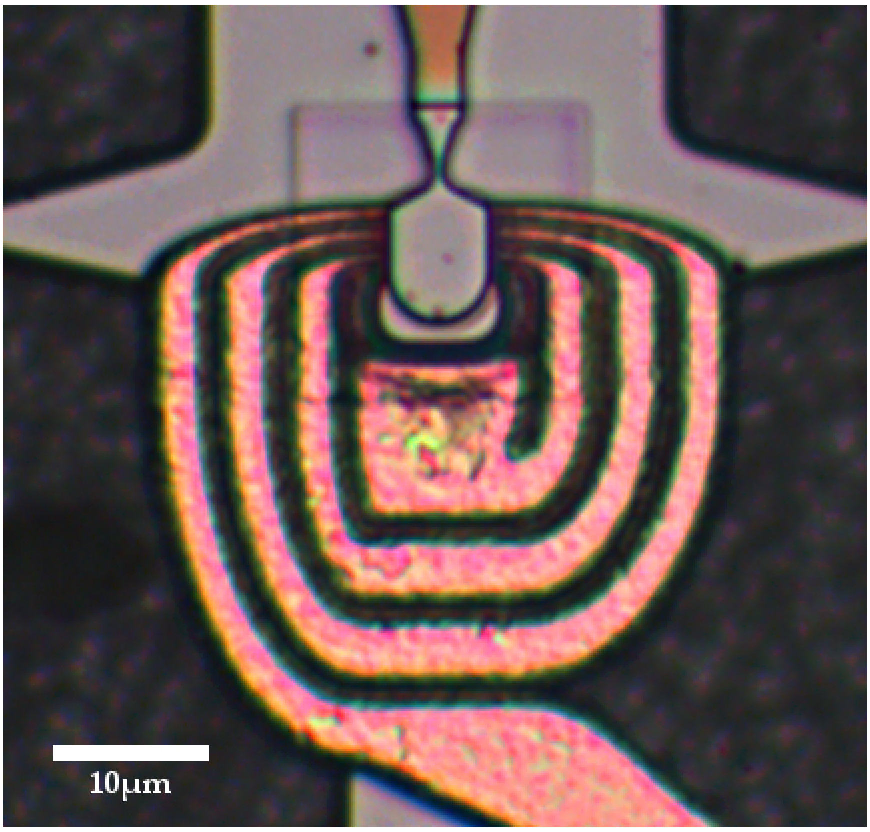

Figure 2.11: A sample write head provided by Seagate. The write coils (copper-coloured) are arranged in a pancake geometry beneath the yoke. The paddle design and dimensions are varied between writer designs.

two geometries: helical coils or “pancake” coils. Helical coils are arranged as a single conductive wire in a three-dimensional helix wrapped around the writer. This is effectively a traditional electromagnet layout. The pancake geometry (shown in Figure 2.11) uses a number of separate coils arranged in a two-dimensional plane perpendicular to the air-bearing surface. This relies on the flux around each individual current-carrying wire to trigger the write process, allowing finer control over the magnetodynamics.

2.7.3 Air Bearing Surface

To provide freedom of movement of the read/write head over the disk surface, modern hard disk drives make use of an air bearing.[29] The bearing is hydrodynamic, relying on the high speeds of hard disk drive components to maintain a supporting layer of air between the recording medium and the read/write head.

The air bearing surface exhibits a number of advantages over more traditional bearing mechanisms, such as steel ball bearings. As the air bearing has no components, its lifetime is effectively infinite. Noise and vibration are also reduced. More importantly, however, is the low static friction of the bearing. This allows for precision placement and movement of the read/write head necessary for fine track widths.

However, it must be noted that the air bearing carries with it a significant disadvantage. With no mechanical components physically separating the head from the media surface it is possible for the read/write head to impact the recording medium during mechanical shock, an event known as a “head crash”. With the grains making up the recording medium having a size on the order of 25 nm,[30] this impact can cause massive data loss and damage to the head.

2.7.4 Perpendicular Recording

Perpendicular magnetic recording stores data encoded in the magnetisation direction of magnetic grains deposited on the surface of the media. The magnetisation direction lies normal to the plane of the media surface, as shown in Figure 2.12(a) on the next page. The recording medium features a soft magnetic underlayer (SUL). A typical layer stack for perpendicular media is shown in Figure 2.12(b) on the following page. The SUL carries with it a significant advantage in terms of stability and areal density. The SUL allows the write field to penetrate the recording layer completely, as shown in Figure 2.12(a) on the next page. This causes an effective increase in the write field within the recording layer, allowing materials with a higher coercivity to be used. A higher coercivity recording medium will be more thermally stable, permitting the size of individual bits to be decreased, therefore increasing areal density.

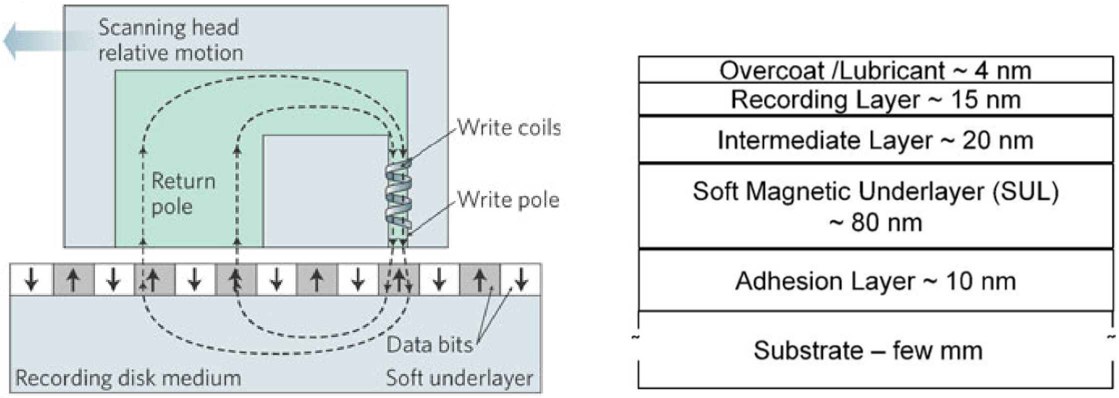

(a) Perpendicular recording geometry. Reproduced from Pan et al. [31].

(b) Layer stack for typical perpendicular media. From Piramanayagam [32].

Figure 2.12: Perpendicular recording technology makes use of a SUL to aid field density through the bit being written to. The stack structure for perpendicular media therefore differs from longitudinal media to reflect this added complexity.

By nature of the decreasing bit size, the write pole is required to undergo a similar size decrease. This often results in the pole tip being chamfered or “wedge-shaped”, resulting in enhanced flux beaming (see Section 2.7.5) and a more focused write field.

2.7.5 Magnetic Processes in the Write Head

In the ground state, a single layer yoke typically forms the domain structure shown in Figure 2.13(a) on the next page. During the write process the pulse of electric field through the coils serves only to trigger slight domain wall motion in the first instance. At higher driving fields it is possible to cause the domains to reorient and resize, resulting in net magnetisation and flux through the pole tip. This is, however, not the most efficient method for generating a write field.

Yokes made from multilayers of ferromagnetic and antiferromagnetic layers can help to eliminate domain walls in the transverse direction, reducing domain wall resonance and eddy currents (see Figure 2.13(b) on the facing page). However, this can create its own problems. Conduction of flux in the lateral direction is

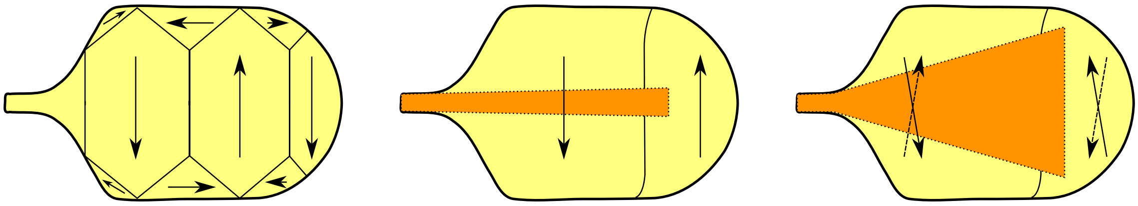

(a) A single layer writer exhibits the closure domain structure shown, minimising energy lost to stray field.

(b) A multilayer writer reduces these transverse domains. However, flux is concentrated in a narrow high impedance path (orange).

(c) Slight rotation of the magnetisation between layers creates a wider flux beam with reduced impedance.

Figure 2.13: The stack structure of a writer plays a crucial role in the formation of flux beams.[26]

necessary to spread out flux widthwise, reducing magnetic impedance. Without this spreading, caused by domain wall motion, the flux is forced into a narrow, high-impedance path during the write process.

This problem is overcome by slightly rotating the easy axis of each pair of ferromagnetic layers within the stack by approximately $10°$ to the transverse direction, whilst keeping pairs of layers antiparallel (as shown in Figure 2.13(c)). This pattern allows for transverse flux conduction equal to $\sin 10° \approx 0.174$ times the longitudinal flux conduction. This encourages *flux beaming*: the formation of a wide, low impedance beam at the back via, focusing into a narrow, high flux beam in the confluence region and pole piece.[26]

In practise, a multitude of different stack structures are used by different hard disk drive manufacturers based on their particular advantages and disadvantages, e.g. manufacturing complexity, stability of ground state, confinement of the generated field. Throughout this thesis, the stack structure of the devices being studied is noted in the relevant chapters.

2.8 Summary

In this chapter both the classical and quantum mechanical descriptions of magnetism, and particularly ferromagnetism, have been discussed. The specific details of micromagnetism and magnetisation precession have also been covered. Finally, the particular features of hard disk recording heads and the role of magnetic processes within the head were explored. We are now ready to approach the experimental techniques which form the foundation of the measurements presented throughout this thesis. In particular, the first half of the next chapter discusses magneto-optical effects, their origin and how they may be used as a measurement tool. The latter half of the chapter describes the interaction between x-rays and magnetism, particularly magnetic dichroism techniques.

CHAPTER 3

Experimental techniques

3.1 Introduction

This chapter introduces the experimental techniques used to investigate the magnetic state of both hard disk write heads and other thin films of interest for magnetic and spintronic devices.

All of the laser-based MOKE measurements presented in this thesis were carried out at the University of Exeter in the ultrafast laser laboratories of Prof. Rob Hicken. This chapter begins by setting forth the general principles of the MOKE measurement technique, as well as the detection methods used and extension to TRSKM.

X-ray based measurements were carried out at three different synchrotron light sources around the world: the Advanced Light Source at Lawrence Berkeley National Laboratory in California; Berliner Elektronenspeicherring-Gesellschaft für Synchrotronstrahlung (BESSY II) in Berlin; and Diamond Light Source (DLS) in Didcot, Oxfordshire. The second half of this chapter outlines the basic principles of x-ray absorption spectroscopy (XAS), its specific relevance to magnetism through XMCD and the application of XMCD in XPEEM. Specific experimental details are provided in the relevant chapters, along with detail of XFMR—a further experimental technique used for some thin-film studies.

3.2 Magneto-optical effects

The MOKE forms part of a group of physical phenomena collectively known as "magneto-optical effects". When an electromagnetic wave is transmitted through or reflected from a magnetic sample it undergoes two changes: to its polarisation and its intensity.[33] These changes stem from off-diagonal components of the permittivity tensor, $\boldsymbol{\epsilon}$, causing the material to appear electrically anisotropic to incident electromagnetic waves. This anisotropy causes light of different incident directions and polarisations to travel at different speeds and with different absorption, resulting in an overall change to the polarisation of light. When the effect is observed in transmission, it is known as the Faraday effect. In reflection, it is termed the magneto-optical Kerr effect (MOKE).

MOKE is a commonly used and well-understood physical effect ultimately stemming from magnetic circular dichroism, caused by the exchange interaction and spin-orbit coupling. Magnetic circular dichroism leads to different absorption and reflection for left- and right-circularly polarised light. Measuring the change in the polarisation state of reflected light allows information to be extracted about the magnetic state of the material causing the reflection.[34]

In general, all magneto-optic effects can be represented by a general dielectric permittivity tensor, $\boldsymbol{\epsilon}$:

$$\boldsymbol{\epsilon} = \epsilon \begin{bmatrix} 1 & -iQ_\mathrm{V}m_3 & iQ_\mathrm{V}m_2 \\ iQ_\mathrm{V}m_3 & 1 & -iQ_\mathrm{V}m_1 \\ -iQ_\mathrm{V}m_2 & iQ_\mathrm{V}m_1 & 1 \end{bmatrix} + \begin{bmatrix} B_1{m_1}^2 & B_2m_1m_2 & B_2m_1m_3 \\ B_2m_1m_2 & B_1{m_2}^2 & B_2m_2m_3 \\ B_2m_1m_3 & B_2m_2m_3 & B_1{m_3}^2 \end{bmatrix} \tag{3.1}$$

where $\boldsymbol{m}$ is the magnetisation of the material (m_n being components of the unit vector along the cubic axes) and Q_V is the Voigt constant, a complex material "constant" (actually dependent on wavelength) which describes the magneto-optical rotation of the plane of polarisation of the light and any induced ellipticity.[19] B_1 and B_2 are further complex frequency-dependent parameters that describe the Voigt effect (also known as the Cotton-Mouton effect).[19] For the materials discussed in this thesis B_1 and B_2 are typically small, meaning this effect can safely be neglected for the purposes of this discussion.

It is also important to note that a similar tensor exists for magnetic permeability.[35,36] However, it has been shown that the magnetic influence is approximately two orders of magnitude smaller than the electric influence, and can therefore be neglected.[37]

Knowledge of the permittivity allows calculation of the refractive index for the sample under test. This in turn is necessary for the calculation of the Fresnel amplitude coefficients describing the process:[38,39]

$$r_{\mathrm{ss}} = \frac{n_0 \cos\theta_0 - n_1 \cos\theta_1}{n_0 \cos\theta_0 + n_1 \cos\theta_1} \tag{3.2}$$

$$r_{\mathrm{pp}} = \frac{n_1 \cos\theta_0 - n_0 \cos\theta_1}{n_1 \cos\theta_0 + n_0 \cos\theta_1} + \frac{2iQ_{\mathrm{V}} m_2 n_0 n_1 \cos\theta_0 \sin\theta_1}{\left(n_0 \cos\theta_1 + n_1 \cos\theta_0\right)^2} \tag{3.3}$$

$$r_{\mathrm{ps}} = -\frac{iQ_{\mathrm{V}} n_0 n_1 \cos\theta_0 \left(m_1 \sin\theta_1 - m_3 \cos\theta_1\right)}{\cos\theta_1 \left(n_0 \cos\theta_0 + n_1 \cos\theta_1\right)\left(n_0 \cos\theta_1 + n_1 \cos\theta_0\right)} \tag{3.4}$$

$$r_{\mathrm{sp}} = \frac{iQ_{\mathrm{V}} n_0 n_1 \cos\theta_0 \left(m_1 \sin\theta_1 + m_3 \cos\theta_1\right)}{\cos\theta_1 \left(n_0 \cos\theta_0 + n_1 \cos\theta_1\right)\left(n_0 \cos\theta_1 + n_1 \cos\theta_0\right)} \tag{3.5}$$

where θ_0 and θ_1 are the angles of incidence and transmission, respectively, and n_0 and n_1 are the refractive indices for air and the sample, respectively. The reflection can then be summarised as:

$$\begin{pmatrix} E_{\mathrm{s}}^{\mathrm{ref.}} \\ E_{\mathrm{p}}^{\mathrm{ref.}} \end{pmatrix} = \begin{pmatrix} r_{\mathrm{ss}} & r_{\mathrm{ps}} \\ r_{\mathrm{sp}} & r_{\mathrm{pp}} \end{pmatrix} \begin{pmatrix} E_{\mathrm{s}}^{\mathrm{inc.}} \\ E_{\mathrm{p}}^{\mathrm{inc.}} \end{pmatrix} \tag{3.6}$$

With linearly polarised incident light, and $r_{\mathrm{ss}} \neq r_{\mathrm{pp}}$, the reflected light will have both s- and p-polarised components, i.e. it will be elliptically polarised. The angle between the major axis of this ellipse and the incident polarisation, for the case of incident p-polarised light, is defined as the Kerr angle:

$$\theta_{\mathrm{Kerr}} = -\,\mathrm{Re}\left[\frac{r_{\mathrm{sp}}}{r_{\mathrm{pp}}}\right] \tag{3.7}$$

Working backwards it is therefore possible to determine the relative size of a component of the underlying magnetisation of a sample by measuring θ_{Kerr}. This is the principle of Kerr microscopy.

3.2.1 Classical origin of MOKE

While the above descrption gives an idea of what is observed, and how it can be quantified, it is not a satisfying explanation from basic priciples of why the effect actually occurs.

It is easiest for this explanation to consider linearly-polarised light as the sum of left- and right-circularly polarised modes, each with the same amplitude. The circular dichroism of the material, i.e. the different response to left- and right-circularly polarised light, therefore causes both polarisation ellipticity and rotation of the plane of polarisation: differential absorption causing the former, and a difference in propagation velocity causing the latter.

The electrons within the material can be considered as harmonic oscillators, driven by a combination of the incident light's electric field and the magnetic field created by the material's internal magnetisation.* The equation of motion for an electron within the material, and under the influence of an external magnetic field $\boldsymbol{B}$ is therefore given by:[40]

$$\frac{\mathrm{d}^2\boldsymbol{r}}{\mathrm{d}t^2} + m_e\omega_0^2\boldsymbol{r} + \frac{m_e}{\tau}\frac{\mathrm{d}\boldsymbol{r}}{\mathrm{d}t} = -e\boldsymbol{E}(t) - \frac{e}{c}\frac{\mathrm{d}\boldsymbol{r}}{\mathrm{d}t} \times B\hat{\boldsymbol{z}} \tag{3.8}$$

where m_e and e are the mass and charge of an electron, respectively, ω_0^2 is the natural frequency and τ is the electron relaxation time.

---

*While an oscillating optical magnetic field is obviously also present, it is eight orders of magnitude weaker than the electric field, and can therefore be safely neglected.

In the absence of an external magnetic field, i.e. $\boldsymbol{B} = 0$, the electron will follow a circular orbit influenced equally by the left- and right-circularly polarised light. The left-circularly polarised component of the light acts to drive the electron in a left circular orbit, and likewise the right-circularly polarised components drives right circular motion. As the influence of the two polarisations are equal and opposite, the orbit remains circular and no magneto-optical effect is observed.

However, when an external field is applied ($\boldsymbol{B} \neq 0$) an additional Lorentz force acts on the electron. For an electron in a left-circular orbit, this additional force acts to reduce the orbital radius. For a right-circular orbit, this force expands the radius. This difference in oribital radius is proportional to a difference in dielectric constant for the opposing circularly polarised modes.

While this analysis provides a qualitative picture, and indeed a good quantitative estimate for most materials, it fails to describe the significant increase in the strength of magneto-optical effects observed in ferromagnetic materials. To explain this, quantum mechanics is once again required.

3.2.2 Quantum mechanical description of MOKE

Kundt showed in 1884 that the strength of magneto-optical effects was approximately 30 000 times greater for ferromagnetic materials compared to a dielectric such as glass. The proposed origin of such a strong effect was the presence of an effective internal field, in addition to the external applied field. To produce the observed polarisation rotation, this internal field was posited to be on the order of $1 \times 10^{8}\,\mathrm{A\,m^{-1}}$, approximately equal to that predicted by Weiss (see Section 2.2.3).

The origin of the internal field did not become apparent until Heisenberg's development of the exchange interaction. However, the field generated by this interaction was not linked to the motion of the electrons, and therefore could not play a role in determining the optical properties of ferromagnetic materials. It was Hulme who later showed that it was the spin-orbit interaction, the coupling of an electron's spin to its motion, which was responsible for the strength of magneto-optical effects in ferromagnets.[41]

In nonmagnetic materials the overall spin-orbit interaction is weak due to the net balancing of spin-up and spin-down. In a ferromagnet, however, the difference in the number of spin-up and spin-down electrons is far greater, causing a much greater net spin-orbit interaction. While a full quantum mechanical derivation is beyond the scope of this thesis, the interested reader is directed to the derivations provided by Qiu and Bader [40], Argyres [42], Bennett and Stern [43], and Erskine and Stern [44]. It is this interaction which is the true quantum mechanical origin of the experimentally-observed magneto-optical effects, and is responsible for the proportionality between the magnetisation of a material and the rotation and ellipticity of the polarisation of reflected and transmitted light.

3.2.3 Measuring the magneto-optical Kerr effect

Kerr Geometries

It is common to refer to three standard geometries when discussing MOKE, for which the effects can be derived.[19,45] These are shown in Figure 3.1 on the facing page.

The *polar* MOKE geometry orients the magnetisation parallel to the surface normal vector. Here the effect is strongest for $\phi = 0^\circ$ (i.e. normal incidence), consisting of a change of polarisation.

The *longitudinal* MOKE geometry consists of the magnetisation vector lying in the plane of incidence, but perpendicular to the surface normal.

Finally, the *transverse* geometry orients the magnetisation perpendicular to both the plane of incidence and the surface normal. Here, using p-polarised light, only the amplitude of the outgoing beam is changed; the polarisation direction is left unaltered.

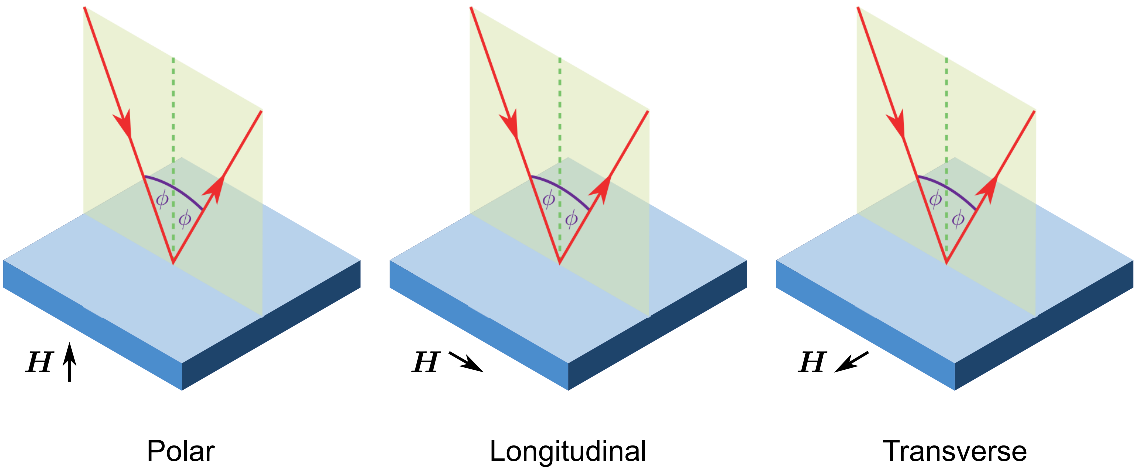

Figure 3.1: The three standard MOKE geometries. The polar and longitudinal geometries have M in the plane of incidence, resulting in a polarisation rotation. In the transverse geometry M is perpendicular to the plane of incidence and the Kerr effect causes a change in reflected intensity.

Each of these geometries is sensitive to the component of magnetisation along one of the three Cartesian axes. A number of techniques, such as changing the measurement geometry or reorienting the externally applied field allow a complete picture of the magnetisation state and magnetic response of a sample to be formed. For example, sweeping an externally applied field in either the longitudinal or polar geometry and recording the photodiode response as a function of the applied field allows for measurement of in-plane and out-of-plane hysteresis loops. In order to detect and analyse the light reflected from a sample, an optical bridge detector is typically employed.

Optical bridge detector

A schematic bridge detector employed in simple MOKE measurements is shown in Figure 3.2. The incoming laser light is typically vertically polarised before reflecting from the sample surface. When entering the bridge detector, the beam is therefore largely vertically polarised, plus a small rotation due to the Kerr effect. Upon entering the detector, the beam is split by a Glan-Thompson polarising beamsplitter, separating s- and p-polarised light to be detected separately by two

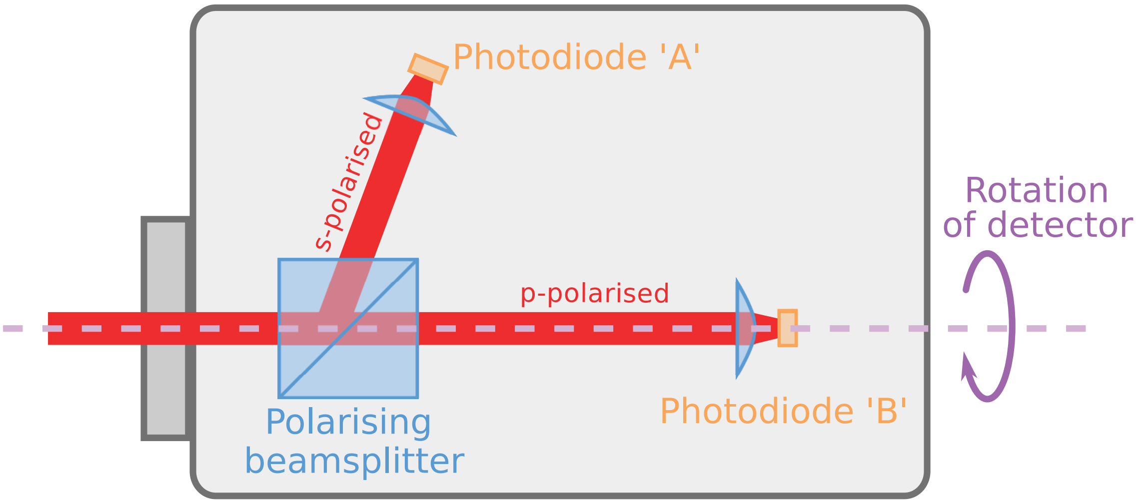

Figure 3.2: A schematic simple bridge detector used in MOKE measurements. The incoming beam is polarised at 45 degrees to the polarisation axis of the beamsplitter, ensuring an equal response from the two photodiodes.

photodiodes. The bridge detector is also mounted on a rotating mount, allowing the detector to rotate about the axis shown in Figure 3.2. Before beginning measurements, the detector is rotated to ensure that an equal response is recorded from the two photodiodes, i.e. that the polarisation axis of the beamsplitter is at 45° to the plane of polarisation of the incident light. This ensures that any change in the incoming plane of polarisation results in a significant and largely linear change in the detected photodiode signal, recorded as the difference between the responses of the two photodiodes.

Calibration between recorded photodiode voltage and Kerr rotation is then a simple matter of rotating the detector about its axis by a known angle (simulating a rotation of the incoming plane of polarisation), and recording the response from the photodiodes.

During measurements the sum of the two photodiode responses, as well as the difference, is also recorded. This allows for minor instabilities in laser intensity and position to be corrected for.

This relatively simple detector works very effectively to measure the Kerr rotation for a single component of the magnetisation, as well as allowing measurement of the Kerr ellipticity by adding a quarter wave plate before the detector. However, for time-resolved measurements it is often necessary to record the component of magnetisation along all three Cartesian axes. For these measurements a more complex optical bridge detector was used, with the simple photodiodes replaced with quadrant photodiodes.[46]

Figure 3.3 shows schematically the principle of operation of the quadrant-photodiode bridge detector. The beam and each quadrant photodiode can be considered as divided into four quadrants, labelled a, b, c and d. By appropriately summing and subtracting different segments of the beam, it is possible to recover the Kerr rotation in two orthogonal directions. To record the component of magnetisation parallel to the applied field, $\boldsymbol{M}_{\parallel}$, the recorded intensity of the beam entering segments a and d and exiting segments b and c can be subtracted from the beam travelling in the opposite direction. This gives a signal proportional to the Kerr rotation angle, θ_{Kerr}, and to $\boldsymbol{M}_{\parallel}$. The beam segments $(a+b) \leftrightarrow (c+d)$ can similarly be used to obtain $\theta_{\mathrm{Kerr}} \propto \boldsymbol{M}_{\perp}$.

Time-resolved MOKE

The MOKE setup used for dynamic measurements of hard disk write heads at the University of Exeter, depicted in Figure 3.4 on page 93, is capable of measuring all three Kerr geometries simultaneously through the use of this quadrant-photodiode polarising bridge detector.

A pulsed Ti:sapphire laser mode-locked at 80 MHz generates a train of pulses with 80 ps duration. The pulse picker reduces the repetition rate to 1 MHz before the pulses are passed through a 50-50 beamsplitter. One path hits a photodiode, triggering the electrical pulse to the coils embedded within the writer structure. The delay between this pump beam triggering the electrical signal and the probe beam hitting the sample is controlled by an electronic delay generator, allowing time resolved measurements to be taken. The second path passes through a

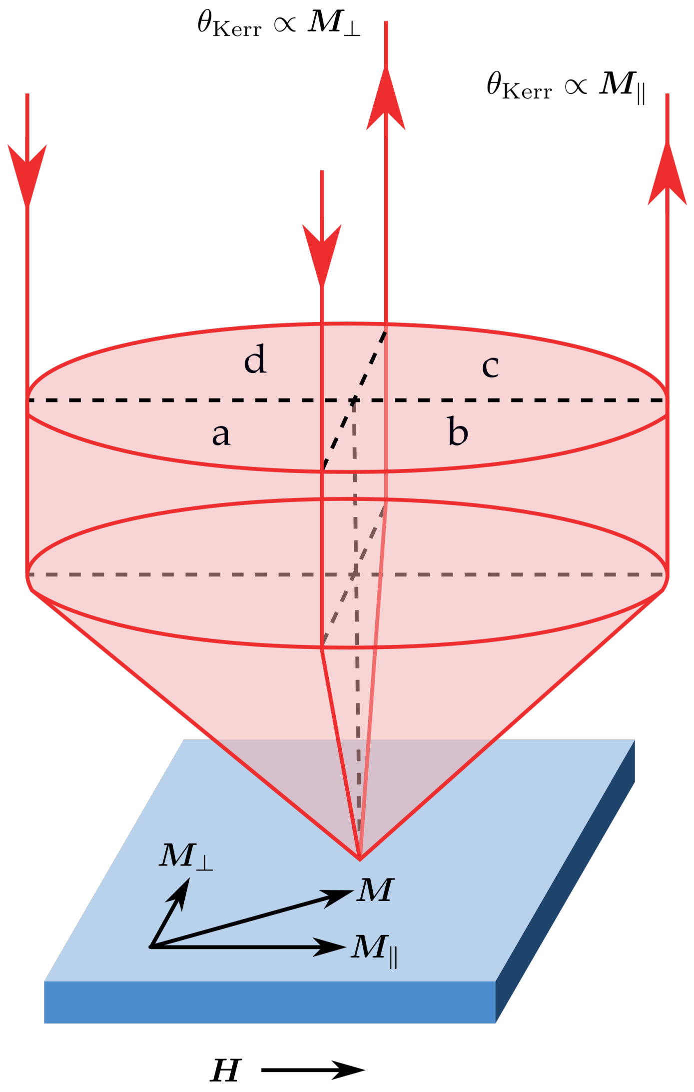

Figure 3.3: A schematic of the beam configuration as considered in the quadrant-photodiode bridge detector.

polariser and second beamsplitter before reaching a $60\times$, 0.85 numerical aperture (NA) microscope objective. This focuses the laser pulse into a $\approx$ 600 nm diameter spot on the surface of the sample. The reflected light is passed into the quadrant-photodiode bridge detector via a non-polarising beamsplitter and analysed to give the Kerr rotation for each geometry. The sample itself is mounted on a three-degrees-of-freedom piezoelectric stage, allowing spatially resolved measurements with a high degree of spatial reproducibility.

The combination of high spatial and temporal resolution provides the ability to build a picture of the magnetisation dynamics as a function of both space and time.

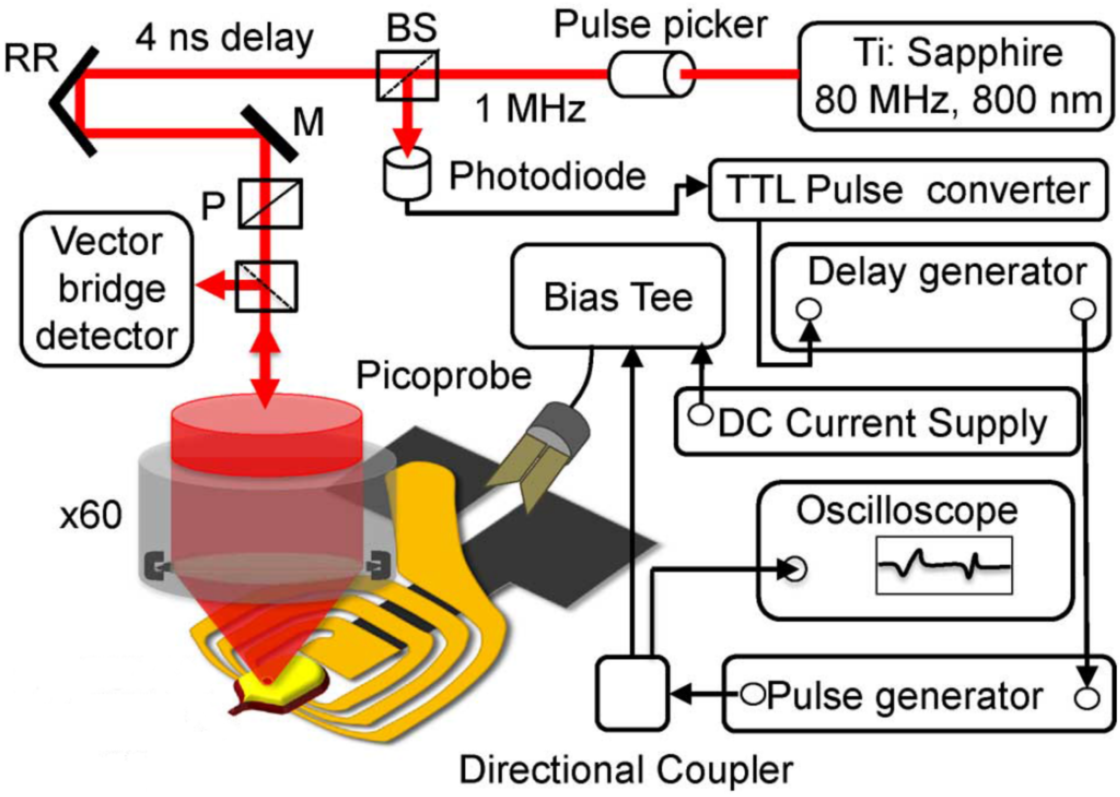

Figure 3.4: The time-resolved scanning Kerr microscope at the University of Exeter. BS: beamsplitter; M: mirror; P: polariser; RR: retroreflector. Reproduced from Yu et al. [47].

The general principle of all time-resolved Kerr measurements presented in this thesis relies on first synchronising the electrical pump stimulus and the laser pulse train to a common clock. This ensures that the same magnetisation dynamics are generated by each electrical pulse, and each laser pulse records the same stage of the dynamics (i.e. at the same relative time after the electrical pump pulse is delivered). All three components of the magnetisation vector are then recorded at a single point on the sample surface via the quadrant-photodiode detector.

To ensure detection of the relatively small Kerr signal against the background noise, the outputs of the quadrant-photodiode detector were fed into lock-in amplifiers (LIAs). The pump stimulus was then amplitude modulated at an arbitrary reference frequency, allowing the lock-in amplifiers to single this signal out from the noise. The amplitude modulation causes each LIA to compare the signal measured while the pump stimulus is active (i.e. the excited state) to the signal measured with no pump stimulus (i.e. the equilibrium state). The experiment therefore measures the change in magnetisation between the equilibrium state and the excited state at a given point in time relative to the arrival of the pump stimulus, rather than measuring the absolute time-resolved magnetisation directly.

By raster scanning the sample beneath the laser beam, and knowing that the magnetisation dynamics are reproducible and in the same state for each laser pulse, a two-dimensional map of the three spatial components of the magnetisation vector can be recorded. This raster scanning is then repeated for a range of different time delays between the triggering of the pump electrical pulse and the arrival of the probe laser pulse at the sample surface, thereby sampling the magnetisation components at different stages of their dynamics. In combination, the raster scanning and variation of delay effectively provide a video of the evolving magnetisation dynamics across the sample surface.

3.2.4 Review of the state of the art

Freeman et al. pioneered the use of Kerr microscopy to study hard drive writer dynamics in the late 1990s.[48–50] The experimental technique employed in the works of Freeman et al. is different to that employed for this research in two crucial aspects. Firstly, the geometry used by Freeman et al. measured the magnetisation from the perspective of the air-bearing surface (i.e. the pole tip, rather than the plane of the device, was in the beam path). While this allowed for detailed studies of pole tip magnetodynamics, no information could be extracted about the dynamics of the yoke. Secondly, the focus of the research was on the time delay between electrical current passing through the coils and magnetic flux being detected at the air-bearing surface. This is of course important for the operation of the hard drive, but again provides no information about the dynamics behind the delay. The development of, and improvements to, the MOKE technique in the context of writer research are however invaluable.

Gangmei et al. previously used the above Exeter setup to investigate the magnetisation dynamics of writer structures with time and spatially resolved MOKE.[51] The results obtained (reproduced in Figure 3.5 on the next page) show the first strong experimental evidence for the process of flux beaming (discussed in Section 2.7.5 on page 80). However, the flux beam path is consistently narrow along the symmetry axis of the device, contrary to the suggestions of Mallary for the most effective design of a writer.[26] Gangmei et al. make the suggestion of studying multilayer devices to further investigate more efficient flux beaming. This is the focus of Chapter 5.

While the MOKE is a excellent experimental technique for observing both static and dynamic magnetic effects, it does suffer from two fundamental limitations stemming from the fact that it is an optical technique. The use of visible and near infra-red laser light, typically 800 nm at Exeter, naturally limits the spatial resolution of the measurement to the diffraction limit of the optics involved. With the 0.85 numerical aperture lens used, this gives a best-case resolution of approximately 470 nm. Secondly, the Beer-Lambert law limits the technique to probing only the very surface of the material or structure in question. To overcome these limitations, the natural next step is simply to use light that has both a shorter wavelength and is able to penetrate further into the material.

3.3 X-rays and magnetism

Measurement techniques based on x-ray photoelectron spectroscopy (XPS) have been recognised with a Nobel prize[52] and are considered one of the best classes of measurement for investigating the electronic and spin structure of solid state materials.[53] Since the construction of the Bevatron at Lawrence Berkeley National Laboratory in the early 1950s, synchrotron light sources have played a major role in advancing in a number of scientific fields as diverse as structural biology,

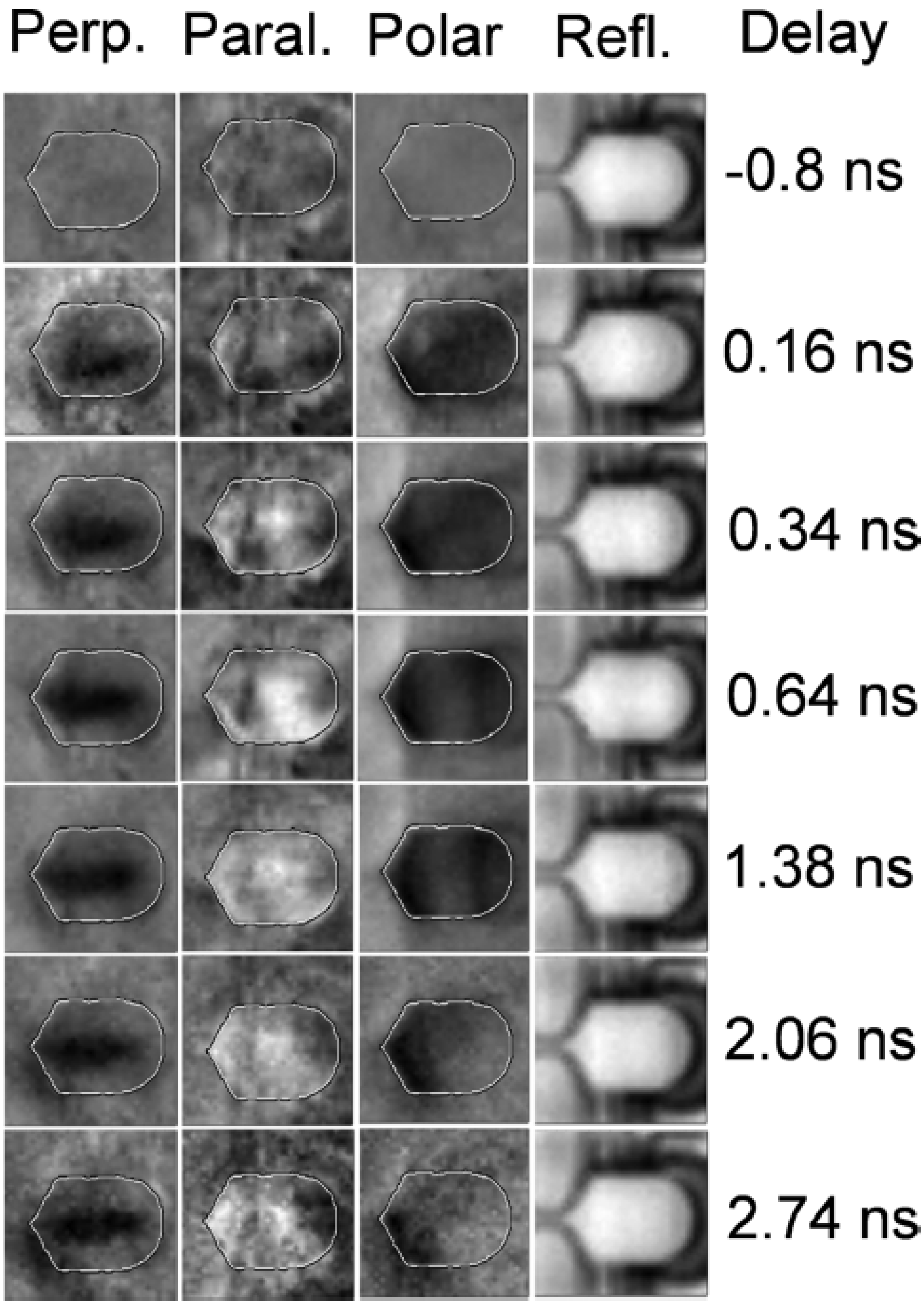

Figure 3.5: The results of Gangmei et al. [51]. Pulses were supplied to the three coils of a single layer writer with variable time delay between pump and probe measurement. Contrast in the perpendicular, parallel and polar channels represent changes to the magnetisation in the left/right, up/down and in/out-of-plane directions, respectively, as depicted here. The perpendicular component shows strong evidence of flux beaming.

oceanography and engineering and have increased the available resolution of XPS techniques length scales on the order of 10 nm.[54,55]

The research presented in this thesis has benefited from access to five beamlines at three synchrotrons, and these have been acknowledged where appropriate in both the declaration (Page 35) and the relevant experimental chapters. The techniques of XAS, XMCD and XPEEM have formed the basis for the research presented herein relating to hard disk drive write heads. Research into magnetic phenomena of other thin films has also made use of XFMR, which is explained in more detail in the relevant experimental chapters.

3.3.1 X-ray absorption spectroscopy

XAS is a technique used to study the electronic structure of solid state samples. XAS makes use of the fact that x-rays have very well-defined energy dependent absorption peaks for different elements and electronic transitions. An example of this can be seen in Figure 3.6 on the next page.

When incident on a sample, an x-ray photon may be absorbed by a core-level electron via the photo-electric effect as long as the energy of the incident photon is greater than the binding energy of that core level, as shown in Figure 3.7 on the following page. Just like any light, the probability that an x-ray photon will be absorbed is given by the Beer-Lambert law:

$$I = I_0 e^{-\mu t} \tag{3.9}$$

where I_0 is the incident x-ray intensity, μ is the absorption coefficient, t is the sample thickness and I is the transmitted x-ray intensity. The absorption coefficient μ depends on the x-ray energy E, the atomic mass A and atomic number Z of the element in the layer and the sample density ρ:[57]

$$\mu \approx \frac{\rho Z^4}{A E^3} \, . \tag{3.10}$$

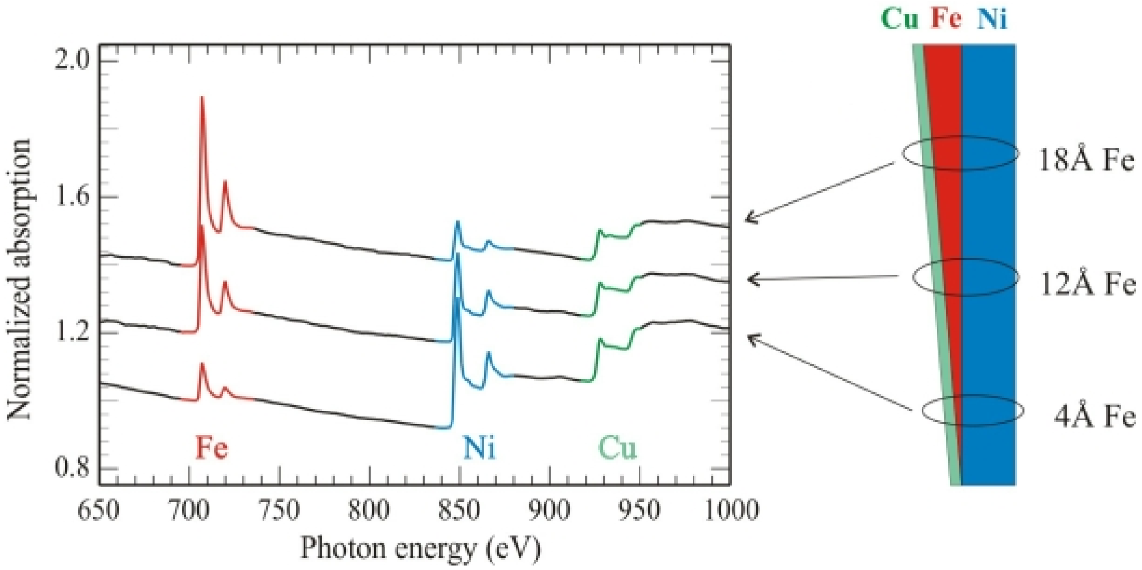

Figure 3.6: An example of x-ray absorption spectra for a sample containing a variable thickness Fe layer. The Fe absorption signal increases as the physical layer increases in thickness. The Ni signal decreases for increasing Fe thickness due to the reduction in electron escape depth. The Cu signal remains constant, reflecting its constant 1 nm thickness. Reproduced from Stöhr [56].

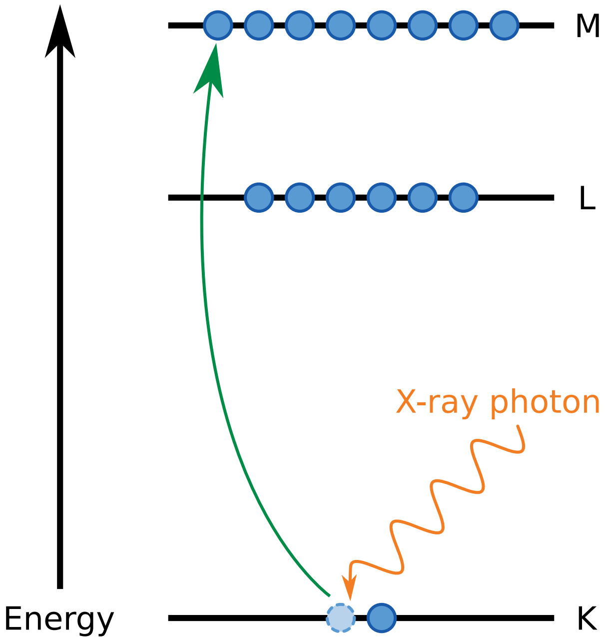

Figure 3.7: A core level electron is excited to a higher energy level upon absorption of an x-ray photon with energy sufficient to overcome the binding energy, leaving behind a hole.

As the incident x-ray energy increases such that it is equal to the binding energy, a characteristic sharp drop in x-ray transmission through the sample is observed. By recording the transmitted x-ray intensity as a function of incident x-ray energy it is possible to determine which electron energy level transitions are permitted in the sample, and the binding energies of these transitions.

This technique therefore allows for identification of the elements present in the sample, as well as the relative thickness of thin film layers. An example spectrum is shown in Figure 3.6 on page 98. The chemical environment of an element also causes characteristic changes in the absorption spectrum, making it possible to determine whether iron is present as elemental iron or a particular iron oxide, for example. However, obtaining information about the magnetic properties of a sample requires use of an additional physical phenomenon—XMCD.

3.3.2 X-ray magnetic circular dichroism

XMCD is the term given to the differing response of a material to left and right circularly polarised light. It is most easily observed by taking two XAS for a sample in a magnetic field: one each for left and right circularly polarised light. However, the same effect can also be observed using fixed helicity and opposite magnetic field directions. This effect fundamentally relies on a number of aspects of quantum mechanics, principally the spin-orbit interaction, precluding any sort of classical explanation. A quantum mechanical treatment is therefore necessary.

Each electron in an atom has a unique state which can be described by four 'quantum numbers': n, ℓ, m_ℓ and m_s. Their names and permitted values are summarised in Table 3.1 on the following page. The transition of electrons between quantum states are constrained by selection rules which limit the possible changes to each quantum number. In the electric dipole approximation, these

Table 3.1: The four quantum numbers required to define the state of an electron within an atom, and their permitted values.

Symbol	Name	Permitted values
n	principal quantum number	$n = 1, 2, 3, \ldots$
ℓ	orbital quantum number	$\ell = 0, 1, 2, \ldots, n-1$
m_ℓ	magnetic quantum number	$m_\ell = -\ell, -\ell+1, \ldots, \ell-1, \ell$
m_s	spin quantum number	$m_s = \pm\frac{1}{2}$

rules are:

$$\begin{aligned} \Delta\ell &= \pm 1 \\ \Delta m_\ell &= 0, \pm 1 \\ \Delta m_s &= 0 \\ \Delta j &= 0, \pm 1 \end{aligned} \tag{3.11}$$

where $j = \ell + m_s$.

As the materials which form the subject of this thesis are the $3d$ transition metals Fe, Co and Ni the explanation given herein will focus on these metals. The magnetic properties of these materials largely stem from the valence electrons in the $3d$ band, which has an energy-dependent density of states. As previously discussed in Section 2.3.2 on page 62, all states with an energy below the Fermi energy are occupied, whereas those above it are vacant. In a ferromagnet the $m_s = +\frac{1}{2}$ and $m_s = -\frac{1}{2}$ sub-bands are shifted in energy relative to one another due to the exchange interaction, resulting in unequal occupation, as shown in Figure 3.8 on the facing page. Similarly, the spin-orbit interaction results in unequal population of the $+m_\ell$ and $-m_\ell$ states. The total magnetic dipole moment for any given electron is proportional to the sum of its orbital and spin moments:

$$\mu_j = g_j \mu_{\mathrm{B}} \frac{\ell + m_s}{\hbar} = g_j \mu_{\mathrm{B}} \frac{j}{\hbar} \tag{3.12}$$

where g_j is the material-specific Landé g-factor.

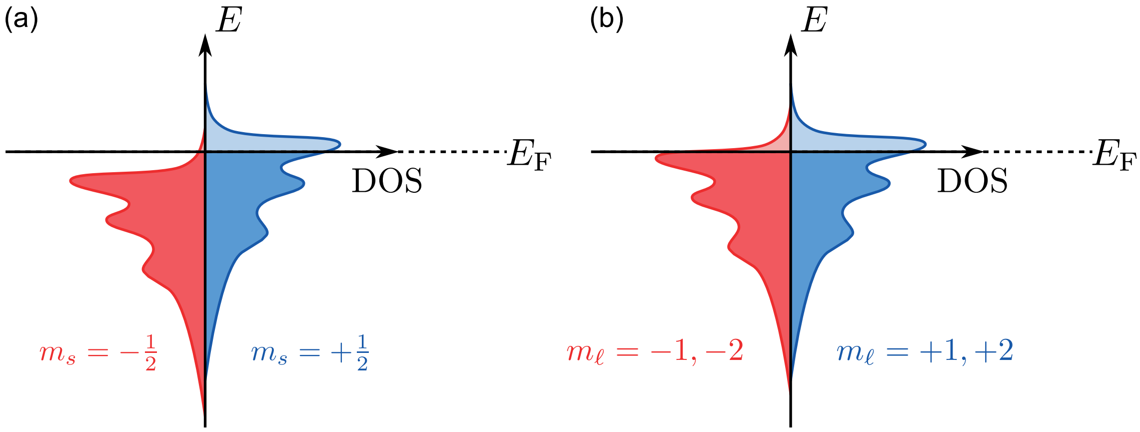

Figure 3.8: Occupation of the $3d$ shell is split by the exchange interaction (a), resulting in unequal populations of spin-up and spin-down electrons, and by the spin-orbit interaction (b), resulting in unequal populations of electrons orbiting in opposite directions around the nucleus.

The properties of the electrons within the $3d$ shell, and the accompanying holes, can be probed by excitation of electrons in the $2p$ core shell into unfilled $3d$ states. The $2p$ shell is split by the spin-orbit interaction into the $2p_{1/2}$ and $2p_{3/2}$ levels, as shown in Figure 3.9 on the next page, where the subscript represents the value of j. Transitions from each of these levels to the $3d$ level are known as the L_2 and L_3 transition, respectively. As the energy required for the L-edge transitions varies greatly between different elements, this gives XAS its element specificity.

In order to add the magnetic sensitivity to the measurement, it is necessary to make the photon absorption process spin-sensitive. The selection rules outlined in Equation (3.11) on page 100 state that a change in spin is forbidden in an electric dipole transition. Therefore spin-up electrons in the $2p$ shell must only be excited into spin-up $3d$ holes, and likewise for spin-down electrons. By favouring spin-up or spin-down transitions under different measurement circumstances, and comparing the intensities of the resulting spectra, it is possible to determine the relative populations of spin-up and spin-down holes, thereby revealing the magnetic spin moment of the sample.

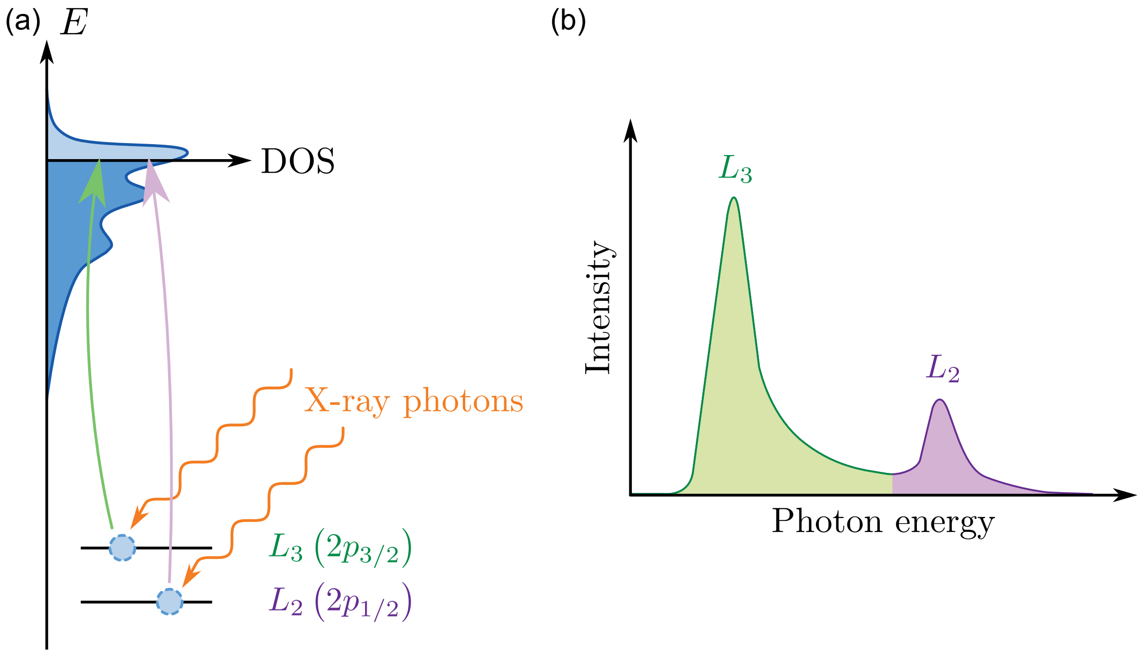

Figure 3.9: Electron transitions at the L edges in a $3d$ transition metal (a), and the resulting x-ray absorption spectrum (b).

XMCD makes use of left and right circularly polarised photons to cause this preferential excitation of spin-up or spin-down electrons. Stöhr explains this using a 'two-step' model.[58] The first step is the absorption of right or left-circularly polarised photons having angular momentum $\hbar$ and $-\hbar$, respectively. When the photon is absorbed, its angular momentum is transferred to the resulting excited photoelectron as some combination of spin and angular momentum, as a result of spin-orbit coupling. Right and left circularly polarised photons, having opposite angular momentum, excite photoelectrons with opposite spin. In the second step the spin-split $3d$ valence shell acts as a detector for the photoelectron's spin, as a result of spin-flips being forbidden in the excitation. The relative absorption of left and right circularly polarised photons therefore reveals the relative populations of spin-up and spin-down holes. For example, in Figure 3.10 on the next page the exchange interaction has resulted in a greater number of spin-up holes. The absorption of right-circularly polarised light is therefore greater than the absorption of left-circularly polarised light, as there are a greater number of vacant spin-up holes states into which photoelectrons can be excited. The difference between

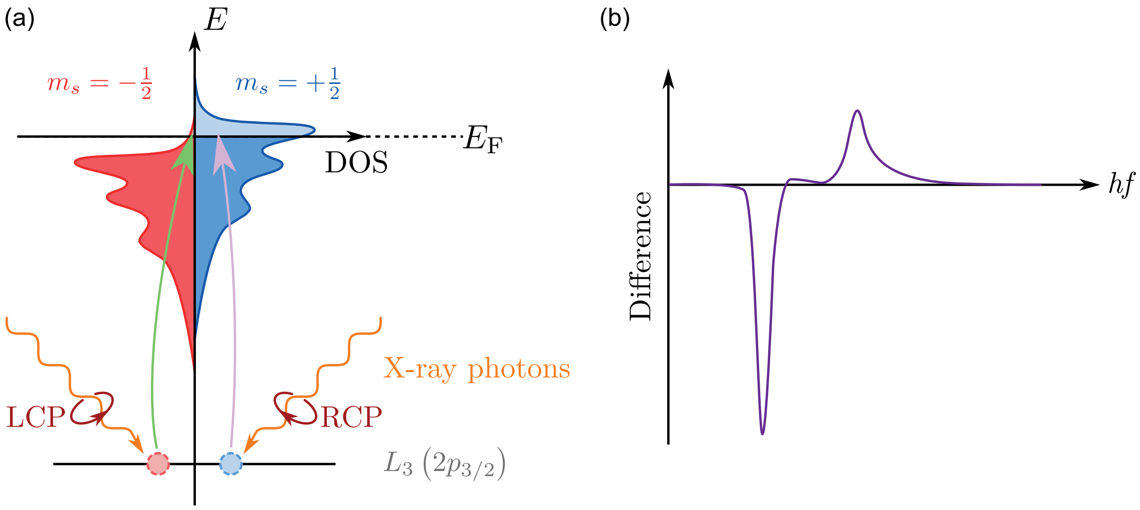

Figure 3.10: Left and right-circularly polarised photons preferentially excite photoelectrons into holes with different spin states (a), and the resulting x-ray magnetic circular dichroism difference spectrum (b).

the two absorptions can therefore be related to the hole populations, and the magnetic spin state of the sample. Additionally, as the $2p_{1/2}$ and $2p_{3/2}$ levels have opposite spin-orbit coupling, summing the contribution from each level eliminates the spin contribution, revealing the orbital moment. The process of obtaining these two values makes use of the 'XMCD sum rules' explained in more detail below. Examples of typical experimental XAS and XMCD spectra are shown in Figure 3.11 on the following page.

3.3.3 Orbital and spin sum rules

One of the prime advantages of XMCD is its ability to carry out separate measurements of L_z and S_z, the orbital and spin moments, through the use of the sum rules.[59] These rules, derived by Thole et al.[60] and Carra et al.,[61] relate the integrated intensity of the signal at the L_3 and L_2 edges to L_z and S_z:

$$\langle L_z \rangle = 2n_{\text{holes}} \frac{\int_{\text{edge}} \mu^+ - \mu^- \, \mathrm{d}\omega}{\int_{\text{edge}} \mu^+ + \mu^- + \mu^0 \, \mathrm{d}\omega} = 2n_{\text{holes}} \frac{\Delta A_{L_3} + \Delta A_{L_2}}{A_t} \tag{3.13}$$

$$\langle S_z \rangle + \frac{7}{2} \langle T_z \rangle = \frac{3n_{\text{holes}}}{2} \frac{\Delta A_{L_3} - 2\Delta A_{L_2}}{A_t} \tag{3.14}$$

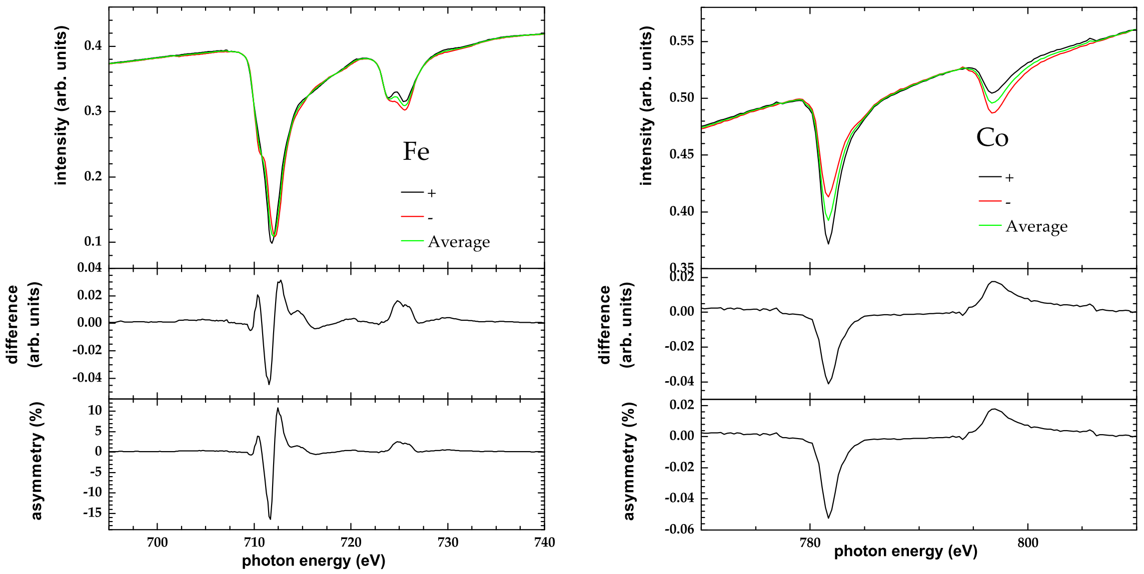

Figure 3.11: Example XAS and XMCD spectra for iron and cobalt within a $Y_3Fe_2(FeO_4)_3$ / Cu / Co spin valve. The upper panels show XAS recorded with positive (black) and negative (red) circularly polarised light, and the average of these two (green). The lower two panels show the XMCD spectra as difference (centre panel) and asymmetry (lower panel). The three peaks in the iron L_3 edge correspond to three iron sites within the YIG crystal lattice.

where n_{holes} is the number of hole states, A_{L_3} and A_{L_2} are the integrated intensities of the XMCD spectra at the L_3 and L_2 edges, A_t is the total intensity of the spectra and μ is the absorption coefficient for left circularly polarised $(+)$, right circularly polarised $(-)$ and unpolarised (0) light. $\langle T_z \rangle$ is the expectation value of the magnetic dipole operator.

These rules, however, are not 100% accurate. It has been shown, for example, that Equation (3.13) can be inaccurate due to the neglect of many-body effects.[62] It has also been shown that the magnetic dipole term can have a significant effect on Equation (3.14).[59] Further effects caused by diffuse magnetic moments have also been identified as having significant aberrant effects for iron, cobalt and nickel samples.[63]

3.3.4 X-ray photo-emission electron microscopy

XPEEM is a microscopy technique based on XAS. While XAS has been described in terms of detecting the transmitted x-ray intensity, this is in practise not always possible or desirable. However, the filling of the hole generated by absorption of a photon is accompanied by the emission of one or more secondary electrons, a process known as the Auger effect. When an electron is excited from a core level to an excited level, it is possible that an electron already in an excited state will relax to fill the vacant core hole, releasing energy. This energy is transferred to another excited electron, overcoming the work function and leading to the ejection of that electron (known as an Auger electron) from the sample, as shown in Figure 3.12 on the next page. As the Auger electron leaves the sample it is scattered, generating a shower of secondary electrons, resulting in many electrons being ejected from the surface for each photon that is absorbed.

These secondary electrons, ejected into the vacuum, pass through an electron optical column. This column begins with the extractor, focus and column optics: a series of electrostatic electron lenses, used to focus the beam of emitted electrons as shown in Figure 3.13 on page 107. The electrons then pass through an intermediate contrast and magnification stage, allowing the magnification power of the set-up to be varied. Finally the beam reaches the projector, a lens configuration used to slow the electrons for the detector's peak sensitivity range.

Acquiring and averaging data for a period of time allows an image of the sample to be formed. A typical XPEEM image is shown in Figure 3.14(a) on page 108. Recording images using both positive and negatively circularly polarised light, and subtracting these images from one another, allows magnetic contrast to be revealed by XMCD (Figure 3.14(c) on page 108). In practise it is necessary to acquire images for a considerable length of time to increase the signal to noise to acceptable levels. This in turn necessitates further image processing to correct for variations in beam intensity, beam position and sample drift with time to produce

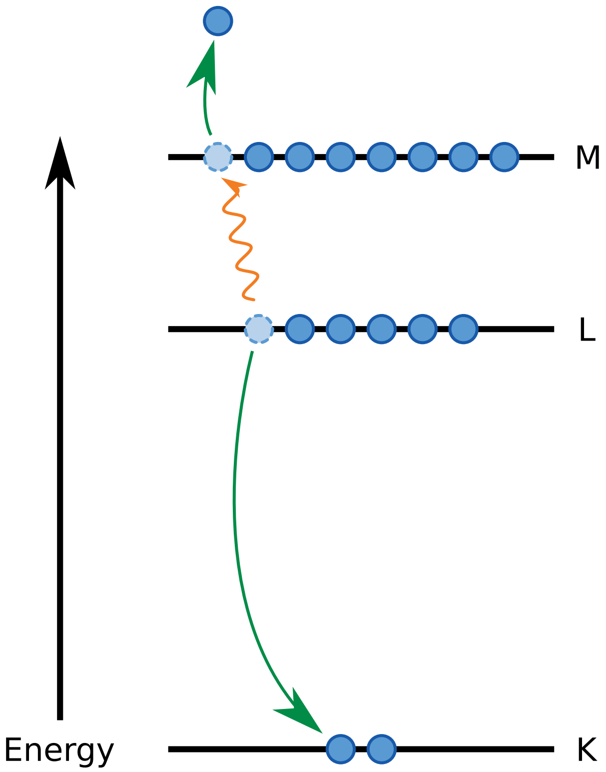

Figure 3.12: Following the absorption of an x-ray photon, a higher-energy electron may transition to fill the now-vacant hole state. In doing so, the released energy may be transferred to a higher-energy electron and may be sufficient to overcome the work function, ejecting that electron from the sample.

an image like that shown in Figure 3.14(d) on page 108.

The combination of XAS, XMCD and XPEEM is a powerful one, allowing element-specific, high-spatial-resolution information about the magnetisation of a sample to be extracted.

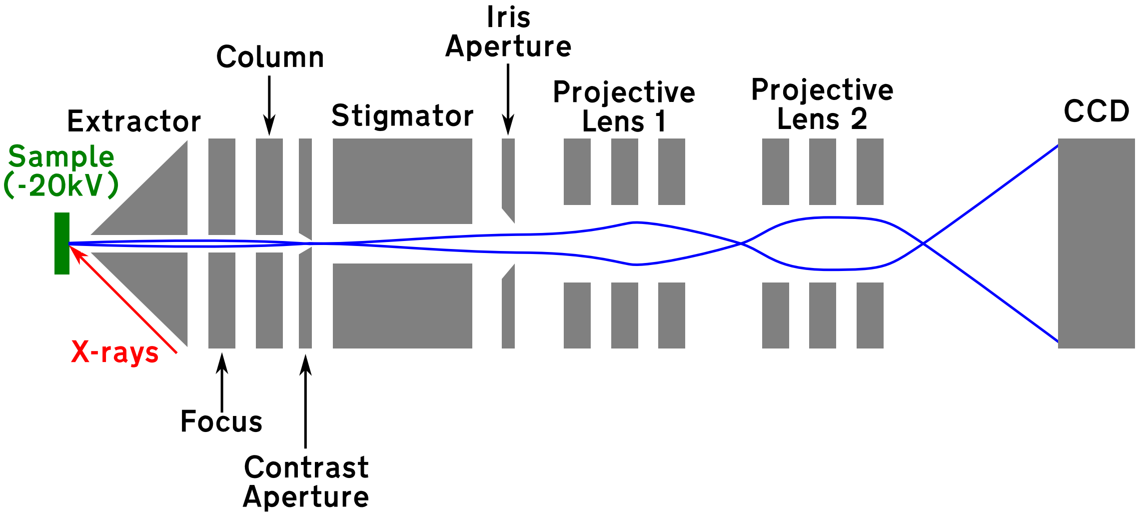

Figure 3.13: Schematic of a simplified XPEEM column. The sample (held at $-20\,\mathrm{kV}$) is excited by the incident soft x-ray, initiating emission of photoelectrons (blue). The extractor, focus and column optics form an objective lens which works with the contrast aperture to focus the beam and provide optimum spatial resolution. The projector decelerates emitted electrons to make detection easier. Note that each lens is made up of a number of electrostatic elements (not shown) with applied potential differences in the kV range. Adapted from Kleimeier [64].

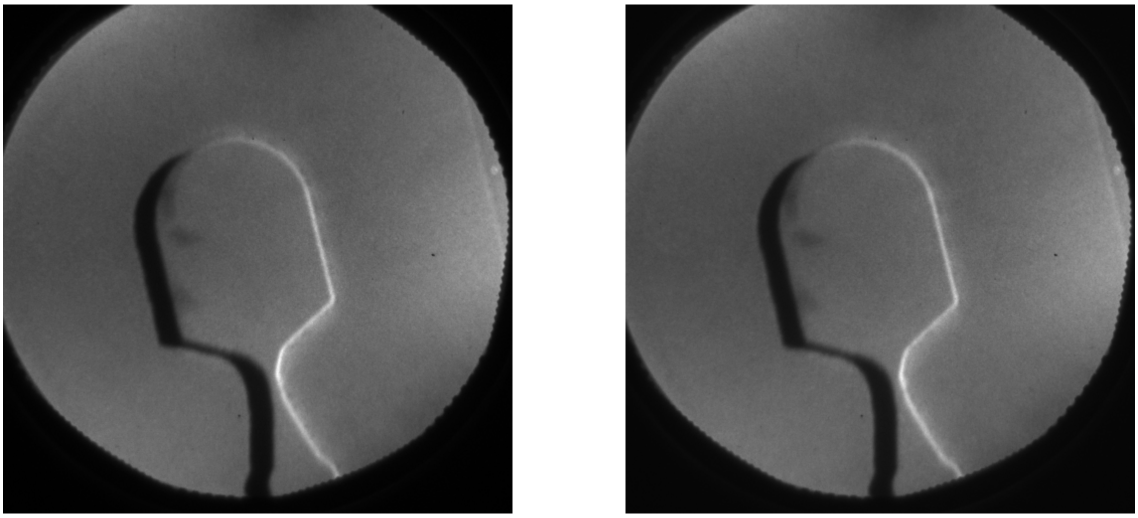

(a) Positive circular polarisation (b) Negative circular polarisation

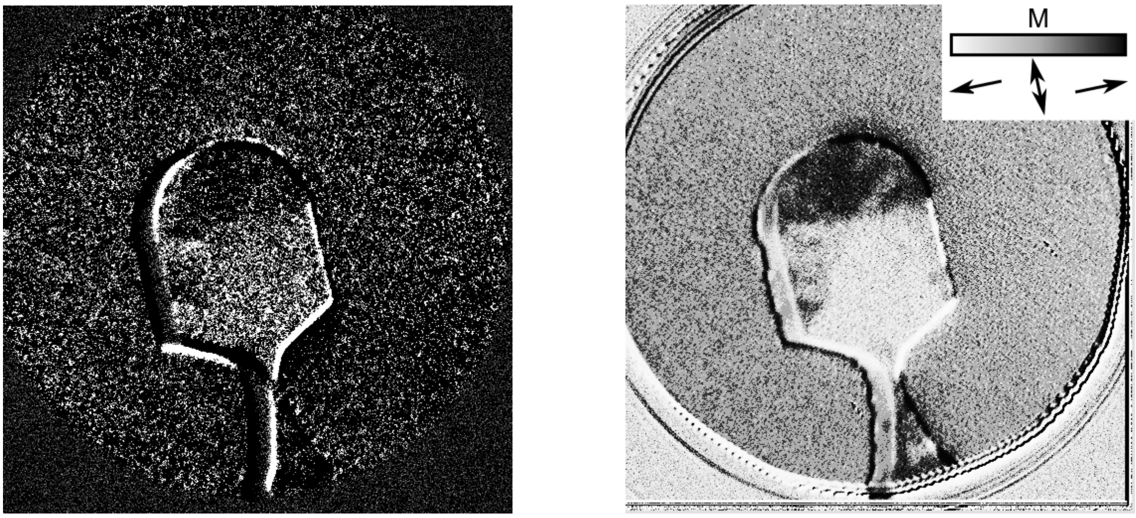

(c) Subtracted (d) Processed

Figure 3.14: Typical XPEEM images of a hard disk write head recorded on beamline I06 at Diamond Light Source. (a) and (b) show images recorded with positive and negative circularly polarised light at the iron L_3 edge (707 eV). The two images are then subtracted (c) to reveal magnetic contrast. Further averaging and drift correction produces an image (d) with magnetic contrast clearly visible.

CHAPTER 4

Imaging the remanent state and magnetisation dynamics of partially-built hard disk writers

Some of the results presented in this chapter have previously been published as ‘Imaging the equilibrium state and magnetization dynamics of partially built hard disk write heads’ by Valkass et al. in *Applied Physics Letters* **106**, 232404 (2015).

4.1 Introduction

The ever present global demand to store more digital data necessitates the continual increase of both data storage densities and data writing rates within perpendicular magnetic recording technology.[66] To accomplish these goals, hard disk write heads capable of producing stronger fields with consistent rise times on the picosecond timescale are required. These must, however, not come at the cost of suffering such problems as erase after write phenomena[67] and popcorn noise.[68] The phenomenon of “flux beaming” (previously discussed in Section 2.7.5

on page 80) is currently the best way to meet these requirements, and crucial to optimising this process is a thorough understanding of both the remanent state and magnetodynamics of the writer structures: a stable remanent state is essential for producing a reliable write field while the magnetisation dynamics within the writer can significantly alter the amplitude and temporal form of the write field.[69]

A number of advanced techniques have been developed to probe the non-uniform magnetic state of writer structures. Optical Kerr microscopy[48–50] provides direct imagery of the magnetic state of the writer, but is unable to provide high enough spatial resolution to resolve detailed magnetic structures within the nanoscale features of the writers.[47,51,70] Time-resolved Kerr microscopy, by its very nature, is also only suited to imaging the magnetodynamics rather than the remanent state; this has to be inferred from the observed dynamics. Photoemission electron microscopy (PEEM)[71] and electron holography[72] are both well suited to high-resolution imaging of the remanent state of the writers, but have not been teamed with dynamic measurements. Also, because of their higher resolution, measurements using these techniques have focused solely on the nanoscale pole tip from the perspective of the air-bearing surface[73,74] rather than the dynamics of the main body of the writer.

In this chapter, static XPEEM images are presented alongside TRSKM data acquired from a range of writers with different geometric designs. In contrast to previous works such as those by Gangmei et al. and Yu et al., the XPEEM images presented in this chapter provide a much greater spatial resolution of the magnetic state of the writers (on the order of tens of nanometres, as opposed to hundreds of nanometres). Furthermore, the stroboscopic TRSKM technique employed by Gangmei et al. and Yu et al. only reveals the change in magnetic state in response to an external excitation, rather than the absolute remanent state of the writers provided by XPEEM. This means that the remanent state must be inferred from TRSKM, which introduces an element of uncertainty which is eliminated with the direct measurement of the remanent state by XPEEM.

The sample preparation technique employed herein has also opened up the entire surface of the writers to exploration by XPEEM while retaining the necessary resolution to image the magnetic state in the nanoscale pole tip. Previous studies with sufficient resolution to image the pole tip, such as those by,[73,74] have focused instead on imaging the writers from the perspective of the air-bearing surface. While such studies provide a good indication of the spatial and temporal field profile to be expected from a writer, no information is provided about the origins of this field or how to improve it. Imaging both the pole tip and body of the writer simultaneously, as presented in this chapter, elucidates both the expected write field and the origins of this field.

Direct experimental observation of both the remanent state and dynamic processes within the same writer structure are presented, as well as how both of these vary with writer geometry. As a measure of the stability of the remanent state, XPEEM images taken before and after the application and removal of an external bias field are also presented. Finally, XPEEM images recorded while an external bias field was applied are presented.

It is shown that the crystalline anisotropy of the writers dominates their remanent domain configuration. However, the effect of attempting to minimise magnetostatic energy is of a similar magnitude and this competition ultimately determines the stability of the remanent state for a given writer geometry. TRSKM images suggest that a longer confluence region may hinder flux conduction throughout the writer. Furthermore, the observed variations in the dynamic responses agree well with the differences in remanent state visible in XPEEM images, confirming that minor variations in geometric structure can have a significant effect on the process of flux beaming.

4.2 Sample Details

Samples were fabricated by Seagate Technology specifically for use in TRSKM experiments using their production manufacturing facilities. Samples arrive at Exeter as wafer “chunks”: pieces diced from a much larger wafer, such that they measure approximately $51.9\,\mathrm{mm} \times 16.4\,\mathrm{mm}$. For use in either XPEEM or TRSKM experiments these wafer chunks must be further reduced in size. The wafer chucks were first coated in approximately $500\,\mathrm{nm}$ of poly(methyl 2-methylpropenoate), also known as poly(methyl methacrylate) (PMMA) to protect them during the dicing process, then baked at $160\,^{\circ}\mathrm{C}$ to cure. The wafer chunks were then diced using a Loadpoint MicroAce Series 3 dicing saw system fitted with a vitrified synthetic diamond blade. The protective PMMA was then removed by sonicating the wafer pieces in warm acetone for five minutes, followed by propan-2-ol, also known as isopropyl alcohol (IPA) for a further five minutes.

Wafer pieces destined for XPEEM were diced down to $9\,\mathrm{mm} \times 9\,\mathrm{mm}$ squares, the largest size which could be accommodated in XPEEM sample cartridges. The exact $9\,\mathrm{mm}$ square region was selected to capture the greatest variety of writer designs possible. Those pieces to be used for TRSKM were reduced to $16.4\,\mathrm{mm} \times 12.8\,\mathrm{mm}$ to make the wafer piece as small as possible while ensuring the probe pads used to deliver a current pulse to the embedded writing coils were preserved. Examples of a wafer chunk, XPEEM wafer piece and TRSKM wafer piece are shown in Figure 4.1 on the next page.

Each wafer piece contained a plurality of different writer designs, with each design being repeated eight times along the gold traces (shown in the horizontal direction in Figure 4.1 on the facing page). However, only one of each writer design, the writer adjacent to the central divide (the dark vertical band in Figure 4.1), has its embedded coils electrically connected to the gold transmission lines and probe pads. This means that only one of each writer design is suitable for TRSKM measurements, whereas up to eight would be accessible by XPEEM. A more

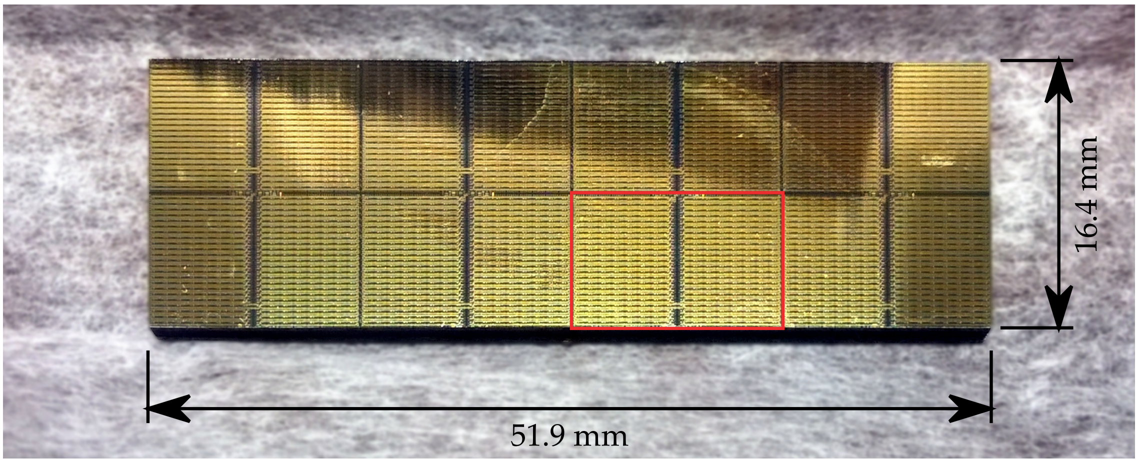

(a) A wafer “chunk” as provided by Seagate

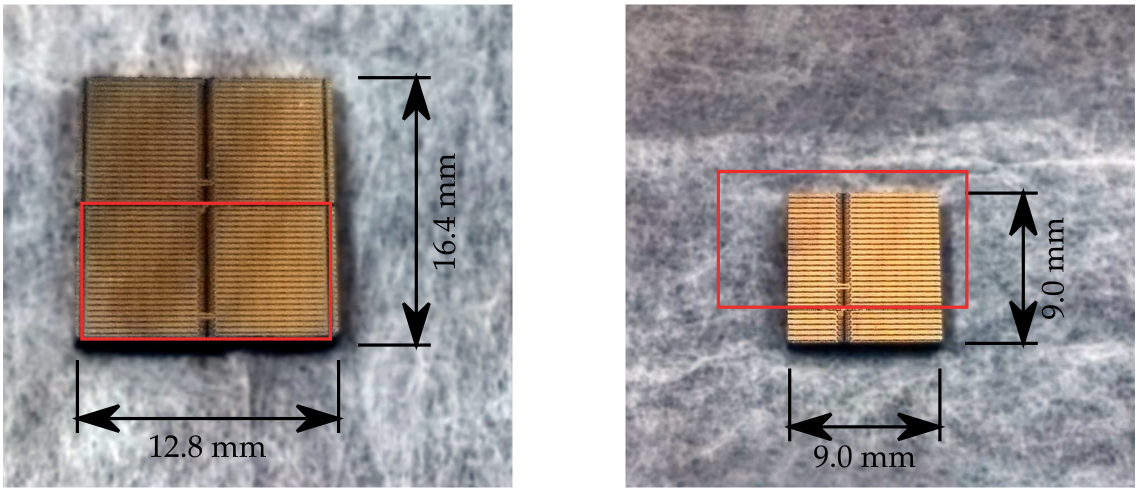

(b) Diced TRSKM wafer piece

(c) Diced XPEEM wafer piece

Figure 4.1: Photographs of a diced wafer “chunk” as provided directly from Seagate, and the diced wafer pieces used for TRSKM and XPEEM experiments. The red outline in each image marks a “unit cell” of one complete set of writer designs.

detailed micrograph of the layout of a wafer piece is shown in Figure 4.2(a) on the next page, with the detail of a writer shown in Figure 4.2(b) on the following page.

To afford the optical access required for TRSKM, the writers studied in this chapter were “partially-built”: the fabrication process was stopped early, resulting in a writer cross section as shown in Figure 4.2(c) on the next page. Compared to the full read/write head design previously discussed in Section 2.7 these structures are missing only the reader part, which is of no interest to this study. The yoke of each writer was formed from four repeats of a NiFe (1 nm) / CoFe (50 nm)

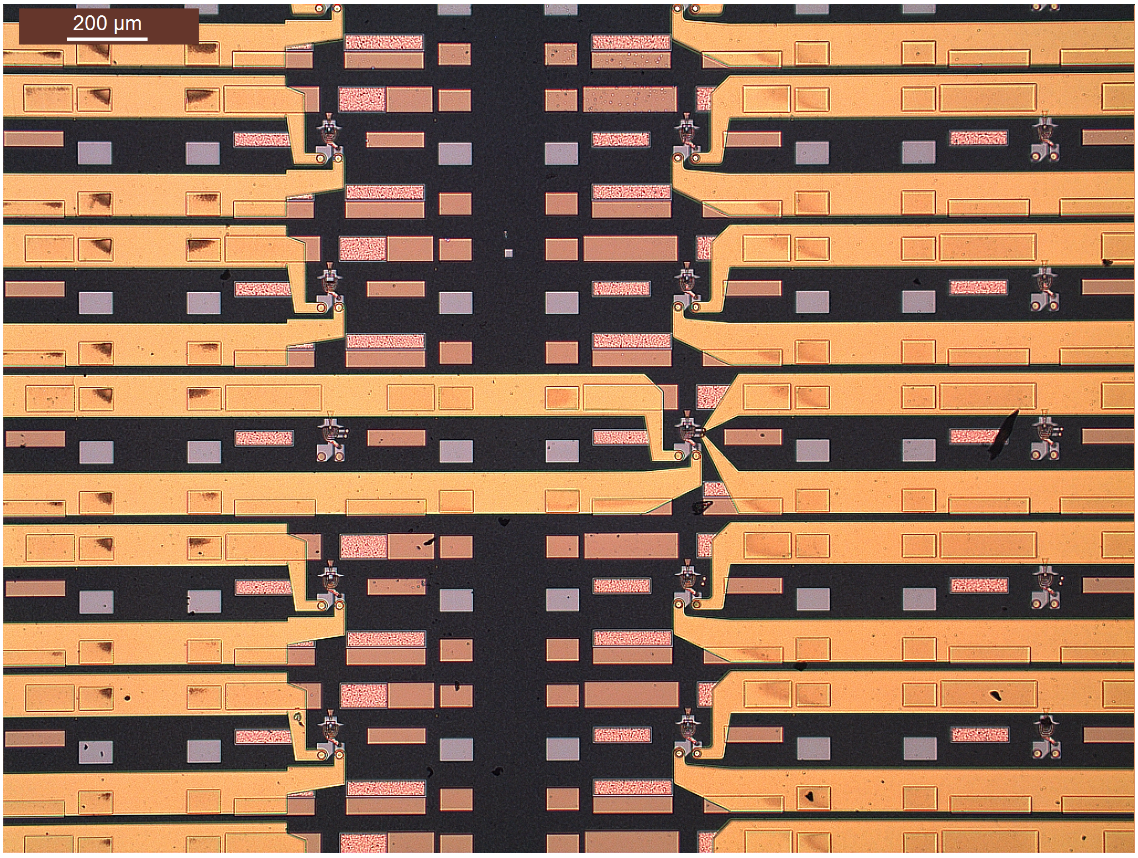

(a) Micrograph of a wafer section showing the gold traces to which one copy of each writer is connected

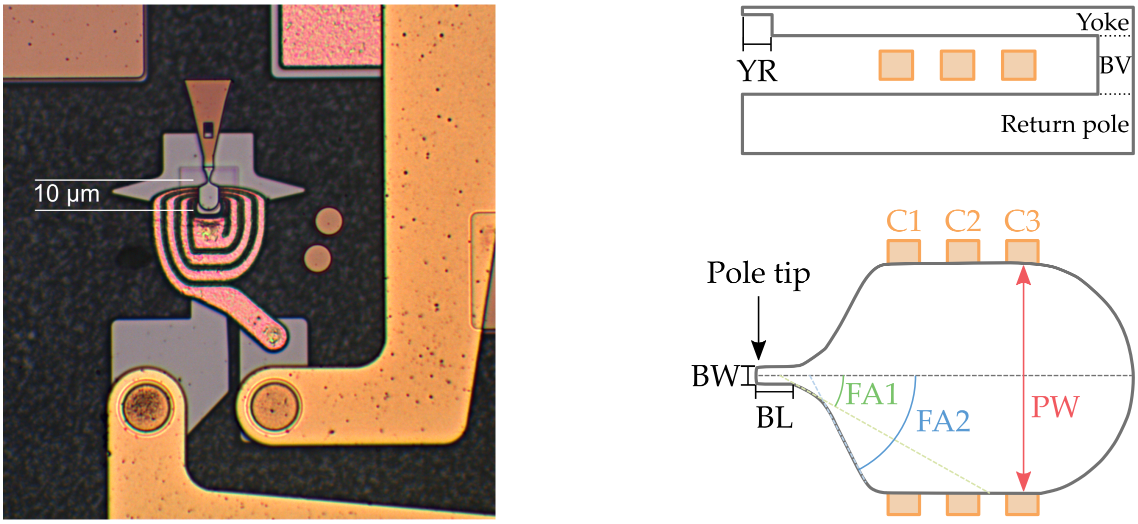

(b) An exemplar writer

(c) Writer schematic

Figure 4.2: Micrographs of the general wafer layout, and detail of an exemplar writer. A schematic of the writer's geometric parameters is shown in panel (c). C1–3 are pancake coils embedded between the yoke and return pole of the writer. The cross section, top, shows the three-dimensional structure of the upper half of the yoke including the yoke recess (YR). The paddle width (PW) in this example is 6.485 µm, with an overall device length of 10.0 µm. The bridge length (BL) and bridge width (BW) are 1.0 µm and 400 nm, respectively.

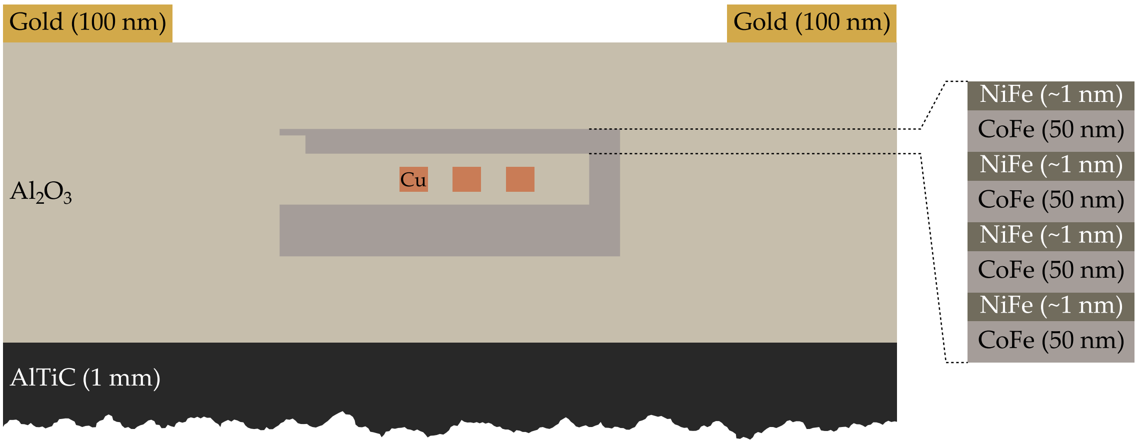

Figure 4.3: The complete stack structure of the writers as they arrive from Seagate and are used for TRSKM. The complex three-dimensional shape of the writer necessitates the use of Al_2O_3 to create a plenum surrounding the magnetic material.

bilayer designed for a high magnetic moment and low coercive field.[70] To define the complex three-dimensional form of the writer, and to fill the voids between the magnetic material and copper coils, the writers are surrounded with Al_2O_3 deposited atop an AlTiC substrate. Transmission lines of Au were deposited on top of the Al_2O_3 layer to provide a conductive pathway to the Cu coils beneath one of each writer design. The full stack structure can be seen in Figure 4.3.

The geometric parameters that were varied between each writer are detailed in Table 4.1 on page 117 and shown on a typical "paddle" shaped writer in Figure 4.2(c) on page 114. All of the writers had uniaxial anisotropy, induced by field annealing, with the easy axis oriented in-plane and perpendicular to the symmetry axis.

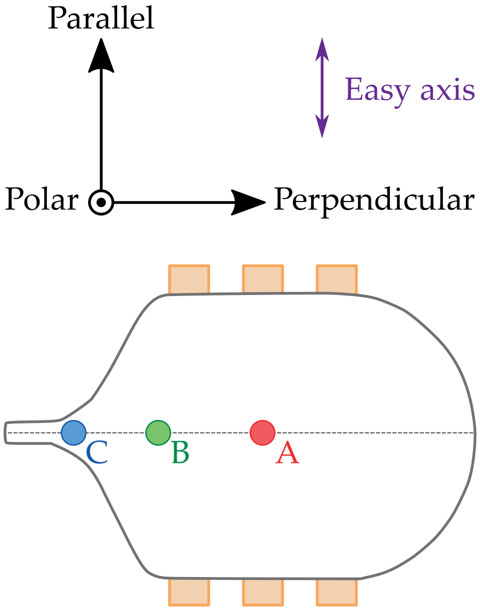

Figure 4.4: The positions at which TRSKM measurements were made and the co-ordinate system based on the writer's easy axis direction, referred to as the "parallel" axis.

Table 4.1: The geometric parameters of each writer imaged in this chapter. The parameters are defined with reference to Figure 4.2(c).

Writer	Shape	Paddle width	Flare angles		Yoke recess	Bridge length	Bridge width	Back via	Return pole
		(µm)	FA1 (°)	FA2 (°)	(µm)	(µm)	(nm)		
F4	Paddle	6.485	30	62	1.6	1.0	400	Gapped	✓
F8	Paddle	6.485	30	62	1.6	1.0	400	Gapped	✓
F10	Paddle	6.485	30	62	1.6	1.0	400	Gapped	✓
F11	Paddle	6.485	30	62	1.6	1.0	400	Full	✓
F12	Paddle	6.485	30	62	1.6	1.0	400	None	✓
F13	Paddle	6.485	30	62	1.6	1.0	400	Full	✗
F14	Paddle	6.485	30	30	1.6	1.0	400	Gapped	✓
F15	Paddle	6.485	45	30	1.6	1.0	400	Gapped	✓
F16	Paddle	6.485	45	45	1.6	1.0	400	Gapped	✓
F17	Paddle	6.485	45	62	1.6	1.0	400	Gapped	✓
F18	Paddle	6.485	62	62	1.6	1.0	400	Gapped	✓
F20	Paddle	6.485	30	90	1.6	1.0	400	Gapped	✓
F26	Rectangle	10.0	45	90	1.6	1.0	400	Gapped	✓
F27	Rectangle	20.0	45	90	1.6	1.0	400	Gapped	✓
F28	Paddle	6.485	30	62	2.6	1.0	400	Gapped	✓
F29	Paddle	6.485	30	62	3.6	1.0	400	Gapped	✓
F30	Paddle	9.775	30	62	1.6	1.0	400	Gapped	✓
F31	Paddle	3.735	30	30	1.6	1.0	400	Gapped	✓
F32	Circle	8.555	30	62	1.6	1.0	400	Gapped	✓
F33	Paddle	6.885	30	62	1.6	2.0	800	Gapped	✓

4.3 Experimental Details

4.3.1 X-ray photo-emission electron microscopy

XPEEM was used to image the remanent state of different writer designs, and to confirm the reproducibility of this remanent state between nominally identical copies of the same writer. Further XPEEM images were acquired after the application of an externally applied field to the writers to test the stability of the observed remanent state. Finally, images of the domain state were also acquired during the application of an external field, to detect any minor deviations from the remanent during the field application.

XPEEM images were acquired at two synchrotron sources: the PEEM end-station of beamline I06 at DLS, and the spin-resolved photo-emission electron microscope (SPEEM) end-station of beamline UE49_PGM at BESSY II. The fundamental theoretical principles of XPEEM have been previously discussed in Section 3.3.4, and so will not be reiterated here. However, the experimental details specific to DLS and BESSY II are outlined below.

At both DLS and BESSY II the remanent domain configuration of the writers was imaged directly by XPEEM using XMCD as the contrast mechanism. Images were obtained using left and right circularly polarised soft x-rays at the iron L_3 edge and pre-edge (707 eV and 703 eV, respectively). Between 10 and 40 images of each writer were averaged together to reduce noise, before being programatically corrected for sample drift over the course of the acquisition. On-edge images were then normalised relative to their corresponding pre-edge image before the subtraction of opposite polarisations, producing an image showing magnetic contrast.

Images comparing the magnetic state before and after the application and removal of an external bias field were acquired at both DLS and BESSY II but in slightly different ways. At DLS all writers were imaged one after another in their remanent state. The sample was then removed from the vacuum and placed between the poles of an electromagnet, with a 200 mT field applied oriented parallel to the symmetry axis of the writers. The wafer piece was then placed back into the PEEM and each writer was re-imaged in sequence. In contrast, the SPEEM at BESSY II has sample holders containing an embedded electromagnet. This facilitated the application of a field *in vacuo*, meaning each writer was imaged immediately before and after the application and removal of a field oriented perpendicular to the writers' symmetry axes. The embedded electromagnet also allowed the imaging of a writer while the field was applied. These results are presented in Sections 4.4.1 to 4.4.2.

4.3.2 Time-resolved scanning Kerr microscopy

A schematic layout of the TRSKM setup used for dynamic imaging is shown in Figure 4.5 on the next page and was previously described in detail in Section 3.2.3.

The writers were excited with an electrical pulse of 2.2 ns full width at half maximum (FWHM) duration and 12.7 V amplitude, shown in Figure 4.6 on page 121. While the amplitude and duration are approximately prototypical of the pulses used in production devices, the shape of the pulse differs somewhat from that typically used. The write pulses used in consumer hard disk drives typically feature an initial amplitude 'overshoot' above the square-wave amplitude[75] which helps to ensure sufficient flux in areas with a high frequency of bit transitions, while avoiding far track erasure in areas without many transitions (i.e. long sequences of either 0's or 1's). The precise details of the write pulse are, however, typically commercially sensitive information which was not available. This pulse passed through the embedded driving coils C1 and C2 at a 1 MHz repetition rate, corresponding to an in-plane field of approximately 20 mT throughout the yoke. The magnetodynamic response of the writer was probed by an 800 nm laser pulse of 100 fs duration focused onto the writer surface by a 60× microscope objective

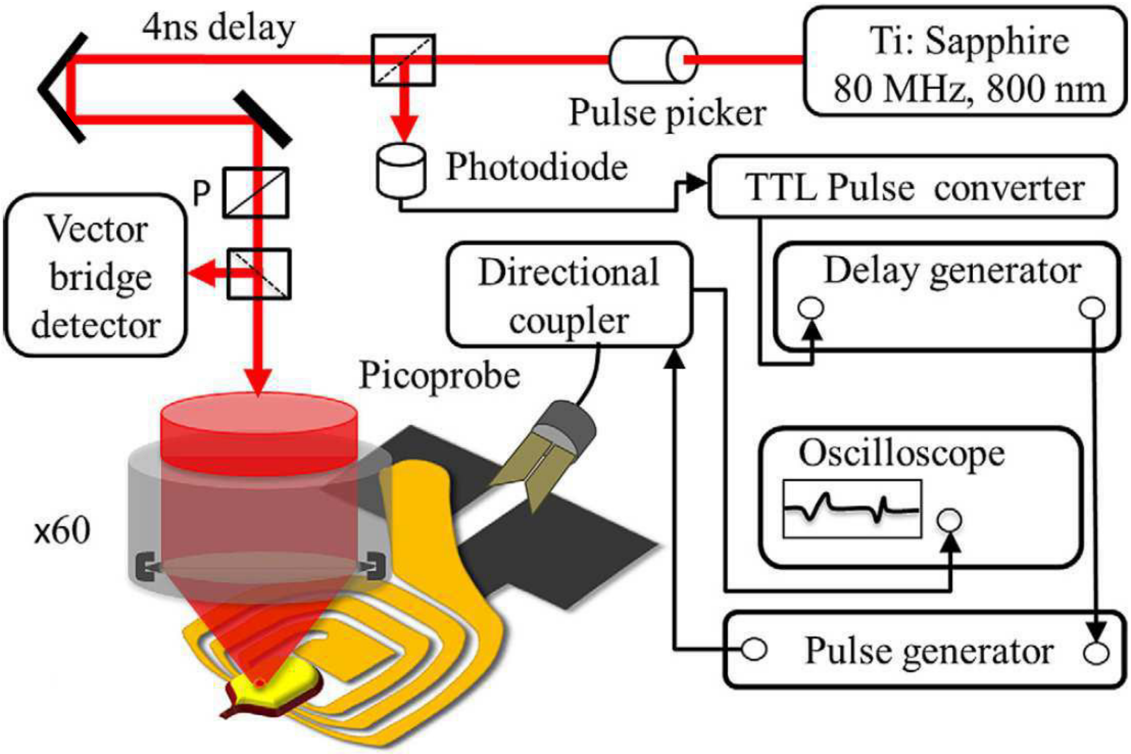

Figure 4.5: The TRSKM setup for measurement of magnetodynamics. P represents a polariser.

to give a spot size of approximately 600 nm diameter. Each image took approximately 20 minutes to acquire, with pulses being acquired for 100 ms at each pixel. A 150 mT field was applied perpendicular to the symmetry axis of the writer to set the remanent state before beginning the dynamic measurements. No external bias field or direct current was applied during the measurements. These results are presented in Section 4.4.3 on page 132.

4.4 Results and Discussion

4.4.1 Consistency of remanent state across nominally identical writers

A piece of wafer HU01D, sonicated in $0.1\,\mathrm{mol\,dm^{-3}}$ NaOH solution at 55 °C for 10 min to remove the Al_2O_3 capping layer thus allowing photoelectrons to escape

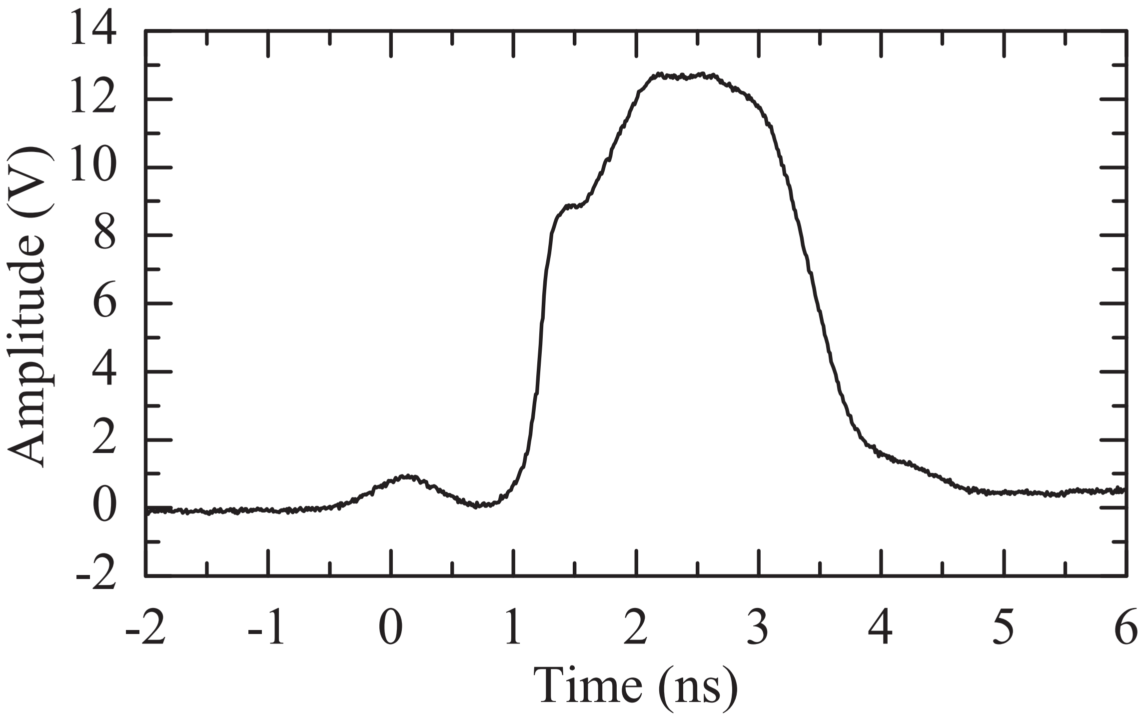

Figure 4.6: The driving pulse used to excite the writers during TRSKM measurements. The 12 V amplitude is similar to that used in consumer hard disk drives.

from the sample, was studied to investigate the consistency of remanent states across nominally identical copies of the same writer design. The geometric parameters of the writer designs are given in Table 4.1 on page 117 and shown schematically in Figure 4.2(c) on page 114. The sample was mounted on a holder featuring a built-in electromagnet with a 5 mm pole gap, maximum instantaneous field of 40 mT and maximum sustained field of 20 mT. The 100% circularly-polarised x-rays impinged on the sample at a grazing angle of 16°. The projection of the incident x-ray beam onto the plane of the sample was perpendicular to the writer's symmetry axis. Therefore in all images presented here the red and blue colours correspond to in plane magnetisation parallel and antiparallel to the direction perpendicular to the writer's symmetry axis. Magnetisation parallel and antiparallel to the writer's symmetry axis shows up as white. The field was also applied perpendicular to the symmetry axis.

As previously mentioned, the XPEEM images presented herein were each formed as a composite of between 10 and 40 images averaged together to reduce noise, as well as being programatically corrected for movement of the sample within the field of view over the course of the acquisition. Despite these corrections, some visible noise remains in each image. There are a number of potential sources of this noise, chief among which is likely to have been the failure to fully and consistently remove the Al_2O_3 capping layer across the entire sample. This leads to certain areas of the sample being more susceptible to charging, which considerably degrades the quality of the resulting image and increases observed noise. Furthermore, the drift correction algorithm applied to each image utilised a relatively simple two-dimensional translation and rotation correction, rather than accounting for the fully three-dimensional translation, rotation, skew and other distortions which occur in the real world. This, combined with the physical height of each writer above the substrate, has a tendency to create artefacts around each writer in the presented images. While these sources of noise may have a minor impact on details of images, they are not considered to have affected the large-scale domain patterns observed in these images, nor the qualitative conclusions drawn therefrom.

Initially, the repeatability and reliability of the remanent state between nominally identical copies of the same writer design was characterised. Three nominally identical copies of writer design F10 were imaged in zero applied field, as shown in Figure 4.7 on the facing page. These writers were all located on the same wafer, approximately 800 µm apart. The three writers all show qualitatively similar domain structures to one another: a large domain occupying the confluence region and main body of the yoke, oriented perpendicular to the symmetry axis, with a second antiparallel domain towards the rear of the writer. Smaller domains exist along the straight edges of the writer, oriented parallel to the writer's edge. While the domain structure is broadly similar, the precise size and orientation of these domains varies between writers.

Writer F11 features the same geometry as writer F10 except for the full back via being present, as opposed to the gapped configuration of writer F10. Three

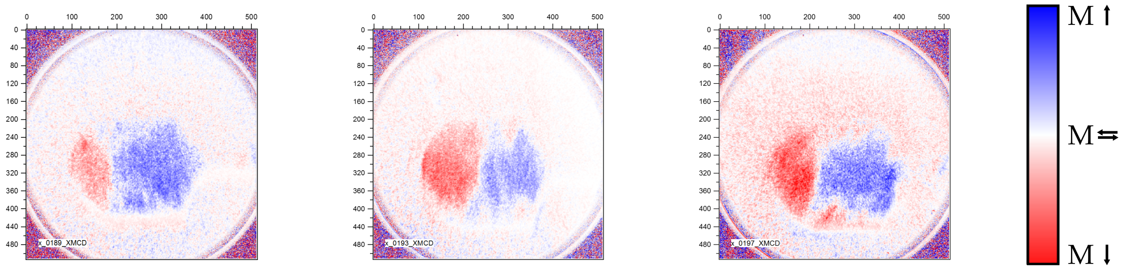

Figure 4.7: Three nominally identical copies of writer F10, imaged in zero applied field. All three show qualitatively similar domain structures, though the size and orientation of domains along the straight edges of the writer varies between writers.

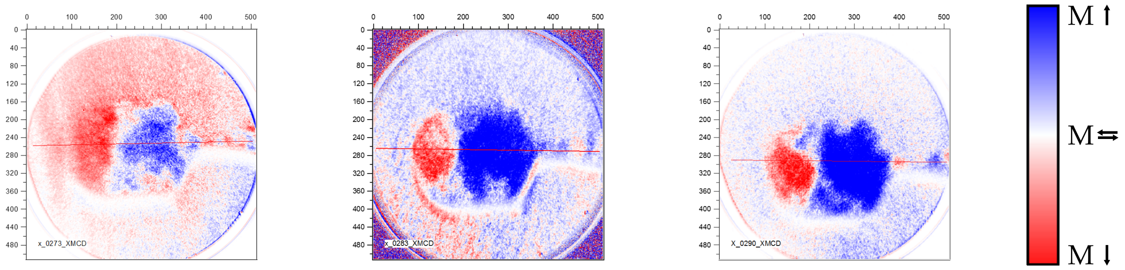

Figure 4.8: Three nominally identical copies of writer F11, imaged in zero applied field. The three writers all show a Landau flux closure pattern, although the third writer (right) shows a stronger component parallel to the symmetry axis along the side walls of the writer.

nominally identical copies of writer F11, imaged in the same way and shown in Figure 4.8, reveal greater consistency in the remanent state. All three writers show a close approximation to a Landau flux closure pattern, with the central domain wall positioned above the vertical wall of the back via. The resolution of these images is also sufficient to reveal the striped domain pattern in the pole tip of this writer design.

Writer F12, shown in Figure 4.9 on the following page again differs only in terms of the back via: writer F12 has no back via at all. The influence of the back via, or lack thereof, is immediately clear. The three copies of writer F12 exhibit markedly different remanent states, with no evidence of a flux closure state. The domains themselves, rather than having straight walls as in writers F10 and F11, have irregular and curved walls.

As writer designs F10–12 differ only in their back via, it is possible to use these

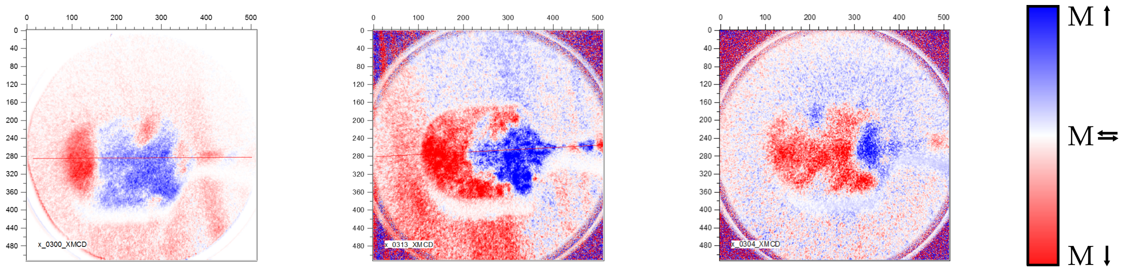

Figure 4.9: Three nominally identical copies of writer F12, imaged in zero applied field. The three writers show markedly different remanent states.

writers to draw conclusions about the influence of the back via on the remanent state in the main body of the yoke. Writers F10 and F11 both feature a back via. With these designs there are only minimal differences between the remanent states of nominally identical structures. Writer F12, however, completely lacks a back via. In this design the remanent state is far less predictable between nominally identical structures. This strongly suggests that the presence of the back via below the yoke is key in determining the remanent state of the main body of the yoke. This is further supported by the consistent presence of a domain wall just behind coil C3 in writers F10 and F11, the location of the vertical edge of the via, again suggesting that the via is controlling the domain configuration. However, given the relatively small number of nominally identical devices studied here, and particularly in light of the range of different remanent states observed in writer F12, it would be prudent to further investigate a greater number of carefully controlled back-via configurations in a larger number of nominally identical devices before drawing firm conclusions.

Other writer designs differ instead in the flare angles FA1 and FA2, which define the shape of the confluence region at the front of the writer. These writers all feature a gapped back via, the same as writer F10. Writer F16 features a relatively long, uniform confluence region, with $\mathrm{FA1} = \mathrm{FA2} = 45^\circ$. Three nominally identical copies exhibit different remanent states, as seen in Figure 4.10 on the next page. One writer shows a relatively uniform flux closure state, with the central domain wall pulled away from the back via and towards the centre of the writer.

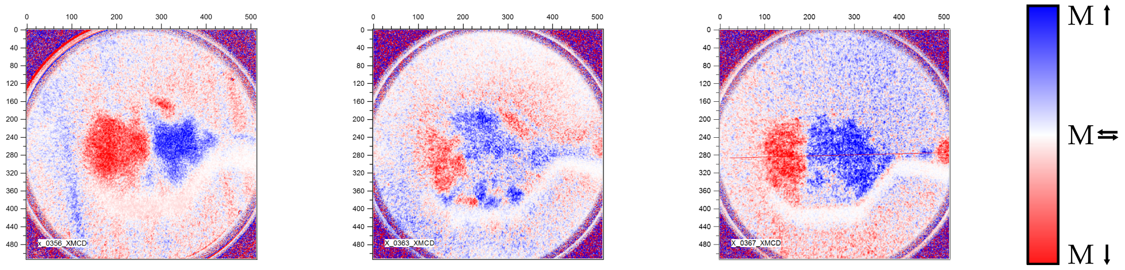

Figure 4.10: Three nominally idential copies of writer F16, imaged in zero applied field. The three writers exhibit different remanent states in both the yoke and pole tip.

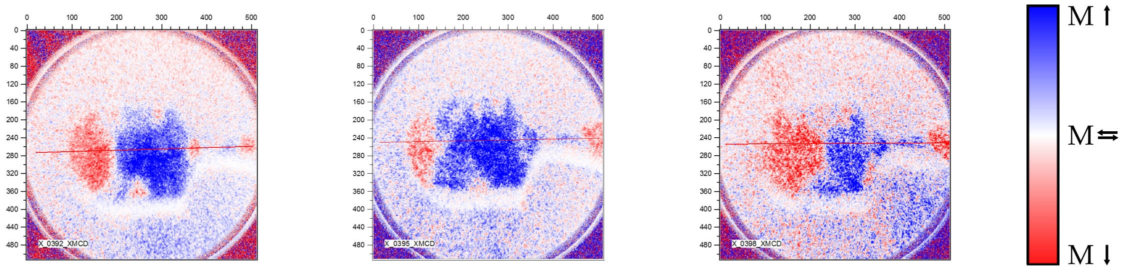

Figure 4.11: Three nominally identical copies of writer F17, imaged in zero applied field. The remanent state of the writers varies significantly, particularly the position of the central domain wall. The magnetisation direction in the confluence region also differs between writers.

This suggests the pinning of this domain wall seen in writer F10 is only very weak, and can be overcome by a slight lengthening of the writer. The second example of this writer shows a disorganised remanent state with no clear pattern in either the yoke or pole tip. The final example of this writer shows two major domains oriented orthogonal to the symmetry axis, with a third smaller domain parallel to the symmetry axis. This writer also has a clearly visible striped remanent state in the pole tip.

By contrast, writer design F17 has a shorter confluence region ($\mathrm{FA1} = 45^{\circ}$, $\mathrm{FA2} = 62^{\circ}$). The three copies of this writer design, shown in Figure 4.11, exhibit some similarities in the domain structure of their yokes. All three writers have two antiparallel domains occupying the majority of the yoke, although the relative size of these domains does vary. All three also show a similar domain structure along the straight edges of the yoke. Differences are apparent in the crucial domain

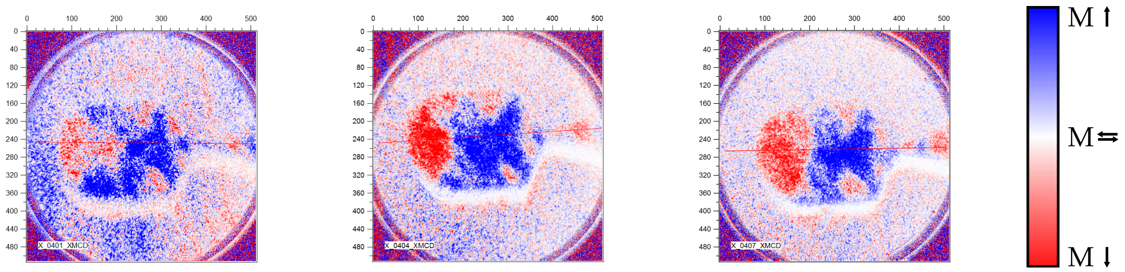

Figure 4.12: Three nominally identical copies of writer F18, imaged in zero applied field. These writers all exhibit the same domain structure, include the fine structure in the confluence region.

structure of the pole tip, although all three writers show a variation on the desired striped domain structure in this region.

Writer design F18, shown in Figure 4.12, has a short, uniform confluence region ($\mathrm{FA1} = \mathrm{FA2} = 62^\circ$). While there are very minor variations, these writers all exhibit the same remanent domain structure. As in previous writers, the main body of the yoke is occupied by two antiparallel domains oriented orthogonal to the symmetry axis of the writer. The domain at the rear of the writer extends approximately the same distance into the main body of the yoke in all cases. At the meeting of the main body of the yoke and confluence region, all three writers have two smaller domains encroaching on the larger domain. This pattern repeats again deep in the confluence region at its meeting with the pole tip. Finally, a striped domain structure is observed in the pole tip of all three writers.

This large variation in remanent states would suggest that the stability afforded by the back via in devices F10 and F11 is comparable to the influence of the minimisation of magnetostatic energy, and is easily overcome by minor changes in yoke shape. Again, the large variation in observed remanent states across a relatively small number of nominally identical writers suggests that a follow-up study of a greater number of writers would be beneficial to completely explore the range of different equilibrium states and patterns between these.

Writer F20, shown in Figure 4.13 on the facing page, has an unusual confluence region featuring a sharp corner rather than a smoother profile ($\mathrm{FA1} = 30^\circ$,

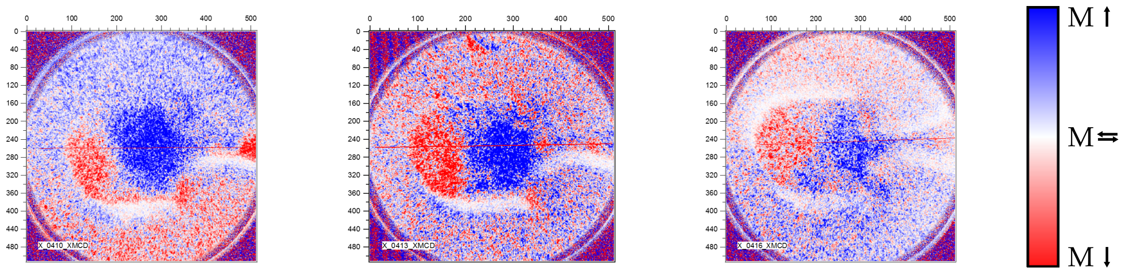

Figure 4.13: Three nominally identical copies of writer F20, imaged in zero applied field. All three writers show a similar flux closure pattern.

$\mathrm{FA2} = 90^\circ$). Somewhat surprisingly, this sharp feature does not act as a pinning site for the domains in the confluence region. Instead, the writers all have an remanent state resembling a Landau flux closure pattern.

These results reveal key information about the relative strengths of the influences on the remanent state. The stability afforded by the presence of the back via beneath the yoke is of similar magnitude to the influence of the drive to minimise magnetostatic energy on the remanent state. This places the two in competition, meaning minor variations to either the back via or writer shape can significantly alter the domain structure of the remanent state and its stability. Such information in invaluable in the future development and design of hard disk drive write heads, as well as providing potential indication of areas on which a focus should be placed in numerical models and simulations of such devices.

4.4.2 Effect of applied field on remanent state

In vacuo application and removal of field

To test the stability and reliability of the remanent state of the writers, selected writers were imaged before and after the application and removal of a $\pm 20\,\mathrm{mT}$ field applied orthogonal to the writers' symmetry axes. The sample holder was fitted with two electromagnet coils and pole pieces approximately $5\,\mathrm{mm}$ long with a pole gap of $5\,\mathrm{mm}$. This ensured that the field was applied uniformly across the

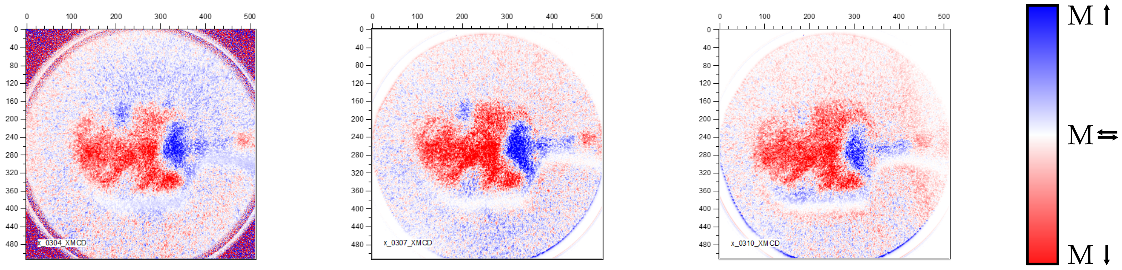

Figure 4.14: Writer F12 imaged (left) in zero field, (centre) after the application and removal of a $+20\,\mathrm{mT}$ field, and (right) after the application and removal of a $-20\,\mathrm{mT}$ field. The three images show the same remanent state, suggesting a $20\,\mathrm{mT}$ field is insufficient to reorient the domains in this writer design.

sample area that was accessible with the XPEEM. The sample was oriented such that the field was applied perpendicular to the writers' symmetry axes.

Writer F12 had previously shown very different remanent states between nominally identical writers (Figure 4.9 on page 124). This suggested that perhaps the remanent state is not actually that stable, instead being a local energy minimum with a true ground state available at lower energy cost. Applying a $20\,\mathrm{mT}$ field to the writer, however, made no observable difference to the domain state (Figure 4.14). Even small domains at the junction between the confluence region and pole tip remained stable.

Writer F13 exhibited a desirable striped domain pattern in the confluence region and pole tip. This domain structure is believed to be conducive to "flux beaming", which generates write fields with high spatial and temporal confinement. The application and removal of the same field to writer F13 (Figure 4.15 on the next page) tells a similar story: the domain structure remains highly stable, including the important pole tip region.

With a field of $40\,\mathrm{mT}$ available from the magnet embedded within the sample holder, we decided to apply this maximum field to writer F16 to see if a larger field could induce a change (Figure 4.16 on the facing page). A field of $40\,\mathrm{mT}$ is approximately twice that generated by the write coils embedded beneath the writer. Despite the two copies of this writer having different remanent states, both

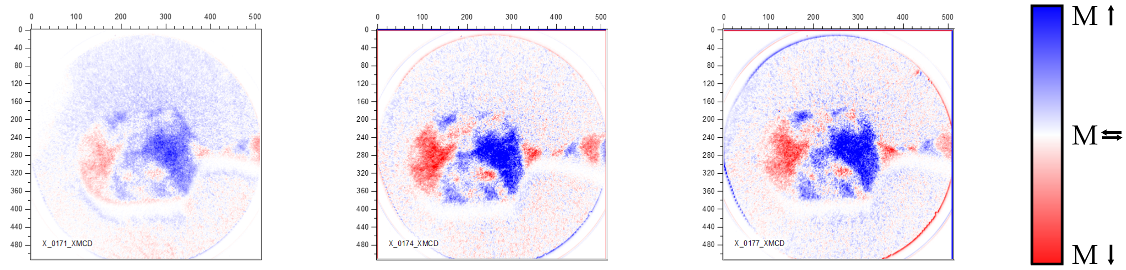

Figure 4.15: Writer F13 imaged (left) in zero field, (centre) after the application and removal of a $+20\,\mathrm{mT}$ field, and (right) after the application and removal of a $-20\,\mathrm{mT}$ field. The three images show the same remanent state, suggesting a $20\,\mathrm{mT}$ field is insufficient to reorient the domains in this writer design.

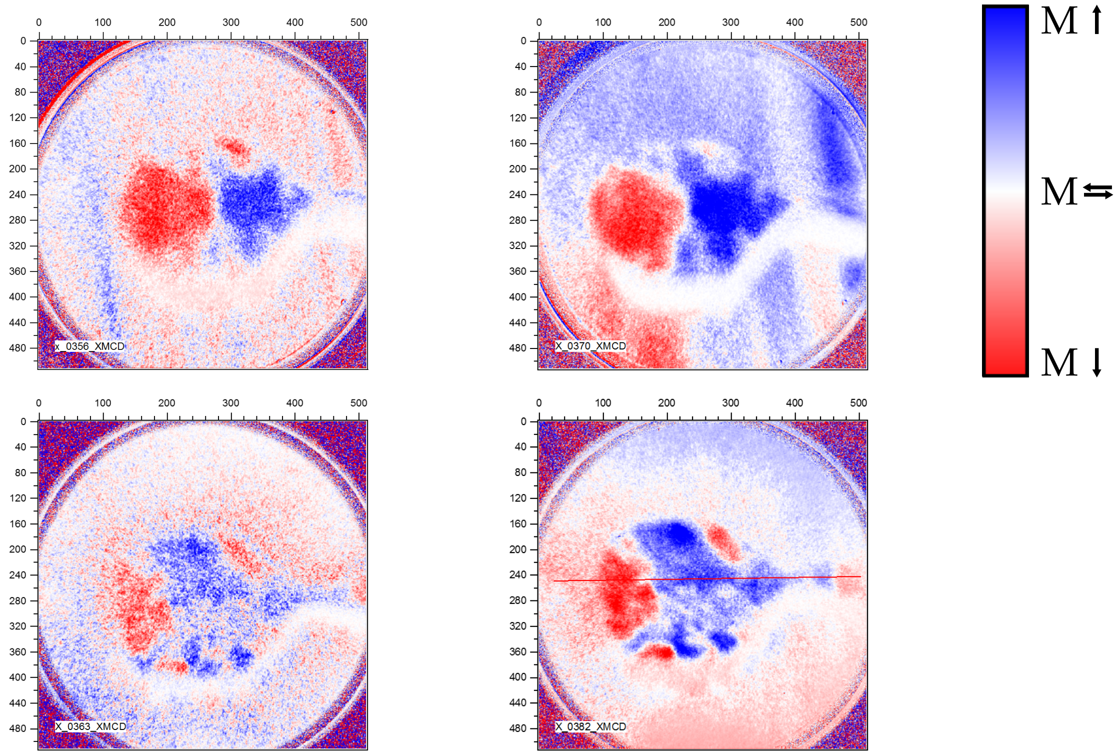

Figure 4.16: Two nominally identical copies of writer F16, imaged in their remanent state (left) and after the application and removal of a $+40\,\mathrm{mT}$ field perpendicular to the symmetry axis (right). Despite the two writers having slightly different remanent states, both remain unchanged after the field application.

remain unchanged after the application and removal of this sizeable field.

In vacuo sustained field

It is possible that, after removing the applied field, the writers return to their original remanent state. This would mean that no change would have been observed in

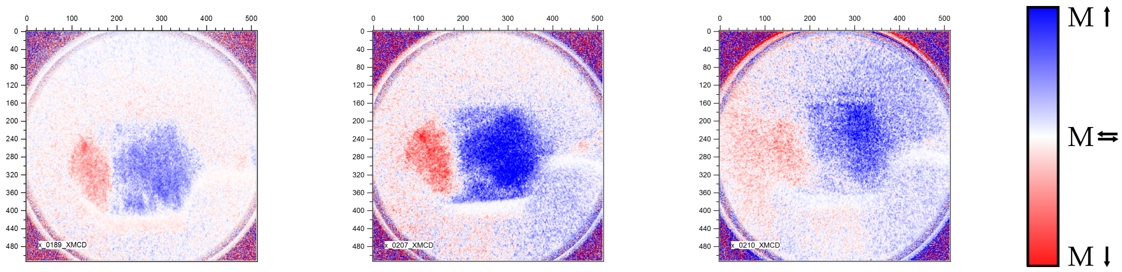

Figure 4.17: Writer F10, imaged in (left) zero applied field, (centre) +20 mT and (right) −20 mT. The magnetic state of the writer appears stable under these field conditions.

Figures 4.14 to 4.16 despite the fact that the magnetic state was changed by the applied field.

To check for this, writer F10 was imaged while an applied field of ±20 mT parallel to the symmetry axis was still on, and the electron optics adjusted to take account of the increased field at the sample surface. These images are shown in Figure 4.17. There are no significant, large-scale changes between the magnetic state of the writer under the different field conditions, suggesting that any changes are small and confined to localised spatial areas. This supports the theory that small-angle rotation is the most likely method of flux conduction along the writer's symmetry axis,[76] rather than larger scale reorientation of domains as a whole, or of considerable domain wall motion.

Out-of-vacuum application and removal of field

Figure 4.18(a) on the facing page shows the remanent state of writer F31 measured by XPEEM both before and after saturation by a 200 mT field oriented along the symmetry axis. Prior to the application of the field the magnetisation appears to form a large single domain, with orientation orthogonal to the symmetry axis, occupying the yoke and confluence region, with a smaller domain above the back via. After the application of the field, the magnetisation has reversed throughout most of the writer. Crystalline anisotropy is clearly dominant since both domains have magnetisation perpendicular to the symmetry axis rather than parallel to the

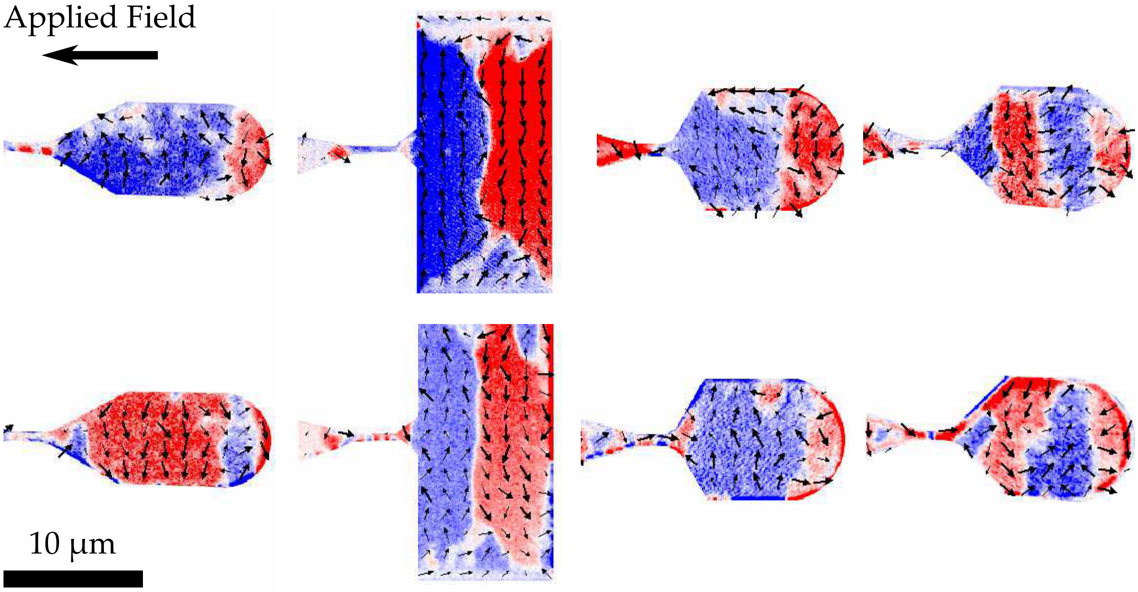

(a) Writer F31 (b) Writer F27 (c) Writer F8 (d) Writer F16

Figure 4.18: XPEEM images of the magnetic domain structure of devices 1–4 both before (top) and after (bottom) the application and removal of a 200 mT magnetic field parallel to the symmetry axis of the devices. The colour represents the component of magnetisation perpendicular to the symmetry axis, as in previous images. All images are shown on the same colour scale. Arrows were generated by averaging the magnetisation in approximately 1 μm square cells, wherein the direction and length of the arrows represent the in-plane orientation and magnitude of $\boldsymbol{M}$ respectively. As such, the arrows are intended as a guide for the eye only, and may appear inaccurate due to noise inherent in the collected data, or cells including domain walls or the device edges. The variation of $|\boldsymbol{M}|$ across each writer is likely due to inhomogeneity on a scale beyond the spatial resolution of the XPEEM, or out of plane components of $\boldsymbol{M}$.

symmetry axis as preferred by the shape anisotropy in the device. As the magnetisation rotates to align with the applied field it does so asymptotically through a process of domain rotation. Upon reaching the saturation field, the magnetisation may irreversibly jump across the hard axis,[77] relaxing into the antiparallel state. Whether the magnetisation actually jumps across the hard axis is likely the result of slight misalignment of the applied field compared to the symmetry axis.

The sample drift over time, combined with the $\approx$ 300 nm height of the writer above the substrate surface, led to the appearance of high-contrast edge artefacts around some devices. These artefacts have been largely, but not completely, cropped from the images presented here to maximise the available contrast range.

The remanent state of writer F27, a rectangular reference device, is shown in Figure 4.18(b) on page 131. Both before and after the application of the external field the writer exhibits the same flux closure state, with the same magnetisation orientation. This was expected, as both the crystalline anisotropy and minimisation of magnetostatic energy favour the magnetisation aligning perpendicular to the symmetry axis of the device.

Writers F8 and F16 (Figures 4.18(c) and 4.18(d) on page 131) represent more typically-shaped devices. Only the flare angles differ between the two devices, giving writer F16 a longer, more uniform confluence region than writer F8. Writers F8 and F16 both exhibit a qualitatively similar remanent state both before and after the application of the external field, with the magnetisation within the domains lying largely perpendicular to the symmetry axis. In contrast to writer F31, the magnetisation does not switch in response to the field applied parallel to the symmetry axis. Here the higher saturation field prevents the magnetisation from jumping across the hard axis, meaning the magnetisation relaxes back into its original orientation. While the crystalline anisotropy determines the magnetisation orientation within an remanent domain configuration, the competition between crystalline anisotropy and desire to minimise magnetostatic energy determines the stability of that configuration. The smaller domains within the pole tip, coupled to this region's complex three-dimensional shape, makes a detailed analysis of the behaviour of the writer within this region difficult.

4.4.3 Magnetodynamics

In order to study the dynamic behaviour of different writer designs, nominally identical copies of writers F8 and F16 were also studied by TRSKM. The results are compared to XPEEM images obtained before the application of the field parallel to the symmetry axis, as this latter field was intended to test the stability of, rather than reset, the remanent state. While minor variations in the remanent state are

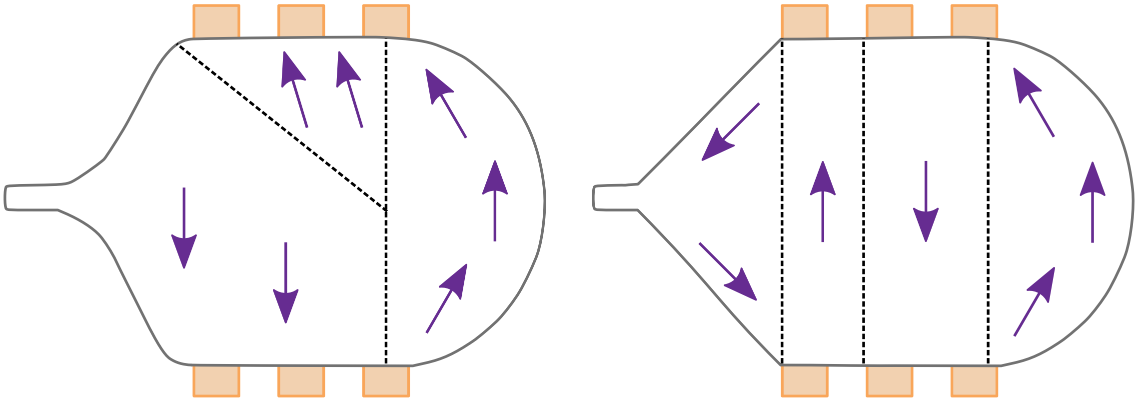

(a) Writer F8 (b) Writer F16

Figure 4.19: Remanent states derived from TRSKM measurements.

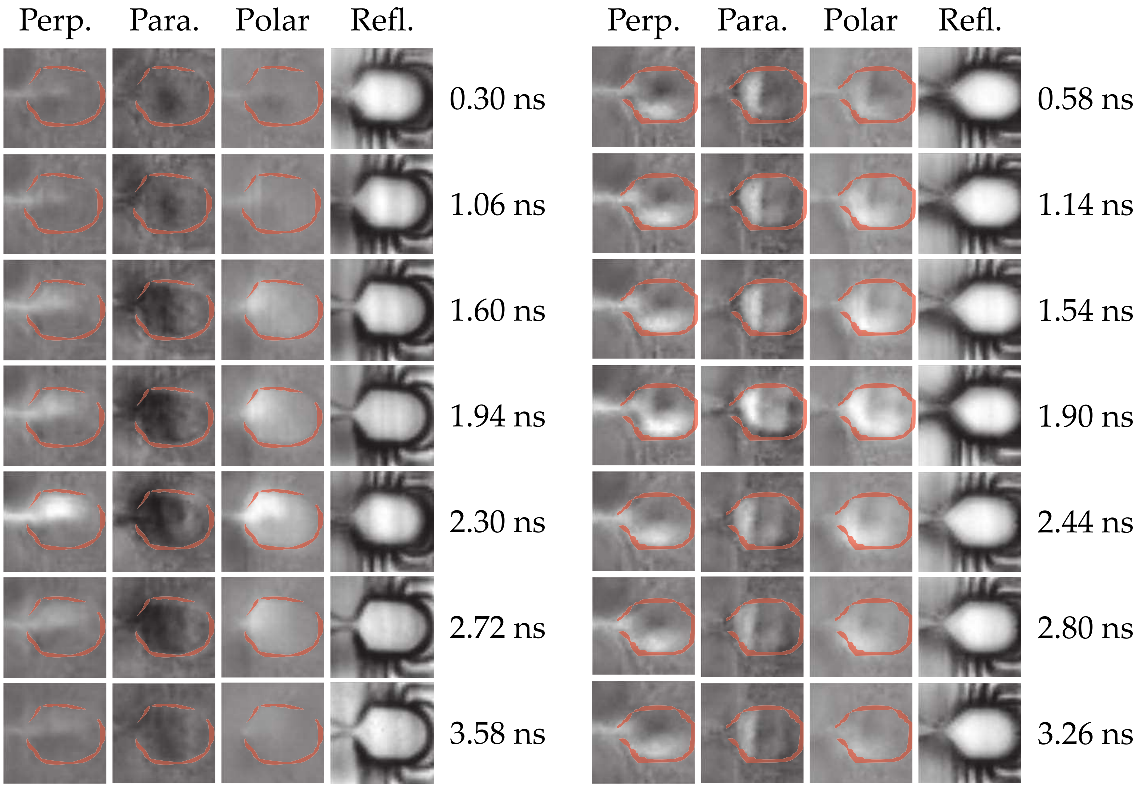

(a) Writer F8 (b) Writer F16

Figure 4.20: Time-resolved imagery of writers F8 and F16. Black and white correspond to changes in the magnetisation in the $-/+$ x-direction, $+/-$ y-direction and $-/+$ z-direction for the perpendicular, parallel and polar components respectively. The co-ordinate system is defined in Figure 4.4 on page 116. The red outline, derived from the reflectivity image of the device, has been overlaid to guide the eye.

expected between nominally identical devices, these variations do not change the character of the observed dynamic response. Figures 4.20(a) and 4.20(b) on page 133 show the dynamic response of writers F8 and F16, respectively. The pulsed current is flowing upwards in all frames, resulting in an in-plane magnetic field pointing to the right.

For writer F8 the perpendicular channel shows a strong signal along the symmetry axis, and also in the middle of the upper half of the yoke from $1.94\,\mathrm{ns}$ onwards. The remanent state suggested by the TRSKM imagery for writer F8 is shown in Figure 4.19(a) on page 133, and is in qualitative agreement with the XPEEM results presented here. However, the perpendicular channel also shows weak contrast at $0.3\,\mathrm{ns}$ delay, before the arrival of the driving pulse, suggesting poor relaxation behaviour for this design under these driving conditions.

TRSKM images of writer F16 show flux conducted along the bottom edge of the writer in the perpendicular channel. With the driving field oriented towards the back of the device, this suggests that the magnetisation within the bottom half of the confluence region is canted towards the back of the device, whereas the magnetisation within the upper half of the confluence region is canted towards the pole tip. Flux conduction along the top edge of the writer would lead to the formation of a tail-to-tail domain wall in the upper half of the yoke, whereas a head-to-tail wall would be formed in the lower half of the yoke. As the latter costs less dipolar energy, flux conduction along the lower edge of the writer is energetically favourable. While the XPEEM images show that this design has a striped remanent domain structure, which should result in flux beaming along the symmetry axis of the yoke,[76] the minimisation of magnetostatic energy in the longer confluence region appears to be disrupting flux conduction. The parallel channel images of this device (Figure 4.20(b) on page 133) further show strong rotation across the entire width of the confluence region, again demonstrating the lack of a central beam of flux. Furthermore, these images suggest the presence of a domain wall at the back of the confluence region, as shown in Figure 4.19(b) on page 133.

Figure 4.21 on the next page shows the time resolved Kerr rotation observed at different positions on writers F8 and F16 (defined in Figure 4.4 on page 116). In writer F8 the magnetisation initially rotates in unison at each of the three measured points. However, the magnetisation at position B relaxes quicker than at positions A and C. This suggests that the yoke drives flux conduction along the length of the device. In writer F16 the magnetisation exhibits more complex behaviour. This is due to the flux beam in this writer being positioned towards the lower edge, rather than along the symmetry axis. The dynamics of writer F16 are therefore less well defined, and depend on the detailed ground state of the device. Positioning of the focused laser spot on a domain wall may also complicate the signal further. However, it is possible to see that positions B and C, while initially rising with position A, then lag behind position A by $\approx 2\,\text{ns}$, as can also be seen in Figure 4.20(b) on page 133. This indicates the presence of residual flux propagating through the writer after the driving pulse has ceased, potentially leading to erase-after-write errors in devices of this shape.[78]

4.5 Conclusions

XPEEM has been used to image the remanent state of partially-built hard disk write heads, showing detail in the confluence region and pole tip. These images suggest that the crystalline anisotropy dominates the remanent state configuration. The competition between crystalline anisotropy and minimisation of magnetostatic energy determines the stability and repeatability of the remanent state. The remanent state domain structures suggested by the XPEEM images are in agreement with the images obtained by TRSKM. In the devices studied in this chapter, TRSKM images of the magnetodynamics in the differently-shaped writers suggest that a longer, more acute confluence region has negatively impacted

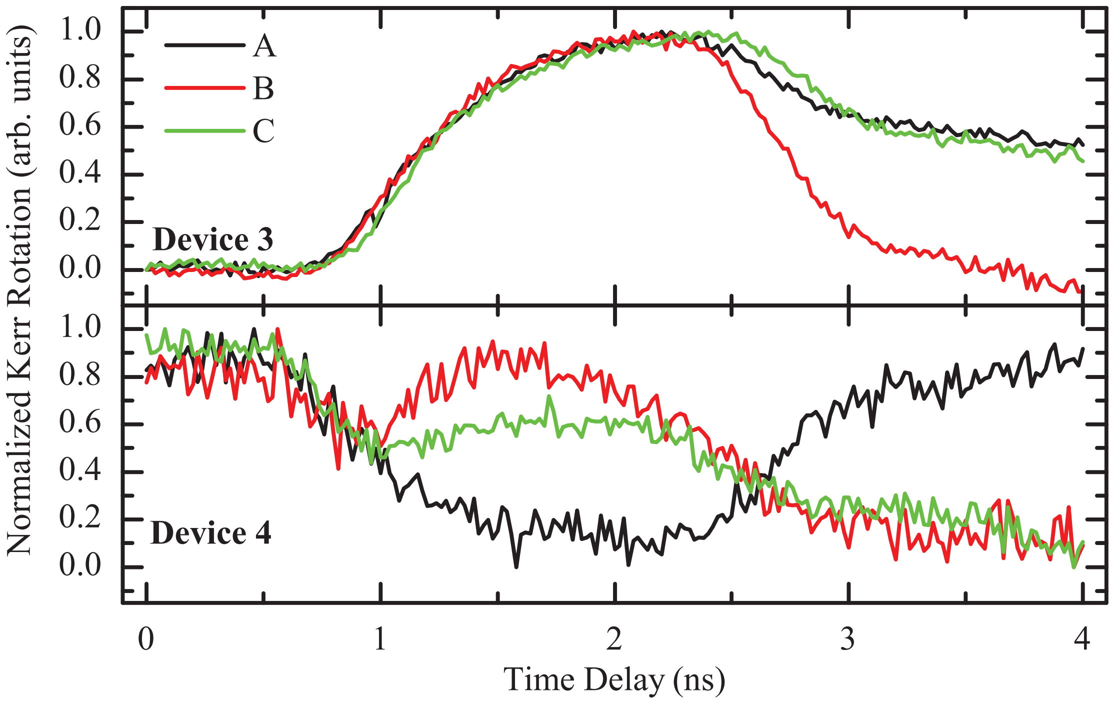

Figure 4.21: Perpendicular component of the time resolved signal acquired at three positions (shown in Figure 4.4 on page 116) in the yokes of writer F8 (top) and writer F16 (bottom). Traces have been normalised for each position.

flux conduction into the pole tip. Given the relatively small number of nominally identical copies of each geometry measured in this study, further investigation of this possibility across both a greater number of nominally identical devices, and further different writer designs, is necessary to fully explore the role of the confluence region geometry in greater depth. By combining the results of both XPEEM and TRSKM it is possible to better understand both the remanent state domain configuration and the dynamics within the yoke. Furthermore, the general principles presented here regarding the influence of geometric parameters on high frequency magnetisation dynamics can elucidate the mechanisms of magnetic flux conduction within other micro- and nano-scale patterned materials. In order to further understand the writer dynamics, particularly within the nanoscale pole piece, a time-resolved XPEEM study is required.

CHAPTER 5

Time-resolved scanning Kerr microscopy of flux beam formation in hard disk write heads

The results presented in this chapter have previously been published as 'Time-resolved scanning Kerr microscopy of flux beam formation in hard disk write heads' by Valkass et al. in *Journal of Applied Physics* **119**, 233903 (2016).

5.1 Introduction

Global data storage needs are currently estimated to be in the region of several hundred exabytes (10^{20} B) and are currently increasing at a rate of $3\,\mathrm{EB\,d^{-1}}$.[80–82] To meet these needs it is necessary to both improve the areal density of data storage devices and reduce the cost per gigabyte of storage.[66] In pursuit of these goals there are a number of potential areas for optimisation, focused on enhancing the write head field. However, this is a challenging task while maintaining a consistent rise time and sufficient spatial confinement of the field. Achieving this not only removes a barrier to an increase in areal density, but also decreases write times and reduces erase after write errors[83] and popcorn noise.[68]

The write heads studied in this chapter are similar to those of Chapter 4. The write heads are effectively formed from a planar electromagnet driven by electrically-conductive coils embedded beneath the magnetic material of the yoke. The write head is designed to maximise the available write field while minimising erase after write errors and wide area track erasure.[84] It was first suggested by Mallary in 1985 that magnetic flux was conducted through structures similar to hard disk write heads by a process of small angle rotation of the magnetisation, rather than by domain wall motion.[76] This leads to the formation of a narrow "beam" of flux along the central symmetry axis of the write head, a highly desirable property for generating both the strongest and most spatially uniform write field at the pole tip.

The presence of flux beams in similar write head structures has previously been observed by Gangmei et al.[51] using TRSKM. These flux beams were observed to form along the writer's symmetry axis towards the pole tip. The work of the previous chapter largely focused on detailed and direct measurement of the remanent state of writers by XPEEM, providing confirmation that the inferences made from these and other previous TRSKM measurements on the same writers[65,70] appear to be accurate. However, the time-resolved imagery of flux beams obtained in these previous works has only been recorded at a temporal resolution on the order of 0.5 ns, and focused largely on the decay of the flux beam rather than its formation. Surprisingly little attention has been paid to the precise nature of the process of formation of these flux beams on the leading edge of the write pulse waveform, and to the detailed spatial character of the flux beams during the write process on the picosecond timescale. Such a characterisation is indispensable in gaining a complete understanding of the processes underpinning the formation and evolution of flux beams and to guide development of write heads with robust flux beams that are more uniform and hence intense, and forms the focus of this chapter.

5.2 Method

The sample under investigation comprised a 17×15 mm^2 wafer piece containing a number of different geometric and electrical configurations of write heads. The shape of the write heads, previously shown in Figure 4.2(c) on page 114, was the same for all devices studied here. Write heads were of the typical "paddle" shape, with an overall paddle width (PW) of 6.485 µm and confluence region flare angles (FA1 and FA2) of 30° and 62° respectively. The bridge measured 1 µm × 400 nm and the yoke was recessed by 1.6 µm. The yoke of each write head was fabricated from four repeats of a NiFe (1 nm)/CoFe (50 nm) bilayer chosen for its high magnetic moment and low coercive field.

To emulate the formation of the flux beam during the data writing process, an electrical pulse was delivered through the coils embedded beneath the centre part of the yoke inciting the magnetisation to rotate. The coils were embedded 500 nm beneath the yoke, with each coil having a cross-section measuring 1 µm × 1 µm and intercoil spacing of approximately 1 µm. The number and position of the active coils varied between write heads and is summarized in Table 5.1 on the next page. The electrical pulse was the same for all write heads, having an amplitude of 4.7 V and 87.0 ps duration FWHM. The temporal form of the pulse can be seen in Figure 5.1 on the following page. This pulse is lower in amplitude and shorter in duration than that used in the previous chapter, and is therefore also smaller and shorter than is typical of commercial hard disk drives. However, this was necessary to match the 80 MHz laser repetition rate necessary to obtain the number of images required for this study. A smaller, shorter drive pulse also has the potential to avoid saturating out fine detail of the flux patterns within the writers.

Changes to the magnetisation were imaged using TRSKM,[48,86–88] which was previously discussed in Chapter 3. A schematic of the experimental setup is shown in Figure 5.2 on page 141. An 800 nm wavelength Ti:sapphire ultrafast

Write head	Coil 1	Coil 2	Coil 3
F3	✓	✓	✓
F5	✓	—	—
F6	—	✓	—
F7	—	—	✓
F8	✓	✓	—
F9	✓	—	✓
F10	—	✓	✓

Table 5.1: The driving coil configuration for each of the write heads studied in this chapter, defined with reference to Figure 4.2(c), where ✓denotes an active coil and — denotes an inactive coil.

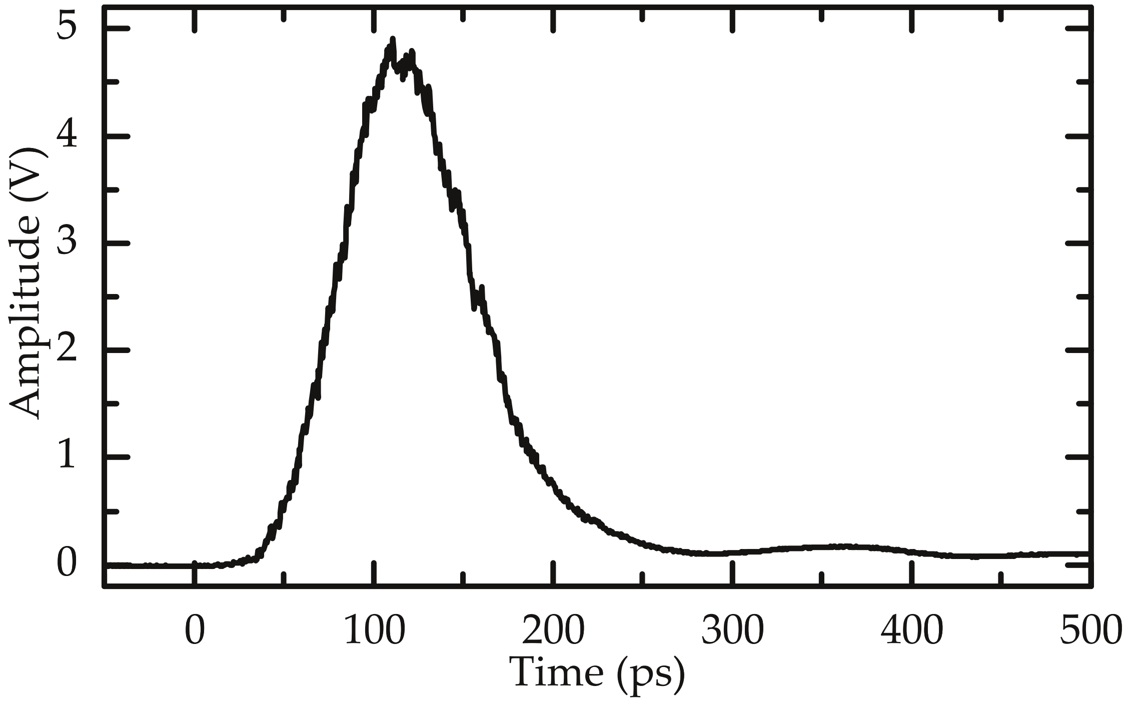

Figure 5.1: The temporal form of the driving pulse used to emulate the data writing process. The pulse was longer and of lower amplitude than that of Chapter 4, having an amplitude of 4.7 V, FWHM duration of 87.0 ps and 10–90 rise time of 48.5 ps. The driving pulse repetition rate was 80 MHz, and locked to the same clock as the laser.

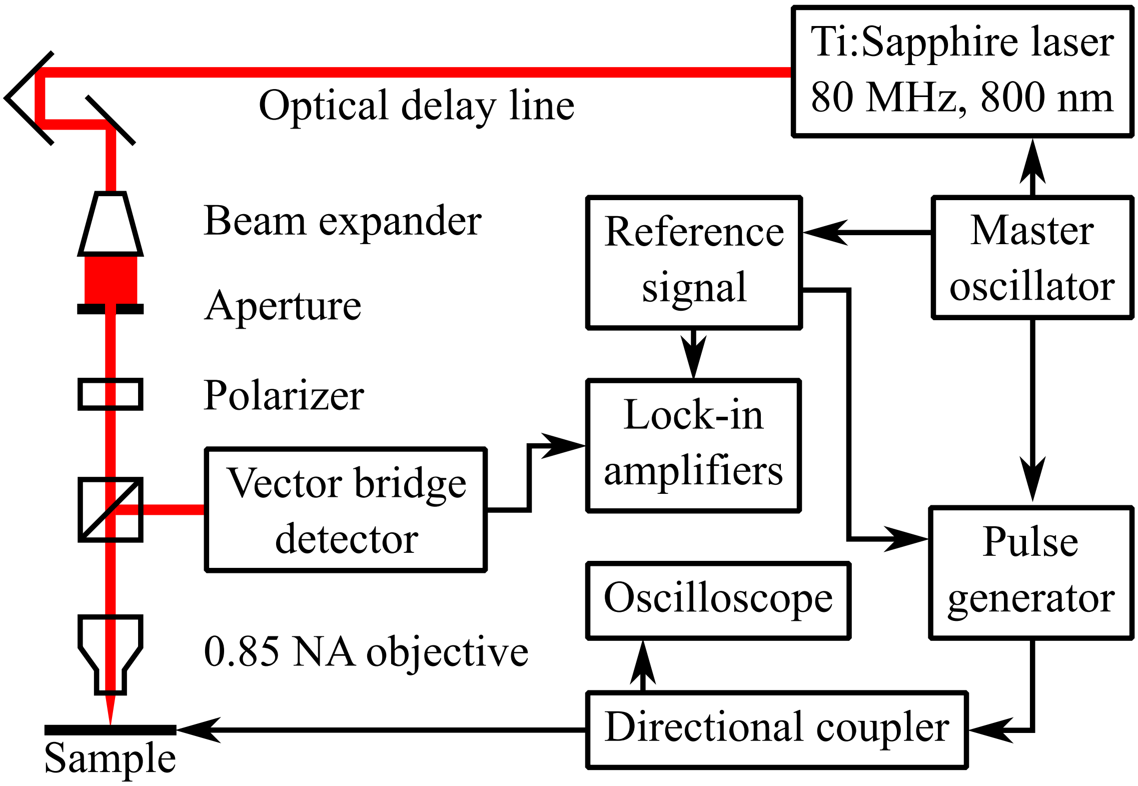

Figure 5.2: A block diagram of the time-resolved scanning Kerr microscope used for measurements of magnetisation dynamics. A vector bridge detector allows for simultaneous detection of the three spatially perpendicular components of the magnetisation.[85]

pulsed laser with 80 MHz repetition rate was used to make the measurements. The laser output was passed along a variable length optical delay line, providing picosecond time resolution to acquired images. The beam was then passed through a $10\times$ beam expander and clipped by passing it through an aperture to improve the uniformity of intensity across the beam profile. Finally the beam was repolarised and delivered to the sample surface through a microscope objective lens with a numerical aperture of 0.85. This gave a diffraction-limited spot on the sample surface of approximately 600 nm diameter.

Light reflected from the sample surface was then collected back through the same microscope objective and passed to a quadrant photodiode bridge detector[85] and lock-in amplifiers by means of a non-polarising $50:50$ cube beamsplitter, as discussed in Section 3.2.3. This allowed simultaneous measurement of changes to the magnetisation along the three mutually perpendicular spatial axes.

A three-axis piezoelectric positioning stage was used to raster scan the sample beneath the beam with nanometre resolution, allowing an image to be built up from individual Kerr measurements recorded at different locations. Images were recorded at time intervals of approximately $10\,\mathrm{ps}$ so as to explore in detail the precise nature of the process of formation of a flux beam during the rise of the driving current.

5.3 Results

Figure 4.2(c) on page 114 shows a schematic of the write head design and geometric parameters shared between all writers studied in this chapter. The three driving coils used to deliver the writing pulse can be seen emerging from the sides of the structure. The coordinate system defined for these measurements is shown in Figure 5.3. Time-resolved Kerr images of the seven write heads are shown in Figures 5.4 and 5.5. For each writer, the presented images have been selected to show the time delays at which changes are most noticeable. A write head with all three driving coils connected, shown in Figure 5.4(a) on the facing page, is expected to produce a uniform beam of flux along the central symmetry axis of the write head due to the uniformity of the driving field created by the coils.[76] However, it was observed that flux along the yoke's symmetry axis in fact nucleates in two smaller spots: one deep within the flared confluence region, and a second further towards the back via. While both of these areas of magnetic activity are located

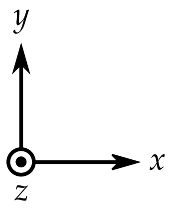

Figure 5.3: The coordinate system used throughout the measurements presented in this chapter.

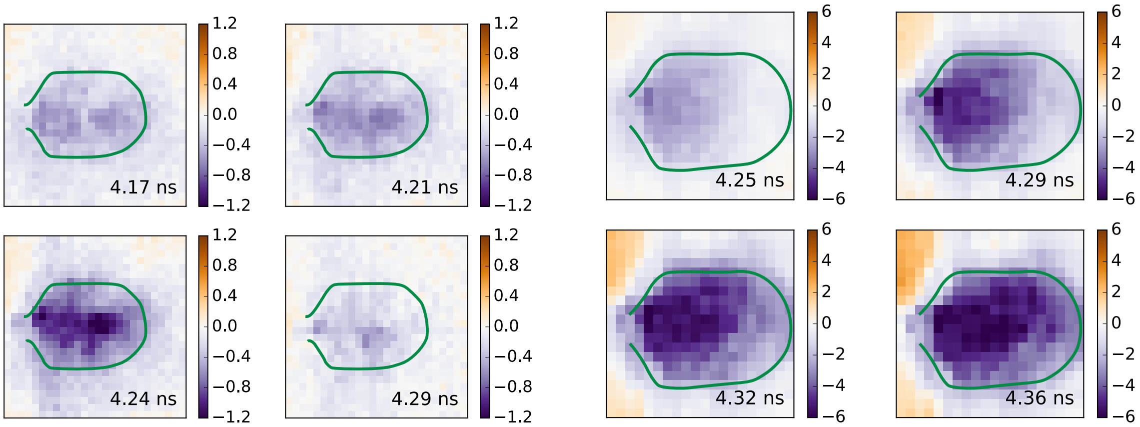

(a) Write head F3 (coils C1, C2 and C3 active)

(b) Write head F5 (coil C1 active)

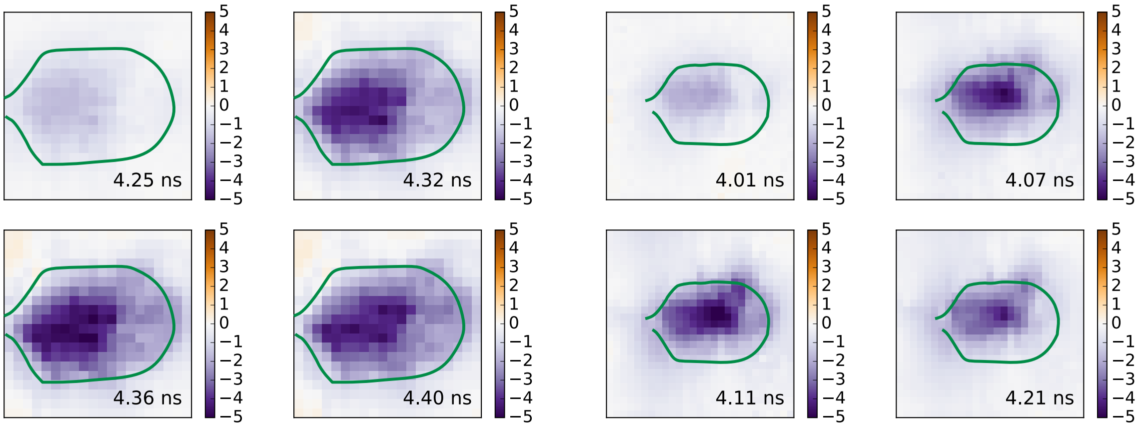

(c) Write head F6 (coil C2 active)

(d) Write head F7 (coil C3 active)

Figure 5.4: Time-resolved Kerr images of write heads F3, F5, F6, and F7. Contrast shows changes to magnetisation in the x direction, ΔM_x, with negative values (purple) representing rotation to the left and positive values (orange) rotation to the right. The green outlines are taken from reflectivity images acquired simultaneously with the magnetic images, and are provided as a guide for the eye.

on the symmetry axis, they remain distinct rather than coalescing to form a single, uniform flux beam (see for example the image at 4.24 ns).

Three of the write heads have only a single driving coil connected, however the spatial form of the flux beam varies greatly between these three structures. The first device (Figure 5.4(b)), having only coil C1 connected, shows a wide, uniform flux beam extending along the write head's symmetry axis. When only the central coil, C2, is connected two distinct narrow flux beams are formed either side of the symmetry axis, as shown in Figure 5.4(c) on page 143 (4.29 ns). With only coil C3 connected a uniform flux beam is formed along the symmetry axis, with outlying areas of flux influencing the shape of the primary flux beam. This beam extends deep into the confluence region along the symmetry axis (Figure 5.4(d) on page 143).

Three of the write heads have two coils connected in various configurations. With the two coils closest to the confluence region connected (coils C1 and C2, Figure 5.5(a) on the facing page) flux nucleates in two separate sites, before joining and extending along the symmetry axis of the write head. Two spatially separated coils (C1 and C3, Figure 5.5(b)) lead to the development of a very broad, incoherent flux beam concentrated in the lower half of the writer with no evidence of further magnetisation rotation towards the pole tip. In contrast, in the write head with two coils towards the back via activated (coils C2 and C3, Figure 5.5(c)) a disjointed flux beam is initially formed along the symmetry axis (4.37 ns), but this rapidly breaks apart into a number of smaller sites (4.42 ns): one in the confluence region, one above the back via and a smaller area of contrast in the lower right of the image.

5.3.1 Field Profiles

To aid in the interpretation of experimental results, the magnetic field produced by each configuration of driving coils was modelled. The model geometry comprised three coils each with a cross section of $1\,\mu\text{m} \times 1\,\mu\text{m}$, with their centres spaced $2\,\mu\text{m}$ apart, and assumed to extend infinitely in the y direction, i.e. the current-carrying wires were modelled as having infinite length. The coils were placed at the centre of an air-filled cylinder of diameter $20\,\mu\text{m}$. The coils were given the material properties of copper, and a constant current density of $5.2 \times 10^{11}\,\text{A}\,\text{m}^{-2}$.

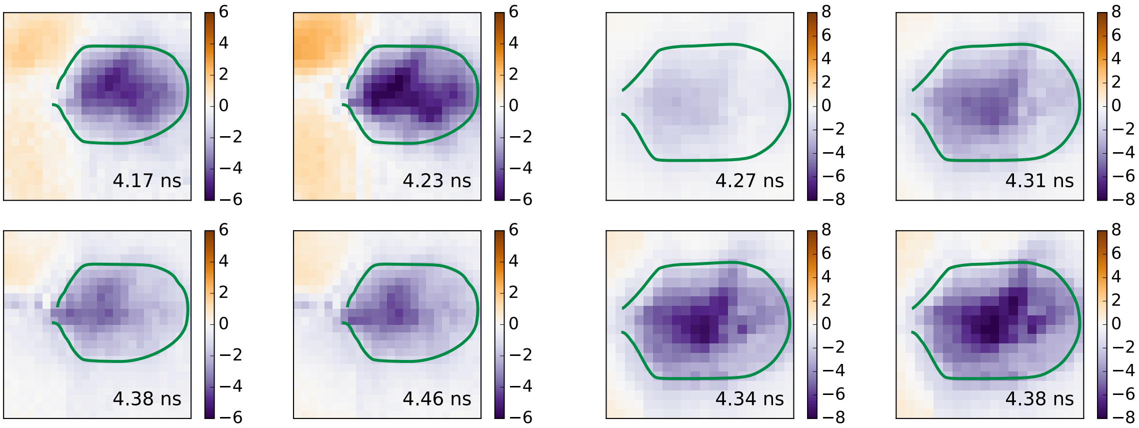

(a) Write head F8 (coils C1 and C2 active)

(b) Write head F9 (coils C1 and C3 active)

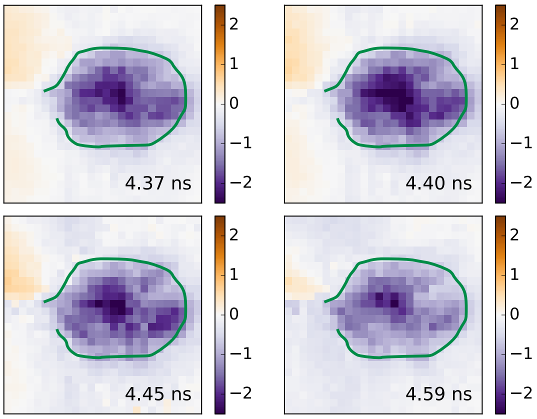

(c) Write head F10 (coils C2 and C3 active)

Figure 5.5: Time-resolved Kerr images of write heads F8, F9, and F10. Contrast shows changes to magnetisation in the x direction, $\varDelta M_x$, with negative values (purple) representing rotation to the left and positive values (orange) rotation to the right. The green outlines are taken from reflectivity images acquired simultaneously with the magnetic images, and are provided as a guide for the eye.

This corresponds to the peak current density during the write pulse given the 9 Ω direct current (DC) resistance of the coils. While the coils will naturally have an impedance which would have been used for modelling in ideal circumstances, the reactance of the coils was unknown, thus precluding this. The modelled fields therefore provide an estimate of the maximum possible magnetic field strength and the spatial form of the field at this peak, and are useful for comparisons of different coil geometries rather than the extraction of absolute field values. The in-plane and out-of-plane components of the field (B_x and B_z, respectively) were then calculated using finite element modelling software COMSOL Multiphysics®, with a cell size of 20 nm. A line scan was then taken at a plane 500 nm above the upper surface of the coils, corresponding to the base of the magnetic material of the yoke. The results for the four fundamentally unique possible coil configurations are shown in Figure 5.6 on the next page.

In all four cases the in-plane component of the field, B_x, has a similar peak value. In the case of a single coil the field peaks at 100 mT directly above the driving coil. This peak value remains unchanged for the case of coils C1 and C3 being active, with two distinct peaks of 100 mT centred above the two coils. Between the two coils B_x drops to 40 mT. When two coils next to one another are activated, however, a slight increase in peak field is observed (120 mT) along with a significant improvement in spatial uniformity of the field compared to two separated coils. All three coils, however, affords little improvement in either peak field (134 mT) or spatial uniformity over two neighbouring coils.

The out-of-plane component, B_z, is a very different case. For the single coil, two neighbouring coils, and three coil cases the out-of-plane component retains a fundamentally bipolar shape. Peak field values increase as expected: 50 mT, 80 mT and 100 mT. However, the space between two separated coils (Figure 5.6(c) on the facing page) creates a fundamentally different spatial profile to the field. The gap between the coils allows the z component of the field to switch sign

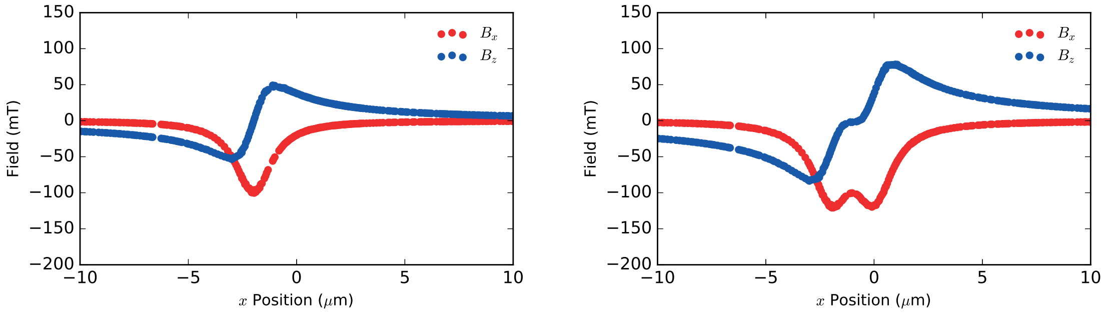

(a) Coil C1 active (b) Coils C1 and C2 active

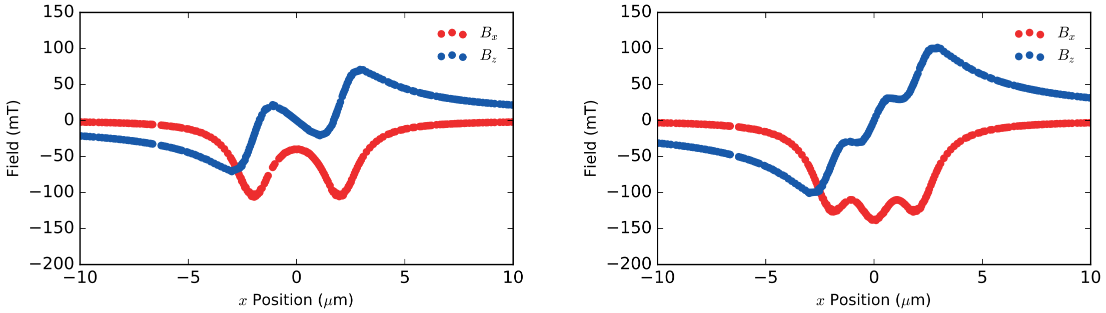

(c) Coils C1 and C3 active (d) Coils C1, C2 and C3 active

Figure 5.6: The driving magnetic field generated by each driving coil configuration. Modelled coils had a cross section of $1\,\mu\text{m} \times 1\,\mu\text{m}$ and were centred at $x = -2\,\mu\text{m}$, $0\,\mu\text{m}$ and $2\,\mu\text{m}$. The in-plane component, B_x, is shown in red and the out-of-plane component, B_z, is shown in blue. The line profiles represent the field 500 nm above the driving coils, at the base of the yoke.

between the coils, creating a quadrupolar spatial variation in B_z. While surprising, such a spaced coil arrangement is not used in commercial devices for this reason.

5.4 Analysis of Observed Flux Formations

An equilibrium magnetic state for a nominally identical device of this shape has been shown previously in Chapter 4 and is reproduced in Figure 5.7 on the next page.[65] This state is known to be consistent between nominally identical writers, and stable after the application of a large external field, as previously shown in Figures 4.7 and 4.17. Three primary domains comprise the equilibrium state. The largest is oriented in the y direction (parallel to the easy axis of the structure) and

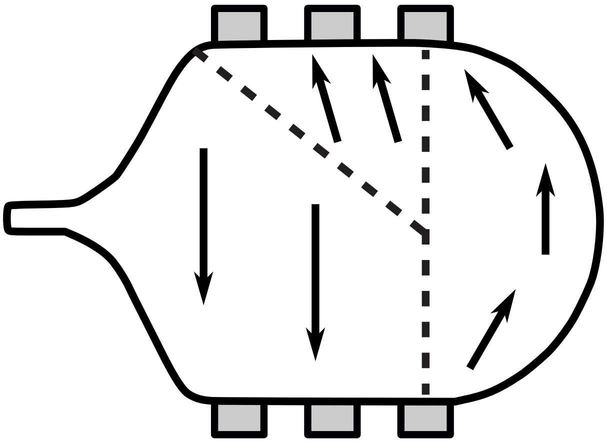

Figure 5.7: The equilibrium state of a write head nominally identical to those presented in this chapter, derived from TRSKM measurements and previously shown in Figure 4.19(a). This domain structure can be considered indicative of the structure of similar writers.

occupies the confluence region and lower half of the write head as presented here. A smaller near-antiparallel domain occupies the upper half of the write head and a third domain covers the back via, with the magnetisation orienting itself to satisfy the shape anisotropy in this region.

With all three write coils activated, as in device F3, the formation of a strong, uniform flux beam directly along the write head's symmetry axis is expected.[76] Instead, flux is observed nucleating in two spatially separated spots along the symmetry axis. This is likely due to the equilibrium state's deviation from the theorised "striped" domain state.[26] The fragmented nature of the flux beam instead suggests the presence of regions where the magnetisation is canted from the y direction and so undergoes smaller rotation in response to the field from the coils.

In the case of write heads with a single active driving coil (writers F5, F6, and F7) the observed behaviour is much as predicted. With a single active coil, it is expected that flux would nucleate above the active coil, and propagate along the symmetry axis by means of a process of small-angle domain rotation, without the need for motion of domain walls.[76] For two of the single-coil write heads, F5 and F7, this behaviour is indeed observed; flux nucleates in a single well-defined location above the driving coil before extending along the symmetry axis. It is possible that the magnitude of the in-plane field must exceed a threshold value to cause rotation of the magnetisation from the equilibrium state. This would occur first directly above the active driving coil, before magnetisation rotation would be observed at steadily greater distances from the coil. Unfortunately the spatial resolution limit of optical Kerr microscopy prevents observation of the detailed magnetic structure within the pole tip during the writing process.

The write head with only the single central driving coil activated (write head F6), however, does not exhibit this expected behaviour. Flux nucleates in two spatially separated areas above the driving coil, either side of the symmetry axis. These then extend independently towards the pole tip, and remain spatially separated. The line separating the two regions of flux might be associated with the presence of a domain wall since a diagonal domain wall has been observed previously in similar devices (Figure 5.7 on page 148). It is possible that an alternative equilibrium domain structure would lead to more favourable conditions for flux beaming.

Two neighbouring active coils, as is the configuration in write heads F8 and F10, should exhibit similar behaviour to their single-coil equivalents. The two coils should produce a region of in-plane field of larger area, nucleating a larger area of flux, hence producing a broader flux beam. However, this is not the observed behaviour in either of these write heads.

The two coils closest to the pole tip (coils C1 and C2, write head F8) nucleate two distinct areas of flux: one in the upper half of the yoke (as presented herein), and a second above the back via. The nucleation of flux above the back via is surprising given the distance from the driving coils. This may suggest movement of a domain wall, contrasting with predictions that flux propagation is the result only of small-angle magnetisation rotation within existing domains. The two distinct areas of flux do, however, then coalesce so as to extend along the symmetry axis towards the pole tip.

Two spatially separated coils, one deep in the confluence region and the second towards the back via (coils C1 and C3, write head F9), produce a broad, incoherent flux beam which fails to extend along the symmetry axis. There are two potential explanations for this behaviour. Firstly, the polar field between the two active coils varies more strongly due to their increased spatial separation, as shown in Section 5.3.1. This quadrupolar variation in B_z, with a field strength on the order of the in-plane field, will significantly disrupt the formation of a flux beam and any potential extension into the confluence region. Alternatively this writer may have a slightly different equilibrium state to that expected, perhaps moving the rear domain wall to be located closer to coil C2.

Conversely, the two coils towards the back of the writer (coils C2 and C3, write head F10) nucleate a number of small areas of flux covering most of the yoke. These areas of flux dissipate rather than coalescing, and fail to form a continuous flux beam. The image at 4.59 ns shows more structure, with a very wide beam covering most of the yoke, and a region of strong contrast above coil C3. This area may align with a domain wall at the back of the device and perpendicular to the symmetry axis, suggesting that once again the domain wall plays a role in disrupting the formation of a continuous flux beam within the yoke.

The apparent role of domain walls in determining the success (or otherwise) of flux beaming in a writer suggests the equilibrium state of the writer is of crucial importance in circumscribing the exact nature of the flux beam formation.

The ultimate aim of these write head structures is twofold. First, to achieve the highest possible data transfer rate through fast switching of both the write head and the underlying magnetic storage medium. Secondly, to shrink the physical size of magnetic storage systems and thereby increase data storage density by increasing the spatial confinement of the write field. While the simplest and most obvious method to increase the write field would be to increase the saturation flux density of the head material, this has previously been shown to be insufficient to obtain desired increases in recording field strength.[89] This increase has therefore conventionally been achieved by increasing the number and density of the driving coils, increasing the driving current and making minor adjustments to the geometry of the write head. However, the time-resolved images obtained from this range of coil configurations show a surprisingly large variation in the precise spatial form of the nucleated flux within the yoke and confluence region. This implies particular attention must be paid to the exact micromagnetic state of the writer.

These results do, however, suggest a potentially preferable configuration for the driving coils. A single driving coil positioned close to the air-bearing surface, driven with sufficiently high current to cause the pole tip magnetisation to rotate parallel to the symmetry axis, would likely produce a wide but uniform propagating flux beam similar to that observed in device F5 (Figure 5.4(b) on page 143). A reduction in the number of driving coils would also assist scaling of the yoke and pole tip to smaller dimensions and would reduce the self-inductance of the coil, promoting reduced switching times.

5.5 Conclusions

In this chapter, it has been demonstrated that the detailed spatial form of the driving field, generated by the embedded write coils, plays a significant role in the magnetodynamics observed within commercial hard disk write heads. Furthermore, direct experimental observations of the process of flux beaming have been presented. While current models for flux conduction[76] sufficiently describe the fundamentals of the process, refinement is required to replicate the actual nature of the magnetic processes observed in real-world devices with complex geometry. Furthermore, the term “flux beaming” appears to be somewhat of a misnomer: dynamic flux rarely forms uniform “beams”, nor does flux propagate on the picosecond timescale and 600 nm resolution presented here.

It is further possible that the considerable variation in observed dynamics may suggest that the equilibrium micromagnetic state also plays an equally important role. However, it is important to note that, due to restrictions in the available wafer layouts, only a single writer of each geometric design and coil configuration has been imaged in this study. This of course means that individual flaws in a particular writer could influence the results presented herein. While these results do not show that every writer of a particular coil geometry behaves in the manner presented, they do show that the occurrence of flux beaming within a writer is not as common as previously suspected. Further measurements on nominally identical writers with the same coil geometry, produced at the same time on the same wafer, would be necessary to confirm (or otherwise) the variation in flux propagation patterns for a given writer and coil geometry.

The work presented in this chapter has immediate application in understanding the magnetodynamics of hard disk write heads and other high-frequency nanoscale magnetic devices. This also provides insight for future write head designs, particularly for HAMR devices, ultimately leading to greater areal density and cheaper magnetic storage.

CHAPTER 6

Spin pumping and spin transfer torque in Co_2MnGe / Ag / $Ni_{81}Fe_{19}$ spin valve structures

Some of the results presented in this chapter have previously been presented as 'Effect of sink layer thickness on damping in CoMnGe/Ag/NiFe spin valves' by Valkass et al. at 8th Joint European Magnetic Symposia, Glasgow (2016) and subsequently published as 'Dependence of spin pumping and spin transfer torque upon $Ni_{81}Fe_{19}$ thickness in Ta / Ag / $Ni_{81}Fe_{19}$ / Ag / Co_2MnGe / Ag / Ta spin-valve structures' by Durrant et al. in *Physical Review B* **96**, 144421 (2017). X-ray measurements were carried out by Rob Valkass and Dr Leigh Shelford. Vector network analyser ferromagnetic resonance measurements and macrospin modelling were performed by Chris Durrant, Prof. Rob Hicken and Dr Leigh Shelford and are included for completeness.

6.1 Introduction

Spin valves are spintronic devices realised as a stack structure comprising three layers: a hard and a soft magnetic layer separated by a normal metal layer. A fourth antiferromagnetic layer is typically placed adjacent to one of the ferromagnetic layers, which acts to ‘pin’ the layer and thus make it hard by means of the large negative exchange interaction between the antiferromagnet and adjacent ferromagnetic layer. This allows the magnetisation direction of the soft layer to be rotated by a much lower applied magnetic field than the hard layer, creating two distinct states: the magnetisation direction of the two ferromagnetic layers being either parallel or antiparallel. Depending on the relative orientation of the hard and soft layers, a current passing through the structure experiences either a higher or lower electrical resistance as a result of GMR. Furthermore, the ability of a spin-polarised current to exert a STT on a ferromagnet layer has prompted the development of a number of novel spintronic devices. The use of pure spin currents avoids a number of downsides associated with typical electrical currents, and have the potential to allow low-power and high-bandwidth information transfer.[92,93] In a commercial hard disk drive, the write heads studied in the previous chapters are accompanied by a read head based on a spin valve. Spin valve devices are also applicable in the emerging field of MRAM technology. Understanding spin valves and the materials used in their fabrication is therefore of utmost importance for the magnetic data storage industry.

The advancement of practical devices able to take advantage of these effects depends on a complete understanding of the generation and propagation of spin currents by means such as the spin Hall effect.[94,95] Previous detection mechanisms for spin currents have typically been indirect, making use of either the inverse spin Hall effect[96–98] or spin-torque driven magnetic precession.[99,100] Both of these techniques are indirect, requiring the properties of any spin current to be inferred rather than directly measured. More recently, synchrotron soft x-ray techniques have been developed allowing direct detection of the local spin density.[101]

It is also known that precessional spin pumping provides a mechanism for generating and propagating spin currents in spin valves.[102] Magnetisation precession driven in one of the spin valve's ferromagnetic layers, termed the "source" layer FM1, pumps a pure spin current into the central normal metal layer, NM. Two additional sources of damping are present in such a structure: spin scattering in the normal metal layer, and absorption of spin in the other ferromagnetic layer (termed the "sink" layer FM2). As FM1 pumps spin current through NM and into FM2, the transverse component of the spin current is absorbed, resulting in a STT on the magnetisation of FM2 and a measurable change in the damping in FM1.[103]

The spin relaxation length in the normal metal layer has been studied extensively.[104,105] Previous studies have also investigated the penetration of spin current into the ferromagnetic sink layer FM2 using magnetotransport techniques.[106,107] These studies found that the longitudinal component of spin (that which is parallel or anti-parallel to $\boldsymbol{M}$) in $3d$ transition metals has an exponential dependence on depth z with the spin current density proportional to $\exp\left(-z/\lambda_{\mathrm{SD}}\right)$ (λ_{SD} being the spin diffusion length). More recently Ghosh et al. used spin pumping to infer that the depth dependence of the transverse component of the spin current instead follows a power law, saturating at a sink layer thickness of $1.2\,\mathrm{nm}$ regardless of the sink layer composition.[108] Such techniques, however, do not provide direct simultaneous observation of the spin dynamics of both the source and sink layers.

Given this, techniques based on ferromagnetic resonance (FMR) naturally lend themselves to the investigation of spin pumping and STT.[100] The non-local origins of the damping on the source layer mean that a thicker source layer can act as a probe for a much thinner sink layer. The effect of changes in sink layer thickness on the order of Ångströms can therefore be more easily detected in the larger FMR signal from the source layer. However, while such techniques avoid magnetostatic[109] and activation volume effects[110] seen in previous measurements, they remain an indirect measurement of the spin current absorption in the sink layer.

The study presented in this chapter therefore aims to present a threefold advance over the prior works: to measure the damping parameter α as a function of sink layer thickness t_{NiFe} by vector network analyser ferromagnetic resonance (VNA-FMR); to resolve the amplitude and phase of the source and sink layer responses individually, and to directly measure the STT acting on the sink layer, by XFMR; and to calculate the real part of the spin mixing conductance, $\mathrm{Re}\left(g^{\uparrow\downarrow}\right)$, by fitting a macrospin model to the XFMR data.

6.2 Experimental Setup

6.2.1 Sample Information

The complete stack structure, including the spin valve, is shown in Figure 6.1 on the facing page. The stack structure was based on that used by Ghosh et al. with a number of modifications. The two stack structures are shown side by side for comparison in Figure 6.2 on the next page.

Each sample was grown on a sapphire wafer with a Ta (5 nm) / Cu (100 nm) / Ta (5 nm) / Ru overlayer. The 100 nm Cu layer was chosen due to the reversal of the spin valve in our structure compared to that studied by Ghosh et al. In Ghosh's structure, the Co source layer is below the CoFeB sink layer, resulting in spin current being pumped towards the Al capping layer. The capping layer was also left to oxidise naturally in atmosphere, likely resulting in a thin layer of metallic aluminium which was covered by the remainder of the layer forming aluminium oxide. The spin scattering properties of this thin, self-passivated aluminium oxide capping layer are therefore not well known. In contrast, our structure places the CoMnGe source layer above the $Ni_{81}Fe_{19}$ sink layer, resulting in spin current being pumped towards the substrate. This allowed for the relatively thick Cu

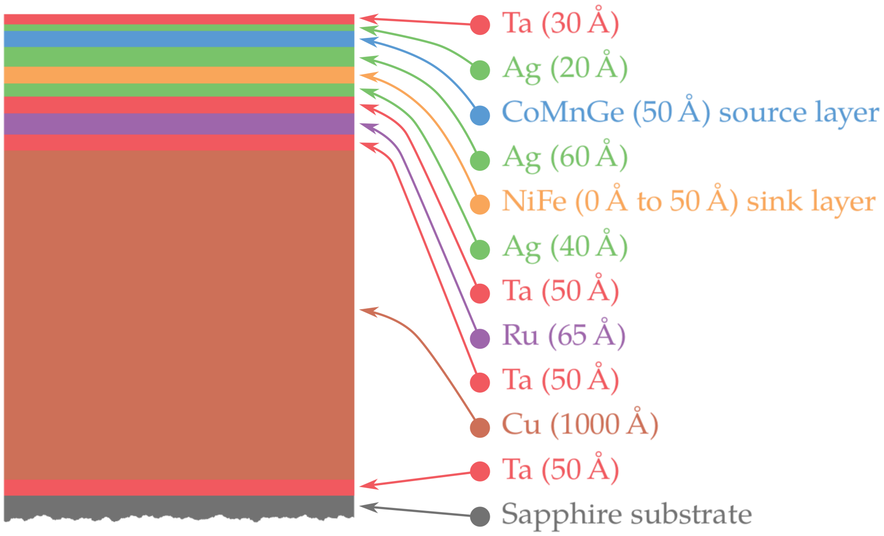

Figure 6.1: The spin valve structure shown in context with the rest of the sample stack. The CoMnGe layer is the source layer FM1, with the thickness of the NiFe sink layer varying between individual samples.

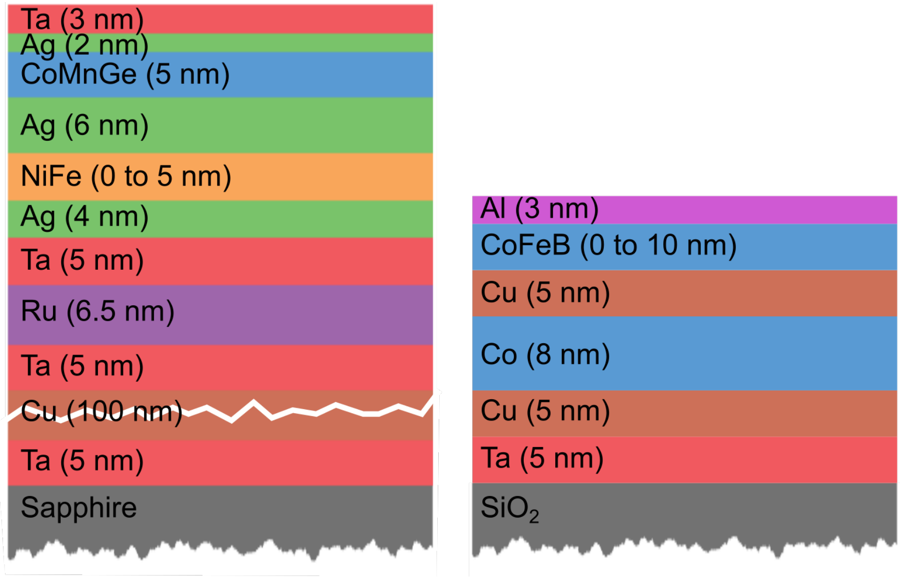

Figure 6.2: The full sample stack used in this study (left) and the one previously studied by Ghosh et al (right).

layer, ensuring consistent spin scattering properties and removing any potential boundary effects.

A 60 s radio frequency (RF) etch was used to remove 3.5 nm of the sacrificial Ru layer, ensuring a clean surface, and leaving a 10 nm Ru layer suitable for subsequent growth of the spin valve. This process ensured that clean samples were produced despite the need for deposition in two different growth systems, and therefore the exposure of the sample to atmosphere.

The spin valve stacks themselves were then deposited in the order Ta (5 nm) / Ag (4 nm) / $Ni_{81}Fe_{19}$ (0.3 nm to 5 nm) / Ag (6 nm) / Co_2MnGe (5 nm) / Ag (2 nm) / Ta (3 nm). The Cu spacers used by Ghosh et al. were replaced with Ag. The thicknesses of Ag were chosen so as to be sufficient to avoid interlayer exchange coupling between the source and sink layers, but also to be small compared to the spin diffusion length. The Ta layer used by Ghosh et al. as a spin scatterer at the base of the spin valve was retained, with an equivalent layer also added to the top of our stack as a cap having more well-defined properties than the oxidised aluminium layer of Ghosh et al.

Control samples, one omitting the $Ni_{81}Fe_{19}$ layer and a second omitting the Co_2MnGe layer were also fabricated. As deposited the Co_2MnGe source layer is not ferromagnetic. Field annealing was used to induce the ferromagnetic state and induce a small in-plane uniaxial magnetic anisotropy within both layers, as shown in Figure 6.3 on the facing page. All measurements were performed on large area 10 mm × 10 mm films.

6.2.2 Vector network analyser ferromagnetic resonance

VNA-FMR measurements were carried out by Chris Durrant and Leigh Shelford at the University of Exeter in the labs of Prof. Rob Hicken. Samples with varying NiFe layer thicknesses were placed face-down on a 50 Ω co-planar waveguide (CPW) with a 500 µm wide central signal line, as shown in Figure 6.4 on page 160.

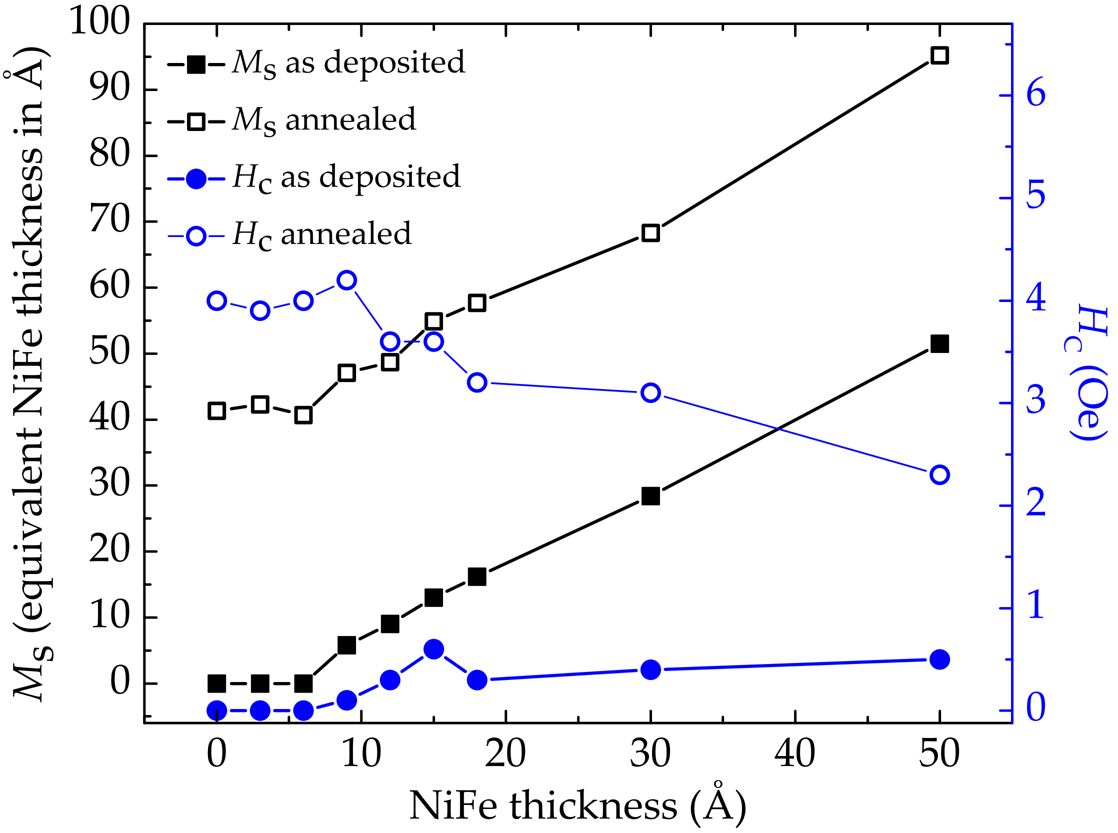

Figure 6.3: Saturation magnetisation, M_s, and coercive field, H_c, of the $Ni_{81}Fe_{19}$ sink layer measured by VSM as a function of $Ni_{81}Fe_{19}$ layer thickness both before and after field annealing.

Each sample was first coated with a 100 nm layer of PMMA to prevent the metallic sample surface short circuiting against the CPW tracks, while keeping the source layer FM1 as close to the CPW as possible.

The CPW was connected to the vector network analyser (VNA) as a two-port device under test using through-hole printed circuit board (PCB) mounted SMA end launchers. The scattering parameters (S-parameters) of the entire network were recorded at frequencies from 0 GHz to 15 GHz as a magnetic bias field was swept between 0 T and 0.13 T in the plane of the sample. The VNA-FMR technique is described in further detail by Durrant et al. [111].

The damping parameter α of source layer FM1 (Co_2MnGe) was then calculated from the frequency dependent FWHM linewidths $\varDelta H(\omega)$ for each sink ($Ni_{81}Fe_{19}$)

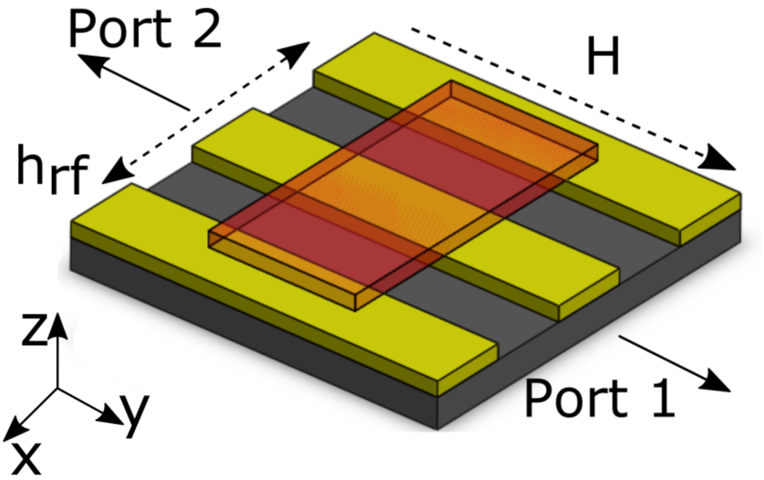

Figure 6.4: The measurement geometry for VNA-FMR experiments. The sample (red) was placed face-down atop a 500 µm wide signal line generating an oscillating in-plane magnetic field h_{rf}. A constant bias field H was maintained as the frequency of h_{rf} was swept.

layer thickness using the expression

$$\Delta H(\omega) = \Delta H(0) + \frac{2\alpha\omega}{\gamma} \tag{6.1}$$

where $\Delta H(0)$ is the contribution due to inhomogeneous broadening and two magnon scattering.[112]

6.2.3 X-ray ferromagnetic resonance

Phase-resolved XFMR measurements[101,113,114] were performed on beamline I10 at DLS using the portable octupole magnet system (POMS) end station made available by the Magnetic Spectroscopy Group. POMS is a vector magnet system capable of generating fields of up to 0.4 T in arbitrary directions, and was indispensible in providing the different field geometries required to perform static XMCD and time-resolved XFMR measurements.

Figure 6.5 on the facing page shows a schematic of the sample measurement geometry. Microwaves with a frequency of 4 GHz were transmitted to the sample by *in vacuo* coaxial SMA cables connected to a CPW fabricated from a PCB with a 1 mm wide signal line. The increased signal line width compared to that

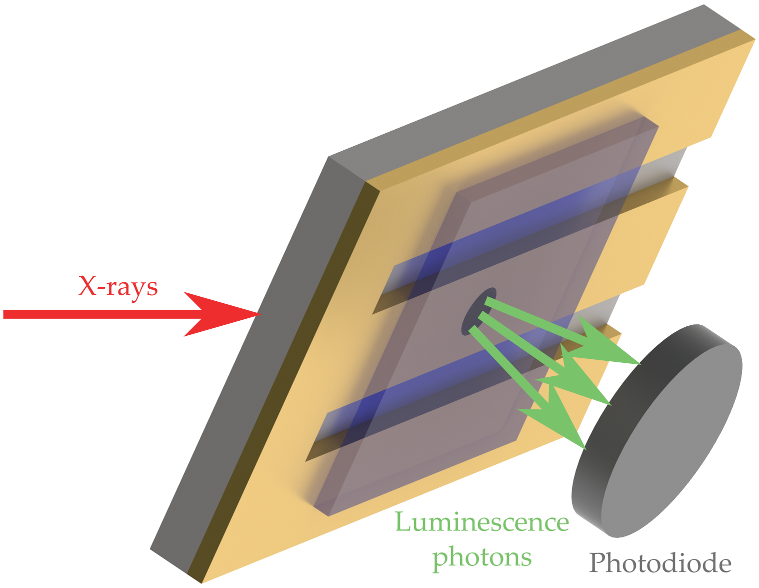

Figure 6.5: The measurement geometry for XFMR experiments. The sample (blue) was placed face-down against the CPW's 1 mm wide signal line. A 500 µm diameter hole provided x-ray access through the PCB, the hole being countersunk on the PCB substrate to allow greater flexibility in incident angle. A photodiode mounted behind the sample indirectly detected the transmitted x-rays *via* x-ray excited optical luminescence in the sapphire substrate.

used for VNA-FMR measurements was necessary to provide space for a countersunk 500 µm diameter hole which afforded x-ray access through the PCB to the sample surface. A multiple-frequency comb generator[115] driven by the 500 MHz synchrotron master clock was used to generate the 4 GHz RF excitation as the eighth harmonic of the master clock. This ensured phase coherence of the RF excitation with the arrival of the x-ray bunches at the sample. A photograph of the CPW is shown in Figure 6.6 on the next page.

Transmitted x-ray intensity was detected indirectly by a photodiode measuring x-ray excited optical luminescence (XEOL) generated in the sapphire substrate. The x-ray incidence angle ϑ was set to 45° with respect to the sample surface. During static XAS and XMCD measurements a bias field was applied parallel with the incoming x-ray beam. For XFMR measurements the bias field was applied parallel with the symmetry axis of the CPW, orthogonal to the incident x-ray beam. This transverse geometry allows phase-resolved measurement of the precession

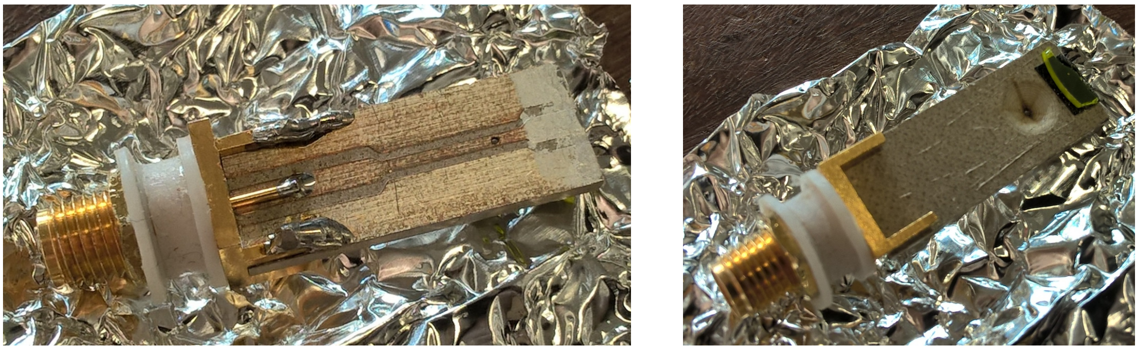

Figure 6.6: The CPW used during XFMR experiments. The sample was placed face-down against the CPW's 1 mm wide signal line, covering the 500 µm diameter hole. The reverse of the CPW shows that the hole is countersunk, allowing a greater range of incident x-ray angles. A green/yellow YAG crystal placed adjacent to the hole aided alignment of the x-ray beam.

by delaying the RF excitation relative to the synchrotron master clock signal.

Layer specificity was achieved by tuning the x-ray energy to either the Co L_3 edge in the source ($\mathrm{Co_2MnGe}$) layer or the Fe L_3 edge in the sink ($\mathrm{Ni_{81}Fe_{19}}$) layer, allowing direct measurement of the spin dynamics in each layer.

6.3 Results and Discussion

6.3.1 Vector network analyser ferromagnetic resonance

Typical VNA-FMR resonance spectra acquired at a frequency of 8 GHz for varying sink layer thicknesses t_{NiFe} are shown in Figure 6.7 on the facing page. For $t_{\mathrm{NiFe}} = 1.2\,\mathrm{nm}$ (panel (b)) and $1.8\,\mathrm{nm}$ (panel (c)) both the source $\mathrm{Co_2MnGe}$ and sink $\mathrm{Ni_{81}Fe_{19}}$ peaks are distinct from one another, and have sufficient amplitude to allow observation of the sink layer resonance directly. For $t_{\mathrm{NiFe}} \leq 0.9\,\mathrm{nm}$, as in panel (a), the amplitude of the $\mathrm{Ni_{81}Fe_{19}}$ response falls below the noise floor. This prevents any information about the behaviour of the sink layer being obtained directly. Instead, information can only be inferred from the dynamics of the source $\mathrm{Co_2MnGe}$ layer response. For the thickest sink layers studied here, $t_{\mathrm{NiFe}} = 3.0\,\mathrm{nm}$ (panel (d)), and $t_{\mathrm{NiFe}} = 5.0\,\mathrm{nm}$ the $\mathrm{Co_2MnGe}$ and $\mathrm{Ni_{81}Fe_{19}}$ layers share similar

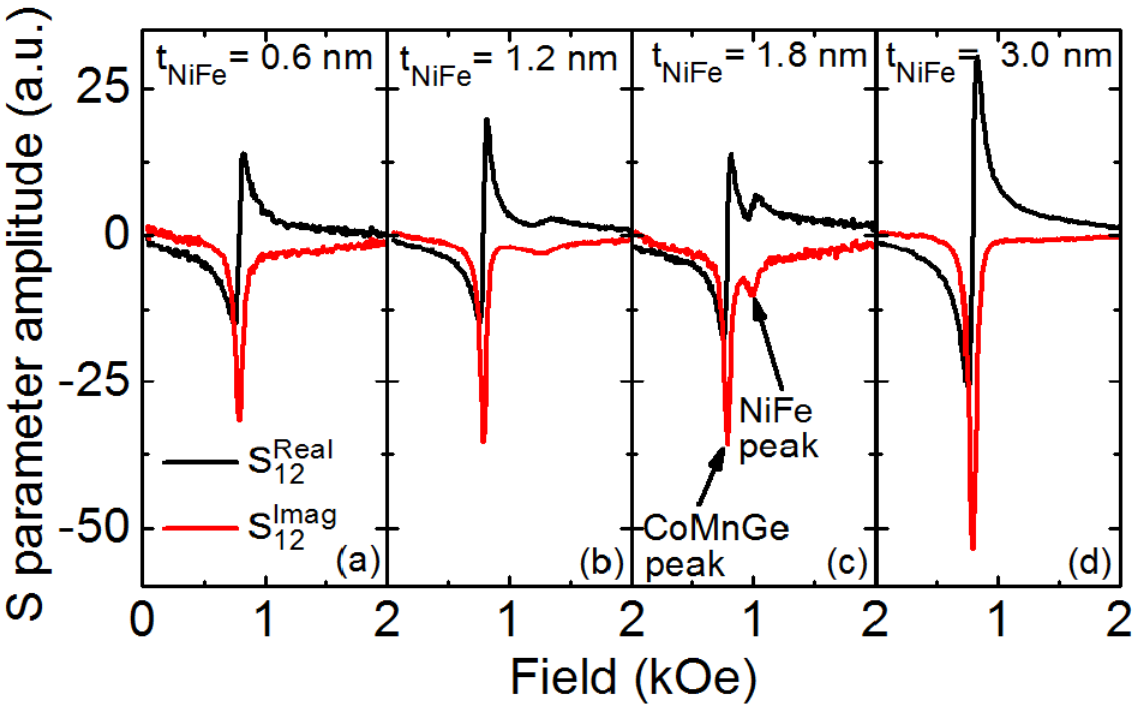

Figure 6.7: Typical experimental VNA-FMR resonance curves at $f = 8\,\mathrm{GHz}$ for sink layer thicknesses of $0.6\,\mathrm{nm}$, $1.2\,\mathrm{nm}$, $1.8\,\mathrm{nm}$ and $3.0\,\mathrm{nm}$ showing the S_{12}^{Imag} and S_{12}^{Real} scattering matrix components.

resonant fields. This causes the peaks to overlap making it impossible to resolve the behaviour of the individual layers.

For each sample a single Lorentzian function was fitted to the absorptive S-parameter, $S_{12}^{\mathrm{Imag.}}$, in order to exctract a frequency dependent linewidth $\Delta H(\omega)$. This in turn allowed calculation of the source layer damping parameter α_{CoMnGe}. The intrinsic damping was isolated using Equation (6.1) as described by Urban et al.[112] It should be noted that this method employing the single S-parameter S_{12} is somewhat of an approximation, neglecting factors such as minor imperfections in the positioning of the sample on the CPW and the small air gap between the signal line and the sample surface. Errors from the 'true' resonant frequency using this technique have been shown to be consistently below 1%. Absolute errors in resonant linewidth can be as high as 10%, however it has been shown that the general trend remains unaffected by the approximation.[116,117]

The inset panel of Figure 6.8 shows the linewidth $\Delta H(\omega)$ as a function of fre-

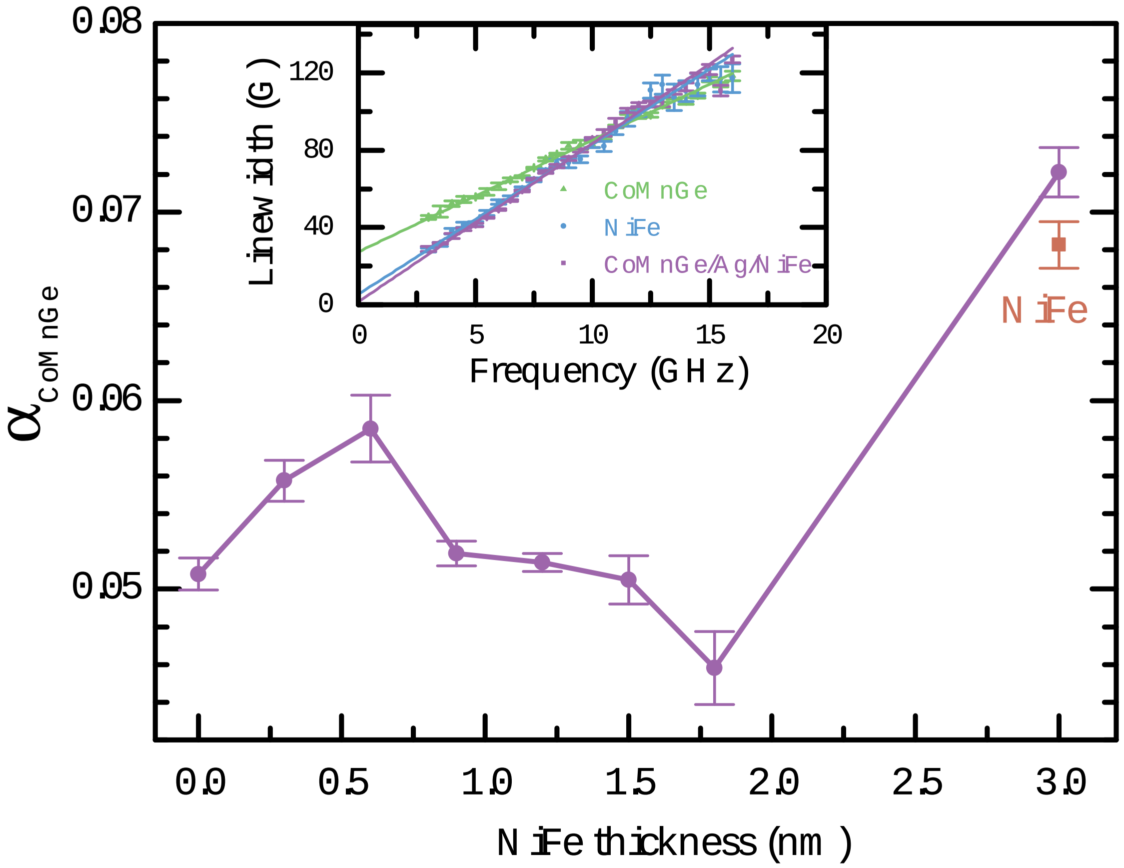

Figure 6.8: Source layer Gilbert damping parameter, α_{CoMeGe}, as a function of sink layer thickness. The red point shows the value recorded for the NiFe reference film. Inset, resonant linewidth as a function of driving microwave frequency for the two reference films and a trilayer stack with $t_{\mathrm{NiFe}} = 3.0\,\mathrm{nm}$. The error bars in this figure derive from the statistical error associated with the Lorentzian fitting.

quency for the two single layer reference films and a complete spin valve with $t_{\mathrm{NiFe}} = 3.0\,\mathrm{nm}$. Here $\Delta H(0)$ is comparatively large for the Co_2MnGe reference film and small for the $Ni_{81}Fe_{19}$ reference film. In the trilayer stacks $\Delta H(0)$ gradually decreased with increasing $Ni_{81}Fe_{19}$ thickness, becoming negligible for $t_{\mathrm{NiFe}} \geq 3.0\,\mathrm{nm}$. This is further shown in Figure 6.9 on the next page. As $\Delta H(0)$ usually results from structural imperfections[118] and as the Co_2MnGe layer is grown after the $Ni_{81}Fe_{19}$ layer, this result suggests that the increased $Ni_{81}Fe_{19}$ thickness enhances the quality of the Co_2MnGe growth.

Figure 6.8 shows extracted α_{CoMnGe} values for each $Ni_{81}Fe_{19}$ sink layer thickness. For $t_{\mathrm{NiFe}} \leq 1.8\,\mathrm{nm}$ the variation of α_{CoMnGe} is relatively small. This was

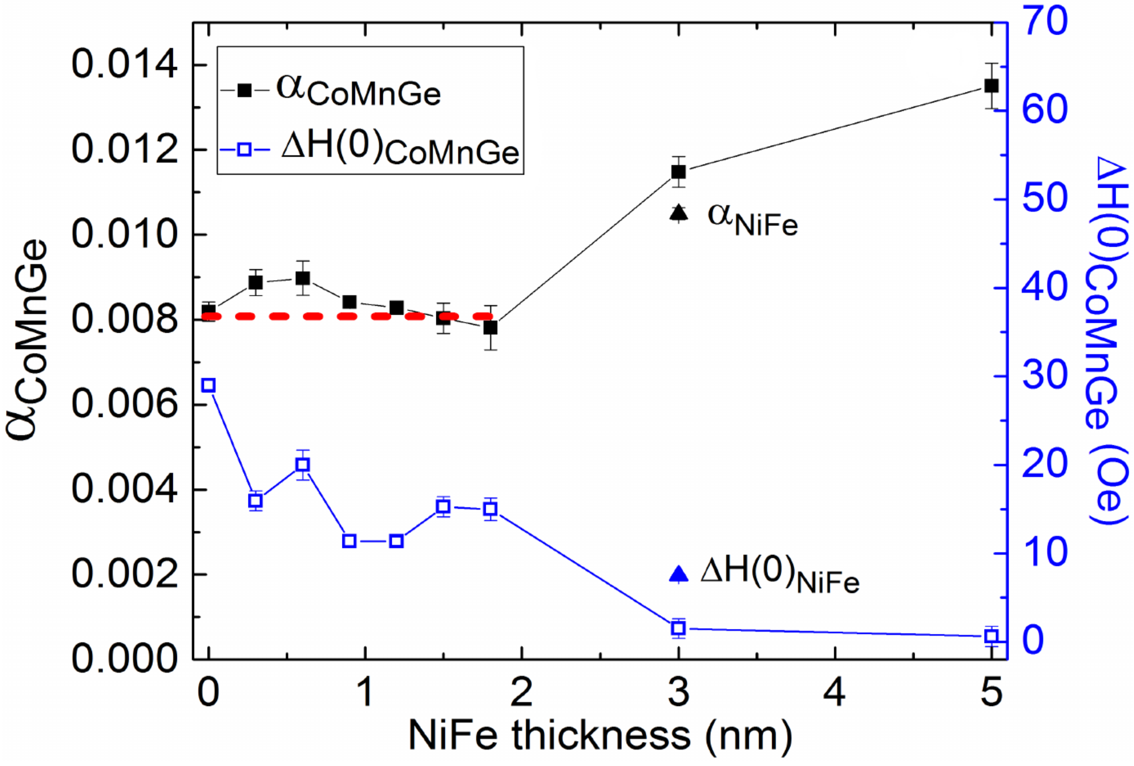

Figure 6.9: Gilbert damping parameter, α_{CoMnGe}, and inhomogeneous broadening $\Delta H(0)$ measured by VNA-FMR for varying sink layer thickness t_{NiFe}.

initially unexpected considering that Ghosh et al. had previously reported a power law dependency for α_{Source} increasing with the thickness of the sink layer.[108] It is possible that the Ta layer adjacent to the $Ni_{81}Fe_{19}$ sink layer, having a relatively large atomic number and spin-orbit coupling, is highly effective at scattering the injected spins. This would result in any spin current passing through the thin $Ni_{81}Fe_{19}$ layer also passing through the adjacent Ag layer and being scattered by the Ta layer.

Samples with $t_{\mathrm{NiFe}} = 0.3\,\mathrm{nm}$ and $0.6\,\mathrm{nm}$ are, however, possible exceptions to the above. The increased damping seen in these samples may be due to the structure of the $Ni_{81}Fe_{19}$ layer. The VSM data shown in Figure 6.3 on page 159 shows that for $t_{\mathrm{NiFe}} \leq 0.6\,\mathrm{nm}$ the $Ni_{81}Fe_{19}$ layer does not exhibit ferromagnetic order. While this could be due to the $Ni_{81}Fe_{19}$ forming a non-magnetic alloy with the surrounding Ag, this is unlikely as Fe and Ni are known to be immiscible in Ag.[119] $Ni_{81}Fe_{19}$ films on Ag have a lattice parameter of 3.58 Å,[120] which is comparable to the film thickness in this case, making it highly unlikely that a continuous single layer film was deposited. Instead the $Ni_{81}Fe_{19}$ layers of these samples are likely discontinuous, comprising superparamagnetic grains with greater structural and magnetic disorder leading to increased spin scattering.

The value of α_{CoMnGe} for the $3.0\,\mathrm{nm}$ $Ni_{81}Fe_{19}$ layer appears to show a significant increase. However, as shown in Figure 6.7, the Co_2MnGe and $Ni_{81}Fe_{19}$ resonances occur at fields close enough to prohibit identification of individual peaks in the VNA-FMR data. A very slight difference in resonant fields would be sufficient to broaden the width of the peak without permitting the individual peaks to be resolved, and therefore artificially increase the extracted value of α_{CoMnGe}. It is for this reason especially that the element specificity of XFMR is necessary to fully understand the spin dyanmics of this system. While the VNA-FMR technique is unable to resolve the individual layer responses, the insight gained concerning $\varDelta H(0)$ is crucial for the fitting and interpretation of the results from the more complex XFMR experiment.

6.3.2 X-ray ferromagnetic resonance

XFMR measurements began with confirmation of VNA-FMR data previously gathered at Exeter. Repeating selected VNA-FMR measurements *in situ* was also useful to confirm the exact resonant field for a particular sample, and to confirm the quality of the coupling between the sample and the microwave field generated at the CPW. Figure 6.10 on page 168 shows a typical VNA-FMR dataset acquired from the sample with a $1.2\,\mathrm{nm}$ NiFe sink layer while mounted within POMS, i.e. as positioned for x-ray measurements. The greyscale shows the real and imaginary components of transmitted RF power, measured as $\mathrm{Re}\left(S_{21}\right)$ and $\mathrm{Im}\left(S_{21}\right)$, in the left and right panels, respectively. For each bias field value the driving microwave frequency was swept from 0 GHz to 20 GHz, producing a plot of transmitted power as a function of both applied bias field and driving microwave frequency.

The brighter upper curve shows the response from the Co_2MnGe layer while the fainter lower curve shows the $Ni_{81}Fe_{19}$ response. In each case the periodic banding as a function of frequency is a property of the CPW and associated microwave end-launchers rather than an inherent property of the sample. The lower panel of Figure 6.10 shows a linescan of S_{21} taken at a fixed frequency of 4 GHz. The solid red line shows a double Lorentzian fit to the imaginary component, the peak of which reveals the resonant field at the chosen frequency.

Before attempting dynamic measurements, static XAS and XMCD spectra were taken to confirm the quality of the samples, particularly the ferromagnetic nature of the sink $Ni_{81}Fe_{19}$ layer. A typical set of XAS and XMCD spectra for the sample with a 3.0 nm sink layer are shown in Figure 6.11 on page 169. These spectra confirm the presence of the expected elements within the sample, as well as the relative amplitude of the XMCD signal relative to the background noise. A very slight shoulder is present on the high energy side of both the Fe and Ni spectra peaks, indicating the presence of a minimal quantity of oxides of Fe and Ni. The small amplitude of the shoulder peak relative to the main peak, however, indicates that this is nothing to be concerned about.

After confirming static x-ray measurements, dynamic measurements began with “delay scans”. These are measurements of the XFMR response as a function of the phase of the driving microwave field relative to the phase of the synchrotron reference clock, essentially probing the magnetic state of the element in question at different stages of its precession. An example of such a measurement is shown in Figure 6.12 on page 170, wherein the XFMR response was recorded at the Ni L_3 edge as a function of driving microwave phase for a sample with a 1.2 nm sink layer at various static bias field values either side of the 19.5 mT Co_2MnGe resonant field.

A variation in both amplitude and phase is observed as the bias field sweeps across the Co_2MnGe resonance. Simple sinusoidal curves were fitted to the data to extract the amplitude and relative phase of the precession, the period of

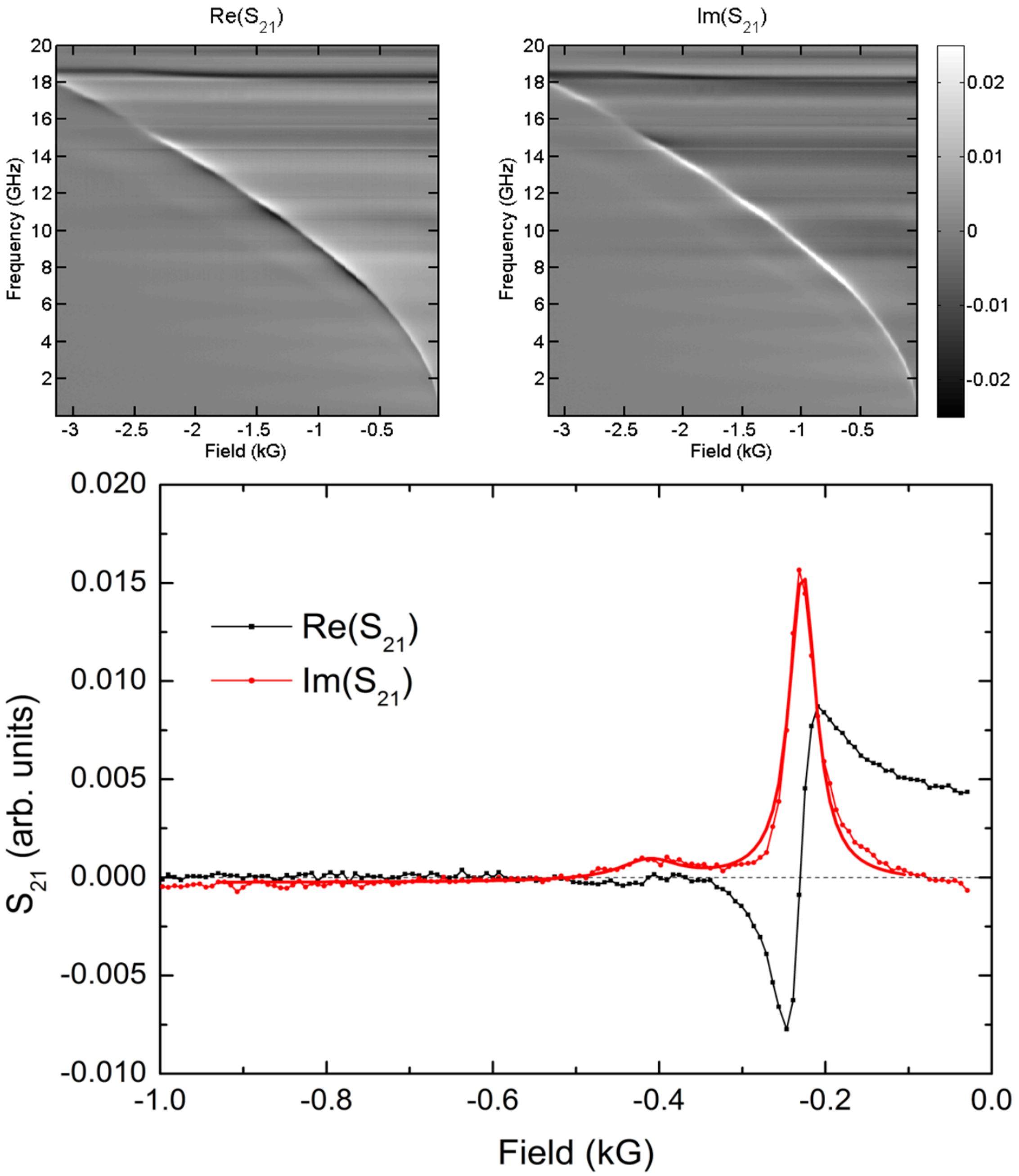

Figure 6.10: VNA-FMR data recorded from a $Ni_{81}Fe_{19}$ (1.2 nm) / Ag (6 nm) / Co_2MnGe (5 nm) spin valve while mounted within POMS. The greyscale shows the real and imaginary components of S_{21} in the left and right panels, respectively, as a function of both applied bias field and driving microwave frequency. The brighter upper curve shows the response from the Co_2MnGe layer while the fainter lower curve shows the $Ni_{81}Fe_{19}$ response. The lower panel shows a linescan taken at a fixed frequency of 4 GHz. The solid red line shows a double Lorentzian fit to the imaginary component.

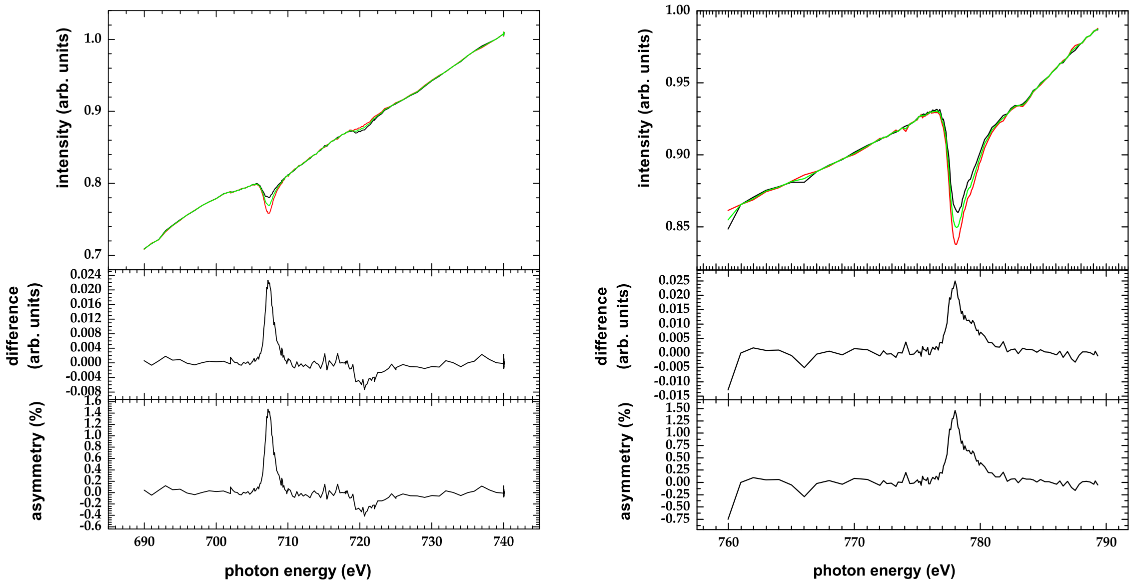

(a) Fe XAS and XMCD

(b) Co XAS and XMCD

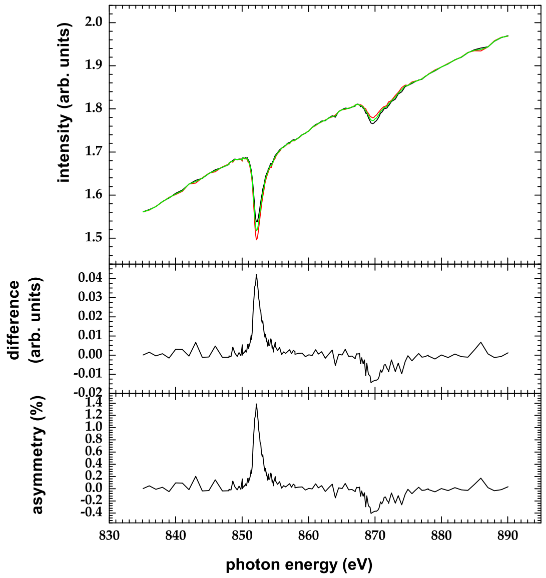

(c) Ni XAS and XMCD

Figure 6.11: Static XAS and XMCD spectra recorded for a spin valve with a 3.0 nm sink layer at each of the Fe, Co and Ni L_3 edges. The XAS, shown in the top graph, was recorded with left and right circularly polarised light (black and red curves) with the average of these shown in green.

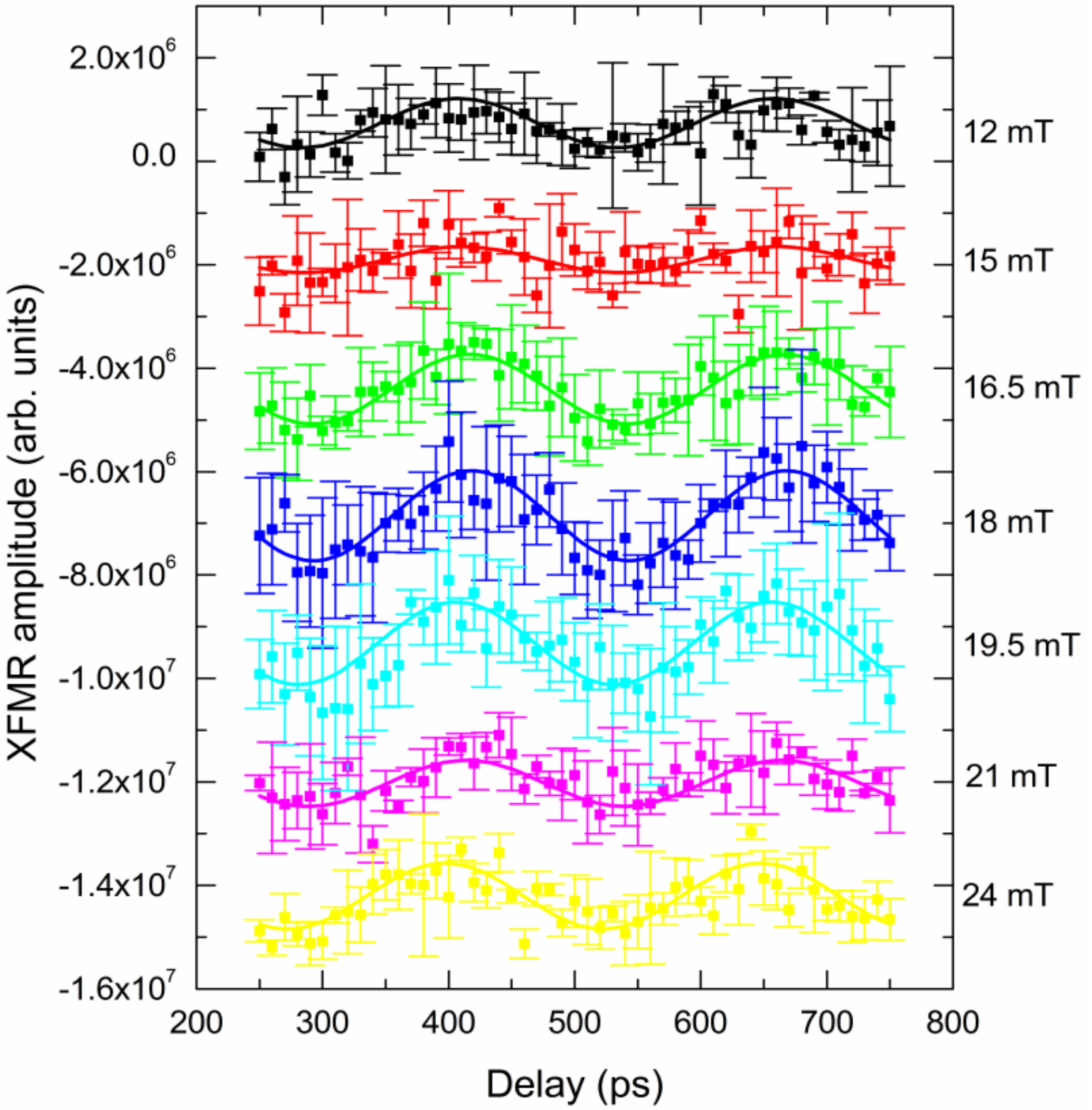

Figure 6.12: XFMR signals from the sample with a 1.2 nm sink layer recorded at the Ni L_3 edge as the phase of the 4 GHz driving signal was varied for different bias field values across the Co_2MnGe resonance. Error bars represent the standard deviation of repeated averaged measurements. Solid lines are simple sinusoidal fits used to extract amplitude and phase information.

the sine function being fixed at 250 ps. Figure 6.13 on the next page shows the extracted amplitude and phase values as a function of bias field, along with the absorptive component of the transmitted microwave signal measured by the VNA as $\mathrm{Im}\left(S_{21}\right)$. A clear peak in the amplitude of the Ni L_3 XFMR signal can be seen at the Co_2MnGe resonance—a direct indication of dynamic coupling between the two layers. However, as can be seen in panel (c), the extracted phase does not exhibit the expected shape. Looking again at the error bars in Figure 6.12, there is considerable scope for the relative phase of each curve to vary from the extracted value as plotted in Figure 6.13 on the following page. It is likely, therefore, that the extracted phase values would be closer to the expected trend with continued data acquisition to improve statistics.

In samples with thicker $Ni_{81}Fe_{19}$ sink layers, the magnetisation of the $Ni_{81}Fe_{19}$ layer is increased, reducing the resonant field such that it approaches that of the Co_2MnGe source layer. Figure 6.14(a) shows the real and imaginary components of the S_{21} parameter as recorded by VNA-FMR on a sample with a 1.8 nm sink layer. Vertical dashed lines in this figure show the resonant fields of the Co_2MnGe and $Ni_{81}Fe_{19}$ layers at $\approx$ 20 mT and $\approx$ 26 mT, respectively. Figure 6.14(b) shows XFMR data recorded at the Co and Ni L_3 absorption edge energies, 777 eV and 852 eV respectively, as a function of static bias field while the sample was driven with a 4 GHz microwave signal. Making pairs of measurements with the phase of the microwaves shifted by a quarter period allowed the real and imaginary components to be recovered.

The imaginary Co signal is well fitted by a single Lorentzian peak. However, the Ni signal is better fitted by the sum of a unipolar peak centred at the $Ni_{81}Fe_{19}$ resonant field, and a second bipolar form centred at the Co_2MnGe resonance. The presence of this bipolar feature is a key signpost towards spin pumping between the two layers due to STT.

Figure 6.15 on page 175 shows field scans taken at $h_{\mathrm{rf}} = 4$ GHz for sink layer thicknesses of 1.5 nm, 1.8 nm, 3.0 nm and 5.0 nm. The response of the source

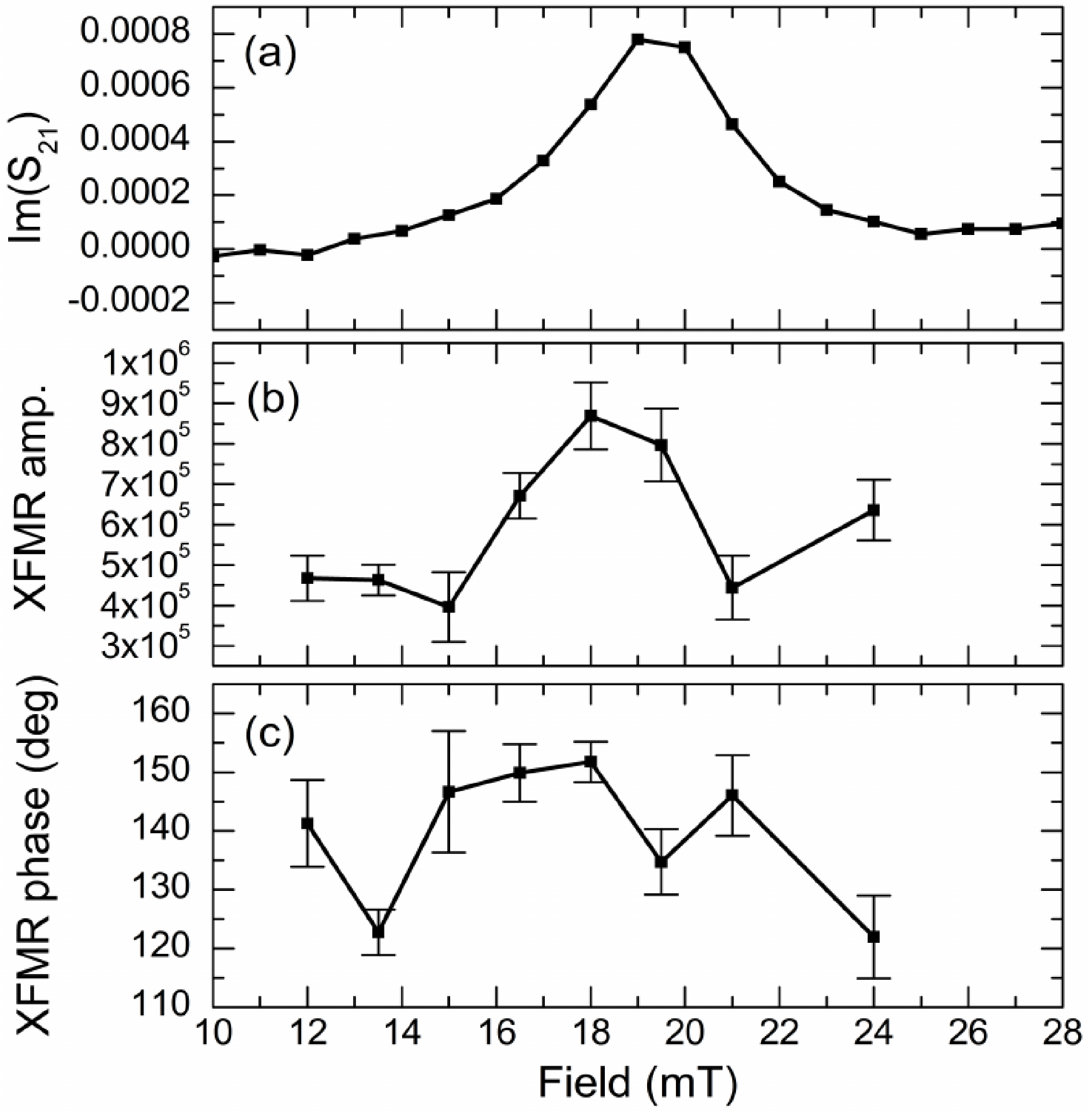

Figure 6.13: Field dependent measurements of the response from the sample with a $1.2\,\mathrm{nm}$ sink layer. (a) The imaginary component of S_{21} measured by VNA-FMR. (b) and (c) The amplitude and phase of the oscillatory XFMR signals shown in Figure 6.12.

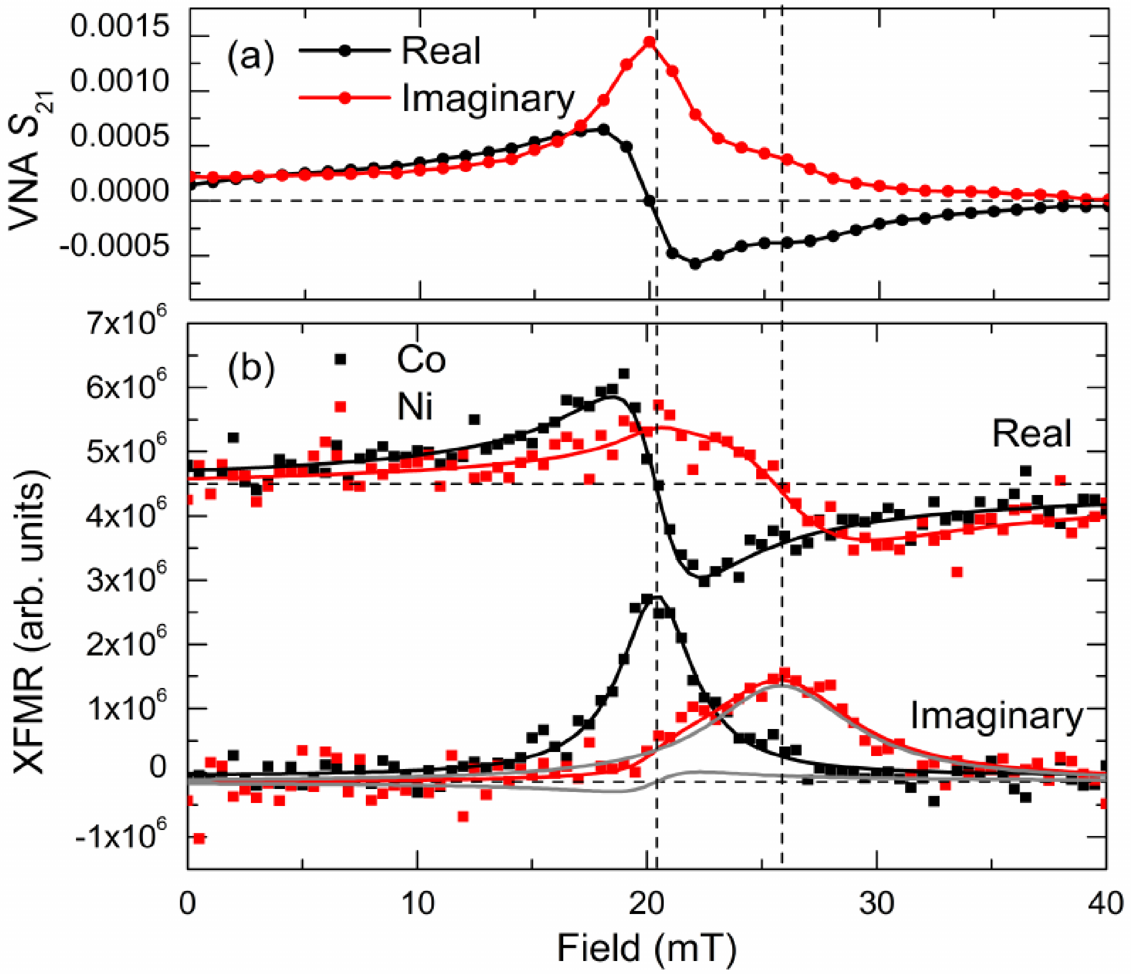

Figure 6.14: (a) Dependence of the real and imaginary components of S_{21} upon the applied magnetic field, recorded by VNA-FMR. (b) XFMR data measured at the Co and Ni L_3 edges, a 4 GHz microwave driving field and a varying bias field. Vertical dashed lines show the resonant fields of the Co_2MnGe and $Ni_{81}Fe_{19}$ layers at $\approx$ 20 mT and $\approx$ 26 mT, respectively. The red fitted curve in (b) is the sum of the two grey curves.

Co_2MnGe layer to the driving microwave field was recorded using circularly polarised x-rays at the Co L_3 edge (777 eV) while the response in the $Ni_{81}Fe_{19}$ sink layer was recorded at the Fe L_3 edge (707 eV). Due to phase delays in the microwave electronics, the dispersive and absorptive (real and imaginary) components of the recovered signal were initially mixed. To obtain the true components, the recovered signal was rotated in the Argand plane so as to achieve a flat response on either side of the resonance, and to align the peak of the absorptive component with the maximum slope of the dispersive component.

For the two thinner films, $t_{\mathrm{NiFe}} = 1.5\,\mathrm{nm}$ (Figure 6.15(a)) and $t_{\mathrm{NiFe}} = 1.8\,\mathrm{nm}$ (Figure 6.15(b)), the Co absorptive and Fe dispersive data show a clear peak at the Co_2MnGe resonant field $H_{\mathrm{res}} = 204\,\mathrm{Oe}$, while the Fe absorptive signal shows a peak at the thickness dependent $Ni_{81}Fe_{19}$ resonant fields of $H_{\mathrm{res}} = 303\,\mathrm{Oe}$ and 258 Oe, respectively.

The advantage of XMCD is the ability to separate out and observe the response of the $Ni_{81}Fe_{19}$ sink layer at the Co_2MnGe source layer resonant field. At the Co_2MnGe resonance the absorptive part of the Co_2MnGe response is unipolar while, at the same field, the real part of the $Ni_{81}Fe_{19}$ response is once again observed to be bipolar. This behaviour is reversed for the dispersive part of the Co_2MnGe response. As previously mentioned, this is a distinct signature of spin pumping driving STT, rather than the effect of dipolar or exchange coupling.[113] For the thicker $t_{\mathrm{NiFe}} = 3\,\mathrm{nm}$ and 5 nm films the resonances overlap. Unlike VNA-FMR, the nature of spin pumping can still be detected as a distortion in the lineshape of each layer's response. This can be seen for example in Figure 6.15(d), the sample with a 5.0 nm sink layer. Here, the Co_2MnGe lineshape shows a difference in height and shape of the lobes in the dispersive component and a difference in gradient between the low and high field sloping regions of the absorptive component.

While XFMR alone provides relatively compelling evidence for spin pumping driven by STT, it has further been possible to combine these experimental results

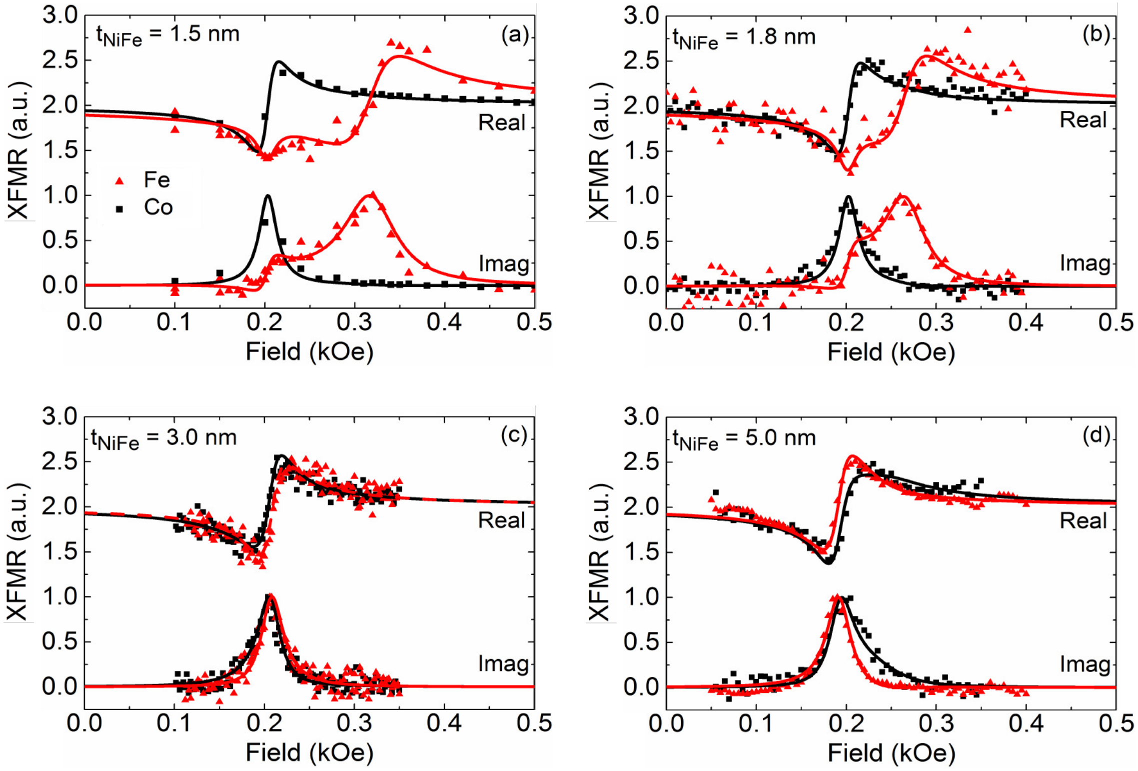

Figure 6.15: The real and imaginary components of element-specific XFMR field scans measured at 4 GHz for spin valves with varying sink layer thickness $t_{\mathrm{NiFe}} = 1.5\,\mathrm{nm},\ 1.8\,\mathrm{nm},\ 3.0\,\mathrm{nm}$ and $5.0\,\mathrm{nm}$. The solid lines are fits based on the macrospin modelling code.

with theoretical modelling. The results of this modelling process are shown as solid lines in Figure 6.15. While the theory of this model is not the subject of this thesis, it is described briefly below for completeness.

6.3.3 Macrospin model

The distorted lineshape observed in XFMR measurements is predicted and described well by numerical modelling, as described by Durrant.[121]

Dynamic behaviour was modelled using coupled Landau-Lifshitz-Gilbert (LLG) equations with additional terms to describe spin pumping between the spin valve layers.[100] The response of the i^{th} layer including interactions with the j^{th} layer was modelled as

$$\frac{\partial \boldsymbol{m}_i}{\partial t} = -|\gamma| \boldsymbol{m}_i \times \left(\boldsymbol{H}^i_{\mathrm{Eff.}} + \beta_i \boldsymbol{M}_j - \frac{\alpha_i^{(0)} + \alpha'_{ii}}{|\gamma_i|} \frac{\partial \boldsymbol{m}_i}{\partial t} \right) - \alpha'_{ij} \boldsymbol{m}_j \times \frac{\partial \boldsymbol{m}_j}{\partial t} \tag{6.2}$$

Table 6.1: Values of $\mathrm{Re}\left(g^{\uparrow\downarrow}\right)$ extracted from fitting a macrospin model to the experimental XFMR data. $*$: Estimation of the uncertainty for $t_{\mathrm{NiFe}} = 3.0\,\mathrm{nm}$ was hampered by degeneracy in the fitting caused by the near identical resonant fields for the source and sink layers.

t_{NiFe} (nm)	$\mathrm{Re}\left(g^{\uparrow\downarrow}\right)$ ($1 \times 10^{15}\,\mathrm{cm}^{-2}$)
1.5	2.52 ± 0.25
1.8	2.22 ± 0.22
3.0	$2.65\ *$
5.0	7.73 ± 2.40

where $\boldsymbol{m}_i$ and $\boldsymbol{m}_j$ are unit vectors parallel to the magnetisations of the i^{th} and j^{th} layers. The four torque terms correspond, from left to right, to: the local effective field (including the applied bias field, crystalline anisotropy and shape anisotropy); dipolar or indirect exchange interaction between the layers; the effective Gilbert type damping (including intrinsic spin-orbit effects, two magnon scattering, and spin pumping with layer i as the source); and spin pumping from layer j to layer i.

XFMR data were then fitted by means of a recursive least squares regression algorithm, with the results shown as solid lines in Figure 6.15 on page 175. The fitted parameters then yield $\mathrm{Re}\left(g^{\uparrow\downarrow}\right)$ through the relationship[122]

$$\alpha'_{ij} = \frac{g_i \mu_B \,\mathrm{Re}\left(g^{\uparrow\downarrow}\right)}{8\pi M_i t_i}\,. \tag{6.3}$$

The extracted values of $\mathrm{Re}\left(g^{\uparrow\downarrow}\right)$ are shown in Table 6.1.

$\mathrm{Re}\left(g^{\uparrow\downarrow}\right)$ is a measure of the efficiency of spin pumping, and is related to the number of conducting channels per spin.[123] Kardasz et al. provide an approximation[122]

$$\mathrm{Re}\left(g^{\uparrow\downarrow}\right) \approx 1.2 n^{\frac{2}{3}} \tag{6.4}$$

where n is the number density of electrons per spin in the normal metal layer. In the case of silver, this gives $\mathrm{Re}\left(g^{\uparrow\downarrow}\right) \approx 1.8 \times 10^{15}\,\mathrm{cm}^{-2}$. While the values in Table 6.1 are not unexpectedly far from this estimate for $t_{\mathrm{NiFe}} =$1.5 nm, 1.8 nm and 3.0 nm, the significant increase for the 5.0 nm sink layer is unexpected, particularly in light of the work of Ghosh et al.[108]

6.4 Conclusions

Spin pumping and STT have been studied in spin valve structures comprising Co_2MnGe / Ag / $Ni_{81}Fe_{19}$ wherein the thickness of the $Ni_{81}Fe_{19}$ sink layer varied between 0 nm and 5 nm.

VNA-FMR has been used to measure the damping parameter of the Co_2MnGe source layer, and absorption of the transverse spin current in the $Ni_{81}Fe_{19}$ sink layer has been inferred from this. Whereas previous studies have shown a power-law decay in spin current absorption with increasing sink layer thickness,[108] the results presented herein show little variation in the absorption of spin current for sink layer thicknesses in the range 0 nm to 1.8 nm. This behaviour is likely the result of additional spin scattering caused by the rest of the stack structure, combined with structural disorder causing a superparamagnetic state in sink layers of thicknesses ≤ 0.6 nm.

Phase-resolved XFMR has been used to make element-specific direct measurements of the time-dependent spin state in both the source and sink layers independently. These measurements revealed a bipolar feature in the absorptive part of the sink layer response when the source layer was driven at resonance—a clear sign of spin pumping due to STT, and thus confirming STT as the mechanism of spin pumping in these spin valve structures. These XFMR measurements are also reproduced well by a macrospin computational model, facilitating extraction of the real part of the spin mixing conductance, $\mathrm{Re}\left(g^{\uparrow\downarrow}\right)$, from the x-ray data. An increase in $\mathrm{Re}\left(g^{\uparrow\downarrow}\right)$ coincides with a reduction in $\mathit{\Delta} H\left(0\right)$ for the sample with the thickest (5 nm) sink layer. This lends further support to the belief that thinner sink layers suffer from structural disorder, whereas the thickest layers have increased interface quality. However, this combined XFMR and modelling approach reaches a limit when the resonant fields of the source and sink layers coincide, leading to degeneracy in the mathematical model.

In conclusion, it has been shown that the expected[108] power-law decay in spin current absorption with increasing sink layer thickness is not consistently observed. Instead, little variation in the absorption of spin current for sink layer thicknesses in the range 0 nm to 1.8 nm is seen. This further suggests measurement of the source layer linewidth does not always provide the complete picture of spin mixing conductance within spin valves. It is necessary to consider spin current absorption in the rest of the sample stack structure, including capping and buffer layers, to fully determine the spin mixing conductance. It has further been shown that XFMR can be used to extract $\mathrm{Re}\left(g^{\uparrow\downarrow}\right)$ from the STT exerted on the sink layer, and that the value of $\mathrm{Re}\left(g^{\uparrow\downarrow}\right)$ depends strongly on the thickness-dependent structural quality of the layers within the stack.

CHAPTER 7

Time-resolved x-ray spectroscopy of thin film yttrium iron garnet

7.1 Introduction

As mentioned in Chapter 6, spintronic phenomena such as GMR are commonly used in magnetic sensor devices, such as the read heads of hard disk drives. The use of spintronics in the storage medium, however, remains an area of intense active research. For example, 'racetrack' memory based on the controlled movement of domain walls by STT has the potential to replace both hard disk drives and semiconductor logic devices.[124,125]

In order to fully investigate and understand spintronic phenomena, it is necessary to obtain phase-sensitive information about the magnetisation dynamics for each material in a given stack structure or device. XFMR, using XMCD as a magnetic contrast mechanism, provides just such element-specific information. XFMR has previously yielded direct evidence of spin pumping of angular momentum in metallic spin valves through the bipolar phase signature of the sink layer,[113] and optical and acoustic resonance modes in strongly coupled metallic ferromagnet systems.[126] However, the majority of research in this area has focused on metallic ferromagnetic materials, with few studies of ferrimagnetic oxides such as YIG.

YIG has the narrowest FMR linewidth of any known material and is therefore favoured for the fabrication of ferrite devices and for research in the areas of spintronics and magnonics.[127] The generation of spin currents by spin pumping using magnetic resonance[128] and with a temperature gradient in YIG[129,130] have both previously been reported. Ferrimagnetic oxides such as YIG contain multiple magnetic sublattices with super exchange interactions promoting antiferromagnetic spin alignment. Soft x-ray spectroscopy technqiues are able to resolve the magnetic moments associated with distinct sublattices due to the small binding energy shifts between these sublattices. Furthermore, site-specific XFMR can detect the relative phase of precession at individual sublattice sites with picosecond resolution.[131]

Earlier XFMR studies of YIG single crystals have revealed multiplet features in the absorption spectrum induced by the resonant absorption of microwaves,[132] as well as microwave-induced spectral changes when measuring with linearly polarised x-rays. These two observations suggest that, for non-metallic systems, XFMR cannot simply be interpreted in the classical sense, i.e. as a measurement of the projection of the precessing component of the magnetisation. It has further been suggested that the simultaneous resonant absorption of both microwave and x-ray photons may be responsible for these observations.[132] These measurements were made on 7 µm thick single crystal YIG, which necessitated detection of x-ray abosorption by fluorescence—a technique known to be hampered by strong saturated self absorption effects. Despite this disadvantage, there are very few studies of YIG by XMCD which do not use fluorescence detection. However, in recent years the fabrication of thin film YIG of sufficient quality to produce viable structures and devices has become much easier. With the availability of films on the order of tens of nanometres in thickness, it has become possible to measure x-ray absorption in transmission, reopening the possibility of applying quantitative soft x-ray techniques such as time-resolved XFMR to YIG.

In this chapter, the magnetisation dynamics in a YIG / Cu / Co trilayer have been investigated by VNA-FMR and both static and dynamic XMCD techniques. This allows for a comparison of XFMR in metallic and non-metallic systems within the same sample, and provides valuable information regarding the behaviour of a ferrimagnetic oxide rather than the more usual metallic ferromagnets previously studied by others. The use of a transmission geometry has avoided artefacts typically associated with fluorescence detection of x-ray absorption used in prior studies, and the absence of any newly-introduced measurement artefacts due to saturation effects has been demonstrated. Static and dynamic XMCD spectra of Co are found to share identical lineshapes, as expected for a metallic ferromagnet. The static XMCD lineshape for Fe in the YIG layer is also as expected, and is well reproduced by multiplet calculations of sublattice spectra. However, there are differences between the static and dynamic Fe lineshapes, similar to those seen by Boero et al.[132] Despite a number of experimental considerations and analytical techniques to identify the source of this discrepancy, it has not been possible to determine its root cause. While this difference in lineshapes alludes to a potential phase delay between Fe on different lattice sites, further research is first needed to identify the origin of the difference in lineshapes before firm conclusions can be drawn.

7.2 Experimental Setup

Samples were preparaed in the laboratory of Prof. Bryan Hickey at the University of Leeds. A YIG $(60\,\mathrm{nm})$ / Cu $(5\,\mathrm{nm})$ / Co $(6\,\mathrm{nm})$ trilayer was grown on a (111) gadolinium gallium garnet ($Gd_3Ga_5O_{12}$) (GGG) substrate by room temperature sputtering, with a $3\,\mathrm{nm}$ MgO cap left to oxidise naturally in air.[133] The $5\,\mathrm{nm}$ Cu spacer layer is sufficient to isolate the YIG and Co layers from direct exchange coupling. YIG was deposited by RF sputtering followed by an annealing process in atmosphere and a chemical ‘piranha’ etch to improve the surface quality and remove dead layers created during the annealing step. The metallic layers were deposited by DC sputtering.

The elementary cell of YIG, shown in Figure 7.1(a) on the facing page, is large, containing 20 Fe^{3+} ions distributed over 12 tetrahedral symmetry (T_d) and 8 octahedral symmetry (O_h) sites. Y ions are located on dodecahedral symmetry (I_h) sites. The strongest magnetic interaction is the O^{2-}-mediated T_d–O_h superexchange which results in antiparallel moments on the nearest neighbour sites. Both T_d and O_h Fe^{3+} ions have a magnetic moment of $5\,\mu_\mathrm{B}$, with the $3:2$ occupancy of antiparallel sites resulting in a net moment of $5\,\mu_\mathrm{B}$ parallel with the T_d moments. The predicted saturation magnetisation at 0 K is ≈ 250 mT, close to the measured low temperature (4.2 K) value of 246.3 mT.[134] Room temperature magnetisation values are reported to be ≈ 180 mT.[134]

Magnetisation dynamics were initially characterised at the University of Exeter by VNA-FMR with the sample placed in contact with a CPW. Static XMCD and dynamic XFMR measurements were made on beamlines I06 and I10 at DLS using the POMS vector magnet end station of the Magnetic Spectroscopy Group, and on beamline 4.0.2 at the Advanced Light Source (ALS) using the vector magnet magnetometer (VMM) end station. Figures 7.1(b) and 7.1(c) on the next page show schematics of the experimental and measurement geometries. X-ray absorption was detected in transmission via the XEOL generated by x-ray absorption in the GGG substrate. Microwave excitation was again provided by mounting the sample in contact with a CPW with a 1 mm wide central signal line. A 500 µm diameter hole in the signal line, countersunk on the CPW substrate, afforded unimpeded x-ray access to the sample surface. Tests using a VNA showed little change in microwave absorption after the addition of the hole, particularly at the frequencies studied by XFMR. Both DLS and ALS share a common storage ring master oscillator frequency of ≈ 500 MHz, allowing synchronisation between x-ray pulses and magnetisation precession at both lightsources to be ensured by generating the microwave driving signal as the 8th harmonic of the storage ring master oscillator

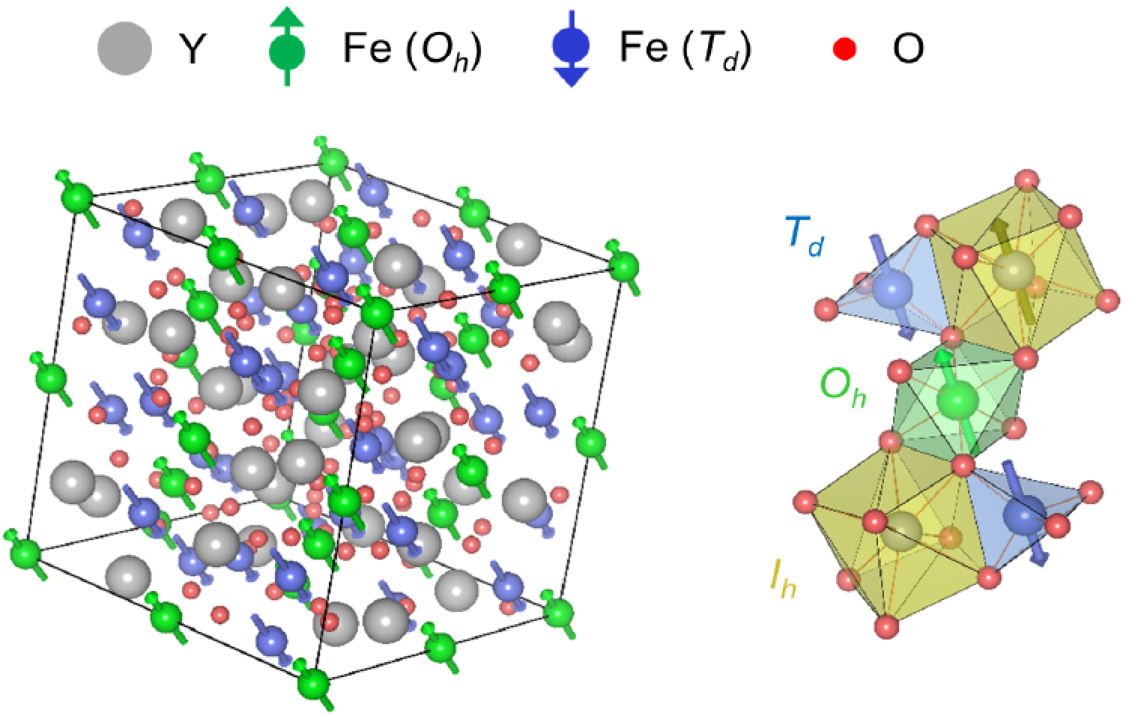

(a) The YIG unit cell

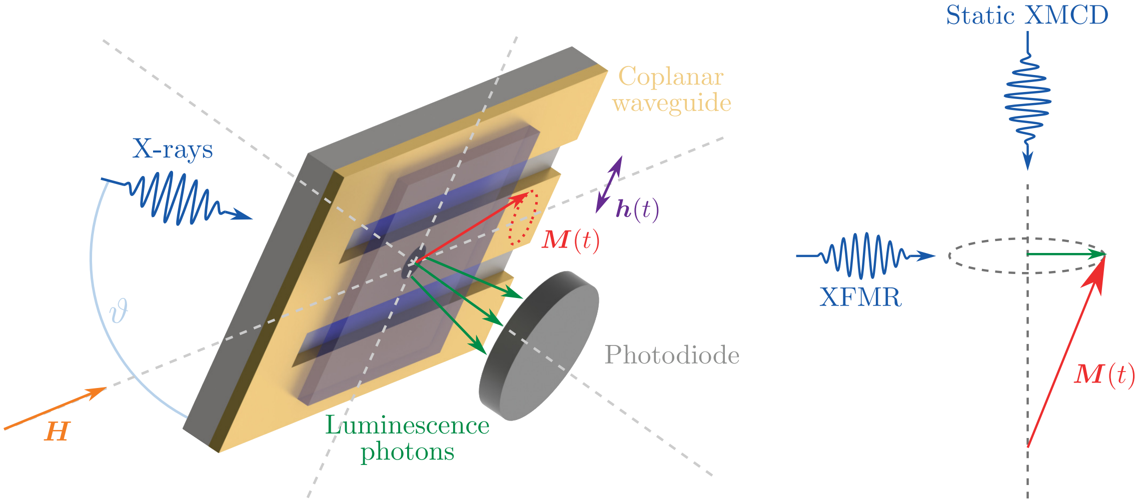

(b) Experimental geometry

(c) X-ray orientations

Figure 7.1: (a) The YIG unit cell, with arrows indicating spins aligned in the (111) plane. Coordination polyhedra for T_d, O_h and I_h cation sites are shown to the right. (b) Schematic of the time-resolved XMCD measurement geometry. The sample was mounted face-down on a coplanar waveguide with x-ray access provided by a countersunk hole through the rear of the PCB and central conducting track. X-ray transmission was detected *via* luminescence photons generated by x-rays absorbed within the sample's GGG substrate. (c) The orientation of incident x-rays for static and time-resolved XMCD measurements.

signal. This 4 GHz driving signal was then amplified to 24 dBm, measured before delivery to the CPW. The relative phase of the microwaves and x-rays was varied using a mechanical delay line in the microwave path with a resolution of 1 ps. Dynamic measurements were made using alternating current (AC)-detection with a lock-in amplifier while modulating the phase of the driving signal through 180° for maximum magnetic contrast. For static measurements a bias field was applied parallel with the x-ray propagation direction, while for dynamic measurements the saturating bias field was applied orthogonal to the incoming x-rays so that XMCD was sensitive to the precessional magnetisation components.

In the static geometry the measurements were corrected for transmission effects by taking the logarithm of the XAS. XFMR measurements were then corrected by normalising to the corresponding static XAS. In dynamic XFMR measurements, the transmitted x-ray intensity I through a sample of thickness L is a function of the phase of the magnetisation precession ϕ, and depends on the relative alignment between the magnetisation vector and the x-ray helicity:

$$I\left(\phi\right) = I_0 \exp\left(-\left(A_0 + A_1 \hat{\boldsymbol{m}}\left(\phi\right) \cdot \hat{\boldsymbol{k}}\right) L\right) \tag{7.1}$$

where A_0 and A_1 are the non-magnetic and magnetic absorption coefficients, respectively, $\hat{\boldsymbol{m}}\left(\phi\right)$ is the unit vector of the precessing magnetisation for a given phase ϕ and $\hat{\boldsymbol{k}}$ is the x-ray helicity unit vector. The driving signal is modulated through 180° such that the signal recorded at the LIA is given by:

$$I\left(\phi\right) - I\left(\phi - 180^{\circ}\right) = -2 I_0 \exp\left(-A_0 L\right) \sinh\left(A_1 \hat{\boldsymbol{m}}\left(\phi\right) \cdot \hat{\boldsymbol{k}} L\right) \tag{7.2}$$

which can be simplified in the case of small angles of precession to:

$$I\left(\phi\right) - I\left(\phi - 180^{\circ}\right) \approx -2 I_0 \exp\left(-A_0 L\right) \left(A_1 \hat{\boldsymbol{m}}\left(\phi\right) \cdot \hat{\boldsymbol{k}} L\right) . \tag{7.3}$$

From this it can be seen that the magnetic component of the signal is obtained by dividing by $\exp\left(-A_0 L\right)$, which is the static absorption obtained from XAS.

7.3 Results and Discussion

7.3.1 VNA-FMR

Figure 7.2 on the following page shows VNA-FMR recorded as a function of both driving frequency and static bias field. The bias field was applied parallel with the Co hard axis. The grey scale contrast represents the amplitude of the real and imaginary components of the S_{21} parameter (i.e. transmitted microwave power) in the left and right panels, respecively. Two curves are visible, with the high and low frequency branches corresponding to the Co and YIG layers, respectively. Measurements made at a fixed frequency of 4.5 GHz are presented in Figure 7.3 on the next page. The black and red curves were measured with the sample rotated through 90° in the bias field, i.e. with the bias field parallel to the Co hard and easy axis, respectively. The YIG resonance shows two clear peaks. With the bias field applied along the hard axis the $\mathrm{Im}\left(S_{21}\right)$ peaks are centred at 93.5 mT and 94.7 mT and have a Lorentzian FWHM of 1.4 mT and 1.2 mT, respectively. For the easy axis case the peak separation is increased, with peaks at 92.6 mT and 95.6 mT having widths of 2.6 mT and 1.5 mT. The linewidth values are quite large compared with single crystal bulk YIG. Analysis of all four S_{xy} parameters suggests that the origin of this broadening may be magnetic inhomogeneity. Parameters S_{12} and S_{21} are effectively measurements of the microwave power transmitted through the CPW and so are sensitive to the full length of the sample in contact with the CPW. Parameters S_{11} and S_{22} are reflection measurements and as such may be more strongly sensitive to the edge regions. Parameters S_{12} and S_{21} show identical signals, while S_{11} and S_{22} show significantly different curves with the peaks shifted in field compared to the S_{12} and S_{21} parameters (Figure 7.4 on page 187). The implication is that the magnetic parameters are not uniform. The fact that the peaks become more widely spaced when the sample is rotated through 90° suggests an anisotropic inhomogeneity.

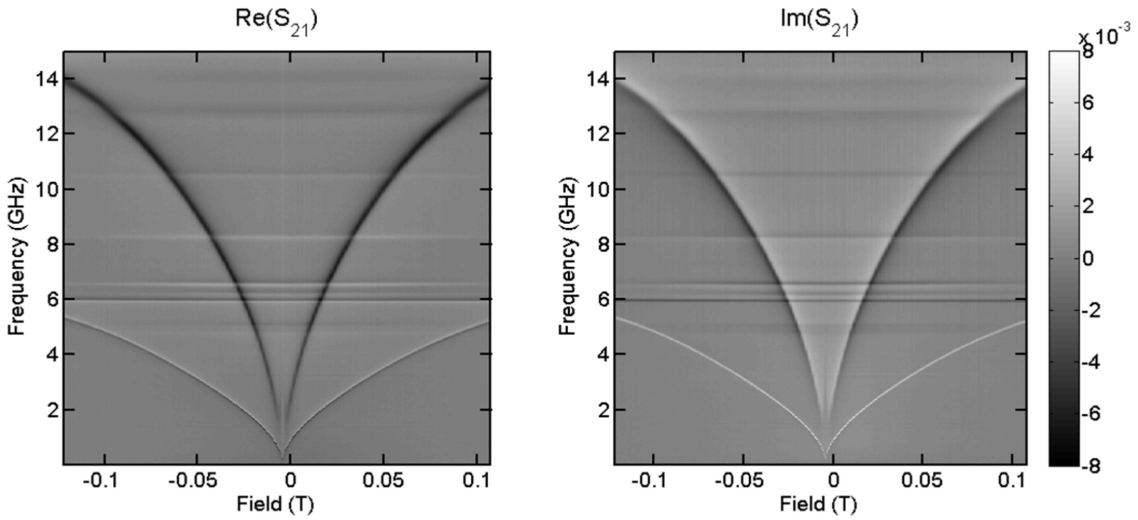

Figure 7.2: VNA-FMR of YIG/Cu/Co, showing the real (left) and imaginary (right) components of S_{21} as a function of both driving frequency and applied bias field. The bias field was applied parallel with the Co hard axis.

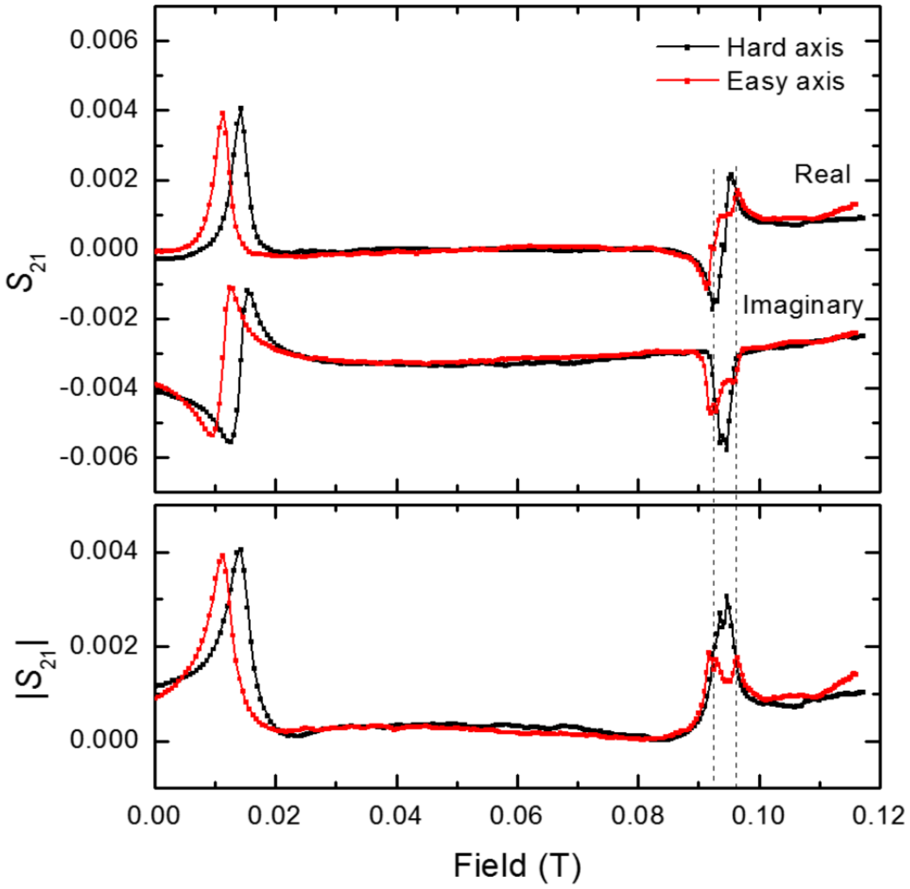

Figure 7.3: $\mathrm{Re}\,(S_{21})$, $\mathrm{Im}\,(S_{21})$ and $|S_{21}|$ measured at a fixed frequency of 4.5 GHz. Black and red curves are measurements taken with the sample rotated 90°, i.e. with the field applied parallel to the Co hard and easy axes, respectively.

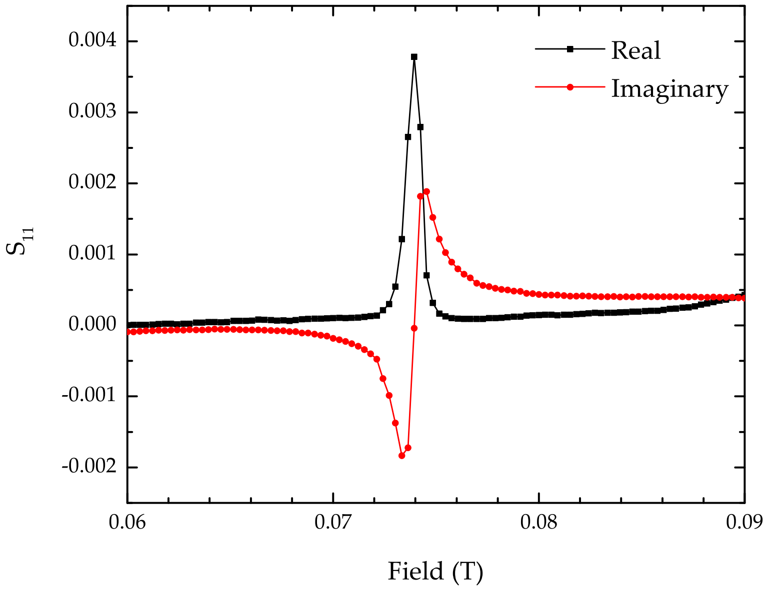

Figure 7.4: $\mathrm{Re}\,(S_{11})$ and $\mathrm{Im}\,(S_{11})$. The resonant frequency is seen to be approximately 0.074 T, significantly different to the approximately 0.09 T resonant field observed in the S_{21} parameter.

7.3.2 Static XAS and XMCD

Static (i.e. without microwave excitation) XAS and XMCD spectra of Co and Fe are shown in Figure 7.5 on the next page.

Transmission x-ray absorption measurements such as these can be subject to artefacts if the incident x-rays are sufficiently absorbed by the sample that the intensity of x-rays reaching the photodiode is below the photodiode's detection threshold. Saturated absorption can also potentially lead to a distorted spectral line shape. To confirm the absence of these artefacts, XAS and XMCD spectra of Fe were recorded with varied incidence angle. This varied the projected sample thickness along the beam direction, and therefore the amount of material the x-ray beam had to pass through before reaching the photodiode. In Figure 7.6 on page 189 the recorded photodiode current, I_d, is shown in panel (a). Over the range of incidence angles used the projected YIG thickness increased from 60 nm (90°) to 105 nm (35°) and the minimum photodiode current fell from 330 pA

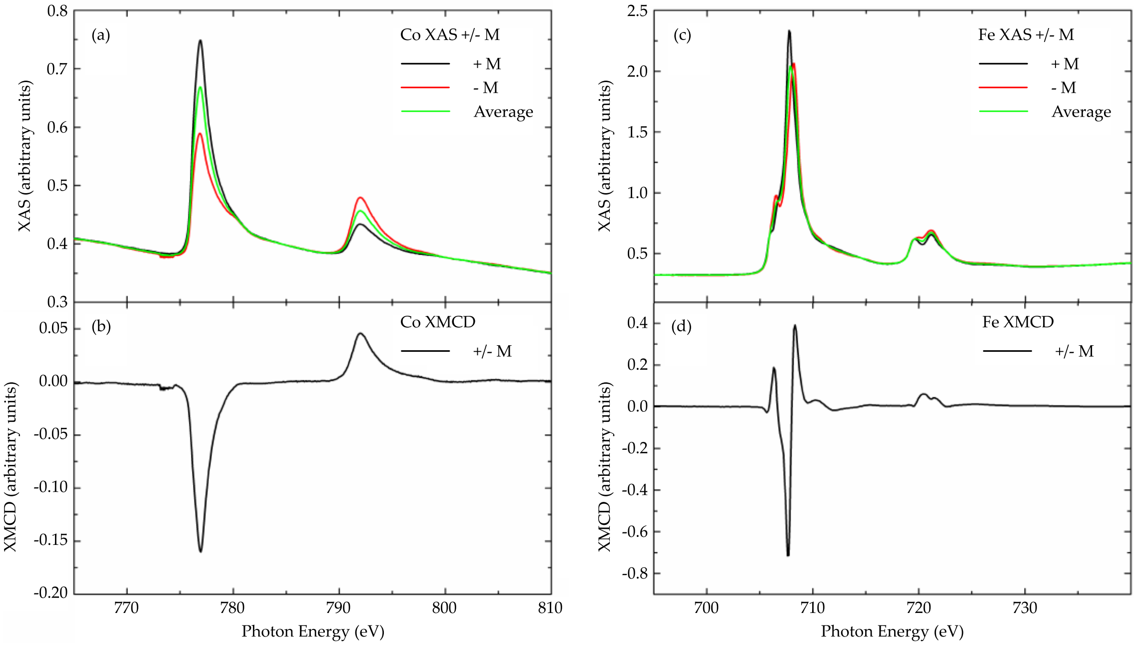

Figure 7.5: Static XAS and XMCD spectra measured for Co and Fe in a YIG/Cu/Co trilayer. (a) Co XAS and (b) Co XMCD. (c) Fe XAS and (d) Fe XMCD.

to 35 pA. Even at the lowest recorded photodiode current, the L_3 peak retains its shape rather than showing evidence of ‘clipping’ at the photodiode’s dark current. Panel (b) shows the absorption calculated as $-\ln\left(I_d/I_0\right)$, according to the Beer-Lambert law where I_0 is the incident x-ray intensity measured upstream. The shape of the XAS is invariant to the beam incidence angle, demonstrating that neither saturation artefacts nor artefacts associated with dropping below the detection threshold were present. XMCD spectra in panel (c) were calculated as the difference between two XAS spectra recorded with a $\pm$300 mT static field applied parallel with the incoming x-rays. For comparison all XAS (XMCD) spectra have been normalised to 1 (-1) at the L_3 peak. With stronger absorption at the Fe L_3 edge than the L_2 edge, saturated absorption or reaching the low detection limit would be apparent as a change in the L_3:L_2 peak ratio as a function of incidence angle. Again, the shape of the spectra remain constant with varying incidence angle, providing further evidence for the lack of artefacts. Unless stated otherwise, all future measurements were recorded with a grazing incidence angle of 45°.

Calculated Fe XMCD spectra have been presented by Coker et al. who used

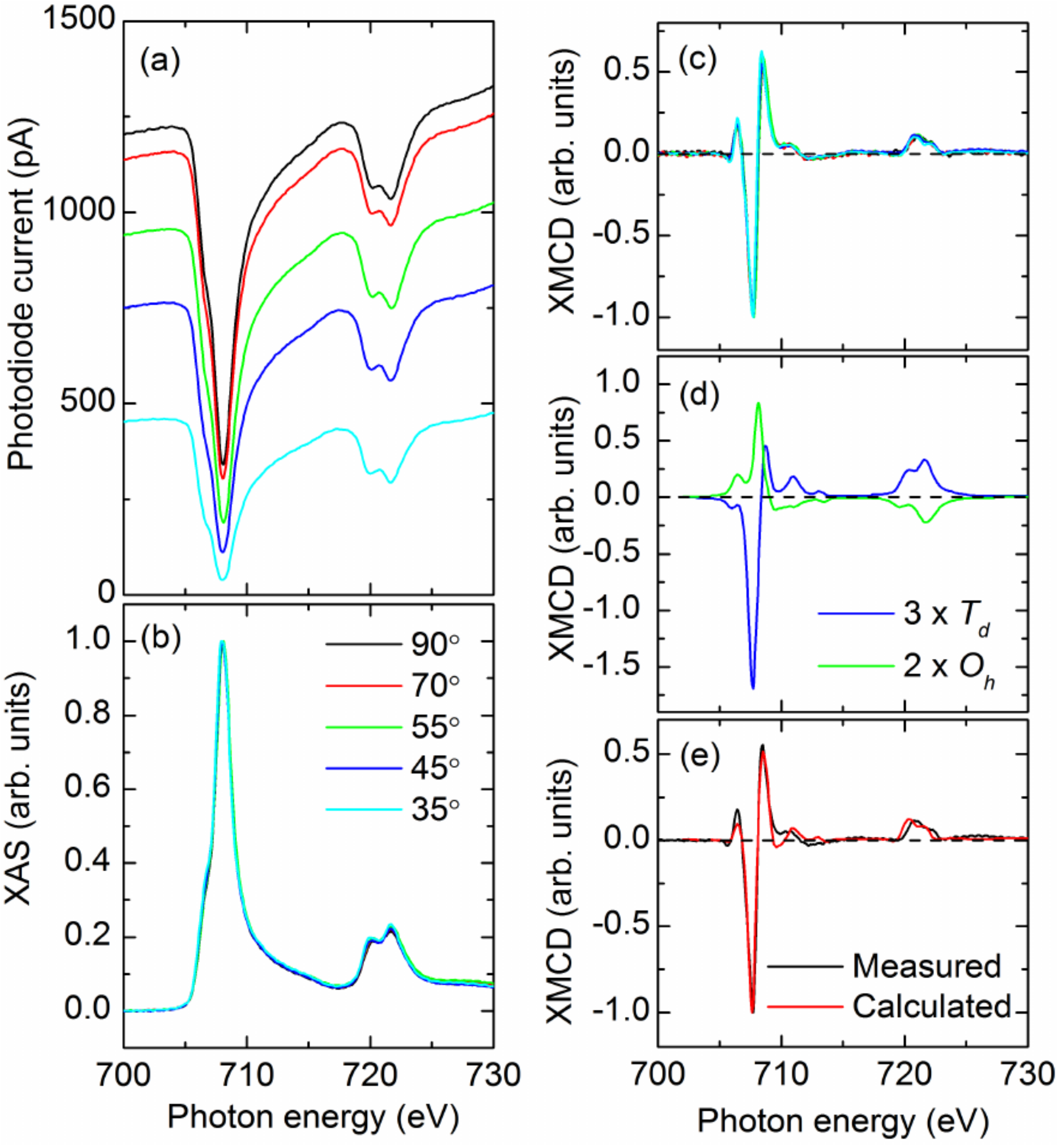

Figure 7.6: Static x-ray spectroscopy. (a) Substrate luminescence, generated by x-ray absorption, as a function of incident photon energy measured with varied grazing incidence angles. (b) XAS calculated as $-\ln$ of the data in (a), normalised to 1 at the L_3 peak. (c) XMCD measured as the difference of XAS spectra with $\pm 300\,\mathrm{mT}$ applied parallel with the incident x-rays, normalised to -1 at the central L_3 peak. Panel (d) shows calculated XMCD spectra for Fe^{3+} T_d and O_h sites, weighted in a 3:2 ratio as expected for YIG. Panel (e) shows the sum of the calculated spectra from (d) (red) against the measured spectrum at an incident angle of $45°$.

XMCD to study the synthesis by bacteria of magnetic iron oxide nanoparticles including magnetite, Fe_3O_4, which contains Fe^{3+} ions on similar T_d and O_h sites to YIG.[135] Figure 7.6(d) shows calculated XMCD spectra weighted in the $3:2$ $T_d:O_h$ ratio expected for YIG. Good agreement between calculated and measured XMCD spectra is shown in panel (e). The lowest energy L_3 peak shows a slight discrepancy, with the measured peak height being greater than the calculated one. This may indicate the presence of a fraction of Fe^{2+} from small amounts of other structural phases. A slight shoulder on the lower energy side of the negative L_3 peak is also not reproduced in the calculated spectra. It is possible that this is due to point defects caused by Fe atoms being located on Y sites.

7.3.3 XFMR spectroscopy

Time-resolved XMCD spectra were recorded by scanning the incident photon energy while the magnetic film was driven at resonance. Figure 7.7 on the next page shows a comparison of static and time-resolved XMCD spectra for Co and Fe in YIG with the driving microwave phase set to give the largest dynamic signal. The spectra have been normalised to -1 at the Co L_3 peak and the central Fe L_3 peak. Static and dynamic spectra of Co show identical line shapes. Indeed, it is noted that the time-resolved XMCD measurement is free of any background noise, and could therefore provide a precise measurement of the spin-orbit moment ratio by comparison with the XMCD sum rules discussed in Section 3.3.3 on page 103.

The static and dynamic spectra for Fe in YIG, however, initially show marked differences from one another. The central negative L_3 peak, which is strongly sensitive to the T_d site moments, is proportionally weaker in the dynamic spectrum (as shown by the higher positive peaks either side). Comparison of the time-resolved XMCD spectrum with calculated spectra suggests a precessing $T_d:O_h$ moment ratio closer to $1:1$, far from the $3:2$ ratio observed in static measurements. The shoulder on the lower energy side of the central L_3 peak of both the static

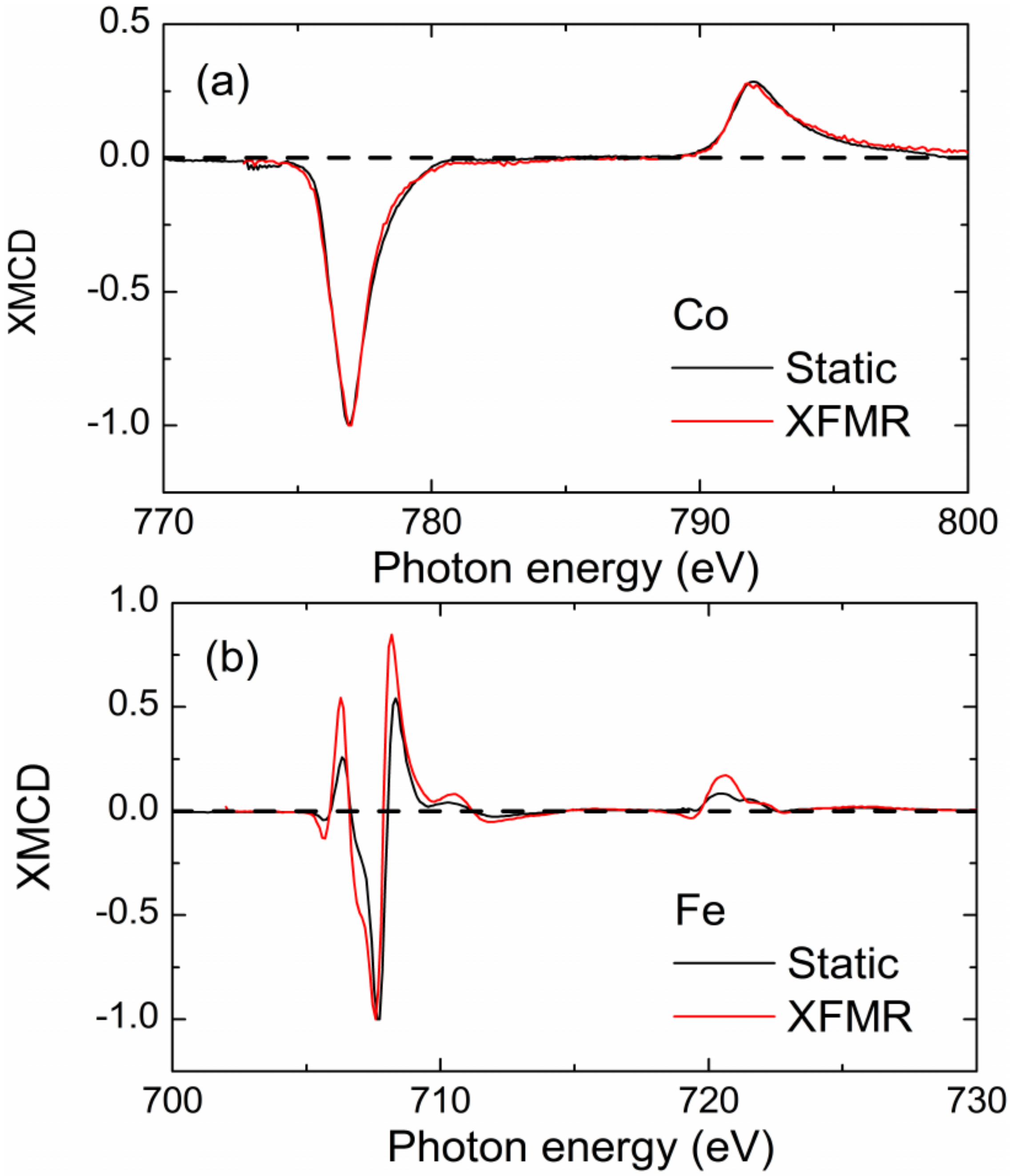

Figure 7.7: Static (black) and FMR (red) XMCD spectra for (a) Co and (b) Fe in YIG. The driving microwave phase was set to give the largest dynamic signal. While the Co spectra are identical, there are marked differences between the static and dynamic spectra for Fe.

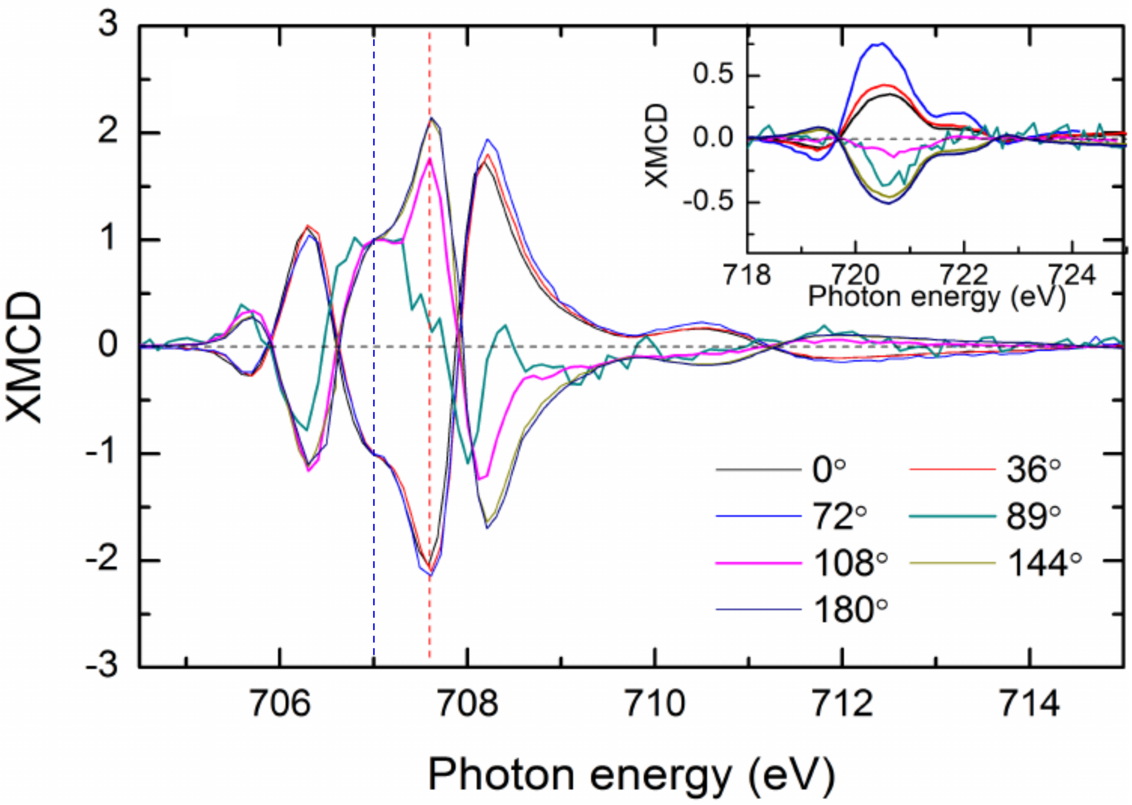

Figure 7.8: Time-resolved XMCD spectra measured at 45° incidence with varied microwave driving phase, normalised to 1 at the 707 eV shoulder (vertical blue dashed line).

and dynamic spectra is also clear here, yet is not so prominent in the calculated spectra.

Time-resolved XMCD spectra recorded at 45° grazing incidence with the phase of the microwave driving signal varied over half a period of precession are shown in Figure 7.8. For comparison of key features all spectra have been normalised to 1 or -1 at a photon energy of 707 eV, at the shoulder in the L_3 peak (vertical blue dashed line). Firstly, it can be seen that the relative intensity of the L_3 and L_2 features changes with driving microwave phase. Spectra measured at phase values of 0°, 36° and 72° show progressively increasing relative peak amplitude at the L_2 edge (inset). The sign of the spectra changes as the phase passes through 90°, as is expected. Secondly, the shape of the XMCD spectrum changes significantly at microwave phase values of 89° (solid teal line) and 108° (solid magenta line). The vertical red dashed line at the energy of the largest L_3 peak

(707.7 eV) highlights that this feature reverses sign at a later phase than other features in the spectrum. The peak is absent at a phase of 89° and is reduced in magnitude at a phase of 108°. From the calculated XMCD spectra, the peak at a photon energy of 707.7 eV is dominated by sensitivity to the T_d site moments, suggesting that the precessing moments at the T_d sites are lagging in phase behind the precessing O_h moments.

Discrepancies between static and dynamic spectra

Ferromagnetic transition metals typically exhibit a dynamic XMCD spectrum which shares the same lineshape as the static spectrum. For example this can be seen in the Co spectrum in Figure 7.7 on page 191. It is therefore important to consider at this juncture the difference in lineshape between the static and dynamic Fe spectra that was observed during the process of acquiring the above data, previously introduced in Figure 7.7. Such differences were observed depending on the precise choice of beam polarisation and measurement geometry. For example, Figure 7.9 on the next page shows how the static and dynamic XMCD lineshape at the Fe L_3 edge could be seen to exhibit significant differences in particular measurement geometries.

The low damping in YIG can result in non-linear dynamics being driven at relatively low microwave powers. To check for this as a potential source of the discrepancy, the microwave source was attenuated to 14 dBm and a dynamic spectrum recorded. The results are shown in Figure 7.10. Although the attenuated driving power reduces the amplitude of the induced dynamics, resulting in a much noisier signal, the line shape remains unchanged. This confirms that dynamics induced at maximum driving power remain in the linear regime, and non-linear effects are therefore not the cause of the observed difference in lineshape. Further sources of error must therefore be considered.

Previously Boero et al. reported a similar difference between static XMCD and dynamic XFMR spectra in a longitudinal geometry detected using fluorescence

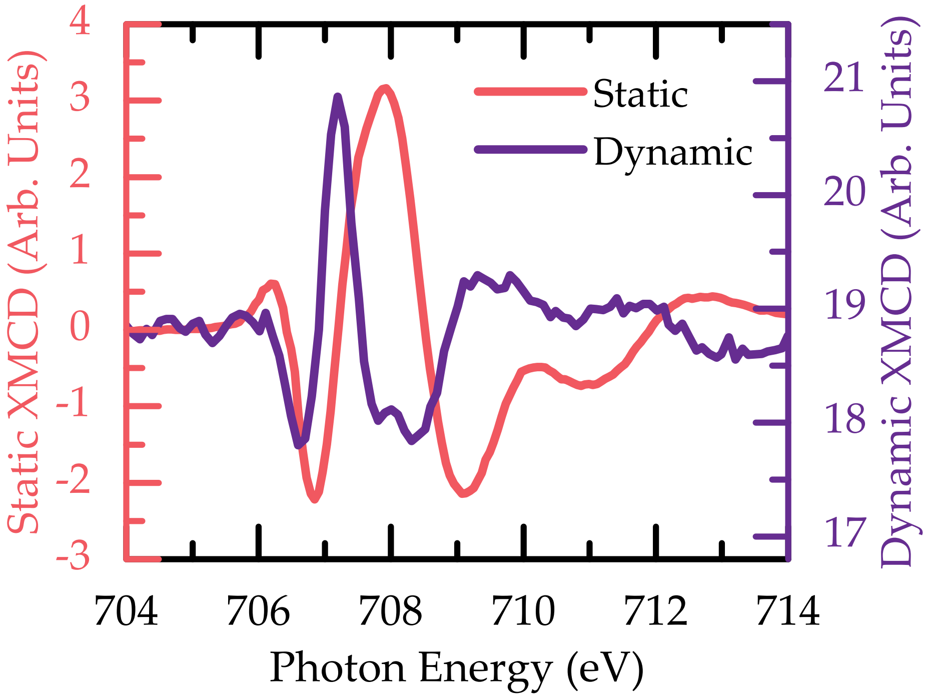

Figure 7.9: The XMCD lineshape at the Fe L_3 edge in YIG is significantly different when measured statically (red) or dynamically under RF excitation (purple) and depends critically upon the bias field and helicity of the light polarisation. In this case, the dynamic spectrum was acquired with positive helicity.

yield. This was attributed to the presence of an XMLD component in the XMCD spectra recorded with a given helicity.[132] They determined that the “true” shape of the dynamic spectrum could be recovered by taking the difference of two dynamic XMCD spectra measured either with antiparallel bias fields or with x-rays of opposite helicities. In Boero’s case, this leads to an XFMR spectrum that agrees entirely with the static spectrum, both in terms of lineshape and amplitude.

Figure 7.11 on page 196 shows the analysis process of Boero et al. applied to the YIG / Cu / Co sample studied throughout this chapter. The static spectrum was acquired using positive helicity x-rays and applied bias fields of $\pm 400\,\mathrm{mT}$. The dynamic spectrum was obtained by taking the difference of dynamic spectra acquired with negative and positive helicity, with the RF power and frequency at $24\,\mathrm{dBm}$ and $4\,\mathrm{GHz}$, respectively.

Application of this analysis technique has brought the locations of the three

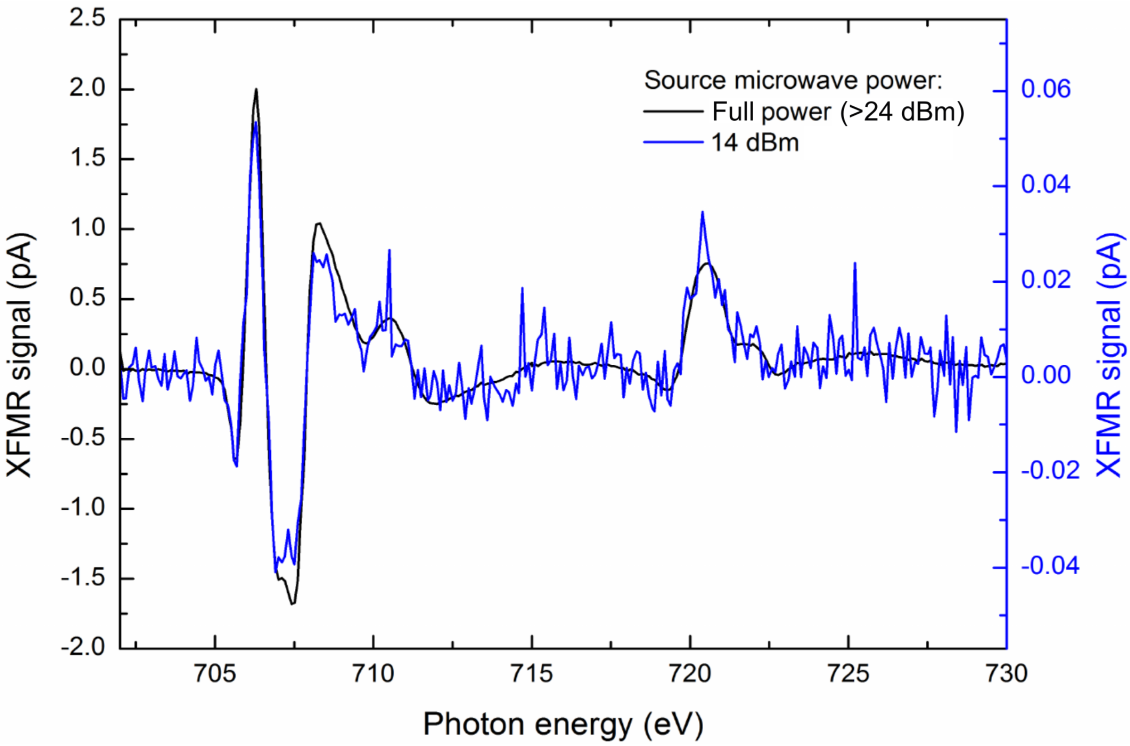

Figure 7.10: Dynamic XMCD spectra of Fe in YIG recorded at full driving microwave power, and at a significantly reduced power of 14 dBm. Although far noisier, the shape of the spectrum remains the same at reduced microwave power.

L_3 peaks into alignment between the static and dynamic spectra in terms of their photon energy (*cf.* Figure 7.9). However, the relative amplitudes of the second and third L_3 peaks remain different for the dynamic and static spectra.

A number of issues prevented the application of this analysis technique across all of the dynamic spectra presented in this chapter. Firstly, the failure to fully correct the original discrepancies, leaving a difference in relative peak amplitudes, suggests that the analysis method of Boero et al. is very likely incomplete or insufficient. As applying this corrective method does not adequately address the discrepancies between dynamic and static spectra, it cannot tell the full story of the observed dynamics. There are a number of potential explanations for this remaining discrepancy. The time-dependent measurements presented in this chapter were carried out in the transverse geometry using XEOL as the detection mechanism. In contrast, the XFMR measurements of Boero et al. were performed using fluroescence detection in the longitudinal geometry, which averages over

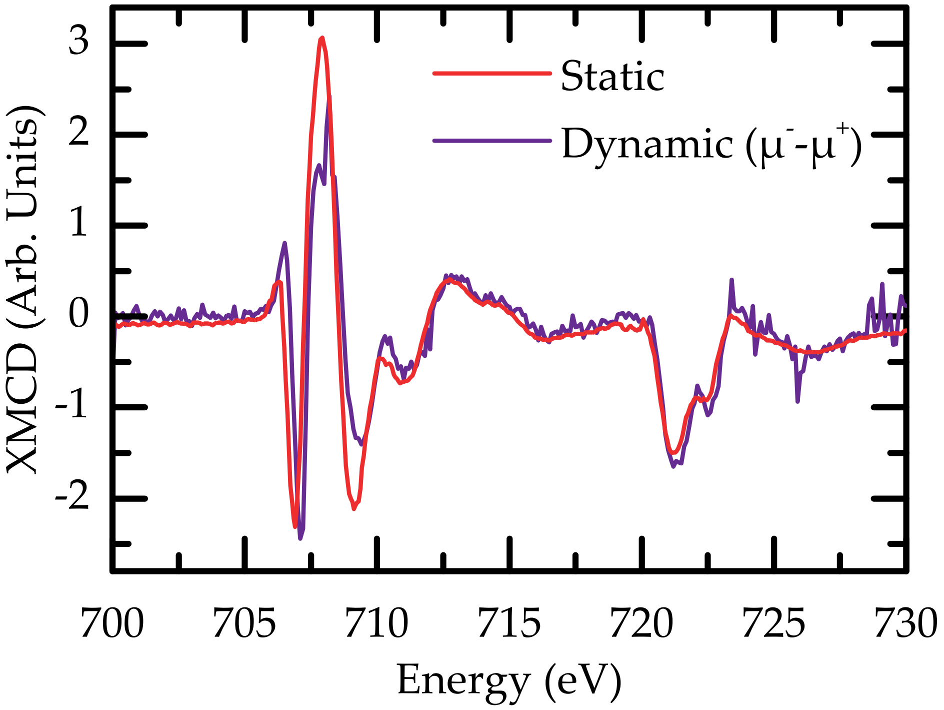

Figure 7.11: The static and dynamic XMCD lineshapes can be brought into closer agreement by subtracting the dynamic spectra acquired with x-rays of opposite helicity. This is reported to give the "true" dynamic lineshape.[132] The relative L_3 peak heights, however, still exhibit significant discrepancies.

time and therefore does not produce a dynamic signal.[132] Further adjustment factors specific to the dynamic transverse geometry may therefore need to be considered to recover the "true" XMCD signal.

Furthermore, the higher RF power used by Boero et al. saturated the precession cone angle, and is likely to have driven significant non-linear dynamics. Figure 7.12 shows the measured dynamic XMCD amplitude at the central Fe L_3 peak as a function of driving RF power. The dynamic XMCD amplitude increases with increasing RF power to a peak at 24 dBm. As power increases beyond 24 dBm the recorded XMCD amplitude decreases, suggesting that precession amplitude is no longer in the linear regime at these higher powers. As Boero et al. used a driving power of 35 dBm, significantly in excess of this turning point, it is likely that the dynamics being driven by Boero et al. were rather different to those being driven in the present case.

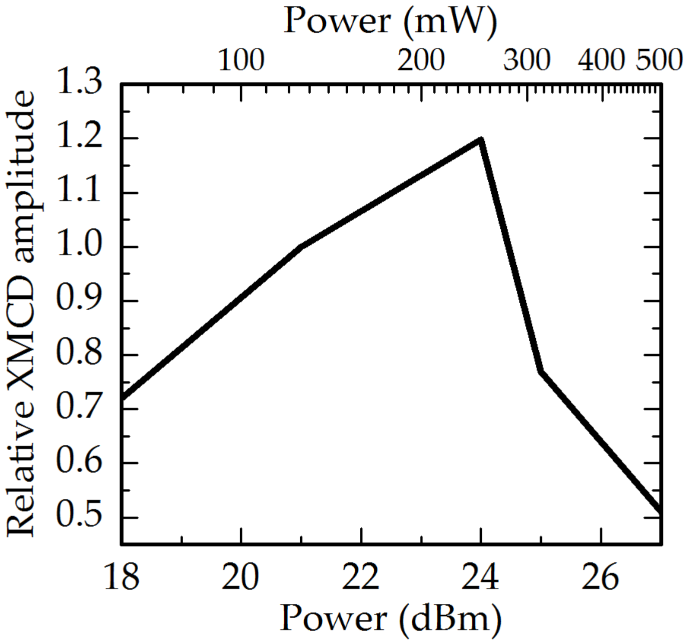

Figure 7.12: Dynamic XMCD amplitude at the central Fe L_3 peak in YIG as a function of driving RF power. Increasing the driving microwave power causes a reduction in measured XMCD intensity, suggesting dynamics have entered a non-linear regime at these higher powers.

Secondly, increased noise was observed when measuring using negatively circularly polarised photons compared to positively circularly polarised x-rays. A comparison of dynamic XMCD spectra recorded with the two helicities can be seen in Figure 7.13 with noise most apparent at e.g. 712 eV and 723 eV to 730 eV). The increased amplitude of intermittent noise when using negatively circularly polarised light, which was also unpredictable in terms of time and duration, hampered the subtraction of one spectrum from the other. The random nature of the noise made it difficult to methodically subtract, coupled with the relatively narrow width of the observed L_3 peaks making them particularly susceptible to apparent changes in amplitude due to noise. The time taken to obtain each spectrum, coupled with gradual beam drift, also precluded averaging large numbers of measurements to remove the noise.

Beam instability when switching between positive and negative helicities also caused concern. Adjusting the x-ray optics of the beamline to switch helicities

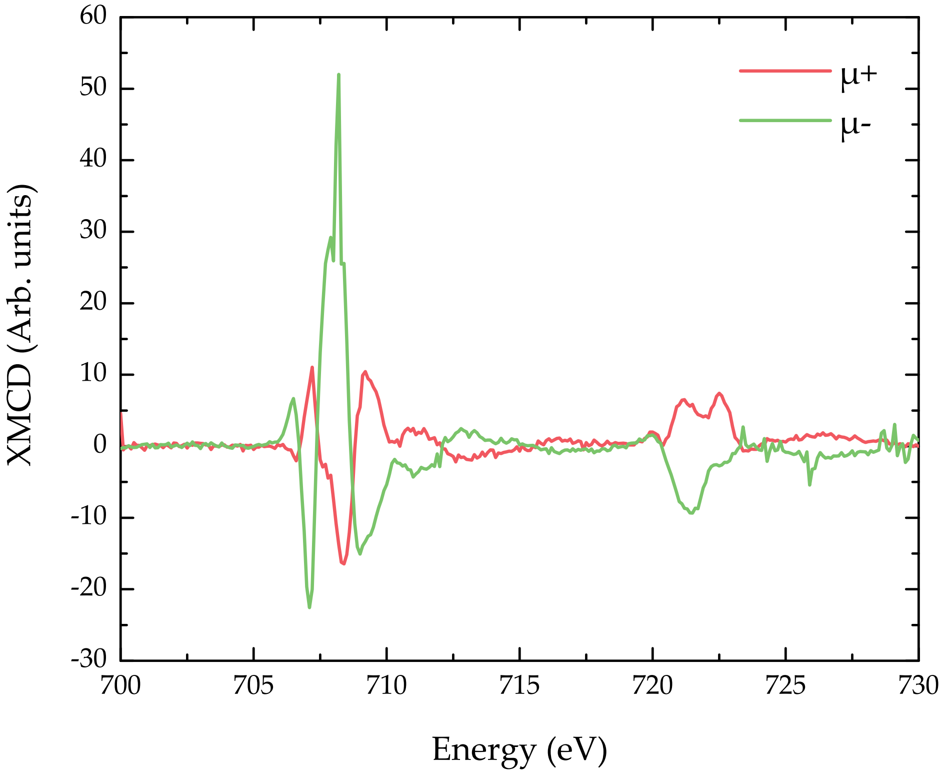

Figure 7.13: Dynamic XMCD measurements recorded with positive (red) and negative (green) circularly polarised x-rays. Significant differences in the lineshape are accompanied by an increase in the amplitude of intermittent noise when using negatively circularly polarised light.

should be able to be carried out without affecting other properties of the beam, such as intensity, size, shape and position. Unfortunately, this was often not the case during our beamtime, meaning that any change in beam polarisation necessitated adjustment of other optics, realignment of the sample, and reconfirming static measurements to maintain consistency between measurement. For each of these reasons, the method of Boero et al. was therefore not applied to the other dynamic spectra presented herein.

There remains, therefore, a potential source of systematic error present in these measurements. It is important to note that this discrepancy exhibits itself in varying manners for different particular combinations of geometry, field direction and photon polarisation. For example, as shown in Figure 7.7 on page 191, maintaining a constant x-ray helicity and reversing the applied magnetic field direction to obtain a dynamic XMCD spectrum can result in differences to the relative L_3 peak heights rather than their positions relative to the static spectrum. While the data presented in Figure 7.8 on page 192 are indeed concerned with the heights of the peaks at the L_3 edge, the conclusions drawn from this figure rely on the relative changes of each individual peak height as a function of delay between the driving RF field and the x-ray pulses (i.e. driving microwave phase). What is important here is therefore not the absolute amplitude of the three peaks, or even their amplitudes relative to one another, but rather each individual peak's changing amplitude and apparent position as a function of microwave delay/phase. The presence of this potential systematic error of course casts doubt over the absolute values obtained from these measurements, however these results do confirm the presence of unusual dynamic behaviour which cannot be adequately corrected for using the XMLD subtraction technique proposed by Boero et al. The later sign reversal of the 707.7 eV peak relative to the other L_3 peaks is suggestive of T_d moments lagging in phase relative to O_h moments, although this cannot be positively confirmed until further research has elucidated an origin for the observed differences between the static and dynamic spectra.

7.3.4 XFMR Field and Delay Scans

XFMR measurements were also performed with the static bias field applied parallel with the harder axis, where the narrowest YIG resonance was observed. Figure 7.14 on page 201 shows XFMR measured with a 4 GHz driving signal at photon energies corresponding with the three main L_3 peaks in the measured static XMCD spectrum: 706.3 eV, 707.7 eV and 708.3 eV. Panels (a) and (b) show respectively the real and imaginary components of the XFMR signal with the bias field swept through the resonant field value. The amplitude was corrected by dividing by the static XAS spectrum. The inset to panel (b) shows the three peaks normalised to 1 for direct comparison of the line shapes, which are found to be identical. These data were obtained by recording the XFMR signal with the driving signal phase shifted by 90°. A fitted single-Lorentzian centred at 76.3 mT has a FWHM of 1.4 mT, however a closer fit is provided by a double Lorentzian function with overlapped peaks at 76.3 mT with FWHM of 1.1 mT and 7.4 mT. The phase shift in panel (a) is slightly misaligned from the peak amplitude at 76.6 mT and is asymmetric. By plotting the two measurements in the complex plane, the real and imaginary signals can be obtained by rotating by a phase angle which produces a unipolar Lorentzian in the imaginary signal. The imaginary signal shows two closely separated peaks at 76.3 mT and 76.7 mT with widths of (0.50 ± 0.01) mT and (0.20 ± 0.02) mT ($\alpha = 2.79 \times 10^{-4}$ and 1.11×10^{-4}, respectively), much closer to values expected for YIG than the values obtained with VNA-FMR. The applied field resolution of 0.2 mT available on the beamlines places a limit on the precision of the measured linewidths. XFMR samples a region of the film with an area equal to that of the x-ray spot, which is $\approx 20 \times 200\,\mu\mathrm{m}^2$, while VNA-FMR is sensitive to the area of the sample in contact with the CPW, $\approx 0.5 \times 8\,\mathrm{mm}^2$. The fact that sampling a smaller region of the sample produces a smaller linewidth provides strong evidence that the broadening is due to sample inhomogeneity.

Figure 7.14(c) shows XFMR measured with a fixed bias field corresponding to the peak amplitude in panel (a) (76.2 mT) while the phase between the 4 GHz driving signal and the x-rays was swept by adding a physical delay to the microwave signal. Fitted sine curves have been used to extract the phase with high precision by restricting the frequency to that of the driving signal. The phase difference measured at the two positive L_3 peaks, 706.3 eV and 708.3 eV, is $(5.02 \pm 0.53)^{\circ}$, while the phase of the oscillation at the negative L_3 peak, 707.7 eV, is shifted by $(181.86 \pm 0.77)^{\circ}$ with respect to the oscillation at 706.3 eV. Antiphase signals are expected from the antiferromagnetic coupling of T_d and O_h site Fe^{3+} ions, with the signals from the positive L_3 peaks more strongly sensitive to O_h sites and the negative L_3 peak dominated by the T_d sites.

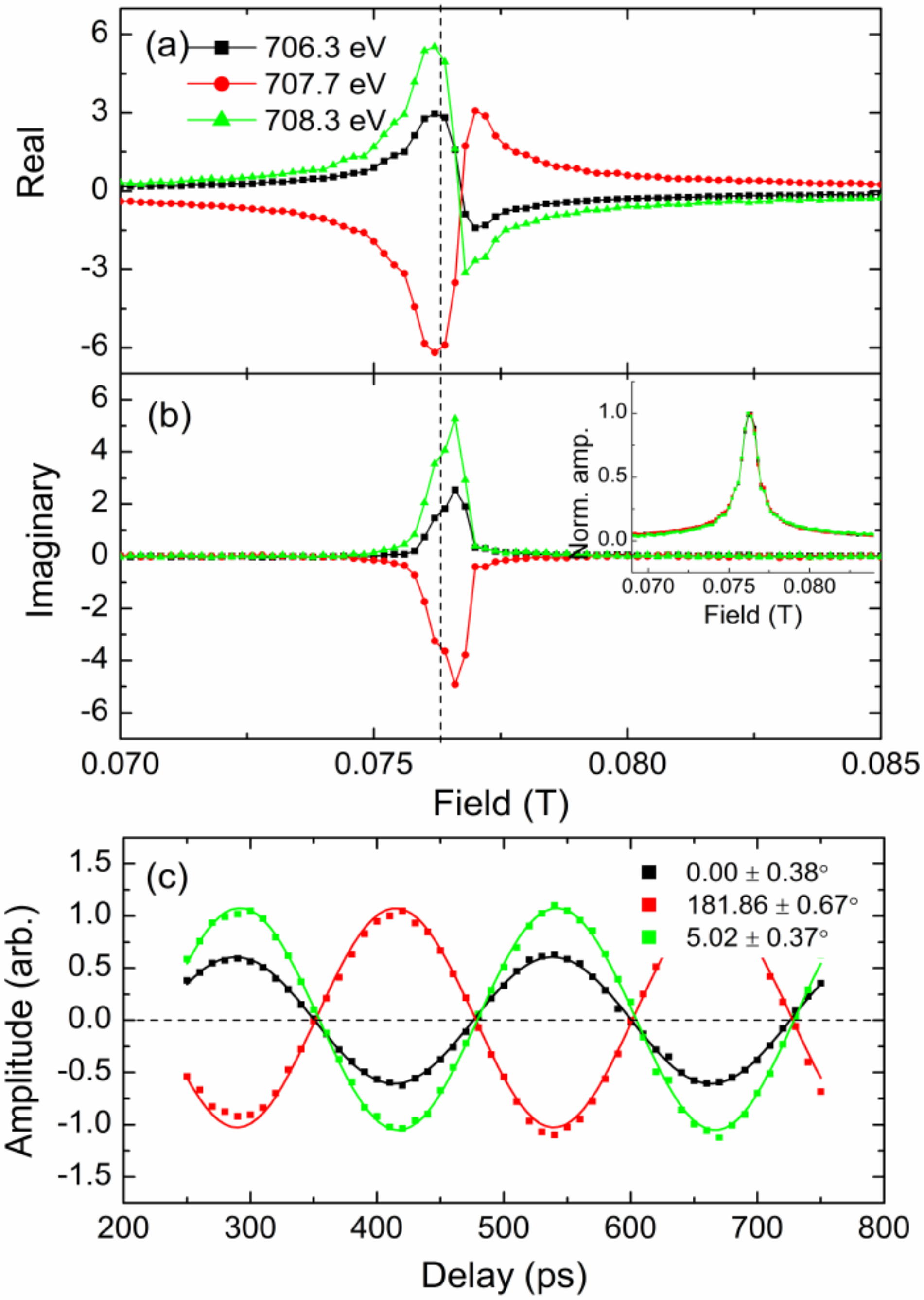

Figure 7.14: Fe XFMR with a 4 GHz driving signal recorded at three photon energies corresponding with the three strongest L_3 peaks in the static XMCD spectrum. Panels (a) and (b) show the amplitude and phase recorded as the bias field was swept across the YIG resonance. The inset to (b) shows all three curves normalised to 1 at the peak value. Panel (c) shows XFMR recorded at a bias field fixed to the peak field from panel (a) with the delay (phase) of the driving signal scanned through two periods of precession. The black, red and green curves were recorded with photon energies of 706.3 eV, 707.7 eV and 708.3 eV, respectively. The phase difference between the 706.3 eV and 708.3 eV oscillations is $(5.02 \pm 0.53)^\circ$ while the phase of the oscillation at the negative L_3 peak, 707.7 eV, is shifted by $(181.86 \pm 0.77)^\circ$ with respect to the oscillation at 706.3 eV.

While the observed deviations from precise antiphase are small, the error bounds initially suggest that they are statistically significant. However, these deviations from precise antiphase do in fact lie within the range of typical phase drifts observed in reference Co FMR measurements. It is also important to consider these measurements in the context of the discrepancies between static and dynamic spectra discussed above. The ratio of the amplitudes in the time-resolved XMCD data does not match the ratio of the amplitudes at the same energy values in the static XMCD spectrum. The amplitude ratio in the static XMCD spectrum is, in order of increasing photon energy, $1.0 : 3.6 : 2.1$, while in the time-resolved XMCD data the ratio is $1.0 : 2.0 : 1.9$. Overdriving of the sample during dynamic measurements was ruled out as a source of this discrepancy, and applying the technique posited by Boero et al. does not satisfactorily address the discrepancy. Therefore, while these data hint at a possible small phase difference between the O_h sites (which are largely responsible for the positive L_3 peaks) and the T_d sites for Fe in YIG, further research is needed before any concrete conclusions can be drawn. In particular, the nature of the source of the discrepancy between the static and dynamic spectra must be identified before it can be determined what action needs to be taken to account for this in future XFMR measurements.

7.4 Conclusions

In this chapter, the behaviour of Fe within the ferrimagnetic oxide YIGhas been studied by VNA-FMR, static XMCD and dynamic XFMR measurements. These have been compared to the static and dynamic x-ray spectra recorded for a metallic Co layer within the same sample. The experimentally obtained YIG spectra have also been compared to spectra generated from multiplet calculations.

Measurements of the YIG resonance linewidth by VNA-FMR suggest an uncharacteristically large linewidth. This contrasts with the linewidth measured by XFMR, which is narrower and as expected. Given that VNA-FMR samples an area three orders of magnitude greater than the x-ray measurements, this provides strong evidence that there are long-range spatial inhomogeneities in the YIG, which lead to a broadening of the linewidth when sampling across a larger area.

The static and dynamic spectra for the metallic Co layer were measured to be identical, as is expected of a ferromagnetic transition metal. However, the static and dynamic spectra for Fe within the YIG layer exhibited marked differences, as can be seen in Figures 7.7 and 7.9 on page 191 and on page 194. Potential sources for this difference were investigated. As YIG has relatively low damping, there is a high chance of driving non-linear dynamics with relatively low RF powers. This was tested and confirmed not to be a contributory factor, as shown in Figure 7.10 on page 195. Boero et al. had previously suggested an influence on the dynamic spectral lineshape as a result of uncharacteristically large breakthrough of XMLD into XMCD measurements.[132] A corrective technique was posited by Boero et al. which, in their case, brought the dynamic and static lineshapes into perfect agreement with one another. This corrective technique was tested, but failed to adequately address the observed discrepancies between the static and dynamic lineshapes in the present case, as shown in Figure 7.11 on page 196.

Therefore while the dynamic x-ray measurements presented herein suggest the possibility of a phase lag between Fe located on T_d and O_h sites within the YIG lattice, it is necessary to consider this in the context of the above discrepancy. As the technique proposed by Boero et al. was insufficient to address the observed discrepancies, and other immediately apparent sources were ruled out, it is therefore likely that there remains a systematic error in these measurements. Further research will be needed to identify the source of this error, and any necessary changes in experimental geometry or analysis required to correct for it, before firm conclusions can be drawn.

In terms of the measurement technique employed herein, a lack of measurement artefacts with the x-ray transmission technique has been demonstrated, showing the power of time-resolved XMCD spectroscopy for the study of both single and multi-site magnetic materials. For typical single site ferromagnets such as Co, time-resolved XMCD with modulated detection via a LIA can provide a precise measurement of the spin-orbit moment ratio. In systems with strong spin-orbit coupling, time-resolved XMCD spectroscopy may in principle also be able to detect a spin-orbit phase lag as a signature of the damping contribution. In multi-site systems, such as ferrimagnetic YIG, time-resolved XMCD spectroscopy provides a site-specific dynamic magnetometry probe.

CHAPTER 8

Spin dynamics of an antiferromagnet driven by interfacial coupling to a ferromagnet

8.1 Introduction

Spin-valve structures, previously introduced in Chapter 6, are important components in magnetic recording heads, MRAM chips, and spin transfer oscillators (STOs). The exchange bias of the ferromagnetic layer by an antiferromagnetic layer is essential to the operation of these structures. The fixed layer magnetisation is pinned, or biased, by exchange coupling to the adjacent antiferromagnet that is unaffected by applied magnetic fields because it has no net magnetic moment. When the spin-valve is driven at high frequency, either by an external magnetic field or STT, the fixed layer may exhibit a significant precessional response, which is often observed to be heavily damped. Although the exchange bias effect is widely used, the exchange bias field is usually much smaller than would be expected for ideal interfacial exchange coupling, and the mechanism by which the antiferromagnet introduces additional damping is not clearly understood. Measurements of both the static and dynamic magnetic configuration within the antiferromagnetic layer are required to understand this behaviour. However, the lack of a net magnetic moment renders the magnetism of the thin film antiferromagnet inaccessible to many conventional measurement techniques.

The study presented in this chapter advances understanding of the exchange bias effect by studying epitaxial CoO / Fe (001) bilayers, in which both the crystallographic and magnetic structure are carefully controlled. XMCD and XFMR were used to study the static and dynamic behaviour of the ferromagnetic Fe. Crucially, epitaxial CoO (001) is one of the few antiferromagnetic materials to exhibit XMLD. It was therefore possible to use XMLD to determine the equilibrium magnetic configuration of the CoO, and make phase resolved measurements of the motion of the Co moments when FMR is induced within the Fe layer.

In XMLD the cubic symmetry of the antiferromagnet is broken by the orientation of the magnetic moments. The absorption of linearly polarised x-rays is hence different for the polarisation direction $\boldsymbol{E}$ of the x-rays parallel and perpendicular to the moments of the antiferromagnet. In the CoO / Fe (001) system the Co moments align perpendicular to the direction of the Fe moments when the material is cooled below the Néel temperature, T_N, of the CoO. However the exchange interaction within the CoO is relatively weak (compared to that in NiO, for example) so that the interfacial Co moments tend to rotate due to interfacial exchange coupling when an applied magnetic field causes the magnetisation of the Fe to reorient.[136] The degree of order of the Co moments and their ability to rotate with the Fe moments is crucial in determining both the strength of the exchange bias field exerted on, and the additional damping experienced by, the Fe moments. When precession is induced in the Fe at the FMR condition, the Co moments at the CoO / Fe interface will also precess, perhaps with some phase lag, leading to the propagation of a coherent spin wave into the CoO. The generation and damping of this spin wave is the key to understanding the enhanced damping of the adjoining Fe layer.

XFMR has previously been used by Yu to study the $Ni_{81}Fe_{19}$ / CoO (001) interface.[137] Polycrystalline $Ni_{81}Fe_{19}$ was chosen for its low FMR frequency and narrow linewidth. However the measured linewidth of the $Ni_{81}Fe_{19}$ was about three times larger than expected and dynamic XMLD was not observed. This was believed to be a consequence of magnetic disorder at the interface between the epitaxial CoO (001) and the polycrystalline $Ni_{81}Fe_{19}$. The results presented herein therefore provide an advance on the results of Yu by applying the measurement technique a fully epitaxial system, thus ensuring magnetic order within the antiferromagnet.

8.2 Experimental Setup

In this study, CoO ($0\,\mathrm{nm}$ to $4\,\mathrm{nm}$) / Fe (3 monolayers) / $Ni_{81}Fe_{19}$ trilayers, in which the CoO thickness is varied along the $\approx 2.5\,\mathrm{mm}$ length of a wedge, were grown by molecular beam epitaxy (MBE) in the laboratory of Prof. Qiu at the University of California, Berkeley. The length and gradient of the wedge varied from sample to sample. The structures were grown on a MgO (001) substrate through a CPW mask with a $100\,\mathrm{nm}$ Ag underlayer to carry the microwave current. XFMR is best suited to materials in which the resonance frequency is $< 10\,\mathrm{GHz}$. Epitaxial Fe has a large magnetocrystalline anisotropy and therefore exhibits FMR frequencies that are too high to be accessible to XFMR. Softer ferromagnets, such as $Ni_{81}Fe_{19}$, have a lower FMR frequency, but are poorly lattice matched at the interface with CoO. The trilayer studied here therefore combines an ultrathin Fe film of 3 monolayers with a thicker $Ni_{81}Fe_{19}$ layer of either $3.6\,\mathrm{nm}$ or $10\,\mathrm{nm}$. This maintains the epitaxial interface between the ferromagnet and antiferromagnet layers while keeping the FMR frequency low enough to be accessible to XFMR. The ultrathin Fe in fact has reduced magnetocrystalline anisotropy compared to

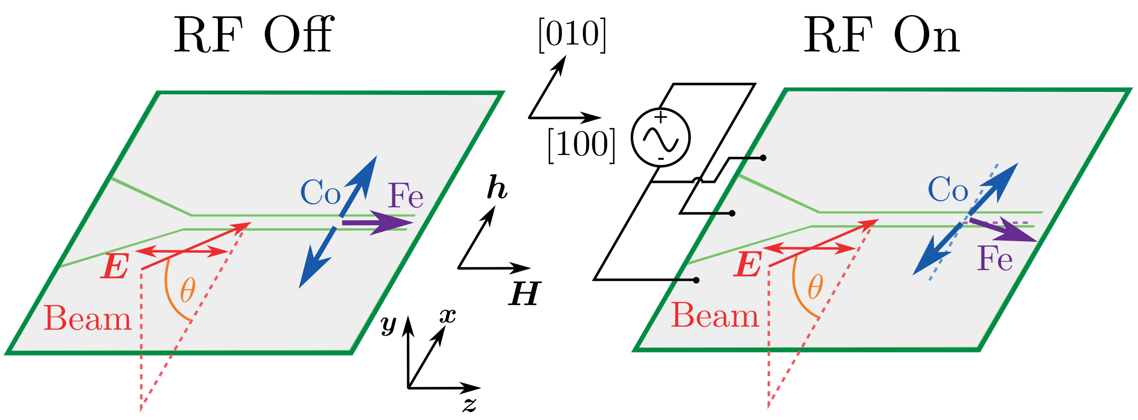

Figure 8.1: Schematic of the time-resolved experimental geometry. A CoO / Fe (001) bilayer was deposited along the signal line of the co-planar waveguide (grey). The Co moments (blue) are ordered orthogonal to the Fe magnetisation (purple) during field cooling. The microwave field $\boldsymbol{h}$ causes the Fe magnetisation to precess, causing the Co moments to also reorient, with their motion being detected by time-resolved XMCD and XMLD, respectively.

the bulk value,[138] and the thicker $Ni_{81}Fe_{19}$ layer, being strongly coupled to the Fe, has a smaller FMR linewidth which further aids the observation of an XFMR response.

The basic XFMR technique has previously been described in detail by Marcham et al.,[113,114,139] and is shown schematically in Figure 8.1. The samples were fabricated directly on the 250 µm wide signal line of a CPW. A static field $\boldsymbol{H}$ was then applied along the signal line to orient the magnetisation $\boldsymbol{M}$ of the ferromagnetic layer of the sample. A microwave current passed through the CPW generates an RF magnetic field $\boldsymbol{h}$ which causes $\boldsymbol{M}$ to precess about $\boldsymbol{H}$.

X-ray measurements were performed on beamlines I06-1 and I10 at DLS using POMS. The vector magnet of POMS was necessary to make both XMCD and XMLD measurements, as well as for field cooling along different directions. A cryostat sample probe was employed with liquid nitrogen cooling to field cool the sample to 80 K, i.e. below the Néel temperature of CoO ($T_N \approx$ 290 K). POMS further incorporates motorised three-axis control, necessary for accurate and repeatable positioning of the wedged-thickness sample within the x-ray beam. The sample was mounted with a photodiode beneath the substrate to detect transmitted x-ray intensity via the XEOL from the MgO substrate.

The microwave current is generated by an RF comb generator using the synchrotron's master RF clock of 500 MHz to output phase-locked harmonics of 2 GHz to 10 GHz. Being phase-locked to the master clock, and therefore to the x-ray pulses, allows XMCD and XMLD measurements to be made stroboscopically.

Static XMCD spectra were recorded with a grazing incidence angle $\theta = 30^\circ$ and orthogonal to the length of the signal line such that the x-rays probe the transverse component of $\boldsymbol{M}$ as it precesses. Static XMLD spectra were recorded at normal incidence $(\theta = 90^\circ)$. The desire to record both dynamic XMCD and XMLD from the same sample posed problems concerning the most suitable geometry. With the magnetisation lying in the plane of the sample, optimum XMCD contrast is achieved with the incidence angle θ as small as possible, i.e. grazing incidence. However, for the largest XMLD contrast, $\theta = 90^\circ$ is required. While realigning the relative sample and beam positions for each measurement technqiue was a possibility, this always carries with it the potential uncertainty as to whether the beam is in exactly the same spot. For isotropic samples, this is not such a crucial issue; however, the wedged sample under consideration here is clearly anisotropic, and therefore a consistent beam position was essential between measurements. It was therefore decided to settle on a compromise grazing angle $\theta = 60^\circ$, sacrificing some contrast for certainty of beam position, and therefore certainty of CoO thickness.

For static XMCD measurements the static bias field was applied parallel and antiparallel with the propagation direction of the circularly polarised incident x-rays. Spectra were then obtained as the difference in absorption spectra with the bias field reversed. This method avoided movement of the x-ray optics to switch polarisations, which could cause a small shift in beam position. For static XMLD the bias field was typically applied in the yz-plane, orthogonal to the incident x-ray beam, with spectra calculated as the difference between absorption spectra recorded with the bias field rotated between the y and z axis. This records a "field-rotatable"

XMLD, which was most relevant to the dynamic XMLD measurements which were sensitive to CoO spins moving at the same frequency as the precessing Fe spins. XMLD recorded with fixed field and rotated x-ray polarisation is typically larger, being sensitive to both frozen and rotatable spins. Such XMLD spectra have also been recorded for completeness, and are presented in Figure 8.9 on page 219.

Dynamic XMCD and XMLD measurements were recorded with the bias field applied orthogonal to the microwave field generated by the CPW, parallel with the signal line, and detected using a lock-in amplifier and 180° phase modulation of the driving microwave field.

Tuning the x-ray energy to the appropriate absorption edges gives the technique element specificity, allowing the dynamics of individual layers of the sample stack structure to be probed. Varying the time delay between the x-ray pulses and the microwave current introduces a phase lag between the two, allowing phase-resolved measurements that reveal the relative phase of the different layers when driven at resonance.

8.3 Results and Discussion

FMR of the trilayer films was studied at Exeter by both VNA-FMR and time-resolved MOKE prior to x-ray measurements. Figures 8.2(b) and 8.2(d) on page 212 show VNA-FMR measured at room temperature as a function of microwave frequency and bias field strength swept from negative to positive values for samples with a $Ni_{81}Fe_{19}$ layer thickness of $3.6\,\mathrm{nm}$ and $10\,\mathrm{nm}$, respectively. The image contrast represents absorbed microwave power with the darker regions showing larger absorption. Up to a bias field of $0.1\,\mathrm{T}$ the FMR frequency is below $\approx 10.5\,\mathrm{GHz}$, within the region accessible to XFMR. The images show quite a broad resonance, with some “ghosting” visible, as the measurement is sensitive to the whole length of the CoO wedge along which the position and linewidth of the ferromagnetic layer resonance may vary. In Figures 8.2(a) and 8.2(c) on page 212 an un-patterned sample of the same composition was measured in the region with zero CoO thickness by mounting the sample face down on a CPW defined on a high frequency printed circuit board. The narrow FMR signal observed from the ferromagnetic layer is clear.

Working with the CoO ($0\,\mathrm{nm}$ to $4\,\mathrm{nm}$) / Fe (3 monolayers) / $Ni_{81}Fe_{19}$ ($3.6\,\mathrm{nm}$) trilayer, FMR as a function of position along the CoO wedge, i.e. CoO layer thickness, was studied by time-resolved MOKE with a driving microwave field at a frequency of $5\,\mathrm{GHz}$. Figure 8.3 on page 213 shows (a) real and (a) imaginary components of the FMR response for six positions along the CoO wedge at room temperature. The resonance position and linewidth were then extracted by fitting a Lorentzian to the imaginary component. The variation of resonance field with CoO thickness is non-monotonic, but in general shows reduced resonance field with increasing CoO thickness. The linewidth increases with increasing CoO thickness.

XMCD and XMLD were then used to study the magnetic state of the ferromagnet/antiferromagnet system before and after field cooling to order the antiferromagnet spins. Figure 8.4(a) on page 214 shows Co x-ray absorption intensity as a function of position along the CoO wedge, with Co $L_{2,3}$ XAS spectra at four positions shown in Figure 8.4(b). The wedge position is clear and the XAS are typical of Co^{2+} ions. In Figure 8.4(c) Co XMCD is plotted for the same four positions along the wedge, where XMCD was obtained from XAS acquired with a field of $\pm 0.1\,\mathrm{T}$ applied in the plane of the sample and parallel to the plane of incidence of the incoming x-ray beam. A weak Co XMCD is found that is constant over a large range of CoO layer thicknesses, suggesting that there is a thin layer of metallic Co at the CoO / Fe interface. Peak Co XMCD as a function of CoO thickness is shown in Figure 8.4(d), with the small Co XMCD saturating for a CoO thickness between approximately $0.2\,\mathrm{nm}$ and $1.7\,\mathrm{nm}$.

Figure 8.5 on page 215 shows Fe and Ni XAS and XMCD recorded at room temperature for three positions along the CoO wedge. The spectra appear similar for each position on the wedge, with no indication of oxidised Fe.

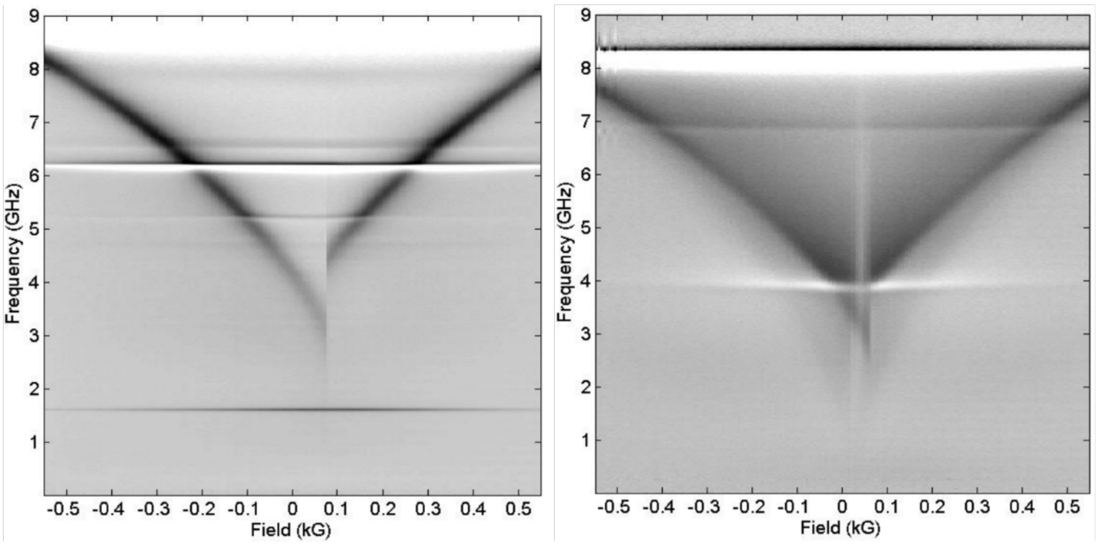

(a) 3.6 nm $Ni_{81}Fe_{19}$, without CoO (b) 3.6 nm $Ni_{81}Fe_{19}$, with CoO

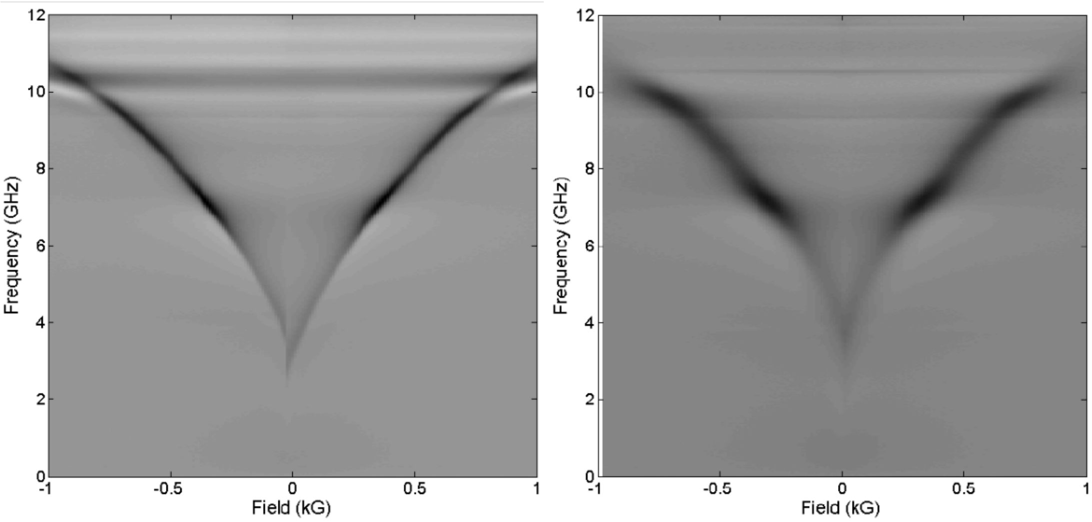

(c) 10 nm $Ni_{81}Fe_{19}$, without CoO (d) 10 nm $Ni_{81}Fe_{19}$, with CoO

Figure 8.2: VNA-FMR of CoO (0 nm to 4 nm) / Fe (3 monolayers) / $Ni_{81}Fe_{19}$ (3.6 nm), showing (b) the average response over the length of the CoO wedge and (a) a nominally identical sample not patterned into the form of a coplanar waveguide, showing the linewidth of the ferromagnetic layer resonance with no CoO present. (c) and (d) show similar measurements from samples with a 10 nm $Ni_{81}Fe_{19}$ layer. The image contrast is proportional to absorbed microwave power, with darker areas indicating higher absorption. Horizontal banding at fixed frequency is an artefact of the measurement.

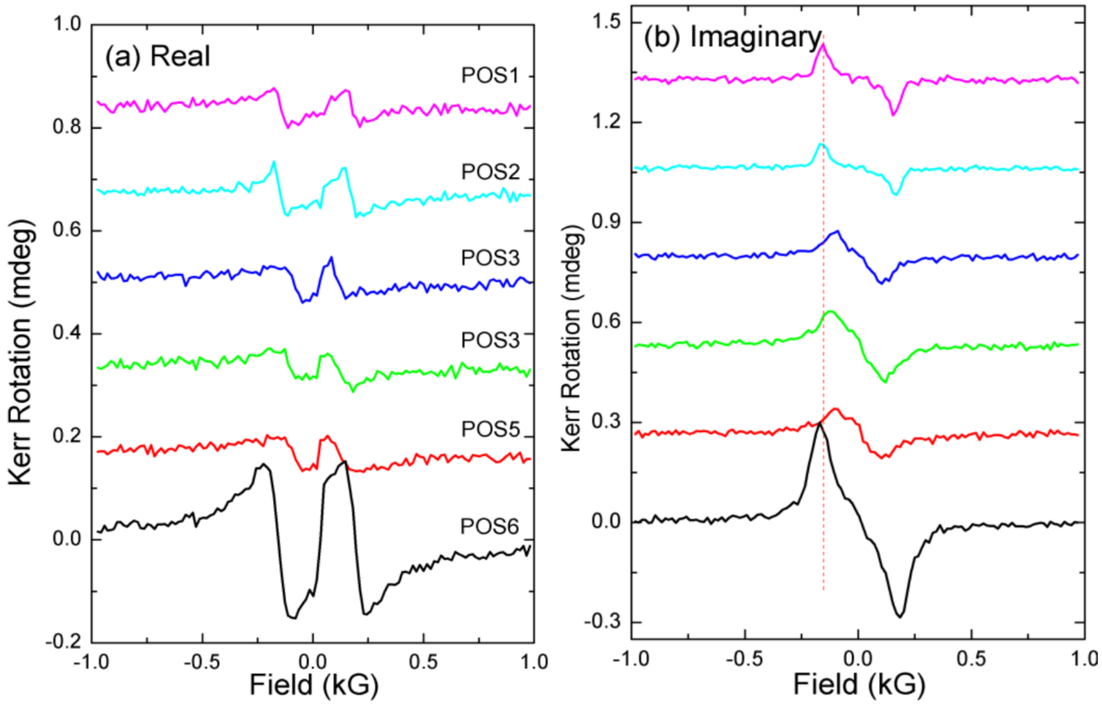

(a) Real (b) Imaginary

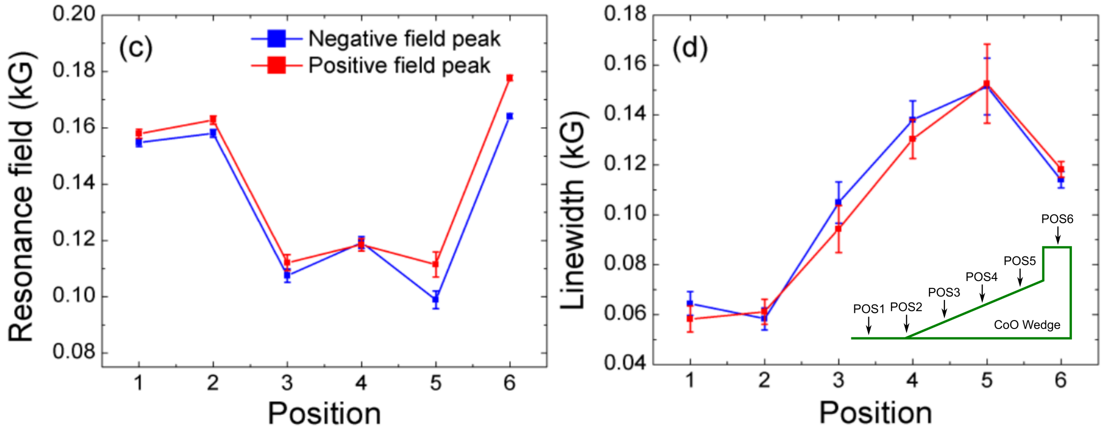

(c) Resonance field (d) Linewidth

Figure 8.3: Time-resolved MOKE measurements of FMR, displayed as (a) the real (dispersive) component and (b) the imaginary (absorptive) component. The focused probe laser beam spot was moved along the CoO wedge, probing the dynamics with the CoO thickness increasing from 0 nm to 4 nm. The imaginary component was used to extract the (c) resonance field and (d) linewidth by fitting a Lorentzian function.

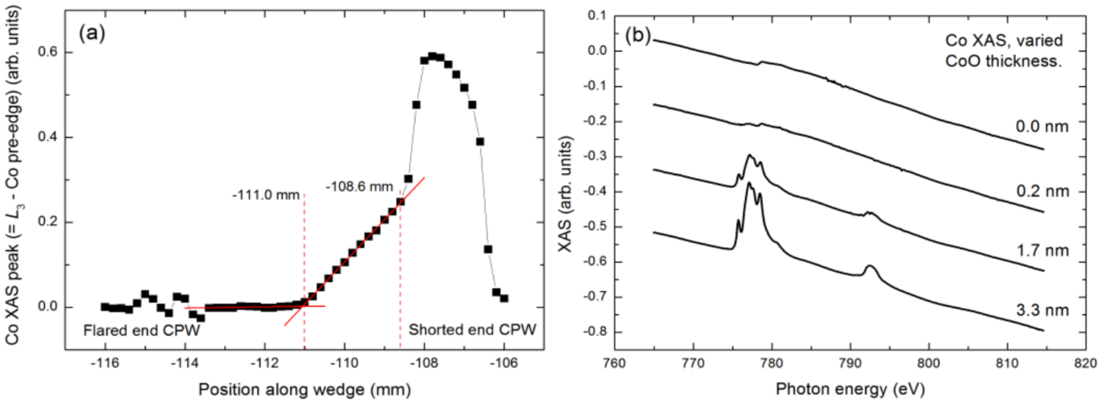

(a) CoO x-ray absorption (b) Co $L_{2,3}$ XAS

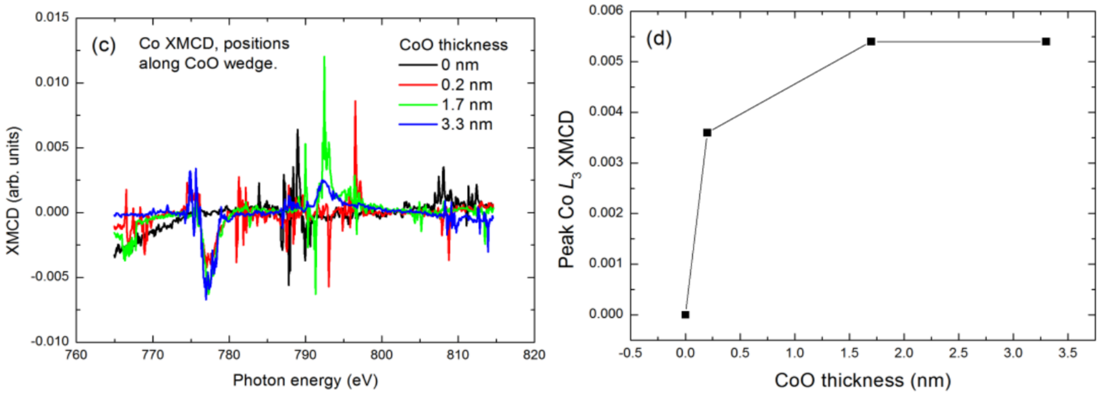

(c) Co XMCD (d) Co peak XMCD

Figure 8.4: (a) Measurement of Co XAS along the length of the CoO wedge. (b) Co $L_{2,3}$ XAS and (c) XMCD recorded for four thicknesses of CoO. The absorption spectra are typical of divalent Co, while the peak XMCD data reaches saturation for a CoO thickness between 0.2 nm and 1.7 nm (d), suggesting the presence of a thin ferromagnetic Co layer at the Co / Fe interface.

Magnetic ordering of CoO at room temperature was explored by XMLD at normal incidence, with spectra shown in Figure 8.6 on page 216. With x-rays at normal incidence to the film surface a 0.4 T bias field was applied in the plane of the film orthogonal to the incident x-ray beam, and XMLD was calculated as the difference of XAS spectra acquired with the electric field of the linearly polarised x-rays in the plane of sample and parallel and orthogonal to the field direction, along the $\langle 110 \rangle$ axes of the CoO. No linear dichroism was observed, indicating no net spin ordering in CoO at room temperature.

To induce spin ordering in the CoO antiferromagnet layer the film was cooled well below the Néel temperature ($T_N \approx$ 290 K) to 80 K in the presence of a 0.4 T

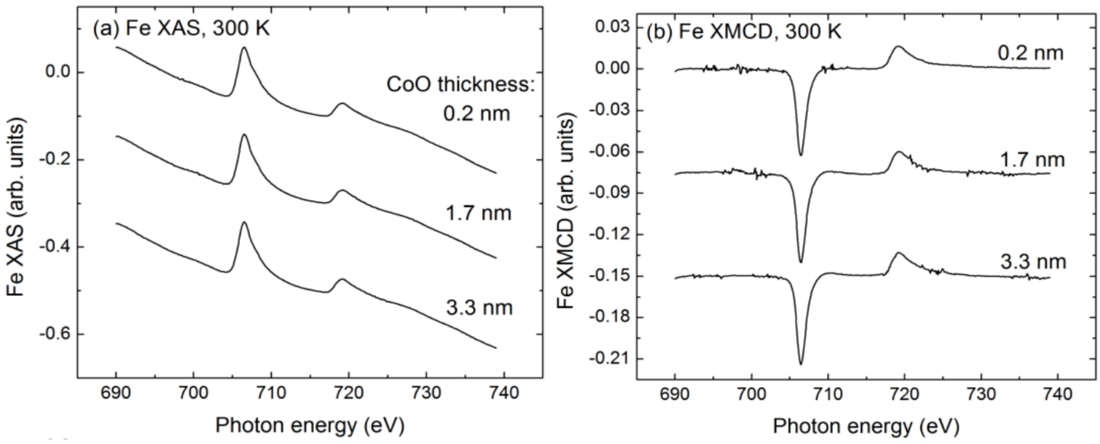

(a) Fe XAS

(b) Fe XMCD

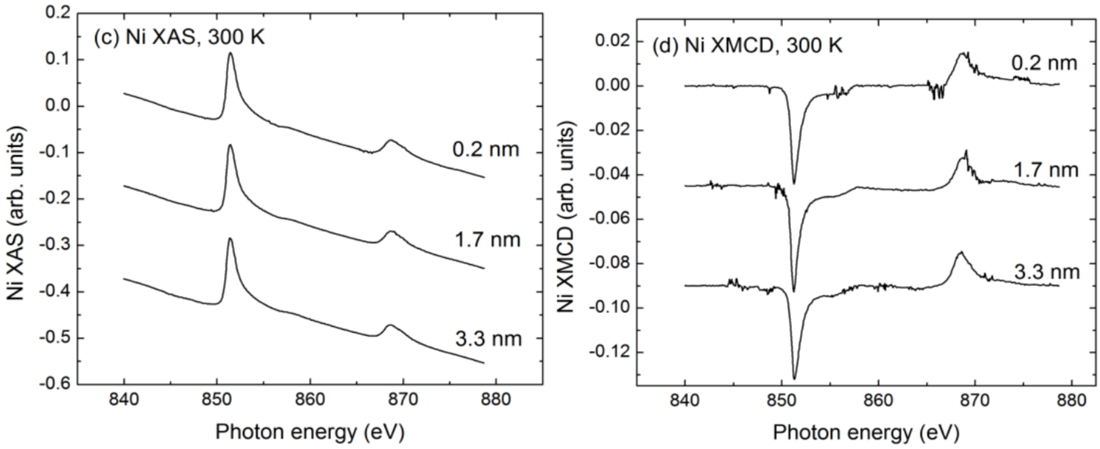

(c) Ni XAS

(d) Ni XMCD

Figure 8.5: Fe $L_{2,3}$ XAS (a) and XMCD (b), and Ni $L_{2,3}$ XAS (c) and XMCD (d) recorded at three positons along the CoO wedge. The spectra appear similar for each positon along the wedge, with no indication of oxidation.

bias field. In the first instance the bias field was applied in the sample plane parallel with the Fe $[100]$ axis, which is parallel to the CoO $[110]$ crystalline axis, and orthogonal to the incident x-rays. In Figure 8.7 on page 217, Ni L_3 XMCD hysteresis loops recorded after field cooling are presented. The same data is included in panels (a) and (b), the loops being overlaid in panel (b) to highlight the reduced XMCD signal at maximum field with increasing CoO thickness. With increasing CoO thickness the Ni loop changes from a square shape with low coercivity to a sloping shape with increasing coercivity and reduced remanence. The XMCD at the maximum field also falls off with increasing CoO thickness. These features

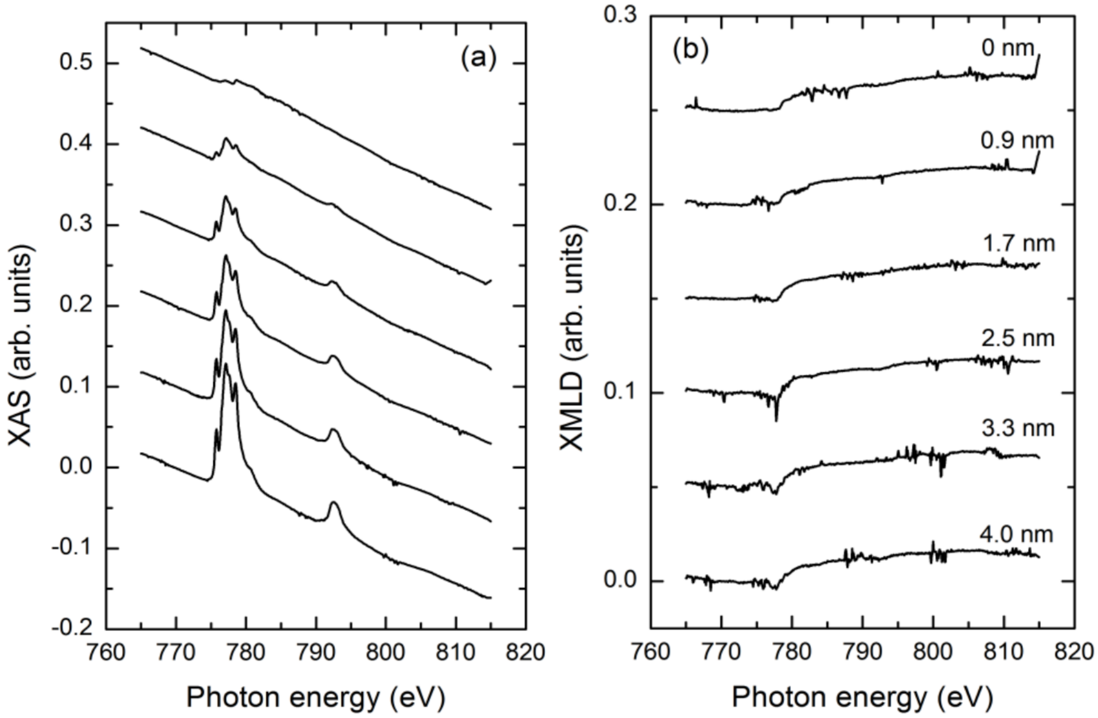

(a) XAS

(b) XMLD

Figure 8.6: Room temperature Co (a) $L_{2,3}$ XAS and (b) XMLD as a function of CoO layer thickness. The absence of linear dichroism implies a lack of spin ordering in the CoO layer at room temperature.

reveal an induced uniaxial anisotropy with increasing CoO thickness. The reduced XMCD amplitude for the largest CoO thickness suggests that the $Ni_{81}Fe_{19}$ magnetisation cannot be aligned parallel with the x-ray propagation axis at 0.4 T, and that it is strongly coupled to rigidly aligned spins within the CoO layer.

X-ray linear dichroism was observed for CoO after field cooling. However, no change in the dichroism was observed as the bias field was rotated, suggesting that the Co spins were rigid and non-rotatable, as can be seen in Figure 8.8. However, the XMLD signal was found to have opposite sign for the two 90° rotated field-cooling directions, confirming that the observed XMLD was of magnetic origin. The spectral shape agrees well with that expected along CoO $\langle 110 \rangle$.[136,140–142] Angular dependent XMLD measurements have shown that the XMLD spectra along $\langle 100 \rangle$ and $\langle 110 \rangle$ in CoO are strongly different, in agreement with multiplet calculations.[140]

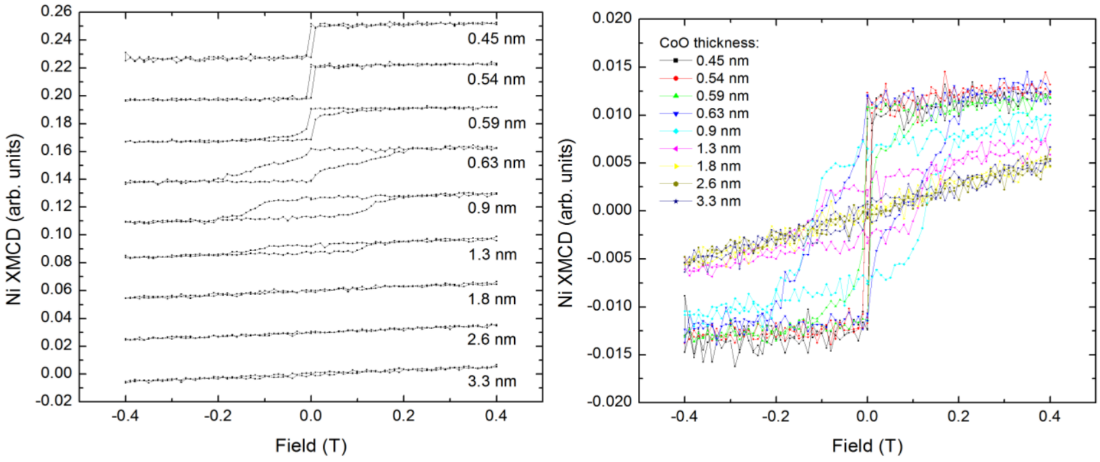

(a) (b)

Figure 8.7: Ni L_3 XMCD hysteresis loops recorded at 80 K after field cooling in a 0.4 T field with varied CoO thickness. The same data is shown in both panels with the data overlaid in panel (b) to highlight the reduced XMCD at maximum field with thicker CoO. With increasing CoO thickness the coercivity of the Ni loop increases and the maximum XMCD at 0.4 T decreases. Increasing the thickness of the antiferromagnetic CoO leads to increased uniaxial anisotropy. In some cases the strength of the coupling prevents the Ni moments aligning parallel with the incident x-rays at 0.4 T.

In Figure 8.10 on page 220 the high field (0.4 T) and zero field Ni L_3 XMCD and coercivity from the loops in Figure 8.7 are compared with the peak Co XMLD signal for increasing CoO thickness. The comparison reveals that reduced Ni XMCD and increased coercivity begins at the same CoO thickness where Co XMLD becomes non-zero: $\approx$ 0.6 nm. Ni XMCD remanance reaches zero for a CoO thickness of $\approx$ 1.8 nm, while Co XMLD continues to rise for CoO thickness up to 3.3 nm. It is not understood why the CoO XMLD signal drops significantly at a thickness of 4.0 nm.

Hoping to improve contrast in the x-ray measurements, particularly given the non-ideal field geometry necessary for dynamic measurements, the sample was replaced with the second wedge sample having a thicker 10 nm $Ni_{81}Fe_{19}$ ferromagnetic layer. The layout of this sample is shown in Figure 8.11 on page 221, and FMR data has previously been shown in Figure 8.2 on page 212. The wedge profile was measured as the difference in x-ray absorption at the Co L_3 energy

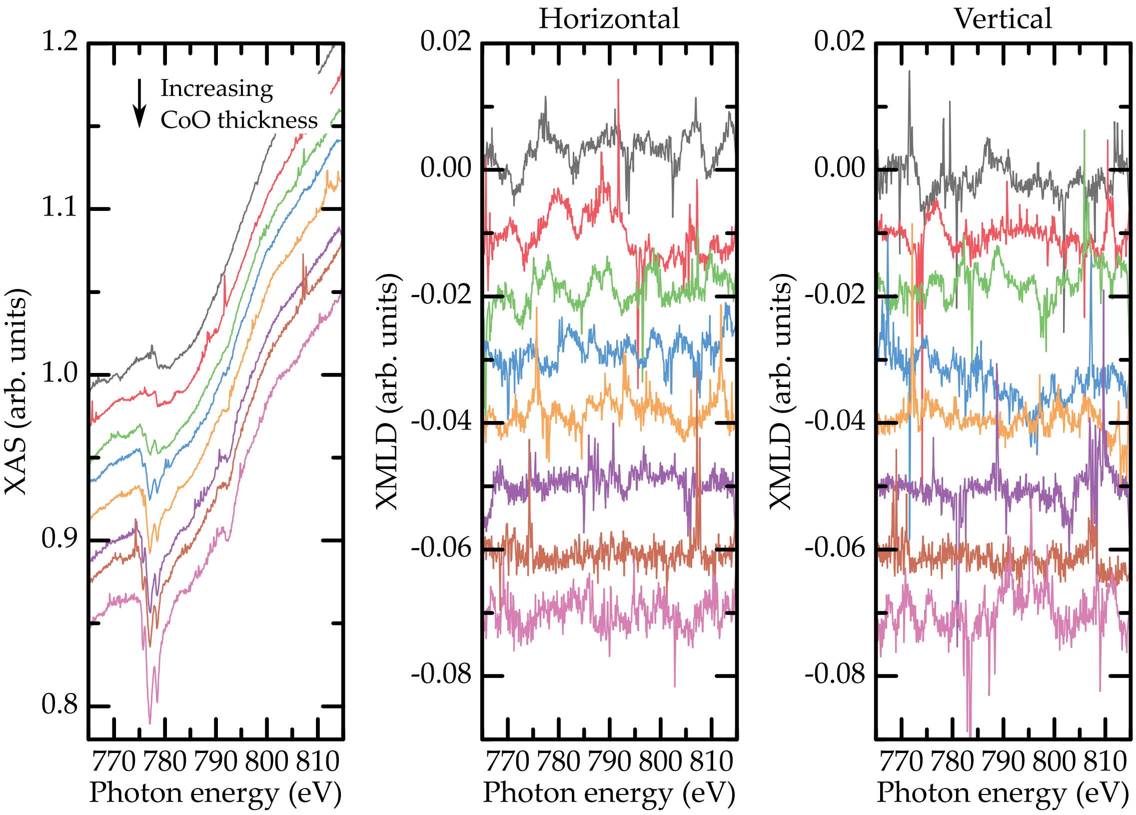

Figure 8.8: Co L_3 XAS (left) for varied CoO thickness at 80 K after cooling in a 0.4 T field applied parallel with the Fe $[100]$ axis, which is parallel to the CoO $[110]$ axis, in the plane of the sample. Co XMLD was measured by taking the difference between XAS recorded with the 0.4 T applied field rotated through 90° in the plane of the sample with fixed linear horizontal (centre) and vertical (right) x-ray polarisation. No XMLD signal was observed, implying that the Co spins were not rotatable in this instance.

(778 eV) and pre-edge energy (770 eV). As before, the thickness of CoO increases linearly over a 2.5 mm long wedge portion, before stepping up to a thicker plateau at the shorted end of the CPW.

Antiferromagnetic ordering in the CoO was measured by first heating the sample to 350 K (above its Curie temperature of 290 K) before field cooling to 80 K with a 0.05 T field applied parallel with the CoO $[110]$ axis, parallel with the CPW signal line. With the previous sample it was found that the spins remained frozen along the entire wedge length at 80 K. This sample was therefore heated to 250 K before starting x-ray measurements. Figure 8.12 on page 222 shows static x-ray measurements for Co measured along the length of the wedge. XMLD (Figure 8.12(b))

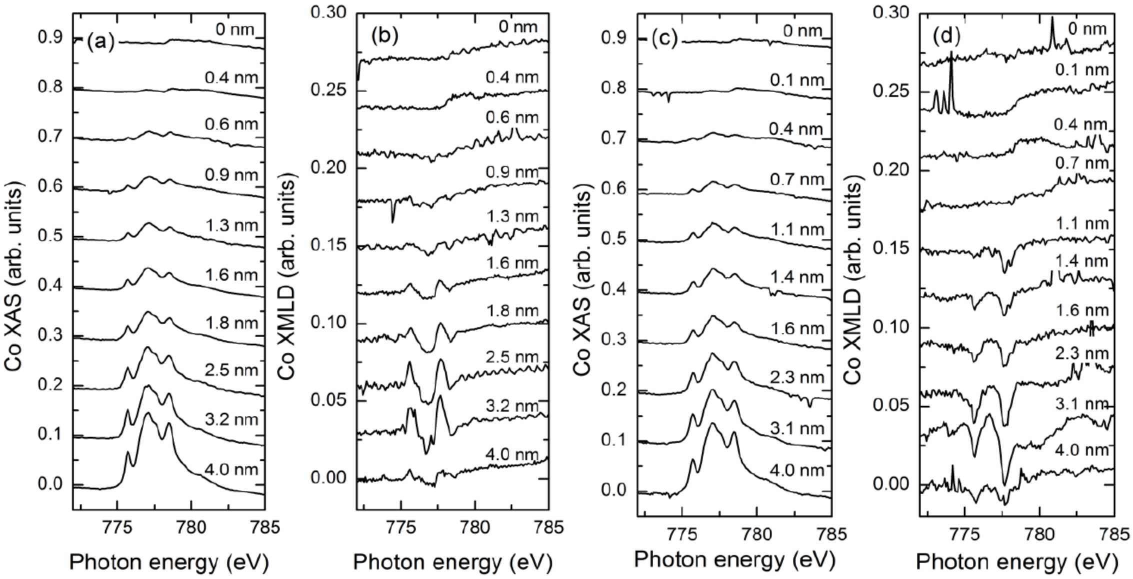

Figure 8.9: Co L_3 XAS (a) and XMLD (b) for varied CoO thickness at $80\,\mathrm{K}$ after cooling in a $0.4\,\mathrm{T}$ field applied parallel with the Fe $[100]$ axis, which is parallel to the CoO $[110]$ axis, in the plane of the sample. Co XMLD was observed as the electric vector of the linearly polarised x-rays was rotated through 90° between the in-plane CoO $\langle 110 \rangle$ axes. Co L_3 XAS (c) and XMLD (d) at $80\,\mathrm{K}$ after cooling in a $0.4\,\mathrm{T}$ field applied orthogonal to that of panels (a) and (b), parallel with the Fe $[010]$ axis in the plane of the sample. The XMLD signal has opposite sign for the two field cooling directions, confirming that the dichroism is indeed of magnetic origin.

was recorded with fixed x-ray polarisation by rotating a $0.4\,\mathrm{T}$ in-plane bias field through 90°. The Co XMLD signal becomes non-zero close to the thin end of the CoO wedge and increases with increasing CoO thickness, as is expected. Figure 8.12(c) shows the peak XMLD at $778.1\,\mathrm{eV}$ as a function of position. The field-rotatable XMLD increases to a peak approximately midway along the CoO wedge before falling for larger thicknesses. This is in agreement with data obtained by Wu et al. which shows that CoO spins are “frozen” in their field-cooled orientation for larger CoO thicknesses.[136] The spectral shape of the XMLD structure in Figure 8.12(b) is also in agreement with previous measurements.[140]

With the static Co XMLD signal characterised the next step was to locate a position along the wedge which showed a shift in the Fe / $Ni_{81}Fe_{19}$ FMR due to spin alignment in the CoO. Time-resolved MOKE measurements shown in Figure 8.13 on page 223 indicate that the region over which a shift in the FMR is

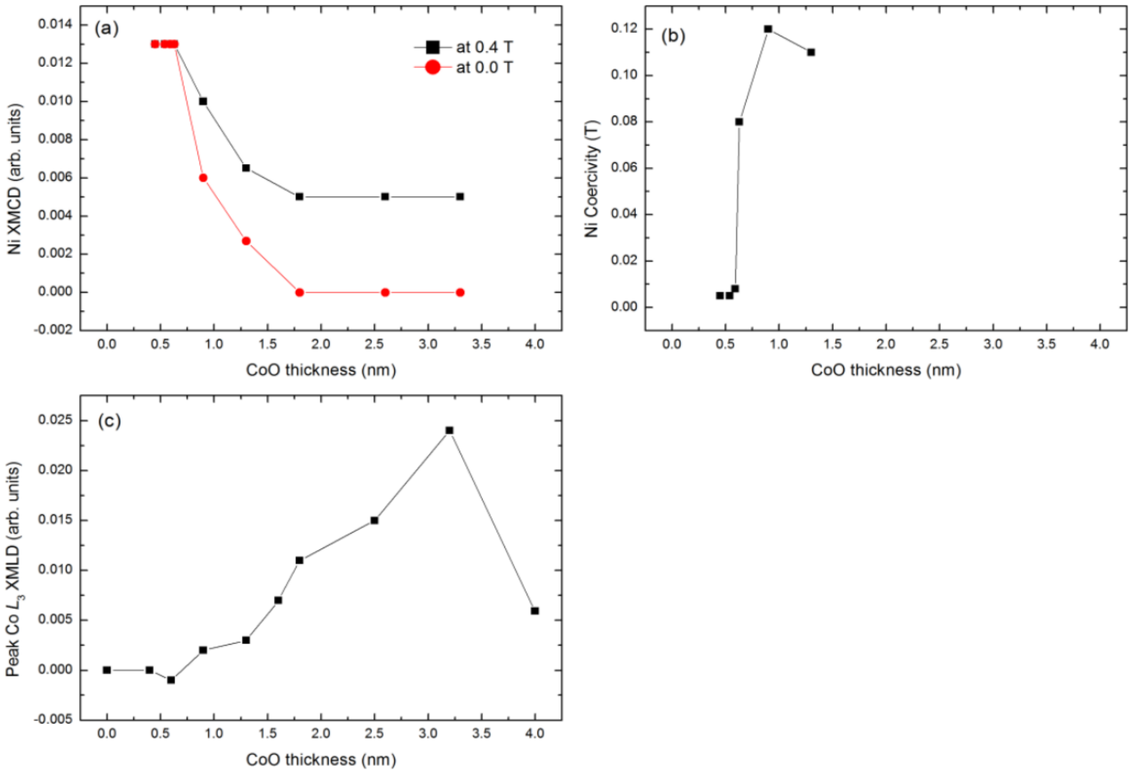

Figure 8.10: Ni L_3 XMCD (a) at 0.4 T (black) and zero field (red), and coercive field (b), extracted from the hysteresis loops in Figure 8.7. (c) Peak Co XMLD at 777.7 eV from the data in Figure 8.9. Comparison shows that increasing Ni coercivity and decreasing remanance begins at the same CoO thickness at which the XMLD becomes non-zero, ≈ 0.6 nm.

detectable is very narrow, on the order of 700 µm. For lower CoO thickness there is no observable shift in the FMR position, while for larger thicknesses the frequency shift is too large to be accessible by XFMR. Furthermore, the FMR shift occurs at the very thin end of the CoO wedge, indicating that even minimal amounts of ordered CoO can significantly modify FMR in a directly adjacent ferromagnetic layer. Figure 8.14 on page 224 shows Fe / $Ni_{81}Fe_{19}$ FMR measured by XFMR at the Fe L_3 energy with a 6 GHz driving field. At positions 5.3 mm and 5.0 mm from the lower edge of the sample, where the CoO thickness is zero, the FMR signal appears the same as that measured at room temperature. At 4.7 mm and 4.6 mm the FMR signal is broadened and shifted to lower field value. At other positions with thicker CoO no FMR signal is observed.

With a location identified that showed static field-rotatable Co XMLD and a

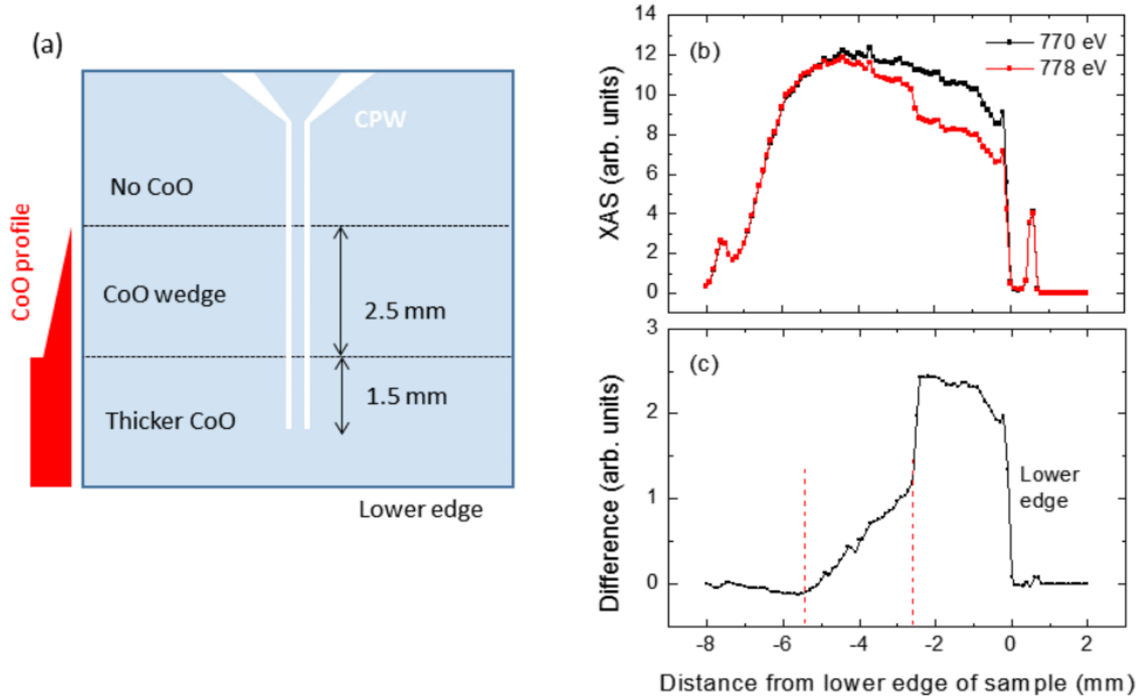

Figure 8.11: (a) Schematic of the CPW-patterned sample, showing the location and profile of the second CoO wedge, having a $10\,\mathrm{nm}$ $Ni_{81}Fe_{19}$ layer. (b) The second CoO wedge was measured by XAS along the sample length at the Co pre-edge ($770\,\mathrm{eV}$) and L_3 peak ($778\,\mathrm{eV}$) energies. The difference is shown in panel (c), with the red dashed lines indicating the extent of the CoO wedge. The wedge has a linear thickness profile before stepping to a larger thickness at the shorted end of the CPW.

shift in the Fe / $Ni_{81}Fe_{19}$ FMR, dynamic Co XMLD measurements were begun. However, repositioning the beam in the correct narrow region was complicated by a number of factors including long-term drifts caused by thermal contraction of the apparatus, long-term x-ray beam drift and more short-term beam movement. The beam position was repeatedly checked by reproducing the plot shown in Figure 8.11(c), and in doing so allowed for drifts by relocating to the same distance from the lower edge of the sample, rather than the same absolute position.

An additional complication arises from the potential for anisotropy in the XMLD spectrum, such that it is not clear at which energy in the static XMLD spectrum one should expect to find the strongest dynamic effect. With XMCD the situation is quite clear, with the largest dynamic signal obtained with circularly polarised x-rays at the energy corresponding with the largest static XMCD contrast. For XMLD the

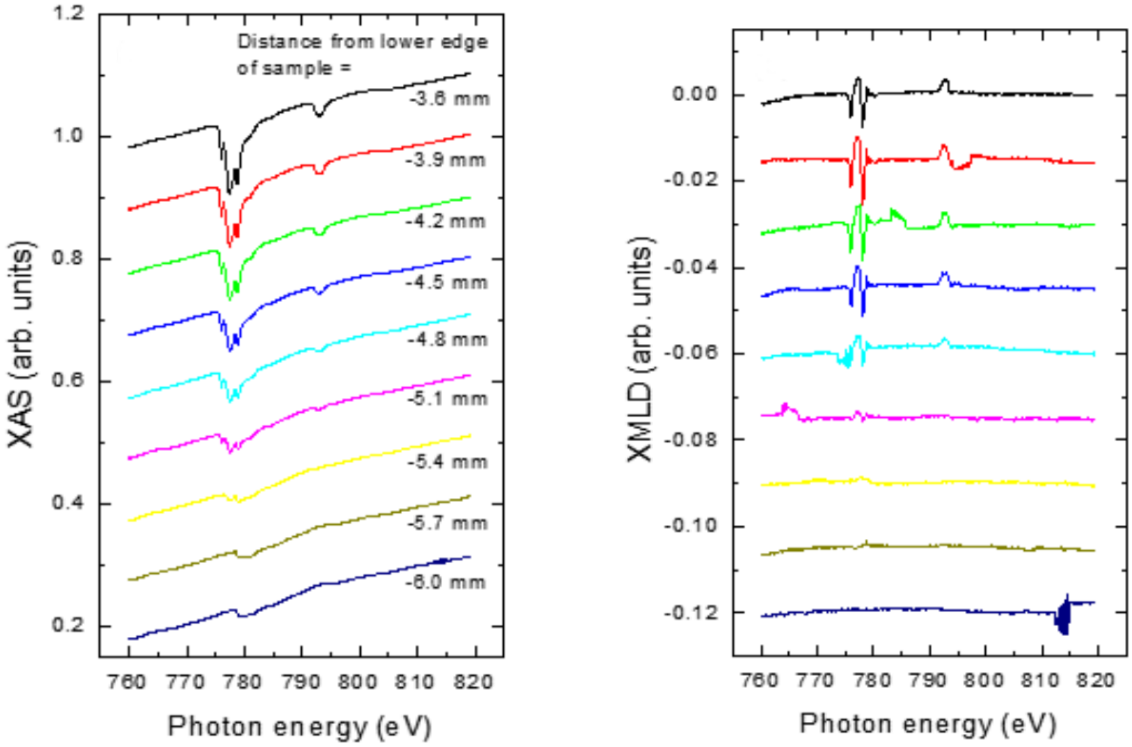

(a) XAS (b) XMLD

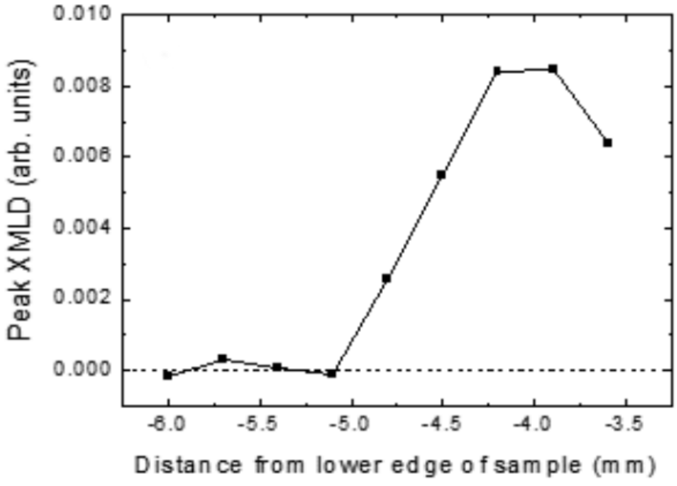

(c) Peak XMLD

Figure 8.12: Co XAS (a) and XMLD (b) recorded along the length of the CoO wedge at 250 K following field cooling to 80 K. XMLD was recorded with fixed x-ray polarisation (linear horizontal) as the difference between XAS recorded with 0.4 T in-plane field rotated through 90°. Peak XMLD along the length of the sample is shown in (c). At 250 K the field-rotatable XMLD becomes non-zero part way along the CoO wedge, at a CoO thickness of about 1.5 nm.

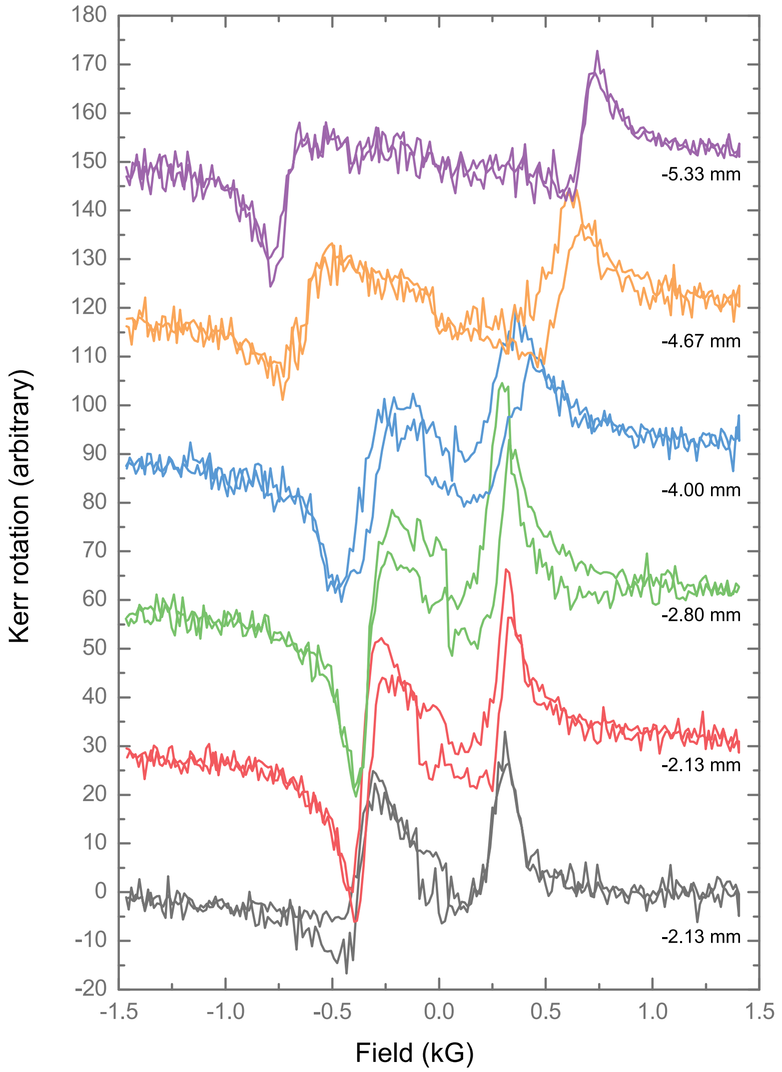

Figure 8.13: 8 GHz FMR recorded by time-resolved MOKE for various locations along the CoO wedge. A shift in FMR is observed at locations from ≈ 4.0 mm to 4.7 mm from the lower edge of the sample—a 700 µm region of the thinnest CoO.

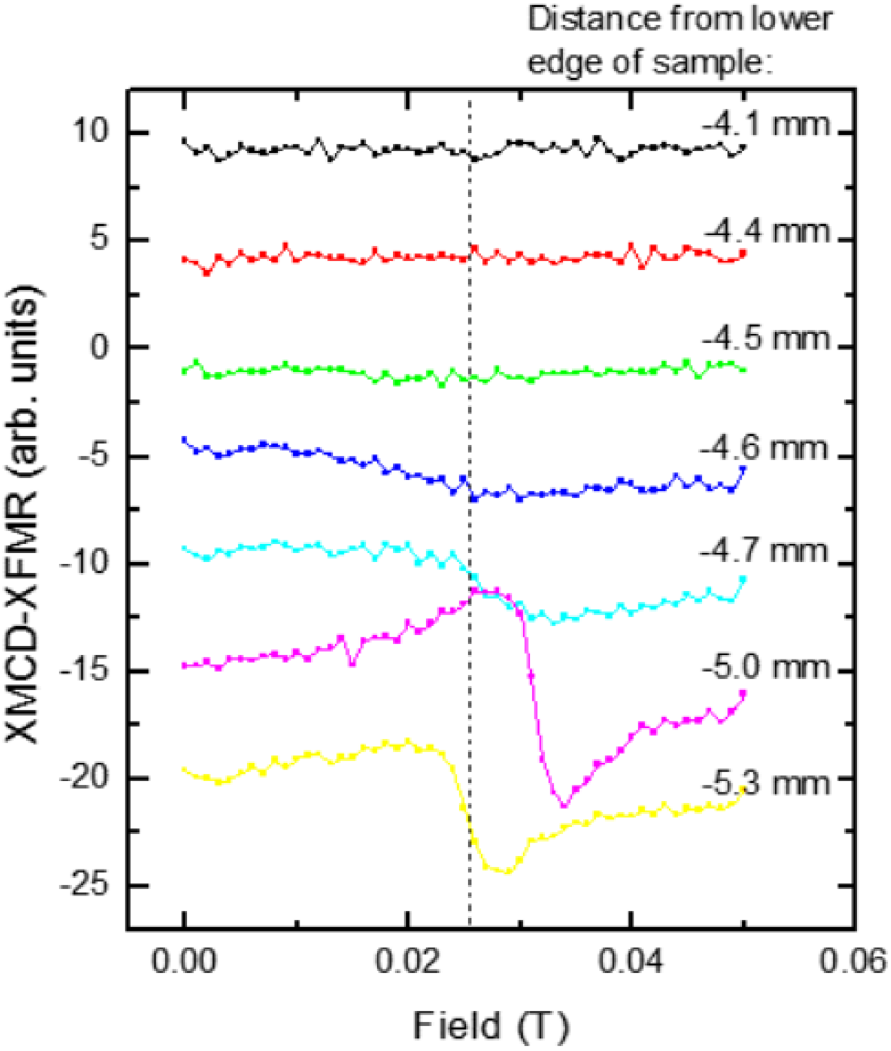

Figure 8.14: Fe XMCD-XFMR measured at 6 GHz along a small range of the CoO wedge. A shift in the position of the FMR signal, along with an increase of the linewidth, is observed for positions between 5.0 mm and 4.5 mm from the lower edge of the sample. Figure 8.11 shows that these positions lie within the very thinnest part of the CoO wedge, and Figure 8.12 shows that for these positions a field-rotatable XMLD is observed.

situation is more complicated as one has the freedom to use any arbitrary axis for the linearly polarised x- rays within the yz-plane (see Figure 8.1). The XMLD spectrum is anisotropic,[140] i.e. its line shape depends on the relative orientation of the magnetisation direction, the linear light polarisation and the crystalline axes. For a cubic lattice structure there are two principal XMLD spectra while for an arbitrary measurement, some admixture of these spectra will be observed.[140]

Without *a priori* knowledge of the photon energy at which the dynamic XMLD signal is largest, measurements began by studying XMLD-XFMR with varied energy at a fixed bias field. The bias field was fixed to the value found for resonance in XMCD-XFMR, and the x-ray polarisation was set as linear vertical, parallel with the CoO $[110]$ axis. Figure 8.15 on the next page shows XMLD-XFMR spectra recorded around the Co L_3 edge at four positions along the wedge. No evidence of a dynamic XMLD signal was found.

In order to study the FMR shift for a region of thicker CoO, where the XMLD signal should be stronger, the temperature was increased slightly to 260 K. At this time the anisotropy of the static Co XMLD spectra was measured to inform the optimum geometry for XMLD-XFMR measurements. Figure 8.16(a) on page 227 shows Co XMLD spectra recorded with varied angle of x-ray linear polarisation axis, where 0° is horizontal polarisation. In Figure 8.16(b) the XMLD signal at 778.05 eV is plotted as a function of x-ray linear polarisation axis angle, with the red curve showing a sinusoidal fit with a period of 180°. From this plot it can be seen that the XMLD signal varies most strongly with CoO spin orientation for a polarisation of 45° from the vertical and the CoO $[110]$ axis, at an energy of 778.05 eV.

The Fe XMCD-XFMR at 6 GHz along the CoO wedge at the higher temperature of 260 K is shown in Figure 8.17 on page 228. There is a clear shift in the FMR position and linewidth between 4.6 mm and 3.6 mm from the lower edge of the sample. Dynamic XMLD-XFMR field scans recorded at the same frequency in this range are shown in Figure 8.18 on page 229, with the left and right panels

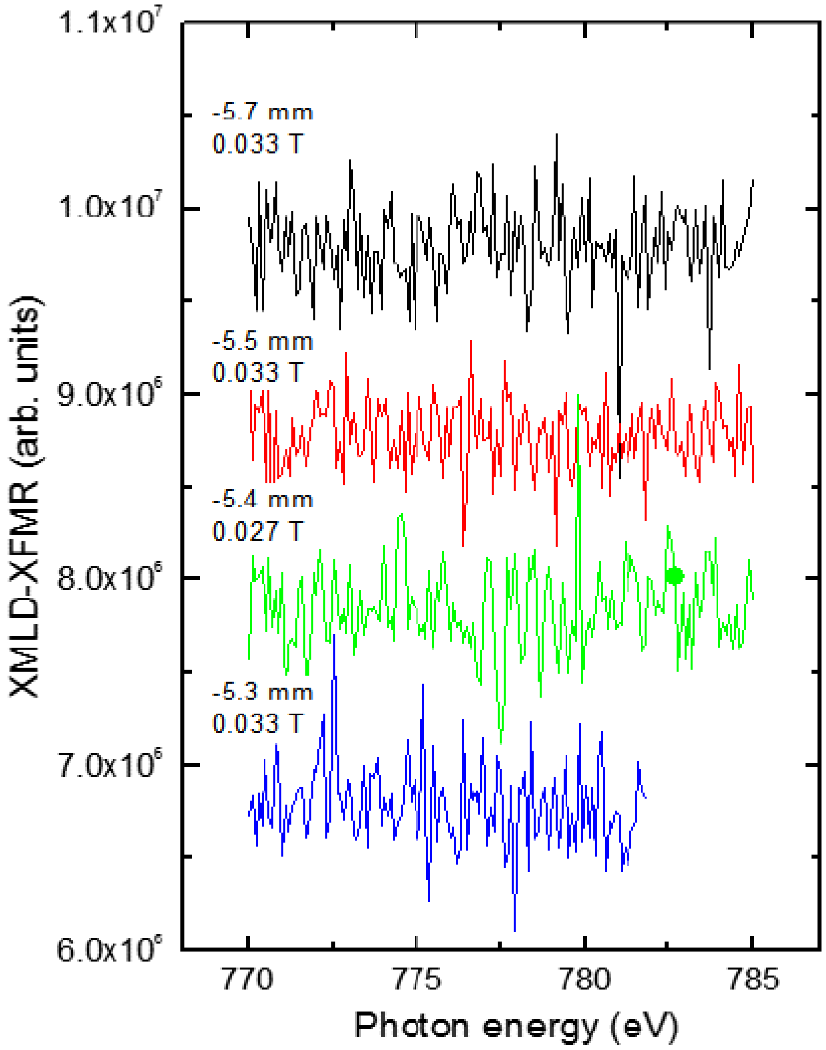

Figure 8.15: XMLD-XFMR energy scans recorded at positions along the wedge showing an FMR shift. Incident x-rays were linearly polarised with vertical polarisation axis, parallel with the CoO $[110]$ axis and the bias field. The bias field was set to the FMR field identified in Fe XMCD-XFMR measurements. No XMLD-XFMR signal was observed.

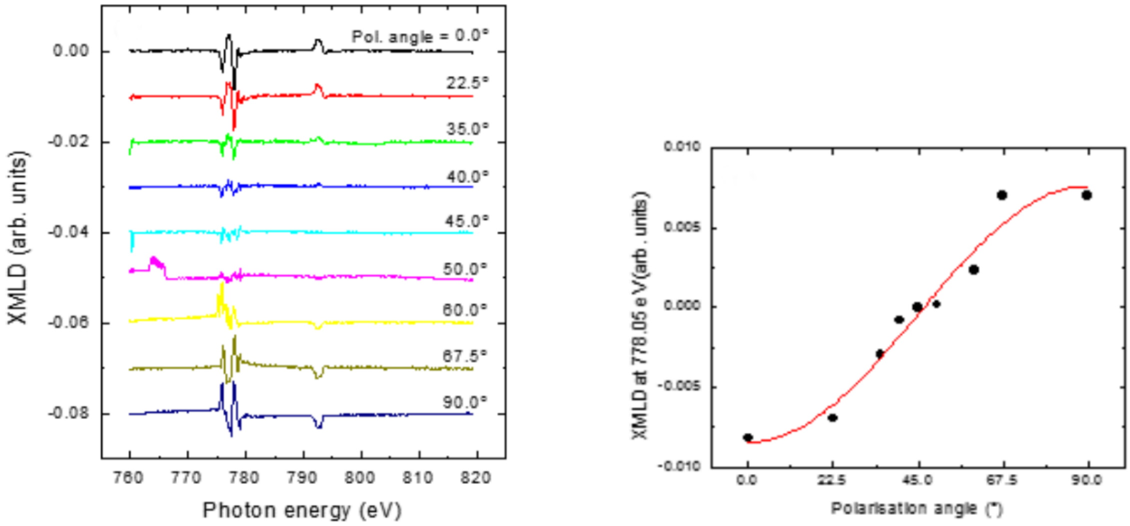

(a) XMLD spectra at different polarisation angles

(b) XMLD at 778.05 eV as a function of polarisation angle

Figure 8.16: (a) Co XMLD recorded with varied angle of linear polarisation axis at 260 K. The polarisation axis angle is measured with respect to the horizontal, with 90° as vertical polarisation, parallel with the CoO $[110]$ axis. At each angle the XMLD spectrum is recorded as the difference between two XAS spectra with in-plane 0.4 T bias field rotated through 90°. (b) XMLD at 778.05 eV plotted as a function of polarisation angle, with a sinusoidal fit with a period of 180°.

showing field scans recorded with the phase of the driving microwaves shifted by 90°. The signal-to-noise ratio is very small, but one can see evidence of a dynamic XMLD, particularly at a position 4.3 mm from the sample edge. For the green experimental data at a position of 4.3 mm, the blue curves highlight the expected real and imaginary line shapes. While weak, this is the first evidence that antiferromagnetic spins are dynamically coupled to precessing ferromagnetic spins during FMR.

8.4 Conclusions

The static magnetic properties of a CoO / Fe / NiFe trilayer have been thoroughly characterised, providing element-specific information that can only be obtained by means of x-ray spectroscopy. Static characterisation of the magnetic state was a prerequisite for time-resolved XFMR studies, and was needed to interpret

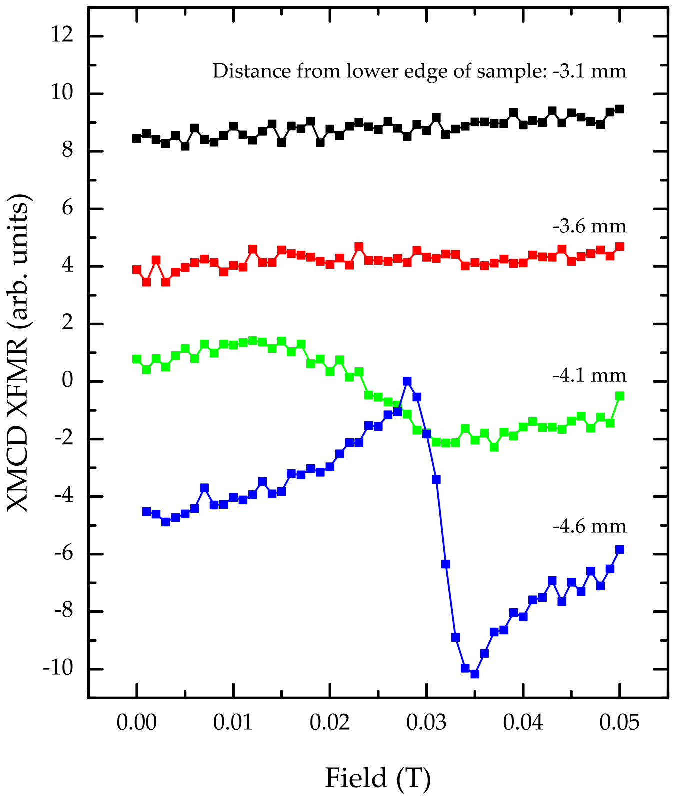

Figure 8.17: Fe XMCD-XFMR recorded along a small length of the CoO wedge, showing a shift in position and width of the FMR signal as the CoO thickness is increased.

time resolved MOKE measurements. It has been confirmed that it is possible to record XMLD in the geometry that is required for XFMR measurements. This was an important step towards the characterisation of magnetisation dynamics at the CoO / Fe interface by time-resolved XMLD. In addition, the static data provide invaluable feedback to our collaborators at University of California Berkeley to support their fabrication processes.

The influence of spin ordering in antiferromagnetic CoO on the dynamics in an adjacent Fe / $Ni_{81}Fe_{19}$ bilayer have also been studied. It has been shown that a small amount of ordered CoO significantly modifies the resonance field and linewidth of the adjacent ferromagnetic layers. The interfacial interaction leading to the modified resonance condition is currently not well understood. Direct measurement of interacting dynamics in the ferromagnetic and antiferromagnetic layers is required to confirm the underlying mechanisms. XMCD-XFMR has been used

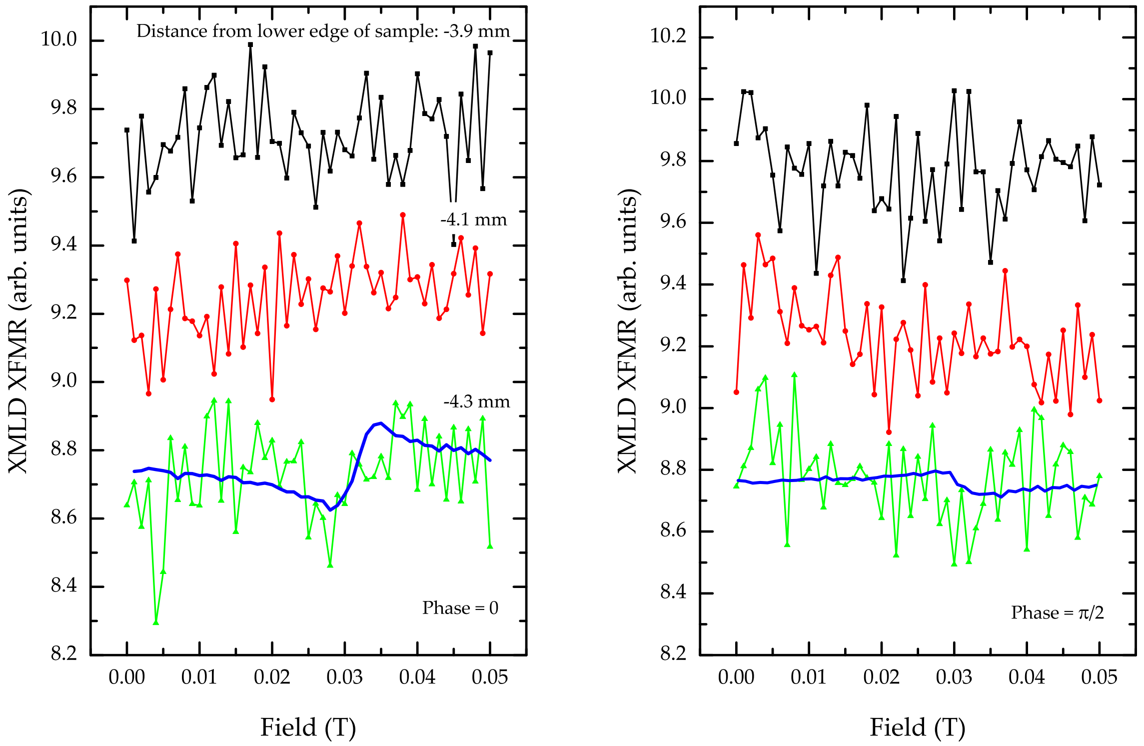

Figure 8.18: Co XMLD-XFMR recorded for a section of the CoO wedge which showed a shift in the Fe / Ni$_{81}$Fe$_{19}$ FMR position. XMLD-XFMR was recorded as a function of bias field strength, with the left and right panels showing two cases with the phase of the 6 GHz driving signal shifted by 90°. At a position 4.3 mm from the lower edge of the sample a weak FMR peak may be observed, with line shape changing as expected for a 90° phase shift. The blue curve shows the XMCD-XFMR signal recorded at a position 4.3 mm from the lower edge of the sample, previously shown in Figure 8.17. Note that the two features share a similar centre and width, providing further evidence that this is indeed the dynamic XMLD response.

to make phase-resolved measurements of precessing Fe moments at positions along a wedged-thickness CoO layer. By applying XMLD-XFMR, antiferromagnetic CoO spins precessing in phase with ferromagnetic Fe moments have been observed. However, this phenomenon can only be observed in a small region of a large parameter space, and despite associated challenges with temperature and position stability, the first evidence of antiferromagnetic spins precessing in phase with an adjacent ferromagnet undergoing FMR has been demonstrated. The next step for this project, now that the range of relevant CoO thicknesses and temperatures has been determined, is to produce either a much shallower wedge or a range of simple trilayer samples focused on this interesting range for further investigation.

CHAPTER 9

Summary and future work

This thesis has presented the results of a number of studies using both optical and x-ray probes to investigate magnetic properties and spin dynamics on the nano scale. These techniques have been applied to both commercial structures, in the form of consumer hard disk drive write heads, and materials of great interest to the emerging world of spintronic data recording and storage.

9.1 Hard disk drive write heads

In Chapter 4 static XPEEM and dynamic TRSKM measurements of different geometric designs of hard disk drive write heads were presented, allowing the role of shape anisotropy in determining the equilibrium state of different writer designs to be determined. Comparing XPEEM measurements across nominally identical writers, as well as under the influence of an applied bias field, allowed evaluation of the stability of the equilbrium state for each writer shape. The equilibrium state inferred from TRSKM measurements was compared to that measured directly by XPEEM for each writer design, and the role of that equilibrium state in the observed dynamics was considered. XPEEM and TRSKM measurements were found to be in agreement, with XPEEM further revealing that crystalline anisotropy dominates the equilibrium state of these write heads, but the competition between shape and crystalline anisotropy determines how stable and repeatable that equilibrium state is.

TRSKM was also applied to the measurement of flux propagation in hard disk write heads in Chapter 5, focusing on the flux dynamics during the rise of the driving pulse delivered through different coil geometries. In contrast to the previous belief that flux formed and propagated in uniform "beams", the increased time resolution presented here revealed considerable non-uniformities in the observed dynamics on the picosecond timescale, and between nominally identical writers. This suggests that the equilibrium magnetic state of an individual writer can be of the same importance as the spatial distribution of the driving coils, and therefore the driving field.

There are a number of potential paths for future work in this area to take. Firstly, the driving pulses used during TRSKM measurements presented here were in the form of a square wave. This is not strictly prototypical, with consumer devices often incorporating an initial amplitude overshoot in the pulse.[75] Such an overshoot ensures sufficient flux is generated to saturate the media in areas of rapid bit transitions, while also allowing a lower 'baseline' pulse amplitude so as to prevent far-track erasures in areas of fewer bit transitions. There is considerable potential in investigating the role of, for example, different amplitudes and durations of overshoot in the observed dynamics.

Secondly, while the static XPEEM measurements presented in this thesis have provided a direct measurement of the equilibrium state of these hard disk write heads, the dynamics have been observed only with TRSKM. The success of static XPEEM measurements opens the door to time-resolved XPEEM measurements to directly measure the flux dynamics, particularly in the nanoscale pole tip, during a write pulse. The duration of the dynamics (i.e. the time taken to relax to equilibrium) would necessitate the use of single-bunch mode at either BESSY II or DLS, along with consistent triggering of the driving current relative to the arrival of the photons.

Finally, the write heads studied throughout this project have been relatively simple perpendicular recording heads. A logical next step would be to apply these same measurement techniques to write heads used with newer, emerging recording technologies. Shingled magnetic recording, for example, typically employs a substantially different write head geometry to those studied here to account for the overlapping data tracks in the media. Understanding the different flux dynamics caused by these changes in geometry would allow data density and data recording rates to be increased.

9.2 Spin pumping in Co_2MnGe / Ag / $Ni_{81}Fe_{19}$ spin valves

In Chapter 6 x-ray measurements of spin pumping and STT in Co_2MnGe / Ag / $Ni_{81}Fe_{19}$ spin valve structures were presented. Phase-resolved XFMR measurements provided element-specific measurements, allowing separation of the time-dependent spin states in the source and sink layers. This offered an extra level of detail beyond that available with VNA-FMR, revealing clear signs of spin pumping due to STT between the layers. XFMR measurements also supported macrospin modelling, leading to the extraction of the spin mixing conductance.

The other layers of the stack surrounding the spin valve of interest may potentially be a source of additional spin scattering which has not been accounted for. Further work in this area may systematically investigate the effect of these layers experimentally, with stack structures either changing the thickness of these layers, or removing them entirely. Alternatively or additionally, further work could be undertaken to improve the macrospin model to include the spin scattering of these layers.

9.3 Spin dynamics of thin film yttrium iron garnet

Chapter 7 detailed static and time-resolved x-ray spectroscopy of thin-film YIG in the context of VNA-FMR measurements on the same sample. While dynamic XMCD spectra of Co within the sample were as expected, XMCD spectra of the Fe within the ferrimagnetic YIG showed significant differences when measured dynamically compared to their corresponding static spectra. The differences, not typically observed in ferromagnetic materials, may hint at a phase difference between spin precession of Fe located on tetrahedral and octahedral sites within the YIG lattice. However, despite consideration of a number of potential origins for this discrepancy, the true source of the difference could not be identified. Further research is needed to confirm the source of this difference, and any necessary corrective analysis, before firm conclusions can be drawn.

9.4 Spin pumping in CoO / Fe / $Ni_{81}Fe_{19}$ trilayers

In Chapter 8 the spin dynamics of antiferromagnetic CoO being driven by interfacial coupling to ferromagnetic $Ni_{81}Fe_{19}$ were studied by time-resolved MOKE, static XMCD and XMLD, and dynamic XMCD XFMR. Phase-resolved measurements of precessing Fe moments adjacent to different CoO layer thicknesses revealed that a small amount of ordered antiferromagnetic CoO significantly modifies the resonant field and linewidth of the adjacent ferromagnetic layer. The first evidence of antiferromagnetic CoO spins precessing in phase with ferromagnetic Fe was also demonstrated.

A difficulty in measuring these samples stems from the very narrow range of conditions in which the resonant field and linewidth are modified, while remaining within the accessible range of XFMR. Now that the interesting range has been identified, the wedged samples could be replaced with a series of trilayer samples, each having a different fixed CoO layer thickness. Minor changes in temperature, for example, could also be investigated with relative ease while largely eliminating problems associated with thermalisation and x-ray beam instability.

Bibliography

[1] D. Huylebrouck. The bone that began the space odyssey. *The Mathematical Intelligencer* **18**, 56–60 (1996) (cited on page 47).

[2] M. Hilbert, and P. López. The world's technological capacity to store, communicate and compute information. *Science* **332**, 60–65 (2011) (cited on page 47).

[3] Seagate Technology. *Seagate reaches one terabit per square inch milestone in hard drive storage with new technology demonstration*. Retrieved 2017-06-02. (2012) `http://www.seagate.com/gb/en/about-seagate/news/terabit-milestone-storage-seagate-master-pr/` (cited on page 47).

[4] R. P. Feynman, R. B. Leighton, and M. Sands. *The Feynman lectures on physics*. Vol. 2 (Addison-Wesley. Reading, MA. 1977) Chap. 37—Magnetic Materials, pages 1–13 (cited on pages 52, 59).

[5] J. F. Schenck. The role of magnetic susceptibility in magnetic resonance imaging: MRI magnetic compatibility of the first and second kinds. *Medical Physics* **23**, 815–850 (1996) (cited on pages 56 sq.).

[6] H. D. Young, R. A. Freedman, and A. L. Ford. *University physics* (Pearson Addison-Wesley. 2008) (cited on page 56).

[7] A. Aharoni. *Introduction to the theory of ferromagnetism*. International Series of Monographs on Physics (Oxford University Press. Oxford, UK. 2000) (cited on pages 57, 74).

[8] P. Weiss. La variation du ferromagnetisme du temperature. *Comptes Rendus* **143**, 1136–1149 (1906). Cited in B. D. Cullity, and C. D. Graham. *Introduction to magnetic materials*. edited by L. Hanzo. 2nd edition (IEEE Press. Piscataway, NJ. 2009) (cited on page 57).

[9] F. Bitter. On inhomogeneities in the magnetization of ferromagnetic materials. *Physical Review* **38**, 1903 (1931) (cited on page 57).

[10] P. Curie. Lois expérimentales du magnétisme: propriétés magnétiques des corps à diverses températures. *Annales de chimie et de physique* **5**, 289–405 (1895). Cited in R. F. Mould. Pierre Curie, 1859–1906. *Current Oncology* **14**, 74–82 (2007) (cited on page 58).

[11] A. H. Morrish. *The physical principles of magnetism* (IEEE Press. 2001) (cited on pages 58, 70).

[12] S. Weinberg. The quantum theory of fields. in. Vol. 1 (Cambridge University Press. Cambridge, UK. 1995) Chap. 10.6—Electromagnetic Form Factors and Magnetic Moment, pages 452–456 (cited on page 59).

[13] P. Hofmann. *Solid state physics: an introduction* (Weinheim, Germany. 2008) (cited on page 61).

[14] E. C. Stoner. Collective electron specific heat and spin paramagnetism in metals. *Proceedings of the Royal Society of London. Series A - Mathematical and Physical Sciences* **154**, 656–678 (1936) (cited on page 62).

[15] G. Bertotti. Hysteresis in magnetism. in (Academic Press. San Diego, CA. 1998) Chap. 1—Magnetic Hysteresis, pages 3–30 (cited on page 65).

[16] E. C. Stoner, and E. P. Wohlfarth. A mechanism of magnetic hysteresis in heterogeneous alloys. *Philosophical Transactions of the Royal Society of London A* **240**, 599–642 (1948) (cited on page 65).

[17] W. F. Brown. Thermal fluctuations of a single-domain particle. *Physical Review* **130**, 1677–1686 (1963) (cited on page 65).

[18] J. Stöhr, and H. C. Siegmann. Magnetism: from fundamentals to nanoscale dynamics. in (Springer Science+Business Media. New York, NY. 2006) Chap. 11—The Spontaneous Magnetization, Anisotropy, Domains, pages 479–520 (cited on pages 65–67, 71).

[19] A. Hubert, and R. Schäfer. *Magnetic domains: the analysis of magnetic microstructures*. Third (Springer Science+Business Media. Berlin. 2009), pages 23–48 (cited on pages 66, 71, 84 sq., 88).

[20] R. M. Bozorth. Ferromagnetism. in (D. van Nostrand Company. Princeton, NJ. 1964) Chap. 18—Special Problems in Domain Theory, pages 811–837 (cited on pages 69, 73).

[21] G. Bertotti. Hysteresis in magnetism. in (Academic Press. San Diego, CA. 1998) Chap. 7—Magnetic Domains and Domain Walls, pages 189–221 (cited on page 69).

[22] R. Carey, and E. D. Isaac. Magnetic domains and techniques for their observation. in (The English Univsersities Press. London. 1966) Chap. 1—Contributions to the Free Energy of a Magnetic System, pages 1–17 (cited on page 72).

[23] A. Viallix, F. Boileau, R. Klein, J. J. Niez, and P. Baras. A new method for finite element calculation of micromagnetic problems. *IEEE Transactions on Magnetics* **24**, 2371–2373 (1988) (cited on page 74).

[24] T. L. Gilbert. A phenomenological theory of damping in ferromagnetic materials. *IEEE Tranactions on Magnetics* **40**, 3443–3449 (2004) (cited on page 74).

[25] E. Grochowski. A commercial IBM giant magnetoresistance read head. Vision for nanotechnology in the next decade. in *Nanotechnology research directions: IWGN workshop report*. edited by M. C. Roco, R. S. Williams, and P. Alivisatos (Kluwer Academic. Dordrecht, The Netherlands. 2001) Chap. 6.7.5—A Commercial IBM Giant Magnetoresistance Read Head, page 124 (cited on page 76).

[26] M. Mallary. Recording head design. in *The physics of ultra-high-density magnetic recording*. edited by M. L. Plumer, J. van Ek, and D. Weller (Springer Science+Business Media. Berlin Heidelberg. 2001) Chap. 11—Recording Head Design, pages 314–348 (cited on pages 76, 81, 95, 148).

[27] A. Taratorin. Magnetic recording systems and measurement. in (Guzik Technical Enterprises. San Jose, CA. 2004) Chap. 7—Perpendicular Recording, pages 155–192 (cited on page 77).

[28] HGST. *Perpendicular magnetic recording technology*. Whitepaper (Western Digital. San Jose, CA. 2007-11) (cited on page 77).

[29] O. Ozatay, P. G. Mather, J.-U. Thiele, T. Hauet, and P. M. Braganca. Handbook of nanoscale optics and electronics. in. edited by G. Wiederrecht (Academic Press. 2009) Chap. 7—Spin-Based Data Storage, pages 239–292 (cited on page 78).

[30] R. Wood, M. Williams, A. Kavcic, and J. Miles. The feasibility of magnetic recording at 10 terabits per square inch on conventional media. *IEEE Transactions on Magnetics* **45**, 917–923 (2009) (cited on page 79).

[31] L. Pan, and D. B. Bogy. Data storage: heat-assisted magnetic recording. *Nature Photonics* **3**, 189–190 (2009) (cited on page 80).

[32] S. N. Piramanayagam. Perpendicular recording media for hard disk drives. *Journal of Applied Physics* **102**, 011301–011322 (2007) (cited on page 80).

[33] J. Kerr. On rotation of the plane of polarization by reflection from the pole of a magnet. *Philosophical Magazine Series 5* **3**, 321–343 (1877) (cited on page 84).

[34] H. J. Williams, F. G. Foster, and E. A. Wood. Observation of magnetic domains by the Kerr effect. *Physical Review* **82**, 119–120 (1951) (cited on page 84).

[35] M. J. Freiser. A survey of magnetooptic effects. *IEEE Transactions on Magnetics* **4**, 152–161 (1968) (cited on page 85).

[36] W. Wettling. Magneto-optics of ferrites. *Journal of Magnetism and Magnetic Materials* **3**, 147–160 (1976) (cited on page 85).

[37] G. S. Krinchik, and G. M. Nurmukhamedov. Magnetization of a ferromagnetic metal by the magnetic field of light waves. *Soviet Physics JETP* **20**, 520–521 (1965) (cited on page 85).

[38] C.-Y. You, and S.-C. Shin. Derivation of simplified analytic formulae for magnetooptical Kerr effects. *Applied Physics Letters* **69**, 1315–1317 (1996) (cited on page 85).

[39] J. Wu, J. R. Moore, and R. J. Hicken. Optical pump-probe studies of the rise and damping of ferromagnetic resonance oscillations in a thin Fe film. *Journal of Magnetism and Magnetic Materials* **222**, 189–198 (2000) (cited on page 85).

[40] Z. Q. Qiu, and S. D. Bader. *Nonlinear optics in metals*. edited by K. H. Bennemann. International series of monographs on physics 98 (Oxford University Press. Oxford. 1998) (cited on pages 86, 88).

[41] H. R. Hulme. The Faraday effect in ferromagnetics. *Proceedings of the Royal Society of London Series A, Containing Papers of a Mathematical and Physical Character* **135**, 237–257 (1932) (cited on page 88).

[42] P. N. Argyres. Theory of the Faraday and Kerr effects in ferromagnetics. *Physical Review* **97**, 334–345 (1955) (cited on page 88).

[43] H. S. Bennett, and E. A. Stern. Faraday effect in solids. *Physical Review* **137**, A448–A461 (1965) (cited on page 88).

[44] J. L. Erskine, and E. A. Stern. Magneto-optic Kerr effects in gadolinium. *Physical Review B* **8**, 1239–1255 (1973) (cited on page 88).

[45] Hinds Instruments. *Magneto optic Kerr effect application notes*. Hinds Instruments (Hillsboro, OR. 2010) (cited on page 88).

[46] P. S. Keatley, V. V. Kruglyak, R. J. Hicken, J. R. Childress, and J. A. Katine. Acquisition of vector hysteresis loops from micro-arrays of nano-magnets. *Journal of Magnetism and Magnetic Materials* **306**, 298–301 (2006) (cited on page 91).

[47] W. Yu, P. S. Keatley, R. J. Hicken, M. A. Gubbins, P. J. Czoschke, and R. Lopusnik. Effect of coil position on magnetization dynamics of multilayered hard disk writer yokes. *IEEE Transactions on Magnetics* **49**, 3741–3744 (2013) (cited on pages 93, 110).

[48] M. R. Freeman, and J. F. Smyth. Picosecond time-resolved magnetization dynamics of thin-film heads. *Journal of Applied Physics* **79**, 5898–5900 (1996) (cited on pages 94, 110, 139).

[49] M. R. Freeman, A. Y. Elezzabi, and J. A. H. Stotz. Current dependence of the magnetization rise time in thin film heads. *Journal of Applied Physics* **81**, 4516–4518 (1997) (cited on pages 94, 110).

[50] M. R. Freeman, G. M. Steeves, G. E. Ballentine, and A. Krichevsky. Noise imaging using magneto-optical sampling techniques. *Journal of Applied Physics* **91**, 7326–7330 (2002) (cited on pages 94, 110).

[51] P. Gangmei, P. S. Keatley, W. Yu, R. J. Hicken, M. A. Gubbins, P. J. Czoschke, and R. Lopusnik. Time- and vector-resolved Kerr microscopy of hard disk writers. *Applied Physics Letters* **99**, 232503 (2011) (cited on pages 95 sq., 110, 138).

[52] K. Siegbahn. From X-ray to electron spectroscopy and new trends. *Journal of Electron Spectroscopy and Related Phenomena* **51**, 11–36 (1990) (cited on page 95).

[53] A. Barinov, P. Dudin, L. Gregoratti, A. Locatelli, T. O. Menteş, M. Á. Niño, and M. Kiskinova. Synchrotron-based photoelectron microscopy. *Nuclear Instruments & Methods in Physics Research, Section A: Accelerators, Spectrometers, Detectors, and Associated Equipment* **601**, 195–202 (2009) (cited on page 95).

[54] T. Warwick, A. Harald, A. P. Hitchcock, H. Padmore, E. G. Rightor, and B. P. Tonner. Soft X-ray spectromicroscopy development for materials science at the Advanced Light Source. *Journal of Electron Spectroscopy and Related Phenomena* **84**, 85–98 (1997) (cited on page 97).

[55] A. Locatelli, and E. Bauer. Recent advances in chemical and magnetic imaging of surfaces and interfaces by XPEEM. *Journal of Physics: Condensed Matter* **20**, 093002 (2008) (cited on page 97).

[56] J. Stöhr. *Synchrotron radiation techniques — magnetic dichroism*. Retrieved 2013-11-15. Stanford Synchrotron Radiation Lightsource. (2002) `http://www-ssrl.slac.stanford.edu/stohr/xmcd.htm` (cited on page 98).

[57] M. Newville. *Fundamentals of XAFS*. University of Chicago. (2004-07) `http://web.archive.org/web/20160913000638/http://xafs.org/Tutorials?action=AttachFile&do=get&target=Newville_xas_fundamentals.pdf` (cited on page 97).

[58] J. Stöhr. X-ray magnetic circular dichroism spectroscopy of transition metal thin films. *Journal of Electron Spectroscopy and Related Phenomena* **75**, 253–272 (1995) (cited on page 102).

[59] W. L. O'Brien, and B. P. Tonner. Orbital and spin sum rules in x-ray magnetic circular dichroism. *Physical Review B: Condensed Matter and Materials Physics* **50**, 672–681 (1994) (cited on pages 103 sq.).

[60] B. T. Thole, P. Carra, F. Sette, and G. van der Laan. X-Ray circular dichroism as a probe of orbital magnetization. *Physical Review Letters* **68**, 1943–1946 (1992) (cited on page 103).

[61] P. Carra, B. T. Thole, M. Altarelli, and X. Wang. X-Ray circular dichroism and local magnetic fields. *Physical Review Letters* **70**, 694–697 (1993) (cited on page 103).

[62] R. Wu, D. Wang, and A. J. Freeman. First principles investigation of the validity and range of applicability of the x-ray magnetic circular dichroism sum rule. *Physical Review Letters* **71**, 3581–3584 (1993) (cited on page 104).

[63] O. Eriksson, A. M. Boring, R. C. Albers, G. W. Fernando, and B. R. Cooper. Spin and orbital contributions to surface magnetism in $3d$ elements. *Physical Review B: Condensed Matter and Materials Physics* **45**, 2868–2875 (1992) (cited on page 104).

[64] F. Kleimeier. *Untersuchung von organischen Schichten mit PEEM, AG Prof. Zacharias, Physikalisches Institut, WWU Münster*. (2014-09) `www.uni-muenster.de/Physik.PI/Zacharias/research/organic_layers/peem/peem.html` (cited on page 107).

[65] R. A. J. Valkass, W. Yu, L. R. Shelford, P. S. Keatley, T. H. J. Loughran, R. J. Hicken, S. A. Cavill, G. van der Laan, S. S. Dhesi, M. A. Bashir, M. A. Gubbins, P. J. Czoschke, and R. Lopusnik. Imaging the equilibrium state and magnetization dynamics of partially built hard disk write heads. *Applied Physics Letters* **106**, 232404 (2015) (cited on pages 109, 138, 147).

[66] R. E. Fontana, S. R. Hetzler, and G. Decad. Technology roadmap comparisons for TAPE, HDD, and NAND flash: implications for data storage applications. *IEEE Transactions on Magnetics* **48**, 1692–1696 (2012) (cited on pages 109, 137).

[67] O. Heinonen, A. Nazarov, and M. L. Plumer. Dynamics of laminated write elements. *Journal of Applied Physics* **99**. 08S302, 08S302 (2006) (cited on page 109).

[68] F. H. Liu, and M. H. Kryder. Dynamic domain instability and popcorn noise in thin-film heads. *Journal of Applied Physics* **75**, 6391–6393 (1994) (cited on pages 109, 137).

[69] Z. Guo, and E. Della Torre. Effect of head domain asymmetry on a recording track. *IEEE Transactions on Magnetics* **32**, 1136–1139 (1996) (cited on page 110).

[70] W. Yu, P. Gangmei, P. S. Keatley, R. J. Hicken, M. A. Gubbins, P. J. Czoschke, and R. Lopusnik. Time resolved scanning Kerr microscopy of hard disk writer structures with a multilayered yoke. *Applied Physics Letters* **102**. 162407, 162407 (2013) (cited on pages 110, 115, 138).

[71] K. Fukumoto, W. Kuch, J. Vogel, F. Romanens, S. Pizzini, J. Camarero, M. Bonfim, and J. Kirschner. Dynamics of magnetic domain wall motion after nucleation: dependence on the wall energy. *Physical Review Letters* **96**, 097204 (2006) (cited on page 110).

[72] J. J. Kim, K. Hirata, Y. Ishida, D. Shindo, M. Takahashi, and A. Tonomura. Magnetic domain observation in writer pole tip for perpendicular recording head by electron holography. *Applied Physics Letters* **92**, 162501 (2008) (cited on page 110).

[73] A. Taratorin, and K. Klaassen. Media saturation and overwrite in perpendicular recording. *IEEE Transactions on Magnetics* **42**, 157–162 (2006) (cited on pages 110 sq.).

[74] P. Czoschke, S. Kaka, N. J. Gokemeijer, and S. Franzen. Real-time direct measurement of field rise time and dynamic instability of perpendicular writers. *Applied Physics Letters* **97**, 242504 (2010) (cited on pages 110 sq.).

[75] J. Contreras, S. Y. Garzon, W. M. Hanson, and R. A. Zakai. Magnetic recording disk drive with write current overshoot amplitude (OSA) responsive to data transitions. US 9111561 B1 (2015-08) (cited on pages 119, 232).

[76] M. L. Mallary. Conduction of flux at high frequencies in permalloy strips by small-angle rotations. *Journal of Applied Physics* **57**, 3952–3954 (1985) (cited on pages 130, 134, 138, 142, 148, 151).

[77] C. Daboo, J. A. C. Bland, R. J. Hicken, A. J. R. Ives, and M. J. Baird. Vectorial magnetometry with the magneto-optic Kerr and effect applied to Co/Cu/Co trilayer structures. *Physical Review B: Condensed Matter and Materials Physics* **47**, 11852 (1993) (cited on page 131).

[78] D. Z. Bai, J.-G. Zhu, P. Luo, K. Stoev, and F. Liu. Writer pole tip remanence in perpendicular recording. *IEEE Transactions on Magnetics* **42**, 473–480 (2006) (cited on page 135).

[79] R. A. J. Valkass, T. M. Spicer, E. Burgos Parra, R. J. Hicken, M. A. Bashir, M. A. Gubbins, P. J. Czoschke, and R. Lopusnik. Time-resolved scanning Kerr microscopy of flux beam formation in hard disk write heads. *Journal of Applied Physics* **119**, 233903 (2016) (cited on page 137).

[80] S. Iwasaki. Perpendicular magnetic recording—its development and realization. *Journal of Magnetism and Magnetic Materials* **324**, 244–247 (2012) (cited on page 137).

[81] S. Creedy. Big data 'to change industry'. *The Australian*. 15th November 2014 (cited on page 137).

[82] C. Carter. Players large and small vie for slice of big data pie. *The Australian*. 17th March 2015 (cited on page 137).

[83] M. S. Patwari, and R. H. Victora. Simulation of erase after write on 2.4 T FeCo solid pole writer. *IEEE Tranactions on Magnetics* **46**, 1212–1219 (2010) (cited on page 137).

[84] H. J. Richter. The transition from longitudinal to perpendicular recording. *Journal of Physics D: Applied Physics* **40**, R149–R177 (2007) (cited on page 138).

[85] W. W. Clegg, N. A. E. Heyes, E. W. Hill, and C. D. Wright. Development of a scanning laser microscope for magneto-optic studies of thin films. *Journal of Magnetism and Magnetic Materials* **95**, 49–57 (1991) (cited on page 141).

[86] W. K. Hiebert, A. Stankiewicz, and M. R. Freeman. Direct observation of magnetic relaxation in a small permalloy disk by time-resolved scanning kerr microscopy. *Physical Review Letters* **79**, 1134–1137 (1997) (cited on page 139).

[87] A. Barman, V. V. Kruglyak, R. J. Hicken, A. Kundrotaite, and M. Rahman. Anisotropy, damping, and coherence of magnetization dynamics in a $10\,\mu\mathrm{m}$ square $\mathrm{Ni}_{81}\mathrm{Fe}_{19}$ element. *Applied Physics Letters* **82**, 3065 (2003) (cited on page 139).

[88] A. Neudert, P. S. Keatley, V. V. Kruglyak, J. McCord, and R. J. Hicken. Excitation and imaging of precessional modes in soft-magnetic squares. *IEEE Transactions on Magnetics* **44**, 3083–3086 (2008) (cited on page 139).

[89] Y. Kanai, R. Matsubara, H. Watanabe, H. Muraoka, and Y. Nakamura. Recording field analysis of narrow-track SPT head with side shields, tapered main pole, and tapered return path for $1\,\mathrm{Tbit\,in}^{-2}$. *IEEE Transactions on Magnetics* **39**, 1955–1960 (2003) (cited on page 150).

[90] R. A. J. Valkass, L. Shelford, C. Durrant, R. Hicken, A. I. Figueroa, A. Baker, G. van der Laan, P. Shafer, E. Arenholz, J. Childress, and J. Katine. Effect of sink layer thickness on damping in CoMnGe/Ag/NiFe spin valves. 8th Joint European Magnetic Symposia, Glasgow. 2016 (cited on page 153).

[91] C. J. Durrant, L. R. Shelford, R. A. J. Valkass, R. J. Hicken, A. I. Figueroa, A. A. Baker, G. van der Laan, L. B. Duffy, P. Shafer, C. Klewe, E. Arenholz, S. A. Cavill, J. R. Childress, and J. A. Katine. Dependence of spin pumping and spin transfer torque upon $Ni_{81}Fe_{19}$ thickness in Ta / Ag / $Ni_{81}Fe_{19}$ / Ag / Co_2MnGe / Ag / Ta spin-valve structures. *Physical Review B* **96**, 144421 (2017) (cited on page 153).

[92] T. Yang, T. Kimura, and Y. Otani. Giant spin-accumulation signal and pure spin-current-induced reversible magnetization switching. *Nature Physics* **4**, 851–854 (2008) (cited on page 154).

[93] I. Žutić, and H. Dery. Spintronics: taming spin currents. *Nature Materials* **10**, 647–648 (2011) (cited on page 154).

[94] Y. K. Kato, R. C. Myers, A. C. Gossard, and D. D. Awschalom. Observation of the spin Hall effect in semiconductors. *Science* **306**, 1910–1913 (2004) (cited on page 154).

[95] J. Sinova, S. O. Valenzuela, J. Wunderlich, C. H. Back, and T. Jungwirth. Spin Hall effects. *Reviews of Modern Physics* **87**, 1213–1260 (2015) (cited on page 154).

[96] M. V. Costache, M. Sladkov, S. M. Watts, C. H. van der Wal, and B. J. van Wees. Electrical detection of spin pumping due to the precessing magnetization of a single ferromagnet. *Physical Review Letters* **97**, 216603 (2006) (cited on page 154).

[97] E. Saitoh, M. Ueda, H. Miyajima, and G. Tatara. Conversion of spin current into charge current at room temperature: inverse spin-Hall effect. *Applied Physics Letters* **88**, 182509 (2006) (cited on page 154).

[98] T. Kimura, Y. Otani, T. Sato, S. Takahashi, and S. Maekawa. Room-temperature reversible spin Hall effect. *Physical Review Letters* **98**, 156601 (2007) (cited on page 154).

[99] S. I. Kiselev, J. C. Sankey, I. N. Krivorotov, N. C. Emley, R. J. Schoelkopf, R. A. Buhrman, and D. C. Ralph. Microwave oscillations of a nanomagnet ddrive by a spin-polarized current. *Nature* **425**, 380–383 (2003) (cited on page 154).

[100] B. Heinrich, Y. Tserkovnyak, G. Woltersdorf, A. Brataas, R. Urban, and G. E. W. Bauer. Dynamic exchange coupling in magnetic bilayers. *Physical Review Letters* **90**, 187601 (2003) (cited on pages 154 sq., 175).

[101] J. Li, L. R. Shelford, P. Shafer, A. Tan, J. X. Deng, P. S. Keatley, C. Hwang, E. Arenholz, G. van der Laan, R. J. Hicken, and Z. Q. Qiu. Direct detection of pure ac spin current by x-ray pump-probe measurements. *Physical Review Letters* **117**, 076602 (2016) (cited on pages 155, 160).

[102] Y. Tserkovnyak, A. Brataas, and G. E. W. Bauer. Enhanced gilbert damping in thin ferromagnetic films. *Physical Review Letters* **88**, 117601 (2002) (cited on page 155).

[103] D. Wei, M. Obstbaum, M. Ribow, C. H. Back, and G. Woltersdorf. Spin Hall voltages from a.c. and d.c. spin currents. *Nature Communications* **5**, 3768 (2014) (cited on page 155).

[104] T. Gerrits, M. L. Schneider, and T. J. Silva. Enhanced ferromagnetic damping in Permalloy/Cu bilayers. *Journal of Applied Physics* **99**, 023901 (2006) (cited on page 155).

[105] X. Lou, C. Adelmann, S. A. Crooker, E. S. Garlid, J. Zhang, K. S. M. Reddy, S. D. Flexner, C. J. Palmstrøm, and P. A. Crowell. Electrical detection of spin transport in lateral ferromagnet-semiconductor devices. *Nature Physics* **3**, 197–202 (2007) (cited on page 155).

[106] J. Bass, and W. P. Pratt. TOPICAL REVIEW: Spin-diffusion lengths in metals and alloys, and spin-flipping at metal/metal interfaces: an experimentalist's critical review. *Journal of Physics Condensed Matter* **19**, 183201 (2007) (cited on page 155).

[107] Q. Yang, P. Holody, S.-F. Lee, L. L. Henry, R. Loloee, P. A. Schroeder, W. P. Pratt, and J. Bass. Spin flip diffusion length and giant magnetoresistance at low temperatures. *Physical Review Letters* **72**, 3274–3277 (1994) (cited on page 155).

[108] A. Ghosh, S. Auffret, U. Ebels, and W. E. Bailey. Penetration depth of transverse spin current in ultrathin ferromagnets. *Physical Review Letters* **109**, 127202 (2012) (cited on pages 155 sq., 158, 165, 176 sq.).

[109] R. D. McMichael, and M. D. Stiles. Magnetic normal modes of nanoelements. *Journal of Applied Physics* **97**, 10J901 (2005) (cited on page 155).

[110] P. Krone, D. Makarov, M. Albrecht, T. Schrefl, and D. Suess. Magnetization reversal processes of single nanomagnets and their energy barrier. *Journal of Magnetism and Magnetic Materials* **322**, 3771–3776 (2010) (cited on page 155).

[111] C. J. Durrant, M. Jokubaitis, W. Yu, H. Mohamad, L. R. Shelford, P. S. Keatley, G. Xiao, and R. J. Hicken. Ferromagnetic resonance of patterned chromium dioxide thin films grown by selective area chemical vapour deposition. *Journal of Applied Physics* **117**, 17B707 (2015) (cited on page 159).

[112] R. Urban, G. Woltersdorf, and B. Heinrich. Gilbert damping in single and multilayer ultrathin films: role of interfaces in nonlocal spin dynamics. *Physical Review Letters* **87**, 217204 (2001) (cited on pages 160, 163).

[113] M. K. Marcham, L. R. Shelford, S. A. Cavill, P. S. Keatley, W. Yu, P. Shafer, A. Neudert, J. R. Childress, J. A. Katine, E. Arenholz, N. D. Telling, G. van der Laan, and R. J. Hicken. Phase-resolved x-ray ferromagnetic resonance measurements of spin pumping in spin valve structures. *Physical Review B* **87**, 180403 (2013) (cited on pages 160, 174, 179, 208).

[114] M. K. Marcham, P. S. Keatley, A. Neudert, R. J. Hicken, S. A. Cavill, L. R. Shelford, G. van der Laan, N. D. Telling, J. R. Childress, J. A. Katine, P. Shafer, and E. Arenholz. Phase-resolved x-ray ferromagnetic resonance measurements in fluorescence yield. *Journal of Applied Physics* **109**, 07D353 (2011) (cited on pages 160, 208).

[115] AtlanTecRF. *Multiple frequency comb generator instrument*. AtlanTecRF. (2014-02) `https://web.archive.org/web/20160416111103/http://atlantecrf.com/pdf_downloads/Custom_Equipment/Comb-Generator.pdf` (cited on page 161).

[116] C. Bilzer, T. Devolder, P. Crozat, C. Chappert, S. Cardoso, and P. P. Freitas. Vector network analyzer ferromagnetic resonance of thin films on coplanar waveguides: comparison of different evaluation methods. *Journal of Applied Physics* **101**, 074505 (2007) (cited on page 163).

[117] C. Bilzer, T. Devolder, P. Crozat, and C. Chappert. Open-circuit one-port network analyzer ferromagnetic resonance. *IEEE Transactions on Magnetics* **44**, 3265–3268 (2008) (cited on page 163).

[118] B. Heinrich, and J. F. Cochran. Ultrathin metallic magnetic films: magnetic anisotropies and exchange interactions. *Advances in Physics* **42**, 523–639 (1993) (cited on page 164).

[119] K. Nomura, S. Kikuchi, M. Yasuda, K. Tokumitsu, and Y. Ujihira. Mössbauer study on Fe–Ag and Fe–Ni–Ag super-laminates prepared by repeated rolling and treated by gas nitriding. *Hyperfine Interactions* **148**, 307–316 (2003) (cited on page 165).

[120] N. A. Rutter. Microstructural development and superconducting parameters of the $YBa_2Cu_3O_7$ coated conductor. PhD thesis (University of Cambridge. 2001) (cited on page 165).

[121] C. Durrant. Magnetisation dynamics of nanostructured spintronic devices. PhD thesis (University of Exeter. 2017) (cited on page 175).

[122] B. Kardasz, and B. Heinrich. Ferromagnetic resonance studies of accumulation and diffusion of spin momentum density in Fe/Ag/Fe/GaAs(001) and Ag/Fe/GaAs(001) structures. *Physical Review B* **81**, 094409 (2010) (cited on page 176).

[123] Y. Tserkovnyak, A. Brataas, G. E. W. Bauer, and B. I. Halperin. Nonlocal magnetization dynamics in ferromagnetic heterostructures. *Reviews of Modern Physics* **77**, 1375–1421 (2005) (cited on page 176).

[124] S. S. P. Parkin, M. Hayashi, and L. Thomas. Magnetic domain-wall racetrack memory. *Science* **320**, 190–194 (2008) (cited on page 179).

[125] S. D. Bader, and S. S. P. Parkin. Spintronics. *Annual Review of Condensed Matter Physics* **1**, 71–88 (2010) (cited on page 179).

[126] G. B. G. Stenning, L. R. Shelford, S. A. Cavill, F. Hoffmann, M. Haertinger, T. Hesjedal, G. Woltersdorf, G. J. Bowden, S. A. Gregory, C. H. Back, P. A. J. de Groot, and G. van der Laan. Magnetization dynamics in an exchange-coupled NiFe/CoFe bilayer studied by x-ray detected ferromagnetic resonance. *New Journal of Physics* **17**, 013019 (2015) (cited on page 179).

[127] A. A. Serga, A. V. Chumak, and B. Hillebrands. YIG magnonics. *Journal of Physics D: Applied Physics* **43**, 264002 (2010) (cited on page 180).

[128] Y. Kajiwara, K. Harii, S. Takahashi, J. Ohe, K. Uchida, M. Mizuguchi, H. Umezawa, H. Kawai, K. Ando, K. Takanashi, S. Maekawa, and E. Saitoh. Transmission of electrical signals by spin-wave interconversion in a magnetic insulator. *Nature* **464**, 262–266 (2010) (cited on page 180).

[129] K. Uchida, J. Xiao, H. Adachi, J. Ohe, S. Takahashi, J. Ieda, T. Ota, Y. Kajiwara, H. Umezawa, H. Kawai, G. E. W. Bauer, S. Maekawa, and E. Saitoh. Spin Seebeck insulator. *Nature Materials* **9**, 894–897 (2010) (cited on page 180).

[130] M. Weiler, M. Althammer, M. Schreier, J. Lotze, M. Pernpeintner, S. Meyer, H. Huebl, R. Gross, A. Kamra, J. Xiao, Y.-T. Chen, H. Jiao, G. E. W. Bauer, and S. T. B. Goennenwein. Experimental test of the spin mixing interface conductivity concept. *Physical Review Letters* **111**, 176601 (2013) (cited on page 180).

[131] P. Warnicke, E. Stavitski, J.-S. Lee, A. Yang, Z. Chen, X. Zuo, S. Zohar, W. E. Bailey, V. G. Harris, and D. A. Arena. Direct observation of symmetry-specific precession in a ferrimagnet. *Physical Review B* **92**, 104402 (2015) (cited on page 180).

[132] G. Boero, S. Rusponi, P. Bencok, R. Meckenstock, J.-U. Thiele, F. Nolting, and P. Gambardella. Double-resonant x-ray and microwave absorption: atomic spectroscopy of precessional orbital and spin dynamics. *Physical Review B* **79**, 224425 (2009) (cited on pages 180 sq., 193–196, 198 sq., 202 sq.).

[133] S. R. Marmion, M. Ali, M. McLaren, D. A. Williams, and B. J. Hickey. Temperature dependence of spin Hall magnetoresistance in thin YIG/Pt films. *Physical Review B* **89**, 220404 (2014) (cited on page 181).

[134] D. D. Stancil. *Theory of magnetostatic waves* (Springer-Verlag. 1993) Chap. Appendix A, pages 210–211 (cited on page 182).

[135] V. S. Coker, N. D. Telling, G. van der Laan, R. A. D. Pattrick, C. I. Pearce, E. Arenholz, F. Tuna, R. E. P. Winpenny, and J. R. Lloyd. Harnessing the extracellular bacterial production of nanoscale cobalt ferrite with exploitable magnetic properties. *ACS Nano* **3**, 1922–1928 (2009) (cited on pages 188, 190).

[136] J. Wu, J. S. Park, W. Kim, E. Arenholz, M. Liberati, A. Scholl, Y. Z. Wu, C. Hwang, and Z. Q. Qiu. Direct measurement of rotatable and frozen CoO spins in exchange bias system of CoO/Fe/Ag(001). *Physical Review Letters* **104**, 217204 (2010) (cited on pages 206, 216, 219).

[137] W. Yu. Time resolved Kerr microscopy of materials and devices for magnetic data storage applications. PhD thesis (University of Exeter. 2014-05) (cited on page 207).

[138] R. J. Hicken, S. J. Gray, A. Ercole, C. Daboo, D. J. Freeland, E. Gu, E. Ahmad, and J. A. C. Bland. Magnetic anistropy in ultrathin epitaxial Fe / Ag (100) films with overlayers. *Physical Review B* **55**, 5898–5907 (1997) (cited on page 208).

[139] M. K. Marcham, W. Yu, P. S. Keatley, L. R. Shelford, P. Shafer, S. A. Cavill, H. Qing, A. Neudert, J. R. Childress, J. A. Katine, E. Arenholz, N. D. Telling, G. van der Laan, and R. J. Hicken. Influence of a Dy overlayer on the precessional dynamics of a ferromagnetic thin film. *Applied Physics Letters* **102**, 062418 (2013) (cited on page 208).

[140] G. van der Laan, E. Arenholz, R. V. Chopdekar, and Y. Suzuki. Influence of crystal field on anisotropic x-ray magnetic linear dichroism at the Co2+ L2,3 edges. *Physical Review B* **77**, 064407 (2008) (cited on pages 216, 219, 225).

[141] J. Li, Y. Meng, J. S. Park, C. A. Jenkins, E. Arenholz, A. Scholl, A. Tan, H. Son, H. W. Zhao, C. Hwang, Y. Z. Wu, and Z. Q. Qiu. Determination of the Fe magnetic anisotropies and the CoO frozen spins in epitaxial CoO/Fe/Ag(001). *Physical Review B* **84**, 094447 (2011) (cited on page 216).

[142] J. Wu, D. Carlton, J. S. Park, Y. Meng, E. Arenholz, A. Doran, A. T. Young, A. Scholl, C. Hwang, H. W. Zhao, J. Bokor, and Z. Q. Qiu. Direct observation of imprinted antiferromagnetic vortex states in CoO/Fe/Ag(001) discs. *Nature Physics* **7**, 303–306 (2011) (cited on page 216).

[143] B. D. Cullity, and C. D. Graham. *Introduction to magnetic materials.* edited by L. Hanzo. 2nd edition (IEEE Press. Piscataway, NJ. 2009) (cited on page 237).

[144] R. F. Mould. Pierre Curie, 1859–1906. *Current Oncology* **14**, 74–82 (2007) (cited on page 237).